Durham E-Theses

The oxidative weathering of organic matter and its carbon dioxide emissions: Insight from the trace elements rhenium and molybdenum

HORAN, KATE

How to cite:

HORAN, KATE (2018) *The oxidative weathering of organic matter and its carbon dioxide emissions: Insight from the trace elements rhenium and molybdenum* , Durham theses, Durham University. Available at Durham E-Theses Online: http://etheses.dur.ac.uk/12663/

Use policy

The full-text may be used and/or reproduced, and given to third parties in any format or medium, without prior permission or charge, for personal research or study, educational, or not-for-profit purposes provided that:

- a full bibliographic reference is made to the original source
- a link is made to the metadata record in Durham E-Theses
- the full-text is not changed in any way

The full-text must not be sold in any format or medium without the formal permission of the copyright holders.

Please consult the full Durham E-Theses policy for further details.

Academic Support Office, Durham University, University Office, Old Elvet, Durham DH1 3HP
e-mail: e-theses.admin@dur.ac.uk Tel: +44 0191 334 6107
http://etheses.dur.ac.uk

The oxidative weathering of organic matter and its carbon dioxide emissions:

Insight from the trace elements rhenium and molybdenum

Kate Horan

A thesis submitted in partial fulfilment of the requirements for the degree of Doctor of Philosophy at Durham University

Department of Earth Sciences, Durham University

November, 2017

Declaration

I declare that this thesis, which I submit for the degree of Doctor of Philosophy at Durham University, is my own work and not substantially the same as any which has previously been submitted at this or any other university.

Kate Horan

©The copyright of this thesis rests with the author. No quotation from it should be published without the author's prior written consent and information derived from it should be acknowledged.

Cover photograph captures the Hooker glacier and its pro-glacial lake in the eastern Southern Alps, New Zealand.

Abstract

Throughout geological history, the exposure of sedimentary rocks to chemical weathering at Earth's surface has profoundly affected the geochemistry of the atmosphere, rivers and oceans. Oxidative weathering reactions can release redox-sensitive trace elements, and the concentration and isotope composition of these elements in geological materials may provide an insight into the environmental conditions and processes occurring both today and over Earth's history. To constrain how Earth's geological carbon cycle operates, and the influence it has on global climate change, a better understanding of the controls on oxidative weathering is required. The oxidation of organic carbon in sedimentary rocks (petrogenic organic carbon, OC_{petro}) releases carbon dioxide (CO_2) from long-term storage in the lithosphere, and consumes atmospheric O_2. Alongside volcanism, the oxidative weathering of OC_{petro} is the main source of CO_2 to the atmosphere over millions of years. However, OC_{petro} oxidation is poorly understood, both in terms of the rate at which it releases CO_2 and the factors that interact to drive the reaction. Trace metals associated with organic matter in rocks, such as rhenium (Re) and molybdenum (Mo), can be released to the dissolved load of rivers during oxidative weathering. Quantifying these element fluxes has the potential, therefore, to provide insight into the oxidative weathering processes involved. Here, rates of OC_{petro} oxidation rates are quantified in rapidly eroding mountain river catchments in the western Southern Alps, New Zealand, and the Mackenzie River Basin, north west Canada. Physical erosion is found to be a first order control on the oxidative weathering fluxes, but catchments dominated by valley glaciers and exposed to frost-shattering processes experience a further two to three times elevation in CO_2 emissions relative to catchments with less glacial cover. The oxidative weathering processes are also found to fractionate metal isotopes (e.g. Mo) in the Critical Zone, which places an important control on the Mo isotope composition of both continental runoff and the World's oceans.

Keywords: Erosion, weathering, river catchments, petrogenic organic carbon, oxidation, redox, rhenium, molybdenum isotopes, carbon cycle, glaciation, global climate

Acknowledgements

The opportunity to study the interactions between geochemistry, Earth's surface processes, carbon cycling and climate change has been very exciting and rewarding. I am grateful to my supervisors Bob Hilton and Kevin Burton for offering me this PhD project and allowing me to pursue my interests. My initial interest in these subject areas was sparked by my school and undergraduate teachers and I am grateful to all those involved in leading me towards this career. Special mentions go to Richard Tighe, Merrick Weems, Ruth Day, Angus Campbell, Diane Hesford, Steve Whittleton and Simon Crowhurst for being especially encouraging and supportive along the way.

During my time in Durham, I have been lucky to be involved with exciting fieldwork in New Zealand and Iceland and I have been able to present my work at international conferences in Prague, France and America; experiences that I thoroughly enjoyed. The opportunities to travel and to meet and interact with diverse groups of people have definitely formed some of the highlights of this research. I am really thankful to Bob and Kevin for allowing me to participate in these trips. I would also like to thank Scott Hawley for providing excellent field assistance in Iceland and New Zealand.

Many thanks go to Dave Selby and Alex McCoy-West for supporting me in the laboratory and enabling me to achieve the geochemical analyses central to this project. Alongside Bob and Kevin, they also both provided insightful discussion on the data collected. Chris Ottley, Becca Neely, Emily Unsworth, Joanna Hesselink, Darren Gröcke and Amanda Hayton provided laboratory support and Xiaomei Xu is thanked for performing ^{14}C analyses. Murray Hicks from the National Institute of Water and Atmospheric Research (NIWA), New Zealand, provided constructive discussion during our visit to New Zealand and is thanked for collaboration. Mathieu Dellinger is also thanked for helpful discussion. Additionally, I would like to thank Bob Hilton, Ed Tipper, Valier Galy, Jérôme Gaillardet, Mathieu Dellinger and Damien Calmels for allowing me to use some of their samples collected in northern Canada in this research. I would also like to thank Matt Hepburn and Dave Stevenson for offering IT support and providing me with a new computer part way through my PhD.

I am very grateful to the Natural Environment Research Council (NERC) for funding the majority of my research. Fieldwork was additionally funded by a Durham University Grant (Building Research Links in New Zealand) and Kevin Burton and Dave Selby kindly covered some additional fieldwork and lab expenses.

Many thanks go to all of my friends in the Earth Sciences department at Durham. It has been a great pleasure to meet so many different people, all of whom have in some way provided me with inspiration and made my time in Durham enjoyable. A special mention has to go to Jordan Phethean for being particularly kind and supportive throughout my time here, and also for leaving me with lots of great memories. Our trips to Yosemite, skiing in the Alps and camping in the Lakes, alongside our many baking endeavours and tea breaks as we were writing up, have always been a lot of fun. My thanks also extend out to Sarah Clancy, Kathi Schweitzer, Alex Peace, Ben Maunder, Erin Scott, Claire Nattrass, Fienke Nanne, Adam Robinson, Emma Gregory, Kate Gallagher and Li Yang, in particular, for positively adding to these experiences. I would also like to thank my friends in the Durham Equestrian Society for providing me with many good memories, especially Charlotte Cass, Ellen Mooney, Galina Badalova, Abi Richards and Maddie Beadle. There's not much that can top our gallops down Crimdon Beach on the horses, come hail or sunshine! Volunteering with Riding for the Disabled Association has also been a thoroughly rewarding experience and playing the flute in the Hill Orchestra and Concert band and touring with these groups in Edinburgh were very enjoyable experiences. During my PhD, I started learning the saxophone and I am grateful to Emma Maslin and my friends in the Cobweb Orchestra for providing a supportive environment that allowed me to gain confidence playing this new instrument.

Additionally, I would like to thank everyone back home for looking out for me. The guys at the Manchester Judo Club, in particular Steve Pullen and Wally Spence, must be thanked for being such a welcoming community to go home to every now and then. Andrew Smith, my piano teacher, is thanked for allowing me to join in with music activities when I'm home. My school and undergraduate friends Sophie Ainscough, Emma Taylor, Chris Barry and Trisna Tungadi have provided that perfect nostalgic break when needed.

Finally, I would like to thank my Mum and Dad for their continued support throughout my studies.

Contents

List of Figures

Chapter 1

Chapter 2

Chapter 3

Chapter 4

Chapter 5

Chapter 6

List of Tables

Abbreviations

AMS	Accelerator Mass Spectrometry
Al	Aluminium
$\alpha_{sec\text{-}diss}$	Isotope fractionation factor between secondary products and the dissolved load
BHVO-1	Basalt, Hawaiian Volcanic Observatory reference material
©	Copyright
C	Carbon
^{14}C	Radiocarbon
Ca	Calcium
Cl	Chloride
CO_2	Carbon dioxide
CrO_3	Chromium trioxide
$\delta^{13}C$	Stable carbon isotope composition, reported as $\delta^{13}C = [((^{13}C /^{12}C)_{sample} / (^{13}C /^{12}C)_{standard}) - 1]$
$\delta^{13}C_{org}$	$\delta^{13}C$ composition of organic matter
$\delta^{98/95}Mo$	Molybdenum isotope composition, reported as $\delta^{98/95}Mo = [((^{98}Mo/^{95}Mo)_{sample} / (^{98}Mo/^{95}Mo)_{standard}) - 1]$
$\delta^{98/95}Mo_{BM}$	$\delta^{98/95}$Mo composition of river bed materials
$\delta^{98/95}Mo_{bulk}$	$\delta^{98/95}$Mo composition of molybdenum in the bulk sample
$\delta^{98/95}Mo_{COL}$	$\delta^{98/95}$Mo composition of colluvium
$\delta^{98/95}Mo_{diss}$	$\delta^{98/95}$Mo composition of dissolved molybdenum
$\delta^{98/95}Mo_{HCl}$	$\delta^{98/95}$Mo composition of molybdenum in hydrochloric acid leach from suspended river sediment
$\delta^{98/95}Mo_{litter}$	$\delta^{98/95}$Mo composition of soil litter
$\delta^{98/95}Mo_{SPM}$	$\delta^{98/95}$Mo composition of river suspended particulate matter
$\delta^{98/95}Mo_{residue}$	$\delta^{98/95}$Mo composition of molybdenum in residue remaining after suspended river sediment leach
$\delta^{98/95}Mo_{rock}$	$\delta^{98/95}$Mo composition of rock
$\Delta^{98/95}Mo_{diss-adsorbed}$	Isotope fractionation between dissolved Mo and Mo adsorbed on to a mineral phase
$\Delta^{98/95}Mo_{diss\text{-}BM}$	Isotope fractionation between dissolved Mo and Mo in river bed materials ($\delta^{98/95}Mo_{diss} - \delta^{98/95}Mo_{BM}$)
$\Delta^{98/95}Mo_{sec\text{-}diss}$	Isotope fractionation factor between secondary products and the dissolved load, also equivalent to "1000 ln ($\alpha_{sec-diss}$)" and given in permil notation

E	East
EA-IRMS	Elemental Analysis – Isotope Ratio Mass Spectrometry
Eh	Reduction potential
ETM	Enhanced Thermatic Mapper
F	Fluoride
f_C	Ratio between the percentage loss of petrogenic organic carbon in soil compared to bedrock versus the percentage loss of Re in soil compared to bedrock
Fe	Iron
$f_{graphite}$	Fraction of OC_{petro} present as graphite
F_{mod}	Fraction of modern carbon
fMo_{diss}	Fraction of Mo left in solution, here calculated as $fMo_{diss} = [Mo]/[Re]_{diss}/[Mo]/[Re]_{BM}$
f_{petro}	Fraction of petrogenic organic carbon
h	Stage height of river
H	Hydrogen
HAc	Acetic acid
HCl	Hydrochloric acid
HCO_3^-	Bicarbonate
HEPA	High Efficiency Particulate Air
HF	Hydrofluoric acid
h_{mean}	Long-term mean stage height of river
HNO_3	Nitric acid
H_2O	Water
H_2O_2	Hydrogen peroxide
HR-ICP-MS	High Resolution – Inductively Coupled Plasma Mass Spectrometry
H_2SO_4	Sulfuric acid
IAPSO	International Association for the Physical Sciences of the Oceans seawater reference material
IC	Ion Chromatography
ICP-AES	Inductively Coupled Plasma Atomic Emission Spectroscopy
ICP-MS	Inductively Coupled Plasma Mass Spectrometry
ID	Isotope Dilution
J_{CO2}	Carbon dioxide oxidation yield
J_{Re}	Dissolved Re yield
K	Potassium
LDPE	Low-density polyethylene

MC-ICP-MS	Multiple Collector – Inductively Coupled Plasma Mass Spectrometry
Mg	Magnesium
Mn	Manganese
Mo	Molybdenum
$[Mo]_{BM}$	Molybdenum concentration in river bed material
$[Mo]_{COL}$	Molybdenum concentration in weathered colluvium
$[Mo]_{diss}$	Dissolved molybdenum concentration
$[Mo]_{SPM}$	Molybdenum concentration in river suspended particulate matter
MQ	Milli-Q ultrapure water
N	North
n	Number of samples
Na	Sodium
[Na*]	Sodium concentration after cyclic correction, [Na*] = [Na] - ([Cl]*0.85)
$[Na^*]_{diss}$	Dissolved sodium concentrations corrected for cyclic input
NaOH	Sodium hydroxide
NH_4NO_3	Ammonium nitrate
NH_4OH	Ammonium hydroxide
NIST SRM	National Institute of Standards and Technology Standard Reference Material
O_2	Oxygen
OC	Organic carbon
$OC_{biosphere}$	Biospheric organic carbon
$[OC]_{BM}$	Total organic carbon concentration in river bed material
$[OC]_{COL}$	Total organic carbon concentration in colluvium
OC_{petro}	Petrogenic organic carbon
$[OC_{total}]$	Total organic carbon concentration
P	Probability value
PES	Polyethersulfone
PFA	Perfluoroalkoxy alkane
pH	Potential of hydrogen
PMP	Polymethylpentane
POC	Particulate Organic Carbon
Q-ICP-MS	Quadrupole – Inductively Coupled Plasma Mass Spectrometry
Q_{mean}	Long-term mean average flow in river
Q_w	Daily water discharge at time of sampling
®	Registered trademark
r^2	Coefficient of determination

Re	Rhenium
$[Re]_{BM}$	Re concentration in river bed material
$[Re]_{COL}$	Re concentration in weathered colluvium
$[Re]_{cyclic}$	Proportion of dissolved river Re derived from precipitation
$[Re]_{diss}$	Dissolved rhenium concentration
$[Re]_{OCpetro}$	Proportion of dissolved river Re derived from OC_{petro}
$[Re]_{silicate}$	Proportion of dissolved river Re derived from silicate minerals
$[Re]_{sulfide}$	Proportion of dissolved river Re derived from sulfide minerals
Ru	Ruthenium
S	South
SARM	Service d'Analyse des Roches et des Minéraux
SBC-1	Bush Creek shale reference material
SCO-1	Cody Shale reference material
SD	Standard Deviation
SE	Standard Error
ΣCations	Sum of cation concentrations
SLRS-5	River water reference material for trace metals
$[SO_4^{2-}]_{diss}$	Dissolved sulfate concentrations
SPA	Super Purity Acid
SPM	Suspended Particulate Matter
T	Temperature
(N)TIMS	(Negative) Thermal Ionisation Mass Spectrometer
TZ^+	Total cation charge balance
TZ^-	Total anion charge balance
USGS	United States Geological Survey
VPDB	Vienna Pee Dee Belemnite
W	West
WSA	Western Southern Alps
wt.	Weight
Zn	Zinc
Zr	Zirconium

Units

%	Percent
‰	Permil
amu	Atomic mass unit
CPS	Counts per second

deg. *or* º	Degree
ºC	Degrees Celsius
kg	Kilogram
g	Gram
mg	Milligram
µg	Microgram
ng	Nanogram
pg	Picogram
L	Litre
mL	Millilitre
M	Molar
mol	Mole
µmol	Micromole
nmol	Nanomole
pmol	Picomole
m	Metre
km	Kilometre
cm	Centimetre
mm	Millimetre
mΩ	Milliohm
t	Tonne
Gt	Gigatonne
Mt	Megatonne
yr	Year
kyr	Thousand year
Myr	Million year
h	Hour
min	Minute
s	Second
ms	Millisecond
V	Volt

Chapter 1

Introduction

Waiho River in the western Southern Alps, New Zealand; September 2014

1.1 Thesis rationale

The desire to understand the carbon transfers accompanying weathering and erosion is the primary stimulus for this research. Redox sensitive elements offer the potential to facilitate this aim and are explored as proxies for quantifying the rates and controls on oxidative weathering reactions in mountain ranges, where high rates of erosion expose rocks to chemical weathering. A secondary motivation of this work is to better understand the imprint of oxidative weathering on the geochemical cycle of Mo and its isotopes, which bears relevance for the use of redox-sensitive trace elements as proxies in the rock record.

1.2 Erosion and weathering in Earth's carbon cycle

On a multimillion-year time scale, the flux of carbon from the solid Earth through volcanic degassing acts as the primary source of carbon dioxide (CO_2) to the atmosphere (Marty and Tolstikhin, 1998). This process is thought to be responsible for the release of ~100 Mt of carbon per year (Berner, 1991). Traditionally, it has been assumed that volcanic CO_2 emissions are removed during silicate weathering by carbonic acid (Ebelmen, 1845; Gaillardet et al., 1999a) at a rate of 140 Mt C yr^{-1} (Gaillardet and Galy, 2008) and via the burial of biospheric organic carbon (Berner, 1982; FranceLanord and Derry, 1997) at a pace of 70 Mt C yr^{-1} (Gaillardet and Galy, 2008) (Figure 1.1). Carbonate weathering by carbonic acid is balanced by carbonate precipitation in the oceans at geological time scales and is generally considered to be CO_2 neutral over $>10^5$ years.

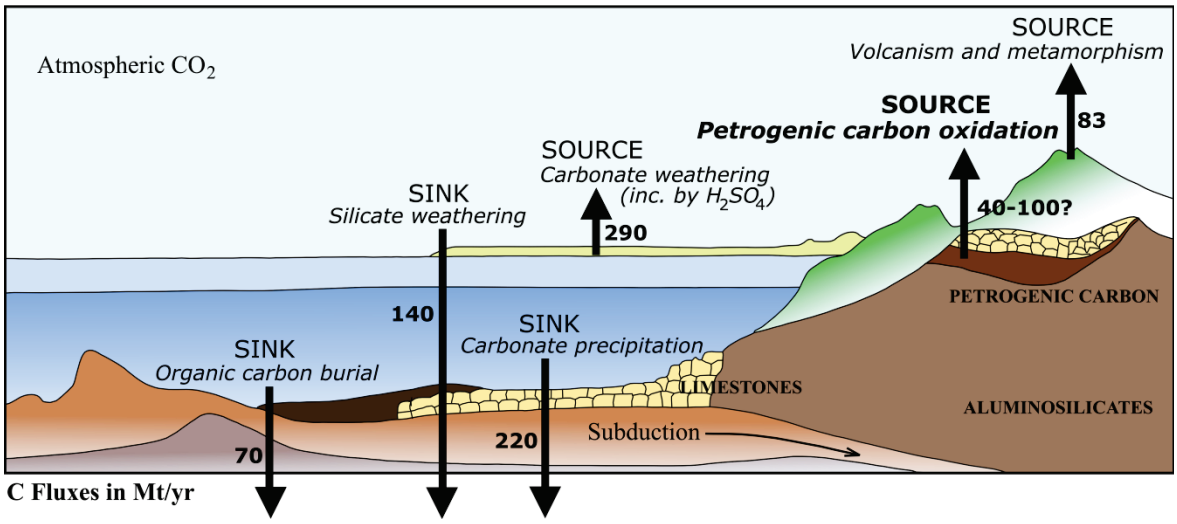

Figure 1.1 Earth's long-term carbon cycle. The Earth hosts distinct carbon reservoirs within the ocean, atmosphere, lithosphere and terrestrial biosphere. These carbon reservoirs interact with each other in biological, chemical and physical reactions over a range of timescales as part of the carbon cycle. The reactions important for understanding long-term (millennial) carbon transfers include organic carbon burial, silicate weathering, petrogenic organic carbon oxidation, carbonate weathering by sulfuric acid, volcanism and metamorphism. The net sequestration of CO_2 by silicate weathering is 70 Mt yr^{-1}. Estimates of carbon fluxes by petrogenic carbon oxidation are from Petsch (2014); other fluxes are from Gaillardet and Galy (2008). Figure is adapted from Gaillardet and Galy (2008).

Recent work has re-emphasised the importance of oxidative weathering reactions in the global carbon cycle. The oxidation of organic carbon in rocks (petrogenic organic carbon, OC_{petro}) during chemical weathering is estimated to release 40–100 Mt of CO_2 to the atmosphere per year (Petsch, 2014) (Figure 1.1). This is comparable to the flux of carbon sequestered during the weathering of silicate minerals, coupled to carbonate precipitation, and the fluxes of carbon from volcanic emissions. In addition, the oxidation of sulfide minerals can produce sulfuric acid that weathers carbonate minerals and results in transient CO_2 release (Calmels et al., 2007; Torres et al., 2014). Although the major geological sources and sinks of CO_2 (Figure 1.1) are recognised, limited case studies exist where they have been measured alongside each other. Nevertheless, the interactions and feedbacks between them lay out the foundations for the evolution of Earth's climate and habitability and are critical for life.

In this research, an assessment of the collective impact of erosion and weathering on CO_2 fluxes is achieved by coupling estimates of OC_{petro} oxidation derived from this work with existing data on the silicate weathering rate, carbonate weathering rate by sulfuric acid and the sedimentary burial of biospheric organic carbon. Consequently, the net transfers of carbon between the atmosphere and lithospheric storage may be understood (Berner and Caldeira, 1997), and the implications of how they potentially act to dampen or amplify Earth's long-term climate may be evaluated.

1.3 Petrogenic organic carbon oxidation

Globally, ~1.5×10^7 Gt of carbon is stored in sedimentary rocks as OC_{petro} (Sigman and Boyle, 2000). This OC_{petro} is initially buried in sediments, but becomes structurally and chemically transformed during diagenesis and metamorphism and may be later re-exposed at Earth's surface. The majority of this organic carbon occurs in sedimentary rocks in the form of solid-phase, macro-molecular organic matter termed kerogen (Chang and Berner, 1999; Petsch, 2014). Although kerogen can be highly concentrated in some rocks, for example coals can contain >75% organic carbon (Dai et al., 2015) and organic-rich black shales can have >5–10 wt. % organic carbon (e.g. Jaffe et al., 2002), most organic carbon in sedimentary rocks is present at very low concentrations of typically less than 1 wt. % (Berner and Canfield, 1989; Raiswell and Berner, 1986; Ronov, 1976; Turekian and Wedepohl., 1961). Graphite, a highly condensed polyaromatic mineral, is also a form of OC_{petro} and develops during the metamorphism of organic matter bearing sedimentary rocks (Beyssac et al., 2007), but it is generally considered to be resilient to oxidation (Bouchez et al., 2010; Galy et al., 2008). Transitional carbon species between kerogen and graphite also form during metamorphism, including black carbon, which is a highly condensed material formed during incomplete combustion of vegetation over geological history (Petsch, 2014).

The reservoir of organic carbon in rocks equates to 25,000 times the total amount of carbon present in the pre-industrial atmosphere (Sigman and Boyle, 2000) and ~30,000 times the mass of carbon stored in all living matter (Keller and Bacon, 1998). At the global scale, about 1100 Gt are estimated to be present in the upper 1 m of the continental surface (Copard et al., 2007), which is similar to the stock of biospheric carbon in soils (1576 Gt: Eswaran et al., 1993). The re-exposure of OC_{petro} at Earth's surface makes it vulnerable to oxidative weathering; a process that acts to release CO_2 to the atmosphere from long-term (>10^6 years) storage in the lithosphere. The oxidation of OC_{petro} may be summarized by Equation 1.1 and is considered to be equivalent to the respiration of the rock (e.g. Hilton et al., 2014).

Equation 1.1 $$CH_2O + O_2 \rightarrow CO_2 + H_2O$$

Oxidative weathering reactions proceed as oxidizing gases and surficial fluids permeate through rocks and attack mineral phases (Petsch et al., 2000). A few studies based on soil profiles have attempted to determine rates of OC_{petro} oxidation (e.g. Keller and Bacon, 1998). However, while the chemical denudation of silicate rocks has been studied in detail (e.g. Berner and Maasch, 1996; Gaillardet et al., 1999b; Walker et al., 1981), quantification of the rate of OC_{petro} oxidation during chemical weathering is limited to only a few river catchments globally, such as in the floodplains of the Beni River (Bouchez et al., 2010), the Ganges River (Galy et al., 2008), the Yamuna River (Dalai et al., 2002) and within mountain river catchments of Taiwan (Hilton et al., 2014). Other studies have tracked the erosion of unweathered OC_{petro} (Blair et al., 2003; Galy et al., 2015; Hilton et al., 2011; Komada et al., 2004). This means there is little constraint on the net exchange of CO_2 with the atmosphere in river catchments that is caused by erosion and weathering.

1.4 Potential controls on oxidative weathering reactions

Chemical weathering depends upon many interrelated parameters that together set reaction rates and fluxes. These include mineralogy (Bluth and Kump, 1994), rainfall and associated runoff (Gaillardet et al., 1999), temperature (White and Blum, 1995), pH (Moulton and Berner, 1998), the age of the surfaces (Chadwick et al., 1999), the surface area of particles (Chang and Berner, 1999), the supply of water and its residence time in the regolith (Maher and Chamberlain, 2014), erosion rates (e.g. West et al., 2005), tectonic activity and vegetation cover (Anderson, 2007; Beaulieu et al., 2012, 2011; Gislason et al., 2008; Lupker et al., 2013). These factors have mainly received attention from the perspective of seeking to understand and quantify silicate weathering. However, they are also relevant to the oxidative weathering of organic matter.

1.4.1 Oxygen

The oxygen (O_2) concentration in the atmosphere may place constraint on the extent to which OC_{petro} oxidative weathering reactions may be effective. The flux of O_2 consumed during the weathering of OC_{petro} is generally set by the organic matter content at depth and the erosion rate (Figure 1.2) (Bolton et al., 2006). Deeper oxidative weathering fronts are encouraged by slow erosion, and/or low organic matter contents, high air porosity, high atmospheric O_2 level and low water saturation (Bolton et al., 2006). Other physical properties of soil materials, such as grain size, may also be important (Bolton et al., 2006). In regions of rapid erosion, or during periods of low atmospheric O_2, the diffusion rate of O_2 into soils and rates of reaction may lead to O_2-dependent weathering (Bolton et al., 2006; Lasaga and Ohmoto, 2002).

The role of variable hydrological conditions, such as changes in precipitation or fluctuations in the water table, may be important for understanding O_2 consumption in the subsurface weathering environment (Chang and Berner, 1999), as O_2 availability for weathering reactions may be reduced in water logged soils. Similarly, in subglacial environments, the O_2 rather than the CO_2 content of waters in the subglacial drainage system can be a major determinant on the chemical weathering potential of meltwaters (Tranter et al., 2002).

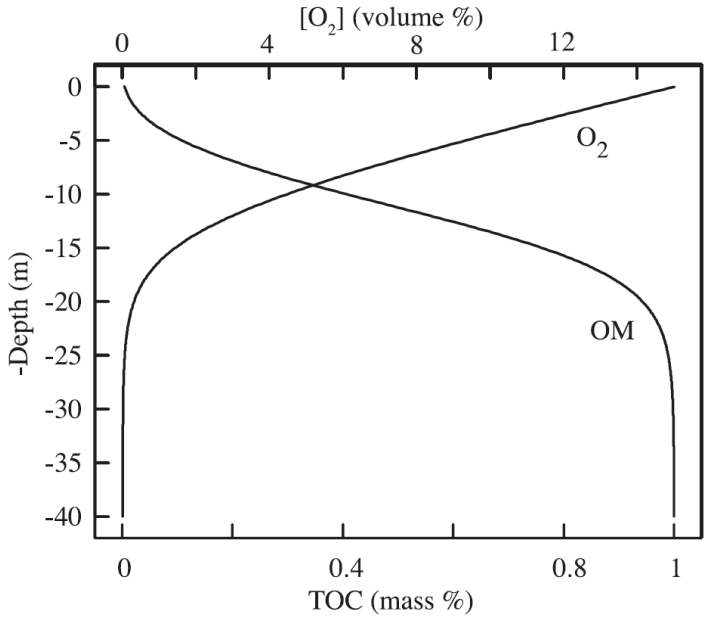

Figure 1.2 Modelled distributions for oxygen and organic matter in a depth profile subject to an erosion rate of 0.5 mm yr^{-1}. Soil profiles may experience a rate limitation by organic matter reactivity and abundance in well-oxygenated depths of a soil profile and O_2 limitation at greater depths. Figure is from Bolton et al. (2006).

1.4.2 Mineral supply by physical erosion

Several studies have alluded to the important link between physical erosion rates and associated chemical weathering fluxes (Gaillardet et al., 1999a; Millot et al., 2002; West et al., 2005) (Figure

1.3). At low physical erosion rates, a long residence time for the particles in the weathering zone leads to a longer contact time between organic matter and oxidising surface waters and an increase in the extent, or intensity, of chemical weathering (Dupre et al., 2003). In contrast, in a small sample set of granitic and basaltic catchments, Millot et al. (2002) determined that a tenfold increase in physical weathering would increase the chemical weathering yield by a factor of 4.6. Data from several catchments in New Zealand hosted in the Alpine Schist, a greywacke/argillite, indicate that a factor of ten increase in physical erosion will result in an increase in chemical erosion rate by a factor of 2.9 (Lyons et al., 2005). In these highly erosive settings, the combination of a continuous supply of fresh, easily weatherable mineral surfaces generated by erosion alongside copious precipitation in contact with fresh minerals is thought to promote high chemical weathering yields (Lyons et al., 2005; Petsch et al., 2000; West et al., 2005). The net large scale erosional potential of a landscape should increase with precipitation, drainage area and slope (Montgomery et al., 2001).

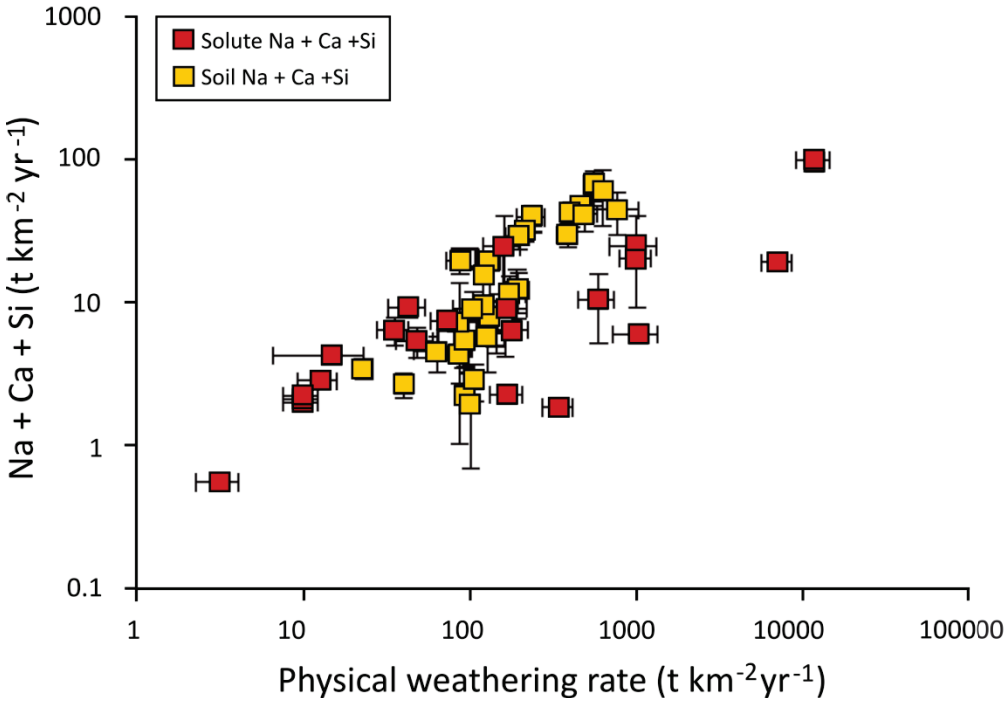

Figure 1.3 Chemical weathering rates for silicate rocks across a range of physical erosion rates in global river catchments. Chemical weathering rates are provided by either soil data or solute data (as indicated in the key) and given as the Na + Ca + Si ion flux. The physical erosion rate is based on either sediment flux data or erosion rate estimates from cosmogenic nuclide accumulation in sediments. Errors are ±1 SD. Figure is adapted from West et al. (2005).

Physical erosion rate has been hypothesised to be a major control specifically on OC_{petro} oxidation rate (Petsch et al., 2000). Models of OC_{petro} oxidation also predict higher oxidative weathering rates as erosion increases (Bolton et al., 2006). This may be particularly relevant in steep mountain

catchments that generate large volumes of sediment with a fresh reactive surface area (Hilton et al., 2014). Data from Taiwanese catchments demonstrate that increases in suspended sediment yield (t km^{-2} yr^{-1}), a proxy for physical erosion rate, are associated with concomitant increases in OC_{petro} oxidation (Figure 1.4). In mountain belts, deep seated landslides and gully erosion processes may entrain older more refractory material derived from deeper soil horizons and sedimentary rocks (Leithold et al., 2013) and landslide deposits can provide loci for weathering of this material (Emberson et al., 2016). In these rapidly denuding basins, the rate of erosion exceeds the rate at which bedrock is converted to regolith, so processes that remove bedrock containing OC_{petro} dominate (Hilton et al., 2008; Hovius et al., 1997).

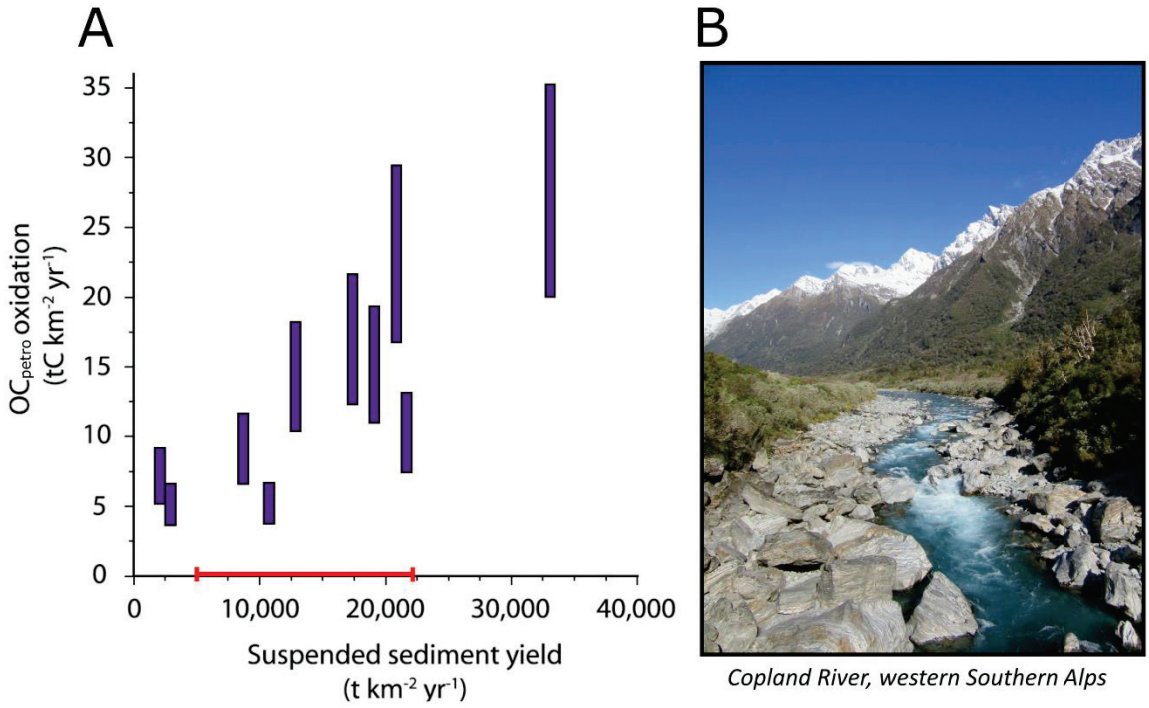

Figure 1.4 Oxidative weathering increases with physical erosion. A. Taiwanese study highlighting mountain river catchments as important sites for oxidative weathering reactions (Hilton et al., 2014). Annual sediment yields (t km^{-2} yr^{-1}) for the catchments provide a means of quantifying physical erosion. The solid red line shows the range of physical erosion rates in the Southern Alps (***Chapter 3***) for comparison. The method used to estimate the carbon fluxes by OC_{petro} oxidation is discussed in section 1.5 'Elemental Proxies'. **B.** Photograph of the Copland River, western Southern Alps, New Zealand; a typical steep sided catchment experiencing high erosion and runoff rates.

Nevertheless, although weathering is dependent on the supply of fresh minerals when erosion rates are low, chemical weathering becomes increasingly kinetically limited as erosion rates increase due to the reduced mineral residence times in soil (e.g. White and Brantley, 2003). For silicate weathering, the kinetics of mineral dissolution mean that weathering fluxes generally become reaction limited at denudation rates above ~100 to 1000 t km^{-2} yr^{-1}; typically in high-relief active regions (West, 2012; West et al., 2005). At this point, silicate weathering rates are regulated by temperature and runoff (Maher and Chamberlain, 2014; West, 2012). This means that locations with high weathering rates (e.g. Taiwan, New Zealand, the Himalaya) may be particularly

important in determining global carbon cycle feedbacks, despite only contributing a relatively small proportion to the total global weathering flux (Milliman and Farnsworth, 2011). During times of global warming and amplification of the hydrologic cycle, weathering fluxes will increase disproportionately between tectonically active and inactive areas, with high-relief tectonic areas having higher chemical weathering fluxes (Maher and Chamberlain, 2014; West, 2012).

By analogy with silicate weathering, OC_{petro} oxidation may have a heightened response rate to kinetic parameters (e.g. temperature, O_2 supply) at high erosion rates. The reaction kinetics of OC_{petro} weathering appear to be ~10 times faster than the kinetics of silicate mineral weathering, according to the O_2 consumption rate of coal organic matter in oxidation experiments (Chang and Berner, 1999). This means that the kinetic limitation of weathering reactions may occur at higher erosion rates for OC_{petro}, given the high concentrations of O_2 in the present day atmosphere (Bolton et al., 2006). Consequently, erosion and associated bedrock weathering of OC_{petro} in mountain belts should have important implications for the long-term evolution of Earth's carbon cycle and may also be important for maintaining climate-stabilizing feedbacks (West, 2012).

1.4.2 Erosion process type (e.g. glaciation)

Mechanical erosion by temperate glaciers may exceed erosion rates in mountainous fluvial catchments by an order of magnitude (Anderson, 2005; Hallet et al., 1996; Herman et al., 2013), implying that chemical weathering fluxes may also be higher in glaciated catchments (Anderson, 2005). Glaciers pluck, abrade and grind material, and frost-cracking processes also disrupt mineral lattices. This results in a sediment load characterized by a wide range of grain sizes, and sediment yields can be substantially higher than in other environments (Anderson, 2005) (Figure 1.5). The high rates of reactive mineral surface area production render these glacial sediments highly weatherable.

Previously, increases in silicate weathering have been inferred to have been promoted by glaciation (e.g. Riebe et al., 2004; West et al., 2005). The results may be similar for OC_{petro} oxidation (Figure 1.6), given that OC_{petro} weathering is thought to be supply limited (Hilton et al., 2014). In glaciated catchments, there are large quantities of fine particles with high reactive surface areas in environments with high water availability (Anderson, 2005; Hales and Roering, 2009), which should promote rapid oxidation of OC_{petro} provided that the cold temperature does not limit the oxidation rate.

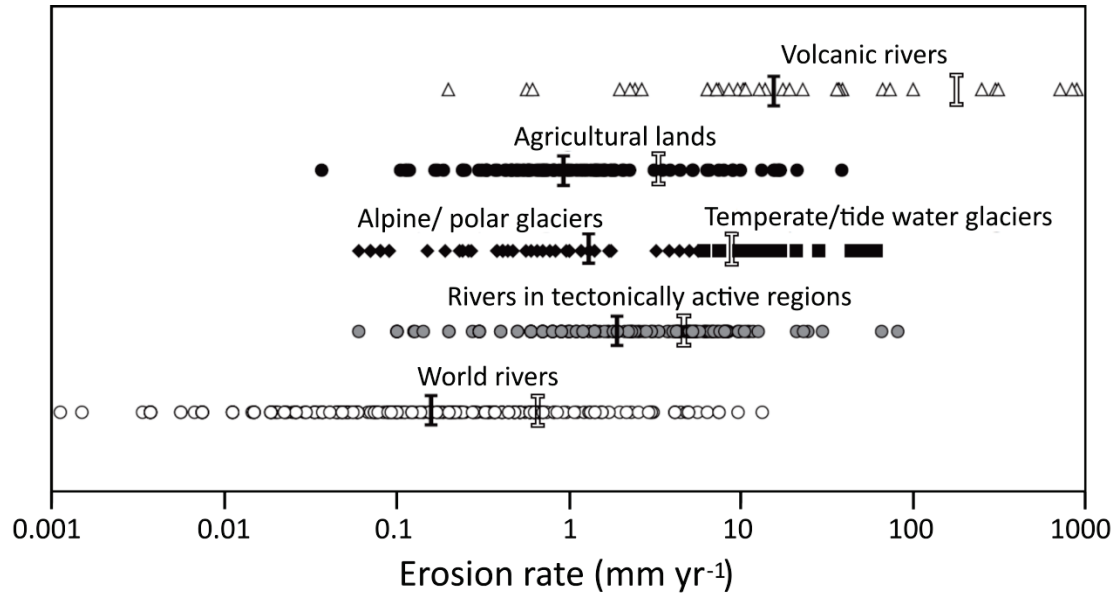

Figure 1.5 Erosion rates across different landscapes. Erosion rates were calculated from measurements of sediment yield over timescales of 1–10 years. The median of each dataset is indicated by a black bar and the mean by a white bar. Figure is from Koppes and Montgomery (2009).

Although low temperatures can inhibit silicate mineral weathering (Anderson, 2007, 2005; West et al., 2005), high rates of OC_{petro} oxidation may be sustained by microbially mediated reactions (Skidmore et al., 2000; Telling et al., 2015). Previous studies have outlined a role for biological activity in driving the solute flux from sub-ice environments (e.g. Wadham et al., 2010) and during primary succession on moraine deposits (Bardgett et al., 2007; Tranter et al., 2002; Wadham et al., 2004). For example, the chemotrophic microbial communities found in the dark conditions that pervade subglacial habitats (Boyd et al., 2014) may enhance subglacial sulfide weathering (Bottrell and Tranter, 2002; Tranter et al., 2002). Microbes may produce oxidizing agents, such as peroxides, which attack the organic structure of rock-bound organic matter (Crawford and Nielsen, 1995; Faison and Lewis, 1990; Ralph et al., 1996) and facilitate oxidation.

In addition, glaciated catchments have low vegetation and soil cover meaning there is less demand for O_2 by heterotrophic respiration and the O_2 content of surface waters, soil horizons and exposed bedrock should be elevated, relative to less glaciated catchments. Limited soil development also means there is less protection against oxidation for deep rock-derived carbon (Bardgett et al., 2007). Consequently, it might be expected that these sites would transfer higher CO_2 fluxes to the atmosphere for a given physical erosion rate (Figure 1.6).

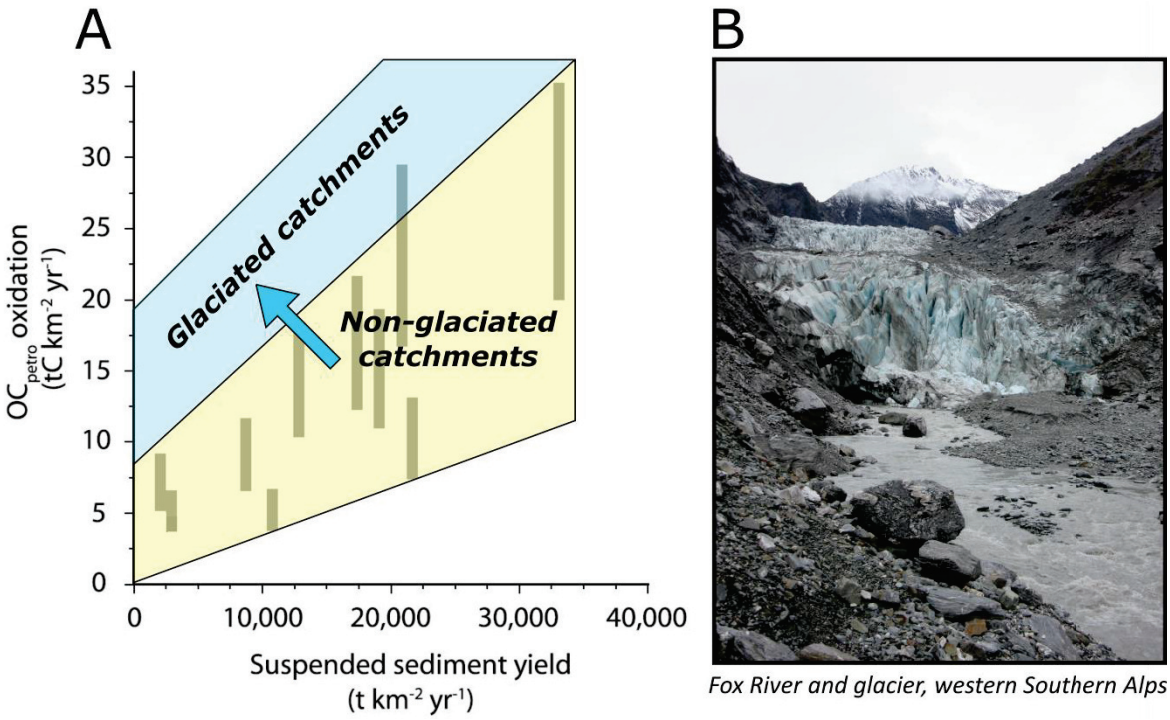

Figure 1.6 Oxidative weathering increases with mountain glaciation. A. Hypothetical relationship between physical erosion yield and oxidative weathering of OC_{petro} as mountain catchments become glaciated. Data for the non-glacial catchments (Taiwan) are from Hilton et al. (2014). **B.** Photograph of the Fox glacier and river in the western Southern Alps, New Zealand. The Fox is a typical steep sided glacial catchment experiencing high erosion rates and the effects of glaciation.

It is not well understood how changes in Earth's climate over millions of years might modify the major CO_2 emission by OC_{petro} oxidation. However, the low temperatures associated with glacial catchments have been hypothesised to contribute to the high sulfide relative to silicate weathering fluxes (Torres et al., 2017) and it is likely that OC_{petro} oxidation may also be enhanced relative to silicate weathering. An increase in OC_{petro} oxidation rates in glacial environments could imply that CO_2 release will be highest during periods of repeated mountain glaciation over millennia (Herman et al., 2013) and provide a mechanism to counter long-term cooling trends in Earth's climate. The connections between glaciation, chemical weathering, and the global carbon cycle could therefore steer the evolution of global climate over geological time.

1.5 Elemental proxies for quantifying oxidative weathering of OC_{petro}

1.5.1 Tracking carbon

Early attempts to assess the chemical weathering of OC_{petro} were made using weathering profiles developed on organic carbon-rich black shales. Here, the loss and degradation of organic matter during oxidative weathering reactions could be tracked through the percentage decrease in organic matter concentration in initial unweathered parent lithology through to surficial highly weathered materials (Petsch et al., 2000). The effects of weathering can be clearly visible at the outcrop scale (Figure 1.7).

In these studies, the extent of weathering was found to be determined by the rate of physical erosion and the exposure of the rock to oxidising surface waters, with organic matter type and composition playing a smaller role. Pyrite loss was also found to coincide with, or precede, organic carbon loss, suggesting that the kinetics of organic matter weathering are no faster than pyrite oxidation (Petsch et al., 2000). Consequently, the oxidative weathering of sulfide minerals continues deeper into soil profiles, while OC_{petro} may still be found at concentrations similar to the unweathered bedrock (Jaffe et al., 2002). These observations support data from coal weathering experiments, where the O_2 consumption rate is found to be two to three orders of magnitude lower than for pyrite oxidation in water, but still rapid on a geological timescales (Chang and Berner, 1999). Nevertheless, tracking OC_{petro} oxidation fluxes at soil profiles presents a significant challenge because the volume of material that has been oxidised and the timeframe over which this has occurred is difficult to quantify.

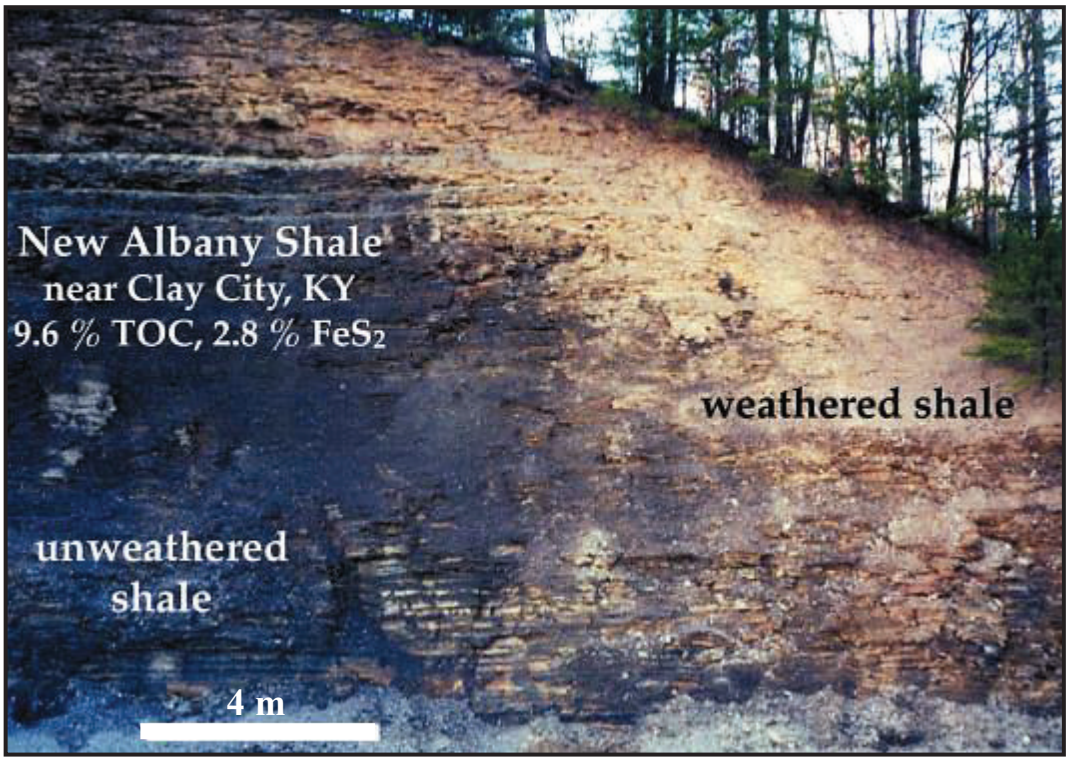

Figure 1.7 Weathering of OC_{petro} in outcrop. Field site near Clay City, Kentucky, USA, showing a weathering profile developed on New Albany Shale that has been exposed in a roadcut. Unweathered shale (left) grades laterally into heavily weathered regolith (right). Evidence for weathering includes changing colour, increased fissility and friability, loss of organic carbon and loss of pyrite. Figure is from Petsch et al. (2001).

Direct capture of CO_2 produced in the subsurface may lend further insight into the extent of OC_{petro} oxidation. In this approach, the CO_2 derived from OC_{petro} has to be identified from the CO_2 produced by recent biospheric respiration and the atmosphere because only the oxidation of OC_{petro} represents an input of carbon to the global carbon cycle. This may be achieved using radiocarbon

measurements (Keller and Bacon, 1998). Applying this approach on a large scale is difficult, however, due to the difficulty in trapping the gas produced and the spatial restriction of measurements to gas sampling wells. The extent of oxidation in a single soil profile may also not be representative at the catchment scale, which makes interpreting the spatial extent of OC_{petro} oxidation challenging.

The oxidation of OC_{petro} is only just beginning to be addressed in mountain river catchments (Bouchez et al., 2014; Galy et al., 2008; Hilton et al., 2014, 2011). In the Himalaya, Raman micro-spectroscopy and transmission electron microscopy have been used to detect OC_{petro} in the rivers (Ganges-Brahmaputra system) and marine sediments (Bangladesh delta) (Galy et al., 2008). Data indicate that up to 70% of the less graphitised forms of carbon may be oxidised during fluvial transport. In the Amazon River system, Bouchez et al. (2010) combined Raman micro-spectroscopy with measurements of particulate organic carbon and ^{14}C activity and observed a tenfold decrease in OC_{petro} content between the black shale outcrops in the Beni River catchment and lowland sampling locations; in the Madeira floodplain only ~15% of the OC_{petro} was preserved. The constancy in the absolute OC_{petro} content measured along depth profiles in this Amazon River system suggests that preferential burial of a given size fraction in the floodplain does not affect the OC_{petro} concentration of suspended sediments and that the observed decrease of OC_{petro} is a consequence of its oxidation. Nevertheless, attempting to assess these processes in mountain headwaters is challenging, particularly in steep active catchments where rapid physical erosion of OC_{petro} can occur faster than its chemical erosion in the weathering zone (Hilton et al., 2011; Petsch et al., 2000). In such instances, suspended sediments in mountain rivers have similar geochemical compositions to bedrocks (Hilton et al., 2010) and the radiocarbon content of OC in suspended load does not have the resolution necessary to quantify OC_{petro} loss from the solid phase (Hilton et al., 2014).

1.5.2 Rhenium proxy

Detailed constraints on chemical weathering processes and inorganic carbon fluxes in mountain catchments (Calmels et al., 2011; Jacobson and Blum, 2003; West et al., 2005) have previously been achieved by tracking the products of chemical weathering that are carried in the dissolved load of rivers (Gaillardet et al., 1999a; Meybeck, 1987). Therefore, it is possible that quantifying the OC_{petro} oxidation yield using the dissolved river load may be achieved more easily and effectively than methods characterizing the solid products of weathering (Figure 1.8).

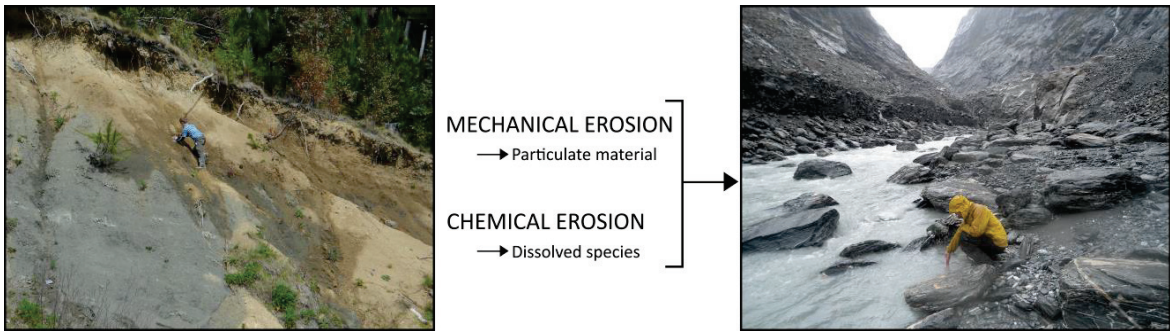

Figure 1.8 Weathering signals in catchments. A. Soil-rock profile in the Waipaoa catchment, New Zealand that has been chemically altered during weathering. **B**. A typical river catchment that was sampled for river bedload material, suspended sediments and the dissolved products of weathering.

The association between organic carbon and redox sensitive metals such as molybdenum (Mo) and rhenium (Re) in sedimentary rocks has been documented in both modern and ancient reducing sediments, including black shales and sulfides (Dalai et al., 2002; Miller et al., 2011; Peucker-Ehrenbrink and Hannigan, 2000). Colodner et al. (1993) estimate that ~43% (~36,000 mol) of the present annual riverine Re input is sequestered by anoxic marine sediments under mildly reducing conditions. The high concentrations of organic carbon, the low pH arising from the oxidation of pyritic sulfur, and the predominantly clay mineralogy render black shales susceptible to alteration. The oxidation of these sediments releases Re, Mo and other platinum group elements associated with the labile organic fraction, and these trace elements become mobile in near-surface environments (Jaffe et al., 2002).

The trace element rhenium (Re) holds strong potential as a proxy for tracking OC_{petro} oxidation during weathering (Dalai et al., 2002; Jaffe et al., 2002) as a result its association with OC_{petro} in rocks and its redox-dependent solubility (Dalai et al., 2002; Hilton et al., 2014; Jaffe et al., 2002; Petsch, 2014). Weathering studies from soils on OC-rich rocks have showed that Re loss tracks OC_{petro} loss (Jaffe et al., 2002) (Figure 1.9). As sedimentary rocks are re-exposed at Earth's surface, for example by erosion and exhumation during orogenesis (e.g. Hilton et al., 2011), oxidising gases and fluids permeate through the rocks, degrading organic matter and converting it to CO_2. At the same time, Re is oxidised and becomes mobile. In oxygenated waters (Eh > 0V), with pH values between 5.5 and 9.5, Re is dominantly present as the soluble perrhenate oxyanion (ReO_4^-) (Brookins, 1986).

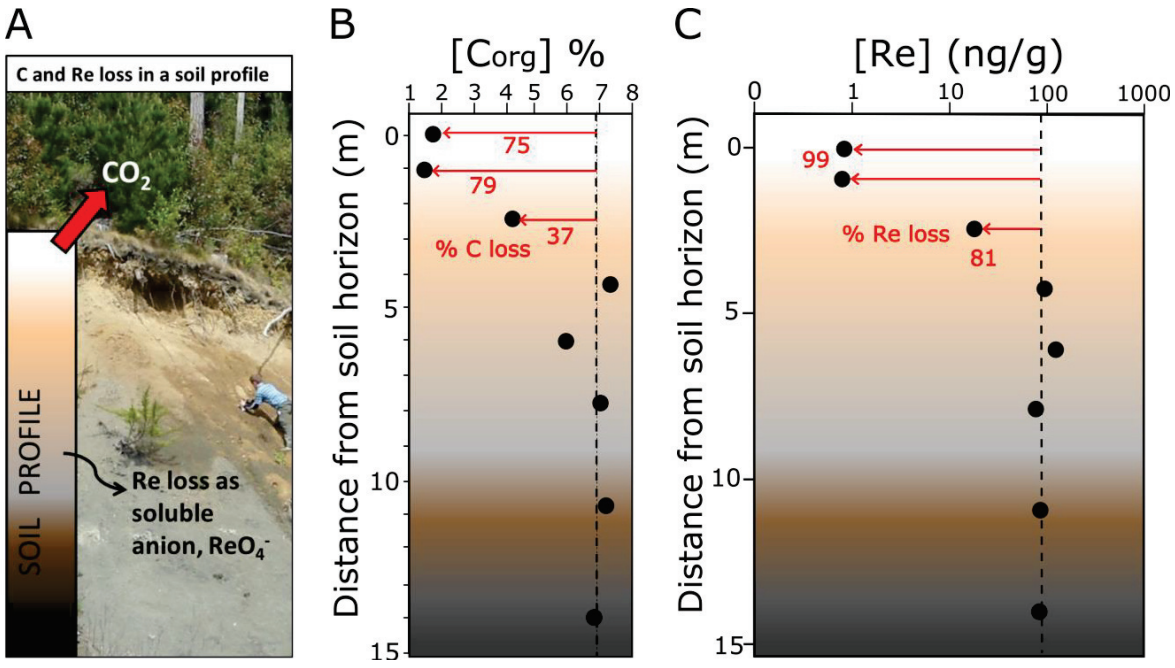

Figure 1.9 Oxidative weathering of OC_{petro} on hillslopes and the relationship between OC_{petro} and Re upon oxidation. A. Soil profile in the Waipaoa catchment in North Island, New Zealand. The changing colour in the soil profile reflects a loss of carbon closer to the surface. **B.** Data on carbon concentrations with depth indicate a loss of carbon occurs close to surface in soil profiles. Data are from Jaffe et al. (2002) for the Ohio Shale. **C.** Loss of Re across the same profile as in **B.** (Jaffe et al., 2002).

Rhenium is not thought to be cycled through the modern terrestrial biosphere (*cf.* Mo: see section 1.6). Consequently, the mobilized ReO_4^- enters the hydrological network (Brookins, 1986; Colodner et al., 1993; Miller et al., 2011) and may be detected in the dissolved river load (Figure 1.10). The degree of mobility is a reflection of the oxidation potential in the soil, the redox-state of the ground water and the amount of organic matter present (Hilton et al., 2014). Rivers integrate chemical reactions and hydrological sources across the landscape (Gaillardet et al., 1999). As a result, the dissolved Re flux can be considered to result from the oxidative weathering reactions occurring upstream (Dalai et al., 2002). Recent Re data from Taiwan highlight the oxidative weathering of petrogenic organic carbon as a potentially important source of CO_2 in mountain belts (Hilton et al., 2014). Expanding on this previous work, which has established the close affinity of Re and OC_{petro} in sedimentary rocks and their coupled behaviour during oxidative weathering, this research aims to examine the transfer of Re in river catchments with high erosion rates with a view to better constraining the main controls on OC_{petro} oxidation (***Chapters 3*** and ***4***).

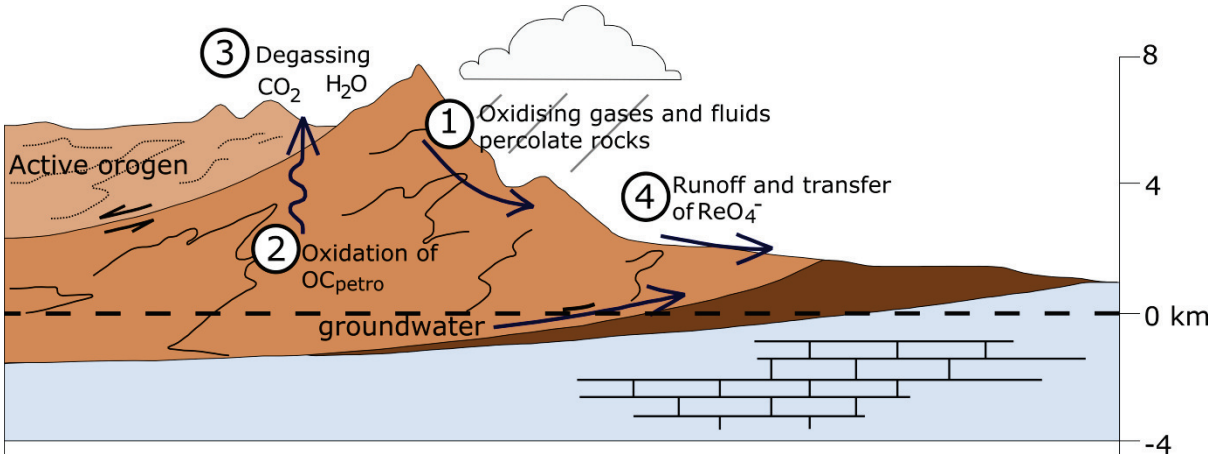

Figure 1.10 Oxidative weathering of OC_{petro} in a mountain belt. Oxidising gases and fluids percolate through soils and rocks and react with Re-bearing OC_{petro}. Carbon dioxide is released to the atmosphere and the Re is oxidised to the ReO_4^- anion, which may be detected within the dissolved products of weathering (e.g. Jaffe et al., 2002; Petsch et al., 2000; Pierson-Wickmann et al., 2002).

The dissolved Re abundance in river water is generally very low, with reported global values falling between 0.72 and 164 pmol L^{-1} (Miller et al., 2011). As a result, in this research two techniques for measuring low-concentration Re in the waters are explored. First, a direct calibration of Re concentrations in the water samples against ICP-MS Re standards. Second, a chemical separation and purification method (anion exchange column chemistry) is used in conjunction with isotope dilution. We discuss the two techniques and compare the Re river water data quantified by each, in order to assess the reliability and validity of the different methods (***Chapter 2***).

By combining measurements on dissolved river Re concentrations with water discharge from gauged rivers it is possible to calculate a dissolved Re flux in mountain river catchments. This flux may be a proxy that will provide constraint on the OC_{petro} oxidation rate and the associated CO_2 release across a range of mountain belts. OC_{petro} oxidation rates (J_{CO2}) may be quantified from the dissolved Re flux (J_{Re}), provided the Re to OC_{petro} ratio ($[OC_{petro}]_{BM}/[Re]_{BM}$) of the rocks that have undergone weathering is known (Equation 1.2). This is the approach that is used by Hilton et al. (2014).

Equation 1.2 $$J_{CO2} = J_{Re} \times ([OC_{petro}]_{BM}/[Re]_{BM})$$

However, other mineral phases may supply Re to the dissolved load, such as sulfides and silicates, and it is possible to improve estimates of OC_{petro} oxidation by accounting for the proportion of Re derived from OC_{petro} versus silicate and silicate minerals (Dalai et al., 2002) and any differences in the relative mobility of Re and OC_{petro} in the weathering zone. These two factors are accounted for by the term f_C in Equation 1.3.

Equation 1.3 $$J_{CO2} = J_{Re} \times ([OC_{petro}]_{BM}/[Re]_{BM}) \times f_C$$

Further improvements to OC_{petro} oxidation estimates may be achieved by considering the uncertainty in the fraction of OC_{petro} which may not be susceptible to oxidation ($f_{graphite}$) (Galy et al., 2008) (Equation 1.4).

.

Equation 1.4 $$J_{CO2} = J_{Re} \times ([OC_{petro}]_{BM}/[Re]_{BM}) \times f_C \times (1 - f_{graphite})$$

1.6 Oxidative weathering and the geochemical cycle of molybdenum

The oxidative weathering of sedimentary rocks can release redox-sensitive trace elements whose isotope composition lends insight into the environmental conditions and/or processes occurring both today and over Earth's history. Molybdenum isotopes may be applied to investigate the weathering and redox reactions that initiated marine and atmospheric oxygenation (e.g. Duan et al., 2010; Voegelin et al., 2010; Wille et al., 2007), drive modern and ancient biological processes (e.g. Boyd et al., 2011; Zerkle et al., 2011) and set the chemical composition of rivers and the oceans (e.g. Archer and Vance, 2008; Pearce et al., 2010a; Voegelin et al., 2012).

There are three major sinks of Mo from the ocean that may be defined according to environmental conditions: well-oxygenated settings, sulfidic sediments overlain by weakly oxygenated bottom waters, and euxinic settings characterized by the presence of hydrogen sulfide (H_2S) in the water column (Figure 1.11) (Kendall et al., 2017). The extent of fractionation of Mo isotopes accompanying Mo removal can be considered to be a function of the local redox state in the depositional environment. The well-oxygenated setting is characterised by the largest Mo isotope fractionations. Under oxidising conditions Mo is present in solution as the stable molybdate ion, MoO_4^{2-}. In this form, Mo is slowly removed from the water column through uptake into ferromanganese phases, which preferentially incorporate isotopically light Mo (Barling et al., 2001; Barling and Anbar, 2004; Goldberg et al., 2009; Miller et al., 2011; Wasylenki et al., 2011). As a result of this fractionation, the modern oceans are the heaviest Mo reservoir on Earth (Kendall et al., 2017).

In contrast, Mo is readily removed from solution in anoxic-sulfidic waters with very little net isotope fractionation. In the presence of reduced sulfur, Mo forms oxothiomolybdate ions, $[MoO_4\text{-}xSx]^{2-}$, which are highly particle-reactive and thus rapidly removed from solution (e.g. Barling et al., 2001). In the deep waters of restricted euxinic basins, the reaction of Mo with H_2S in anoxic aqueous solutions to form thiomolybate results in little or no offset between sediments and Mo source (seawater) as Mo is quantitatively scavenged from solution (Dahl et al., 2010; Nägler et

al., 2011; Neubert et al., 2008; Noordmann et al., 2015). Therefore, in the most reducing conditions organic rich sediments can directly capture the seawater Mo isotope composition.

Molybdenum isotope variability amongst marine sediments in the geological record can provide important constraints on palaeo-redox states and may be used to estimate the spatial extent of past oceanic euxinia and the extent of atmosphere–ocean oxygenation (e.g. Arnold et al., 2004; Barling et al., 2001; Dahl et al., 2011; Dickson et al., 2012; Kendall et al., 2011, 2009, Pearce et al., 2010b, 2008; Siebert et al., 2003). However, the use of Mo isotopes as a palaeo-redox proxy in marine sediments requires quantification of the controls on the isotope composition of Mo inputs to the ocean. Oceanic Mo input is dominated by river supply, with only a small (~5–10%) contribution from low temperature hydrothermal systems (McManus et al., 2002; Miller et al., 2011; Reinhard et al., 2013; Wheat et al., 2002) and a negligible input from dust and aerosols (Morford and Emerson, 1999) (Figure 1.10). The Mo isotope composition is reported as shown in Equation 1.5

Equation 1.5
$$\delta^{98/95}\mathrm{Mo}_{\mathrm{sample}} = \left[\left(\frac{^{98/95}\mathrm{Mo}_{\mathrm{sample}}}{^{98/95}\mathrm{Mo}_{\mathrm{NIST-3134}}}\right) - 1\right] \times 1000$$

where the $\delta^{98/95}$Mo of the NIST 3134 standard = 0‰. Variability in the Mo isotope composition of rivers is large (Archer and Vance, 2008), ranging from -0.1 to 2.15‰ (Archer and Vance, 2008; Neubert et al., 2011; Pearce et al., 2010a; Voegelin et al., 2012; Wang et al., 2015). It is thought that this variability may be linked to the highly redox sensitive behaviour of Mo and may reflect fractionation occurring during weathering and mobilisation of Mo (Archer and Vance, 2008; Pearce et al., 2010a). In addition, the composition of rocks undergoing weathering may be important (Neubert et al., 2011).

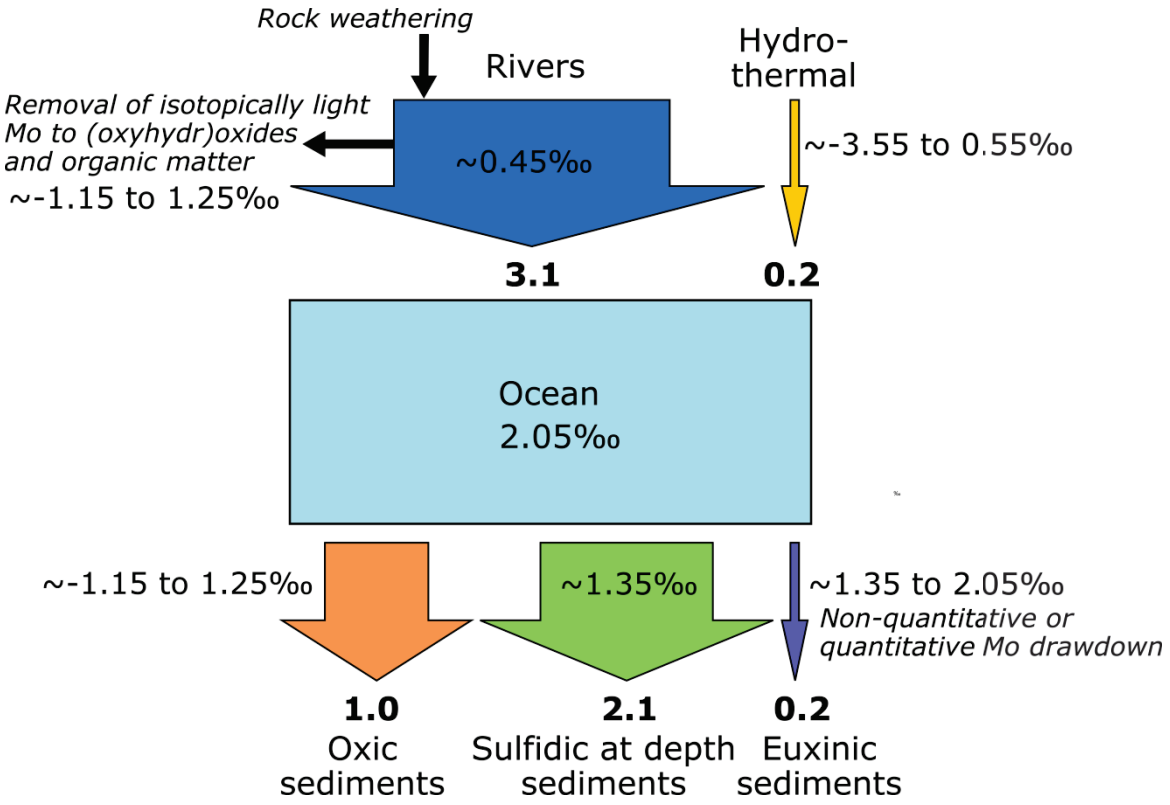

Figure 1.11 Molybdenum isotope fluxes in the environment. Molybdenum fluxes are in 10^8 mol yr^{-1} (Miller et al., 2011; Reinhard et al., 2013; Scott et al., 2008; Wheat et al., 2002). Molybdenum isotope composition ($\delta^{98/95}$Mo) of waters and sediments are reported relative to NIST 3134 ‰ (Archer and Vance, 2008; Arnold et al., 2004; Barling et al., 2001; Brucker et al., 2009; McManus et al., 2002; Nägler et al., 2011; Nakagawa et al., 2012; Neubert et al., 2011; Neubert et al., 2008; Pearce et al., 2010a; Poulson et al., 2006; Siebert et al., 2015, 2003). Figure is adapted from Kendall et al. (2017).

Catchment lithology may exert some control on Mo river chemistry via the incongruent dissolution of easily oxidised phases, such as sulfide minerals and organic matter. These mineral phases typically have higher Mo isotope values than crustal silicate minerals (Neubert et al., 2011; Voegelin et al., 2012) and crustal sulfide minerals and organic rich mudrocks are thought to be the major host phases of Mo in Earth's crust (Kendall et al., 2017). Organic rich mudrocks are characterised by a range in $\delta^{98/95}$Mo from -1.55 to 2.25‰ (Kendall et al., 2017).

In addition, both abiotic and biotic processes operating in river catchments have the potential to fractionate Mo isotopes. Molybdenum may undergo isotope fractionation during adsorption onto particles, such as (oxyhydr)oxides in soils, during river transport or during trapping of Mo by organic matter (e.g. Siebert et al., 2015). A large Mo isotope fractionation is thought to occur during Mo adsorption onto Mn oxides in oxic water (Kendall et al., 2017). Molybdenum is also fractionated during adsorption onto Fe oxides and oxyhydroxides, including magnetite, ferrihydrite, goethite and haematite; light Mo isotopes are preferentially removed from solution (Arnold et al., 2004; Goldberg et al., 2009). Biochemical pathways for Mo uptake and utilisation

are linked to the cycling of nitrogen in ecosystems (e.g. Boyd et al., 2011). For example, Mo assimilation by the nitrogen-fixing bacterium, *A. Vinelandii*, is associated with the preferential incorporation of light Mo isotopes (Liermann et al., 2005; Wasylenki et al., 2007). This isotope fractionation may arise through several mechanisms: i) kinetic effects associated with irreversible Mo transport; ii) coordination changes during incomplete uptake or release from a chelating ligand or Mo transporter protein; or iii) sorption of Mo onto the cell surface (Liermann et al., 2005; Wasylenki et al., 2007). Fractionation may be particularly apparent during nitrogen fixation (*cf.* bacterial growth) because less Mo is bound to storage proteins in times of high Mo demand (Zerkle et al., 2011). Altogether, it is clear we require a better understanding of the factors setting the Mo isotope composition of continental runoff. Refinements in our understanding of the modern oceanic Mo isotope budget, including the significance of biological Mo isotope fractionation and Mo isotope behaviour in association with chemical weathering in river catchments, will improve the use of Mo isotopes as a palaeoredox proxy.

1.7 Thesis Synopsis

Chapter 2 outlines the geochemical methods used to track and quantify the weathering reactions and processes operating in river catchments in New Zealand, Canada and Iceland. Specific information on the developments of analytical techniques used for the acquisition of data presented in subsequent chapters is detailed. These include various approaches to measure Re concentration in a range of geological materials, the development of the Mo double spike method, and the long-term reproducibility of these measurements.

Chapter 3 explores how OC_{petro} oxidation rates vary across the western Southern Alps in river catchments where physical erosion and lithology are relatively constant, but differences in the extent of glacial coverage are apparent. This chapter attempts to answer the question of whether glacial erosion processes increase oxidative weathering reactions relative to fluvial systems and, consequently, if there could be an enhanced CO_2 flux from geological storage during periods of glaciation that serves as a negative feedback on climate change. The net geological carbon budget of several catchments with varying extents of glacial cover is closed with the addition of data on the rate of OC_{petro} oxidation from the Re proxy. The potential for a global link between glaciation and OC_{petro} oxidation is investigated using published data compiled from global catchments.

A version of this chapter has been published in *Science Advances*: 'Mountain glaciation drives rapid oxidation of rock-bound organic carbon', co-authored by Robert Hilton, David Selby, Chris Ottley, Darren Gröcke, Murray Hicks and Kevin Burton. I helped to design the study alongside Robert Hilton and Kevin Burton. I collected the samples used in this work with field assistance

from Scott Hawley and supervision from Robert Hilton. The geochemical analyses were performed under the supervision of David Selby, Robert Hilton and Chris Ottley. The data were interpreted with Robert Hilton, David Selby and Kevin Burton. Darren Gröcke assisted with organic carbon analyses. Murray Hicks provided hydrological data. The paper manuscript was written with Robert Hilton and had input from David Selby and Kevin Burton.

Chapter 4 focuses on constraining the OC_{petro} oxidation rate in the Liard, Peel, Arctic Red and Mackenzie River catchments nested within the Mackenzie River Basin, north west Canada, using Re abundance measurements on a comprehensive set of samples collected from 2009 to 2013. A comparison across these river catchments allows for an assessment of the effects of differing source minerals, sites of weathering and physical erosion on weathering rates. In addition, the distribution of OC_{petro} across the study areas varies from 0.2–0.6 wt. %, allowing the impact of lithology on carbon fluxes by oxidative weathering to be considered. For the Mackenzie, Liard, Arctic Red and Peel river catchments, OC_{petro} oxidation is estimated using Re fluxes and an estimate of the Re/OC composition of the rock being weathered. The estimates of dissolved Re flux provide some insight on the major controls on OC_{petro} oxidation and allow an estimate of the associated CO_2 release to be calculated. Consequently, it is possible to better assess the impact of orogenesis on the carbon cycle. For the Mackenzie River catchment, the geological carbon budget during weathering and erosion can be closed by combining the estimates of OC_{petro} oxidation with published data on silicate and carbonate weathering rates and organic carbon burial.

This chapter is intended for submission to *Earth and Planetary Science Letters*: 'The geological carbon budget of the Mackenzie River Basin' co-authored by Robert Hilton, Mathieu Dellinger, David Selby, Valier Galy, Jérôme Gaillardet, Damien Calmels, Ed Tipper, Chris Ottley and Kevin Burton. The research project and goals were devised by myself with guidance from Robert Hilton. The samples were collected by Robert Hilton, Mathieu Dellinger, Valier Galy, Damien Calmels, Jérôme Gaillardet and Ed Tipper. The analytical work was carried out under the supervision of David Selby and Chris Ottley. The data were primarily evaluated with Robert Hilton. Co-authors assisted with editorial advice and aided the critical scientific evaluation of the data.

Chapter 5 applies the $\delta^{98}Mo$ system to mountain river catchments draining the Southern Alps, New Zealand; the Mackenzie River Basin and the Yukon, Canada; and the Skaftá River, Iceland. This allows new insight to be gained into the role that redox reactions play in supplying Mo to rivers and the ocean. The impact of contrasting lithology and differing erosion processes (glacial versus non-glacial) on dissolved $\delta^{98}Mo$ variability are considered. The extent of Mo isotope fractionation amongst the dissolved and solid sediment fractions, including weathered colluvium and litter samples from hillslopes, allows the significance of redox reactions, adsorption of Mo onto

oxy(hydroxide) particles and biological activity in sequestering and fractionating dissolved Mo to interpreted. The fractionation imparted by these processes is considered in the context of experimental data.

This chapter is intended for submission to *Geochimica et Cosmochimica Acta*: 'Controls on the molybdenum isotope fractionation during weathering and erosion in mountain river catchments', co-authored by Robert Hilton, Alex McCoy-West, David Selby, Chris Ottley & Kevin Burton. The samples from New Zealand were collected with Scott Hawley and Robert Hilton. Samples from Iceland were collected with Scott Hawley. Samples from Canada were collected by Robert Hilton, Mathieu Dellinger, Valier Galy, Damien Calmels, Jérôme Gaillardet and Ed Tipper. The aims of this study were devised alongside Kevin Burton and Robert Hilton. The geochemical analyses were achieved under the supervision of Alex McCoy-West, David Selby and Chris Ottley. The data were interpreted with Robert Hilton and Kevin Burton.

Chapter 6 concludes the main findings of this thesis and highlights the directions for future work that could arise from this research.

1.8 References

Anderson, S.P., 2007. Biogeochemistry of glacial landscape systems, in: Annual Review of Earth and Planetary Sciences. pp. 375–399.

Anderson, S.P., 2005. Glaciers show direct linkage between erosion rate and chemical weathering fluxes. Geomorphology 67, 147–157.

Archer, C., Vance, D., 2008. The isotopic signature of the global riverine molybdenum flux and anoxia in the ancient oceans. Nat. Geosci. 1, 597–600.

Arnold, G.L., Anbar, A.D., Barling, J., Lyons, T.W., 2004. Molybdenum isotope evidence for widespread anoxia in mid-proterozoic oceans. Science 304, 87–90.

Bardgett, R.D., Richter, A., Bol, R., Garnett, M.H., Bäumler, R., Xu, X., Lopez-Capel, E., Manning, D.A.C., Hobbs, P.J., Hartley, I.R., 2007. Heterotrophic microbial communities use ancient carbon following glacial retreat. Biol. Lett. 3, 487–490.

Barling, J., Anbar, A.D., 2004. Molybdenum isotope fractionation during adsorption by manganese oxides. Earth Planet. Sci. Lett. 217, 315–329.

Barling, J., Arnold, G.L., Anbar, A.D., 2001. Natural mass-dependent variations in the isotopic composition of molybdenum. Earth Planet. Sci. Lett. 193, 447–457.

Beaulieu, E., Godderis, Y., Donnadieu, Y., Labat, D., Roelandt, C., 2012. High sensitivity of the continental-weathering carbon dioxide sink to future climate change. Nat. Clim. Chang. 2, 346–349.

Beaulieu, E., Goddéris, Y., Labat, D., Roelandt, C., Calmels, D., Gaillardet, J., 2011. Modeling of water-rock interaction in the Mackenzie basin: Competition between sulfuric and carbonic acids. Chem. Geol. 289, 114–123.

Berner, R.A., 1982. Burial of organic-carbon and pyrite sulfur in the modern ocean - its geochemical and environmental significance. Am. J. Sci. 282, 451–473.

Berner, R.A., 1991. A model for atmospheric CO_2 over Phanerozoic time. Am. J. Sci. 291, 339–

376.

Berner, R.A., Caldeira, K., 1997. The need for mass balance and feedback in the geochemical carbon cycle. Geology 25, 955–956.

Berner, R.A., Canfield, D.E., 1989. A new model for atmospheric oxygen over Phanerozoic time. Am. J. Sci. 289, 333–361.

Berner, R.A., Maasch, K.A., 1996. Chemical weathering and controls on atmospheric O_2 and CO_2: Fundamental principles were enunciated by J.J. Ebelmen in 1845. Geochim. Cosmochim. Acta 60, 1633–1637.

Beyssac, O., Simoes, M., Avouac, J.P., Farley, K.A., Chen, Y.-G., Chan, Y.-C., Goffé, B., 2007. Late Cenozoic metamorphic evolution and exhumation of Taiwan. Tectonics 26.

Blair, N.E., Leithold, E.L., Ford, S.T., Peeler, K.A., Holmes, J.C., Perkey, D.W., 2003. The persistence of memory: The fate of ancient sedimentary organic carbon in a modern sedimentary system. Geochim. Cosmochim. Acta 67, 63–73.

Bluth, G.J.S., Kump, L.R., 1994. Lithologic and climatologic controls of river chemistry. Geochim. Cosmochim. Acta 58, 2341–2359.

Bolton, E.W., Berner, R.A., Petsch, S.T., 2006. The weathering of sedimentary organic matter as a control on atmospheric O_2: II. Theoretical modeling. Am. J. Sci. 306, 575–615.

Bottrell, S.H., Tranter, M., 2002. Sulphide oxidation under partially anoxic conditions at the bed of the Haut Glacier d'Arolla, Switzerland. Hydrol. Process. 16, 2363–2368.

Bouchez, J., Beyssac, O., Galy, V., Gaillardet, J., France-Lanord, C., Maurice, L., Moreira-Turcq, P., 2010. Oxidation of petrogenic organic carbon in the Amazon floodplain as a source of atmospheric CO_2. Geology 38, 255–258.

Bouchez, J., Galy, V., Hilton, R.G., Gaillardet, J., Moreira-Turcq, P., Perez, M.A., France-Lanord, C., Maurice, L., 2014. Source, transport and fluxes of Amazon River particulate organic carbon: Insights from river sediment depth-profiles. Geochim. Cosmochim. Acta 133, 280–298.

Boyd, E.S., Anbar, A.D., Miller, S., Hamilton, T.L., Lavin, M., Peters, J.W., 2011. A late methanogen origin for molybdenum-dependent nitrogenase. Geobiology 9, 221–232.

Boyd, E.S., Hamilton, T.L., Havig, J.R., Skidmore, M.L., Shock, L., 2014. Chemolithotrophic primary production in a subglacial ecosystem. Appl. Environ. Microbiol. 80, 6146–6153.

Brookins, D.G., 1986. Rhenium as analog for fissiogenic technetium: Eh-pH diagram (25°C, 1 bar) constraints. Appl. Geochemistry 1, 513–517.

Brucker, R.L.P.P., McManus, J., Severmann, S., Berelson, W.M., 2009. Molybdenum behavior during early diagenesis: Insights from Mo isotopes. Geochemistry Geophysics Geosystems 10.

Calmels, D., Gaillardet, J., Brenot, A., France-Lanord, C., 2007. Sustained sulfide oxidation by physical erosion processes in the Mackenzie River basin: Climatic perspectives. Geology 35, 1003–1006.

Calmels, D., Galy, A., Hovius, N., Bickle, M., West, A.J., Chen, M.-C., Chapman, H., 2011. Contribution of deep groundwater to the weathering budget in a rapidly eroding mountain belt, Taiwan. Earth Planet. Sci. Lett. 303, 48–58.

Chadwick, O. a, Derry, L. a, Vitousek, P.M., Huebert, B.J., Hedin, L.O., 1999. Changing sources of nutrients during four million years of ecosystem development. Nature 397, 491–497.

Chang, S.B., Berner, R.A., 1999. Coal weathering and the geochemical carbon cycle. Geochim. Cosmochim. Acta 63, 3301–3310.

Colodner, D., Sachs, J., Ravizza, G., Turekian, K., Edmond, J., Boyle, E., 1993. The geochemical cycle of rhenium: a reconnaissance. Earth Planet. Sci. Lett. 117, 205–221.

Copard, Y., Amiotte-Suchet, P., Di-Giovanni, C., 2007. Storage and release of fossil organic

carbon related to weathering of sedimentary rocks. Earth Planet. Sci. Lett. 258, 345–357.

Crawford, D.L., Nielsen, E.P., 1995. Biotransformation of coal substructure model compounds by microbial enzymes. Appl. Biochem. Biotechnol. 54, 223–231.

Dahl, T.W., Anbar, A.D., Gordon, G.W., Rosing, M.T., Frei, R., Canfield, D.E., 2010. The behavior of molybdenum and its isotopes across the chemocline and in the sediments of sulfidic Lake Cadagno, Switzerland. Geochim. Cosmochim. Acta 74, 144–163.

Dahl, T.W., Canfield, D.E., Rosing, M.T., Frei, R.E., Gordon, G.W., Knoll, A.H., Anbar, A.D., 2011. Molybdenum evidence for expansive sulfidic water masses in similar to 750 Ma oceans. Earth Planet. Sci. Lett. 311, 264–274.

Dai, S.F., Seredin, V. V, Ward, C.R., Hower, J.C., Xing, Y.W., Zhang, W.G., Song, W.J., Wang, P.P., 2015. Enrichment of U-Se-Mo-Re-V in coals preserved within marine carbonate successions: geochemical and mineralogical data from the Late Permian Guiding Coalfield, Guizhou, China. Miner. Depos. 50, 159–186.

Dalai, T.K., Singh, S.K., Trivedi, J.R., Krishnaswami, S., 2002. Dissolved rhenium in the Yamuna River System and the Ganga in the Himalaya: Role of black shale weathering on the budgets of Re, Os, and U in rivers and CO_2 in the atmosphere. Geochim. Cosmochim. Acta 66, 29–43.

Dickson, A.J., Cohen, A.S., Coe, A.L., 2012. Seawater oxygenation during the Paleocene-Eocene Thermal Maximum. Geology 40, 639–642.

Duan, Y., Anbar, A.D., Arnold, G.L., Lyons, T.W., Gordon, G.W., Kendall, B., 2010. Molybdenum isotope evidence for mild environmental oxygenation before the Great Oxidation Event. Geochim. Cosmochim. Acta 74, 6655–6668.

Dupre, B., Dessert, C., Oliva, P., Godderis, Y., Viers, J., Francois, L., Millot, R., Gaillardet, J., 2003. Rivers, chemical weathering and Earth's climate. Comptes Rendus Geosci. 335, 1141–1160.

Ebelmen, J.J., 1845. Sur les produits de la décomposition desespèces minérales de la famille des silicates. Anna. Mines 7, 3–66.

Emberson, R., Hovius, N., Galy, A., Marc, O., 2016. Chemical weathering in active mountain belts controlled by stochastic bedrock landsliding. Nat. Geosci. 9, 42–45.

Eswaran, H., Berg, E., Reich, P., 1993. Organic Carbon in Soils of the World. Soil Sci. Soc. Am. J. 57, 192–194.

Faison, B.D., Lewis, S.N., 1990. Microbial coal solubilization in defined culture systems: Biochemical and physiological studies. Resour. Conserv. Recycl. 3, 59–67.

FranceLanord, C., Derry, L.A., 1997. Organic carbon burial forcing of the carbon cycle from Himalayan erosion. Nature 390, 65–67.

Gaillardet, J., Dupre, B., Louvat, P., Allegre, C.J., 1999a. Global silicate weathering and CO_2 consumption rates deduced from the chemistry of large rivers. Chem. Geol. 159, 3–30.

Gaillardet, J., Dupre, B., Allegre, C.J., 1999b. Geochemistry of large river suspended sediments: Silicate weathering or recycling tracer? Geochim. Cosmochim. Acta 63, 4037–4051.

Gaillardet, J., Galy, A., 2008. Atmospheric Science: Himalaya - Carbon Sink or Source? Science 320, 1727–1728.

Galy, V., Beyssac, O., France-Lanord, C., Eglinton, T., 2008. Recycling of Graphite During Himalayan Erosion: A Geological Stabilization of Carbon in the Crust. Science 322, 943–945.

Galy, V., Peucker-Ehrenbrink, B., Eglinton, T., 2015. Global carbon export from the terrestrial biosphere controlled by erosion. Nature 521, 204.

Gislason, S.R., Oelkers, E.H., Eiriksdottir, E.S., Kardjilov, M.I., Gisladottir, G., Sigfusson, B., Snorrason, A., Elefsen, S., Hardardottir, J., Torssander, P., Oskarsson, N., 2008. The feedback between climate and weathering. Mineral. Mag. 72, 317–320.

Goldberg, T., Archer, C., Vance, D., Poulton, S.W., 2009. Mo isotope fractionation during adsorption to Fe (oxyhydr)oxides. Geochim. Cosmochim. Acta 73, 6502–6516.

Hales, T.C., Roering, J.J., 2009. A frost "buzzsaw" mechanism for erosion of the eastern Southern Alps, New Zealand. Geomorphology 107, 241–253.

Hallet, B., Hunter, L., Bogen, J., 1996. Rates of erosion and sediment evacuation by glaciers: A review of field data and their implications. Glob. Planet. Change 12, 213–235.

Herman, F., Seward, D., Valla, P.G., Carter, A., Kohn, B., Willett, S.D., Ehlers, T.A., 2013. Worldwide acceleration of mountain erosion under a cooling climate. Nature 504, 423.

Hilton, R.G., Gaillardet, J., Calmels, D., Birck, J.-L., 2014. Geological respiration of a mountain belt revealed by the trace element rhenium. Earth Planet. Sci. Lett. 403, 27–36.

Hilton, R.G., Galy, A., Hovius, N., Chen, M.-C., Horng, M.-J., Chen, H., 2008. Tropical-cyclone-driven erosion of the terrestrial biosphere from mountains. Nat. Geosci. 1, 759–762.

Hilton, R.G., Galy, A., Hovius, N., Horng, M.-J., Chen, H., 2011. Efficient transport of fossil organic carbon to the ocean by steep mountain rivers: An orogenic carbon sequestration mechanism. Geology 39, 71–74.

Hilton, R.G., Galy, A., Hovius, N., Horng, M.-J., Chen, H., 2010. The isotopic composition of particulate organic carbon in mountain rivers of Taiwan. Geochim. Cosmochim. Acta 74, 3164–3181.

Hovius, N., Stark, C.P., Allen, P.A., 1997. Sediment flux from a mountain belt derived by landslide mapping. Geology 25, 231–234.

Jacobson, A.D., Blum, J.D., 2003. Relationship between mechanical erosion and atmospheric CO_2 consumption in the New Zealand Southern Alps. Geology 31, 865–868.

Jaffe, L.A., Peucker-Ehrenbrink, B., Petsch, S.T., 2002. Mobility of rhenium, platinum group elements and organic carbon during black shale weathering. Earth Planet. Sci. Lett. 198, 339–353.

Keller, C.K., Bacon, D.H., 1998. Soil respiration and georespiration distinguished by transport analyses of vadose CO_2, (CO_2)-C-13, and (CO_2)-C-14. Global Biogeochem. Cycles 12, 361–372.

Kendall, B., Creaser, R.A., Gordon, G.W., Anbar, A.D., 2009. Re-Os and Mo isotope systematics of black shales from the Middle Proterozoic Velkerri and Wollogorang Formations, McArthur Basin, northern Australia. Geochim. Cosmochim. Acta 73, 2534–2558.

Kendall, B., Dahl, T.W., Anbar, A.D., 2017. the Stable Isotope Geochemistry of Molybdenum. Rev. Mineral. Geochemistry 82, 683–732.

Kendall, B., Gordon, G.W., Poulton, S.W., Anbar, A.D., 2011. Molybdenum isotope constraints on the extent of late Paleoproterozoic ocean euxinia. Earth Planet. Sci. Lett. 307, 450–460.

Komada, T., Druffel, E.R.M., Trumbore, S.E., 2004. Oceanic export of relict carbon by small mountainous rivers. Geophys. Res. Lett.

Koppes, M.N., Montgomery, D.R., 2009. The relative efficacy of fluvial and glacial erosion over modern to orogenic timescales. Nat. Geosci. 2, 644–647.

Lasaga, A.C., Ohmoto, H., 2002. The oxygen geochemical cycle: Dynamics and stability. Geochim. Cosmochim. Acta 66, 361–381.

Leithold, E.L., Blair, N.E., Childress, L.B., Brulet, B.R., Marden, M., Orpin, A.R., Kuehl, S.A., Alexander, C.R., 2013. Signals of watershed change preserved in organic carbon buried on the continental margin seaward of the Waipaoa River, New Zealand. Mar. Geol. 346, 355–365.

Liermann, L.J., Guynn, R.L., Anbar, A., Brantley, S.L., 2005. Production of a molybdophore during metal-targeted dissolution of silicates by soil bacteria. Chem. Geol. 220, 285–302.

Lupker, M., France-Lanord, C., Galy, V., Lave, J., Kudrass, H., 2013. Increasing chemical

weathering in the Himalayan system since the Last Glacial Maximum. Earth Planet. Sci. Lett. 365, 243–252.

Lyons, W.B., Carey, A.E., Hicks, D.M., Nezat, C.A., 2005. Chemical weathering in high-sediment-yielding watersheds, New Zealand. J. Geophys. Res. Surf. 110.

Maher, K., Chamberlain, C.P., 2014. Hydrologic Regulation of Chemical Weathering and the Geologic Carbon Cycle. Science 343, 1502–1504.

Marty, B., Tolstikhin, I.N., 1998. CO_2 fluxes from mid-ocean ridges, arcs and plumes. Chem. Geol. 145, 233–248.

McManus, J., Nagler, T.F., Siebert, C., Wheat, C.G., Hammond, D.E., 2002. Oceanic molybdenum isotope fractionation: Diagenesis and hydrothermal ridge-flank alteration. Geochemistry Geophysics Geosystems 3.

Meybeck, M., 1987. Global chemical weathering of surficial rocks estimated from river dissolved loads. Am. J. Sci. 287, 401–428.

Miller, C.A., Peucker-Ehrenbrink, B., Walker, B.D., Marcantonio, F., 2011. Re-assessing the surface cycling of molybdenum and rhenium. Geochim. Cosmochim. Acta 75, 7146–7179.

Milliman, J.D., Farnsworth, K.L., 2011. Runoff, erosion, and delivery to the coastal ocean., in: River Discharge to the Coastal Ocean. A Global Synthesis. pp. 13–69.

Millot, R., Gaillardet, J., Dupre, B., Allegre, C.J., 2002. The global control of silicate weathering rates and the coupling with physical erosion: new insights from rivers of the Canadian Shield. Earth Planet. Sci. Lett. 196, 83–98.

Montgomery, D.R., Balco, G., Willett, S.D., 2001. Climate, tectonics, and the morphology of the Andes. Geology 29, 579–582.

Morford, J.L., Emerson, S., 1999. The geochemistry of redox sensitive trace metals in sediments. Geochim. Cosmochim. Acta 63, 1735–1750.

Moulton, K.L., Berner, R.A., 1998. Quantification of the effect of plants on weathering: Studies in Iceland. Geology 26, 895–898.

Nägler, T.F., Neubert, N., Böttcher, M.E., Dellwig, O., Schnetger, B., 2011. Molybdenum isotope fractionation in pelagic euxinia: Evidence from the modern Black and Baltic Seas. Chem. Geol. 289, 1–11.

Nakagawa, Y., Takano, S., Firdaus, M.L., Norisuye, K., Hirata, T., Vance, D., Sohrin, Y., 2012. The molybdenum isotopic composition of the modern ocean. Geochem. J. 46, 131–141.

Neubert, N., Heri, A.R., Voegelin, A.R., Naegler, T.F., Schlunegger, F., Villa, I.M., Nägler, T.F., Schlunegger, F., Villa, I.M., 2011. The molybdenum isotopic composition in river water: Constraints from small catchments. Earth Planet. Sci. Lett. 304, 180–190.

Neubert Nagler, TF, Bottcher, ME, N., 2008. Sulfidity controls molybdenum isotope fractionation into euxinic sediments: Evidence from the modern Black Sea. Geology 36, 775–778.

Noordmann, J., Weyer, S., Montoya-Pino, C., Dellwig, O., Neubert, N., Eckert, S., Paetzel, M., Boettcher, M.E., 2015. Uranium and molybdenum isotope systematics in modern euxinic basins: Case studies from the central Baltic Sea and the Kyllaren fjord (Norway). Chem. Geol. 396, 182–195.

Pearce, C.R., Burton, K.W., Pogge von Strandmann, P.A.E., James, R.H., Gislason, S.R., 2010a. Molybdenum isotope behaviour accompanying weathering and riverine transport in a basaltic terrain. Earth Planet. Sci. Lett. 295, 104–114.

Pearce, C.R., Coe, A.L., Cohen, A.S., 2010b. Seawater redox variations during the deposition of the Kimmeridge Clay Formation, United Kingdom (Upper Jurassic): Evidence from molybdenum isotopes and trace metal ratios. Paleoceanography 25.

Pearce, C.R., Cohen, A.S., Coe, A.L., Burton, K.W., 2008. Molybdenum isotope evidence for global ocean anoxia coupled with perturbations to the carbon cycle during the early Jurassic.

Geology 36, 231–234.
Petsch, S.T., 2014. Weathering of organic carbon, 2nd ed, Treatise on Geochemistry . Elsevier.
Petsch, S.T., Berner, R.A., Eglinton, T.I., 2000. A field study of the chemical weathering of ancient sedimentary organic matter. Org. Geochem. 31, 475–487.
Petsch, S.T., Eglinton, T.I., Edwards, K.J., 2001. C-14-dead living biomass: Evidence for microbial assimilation of ancient organic carbon during share weathering. Science 292, 1127–1131.
Peucker-Ehrenbrink, B., Hannigan, R.E., 2000. Effects of black shale weathering on the mobility of rhenium and platinum group elements. Geology 28, 475–478.
Pierson-Wickmann, A.-C., Reisberg, L., France-Lanord, C., 2002. Behavior of Re and Os during low-temperature alteration: Results from Himalayan soils and altered black shales. Geochim. Cosmochim. Acta 66, 1539–1548.
Poulson, R.L., Siebert, C., McManus, J., Berelson, W.M., 2006. Authigenic molybdenum isotope signatures in marine sediments. Geology 34, 617–620.
Raiswell, R., Berner, R.A., 1986. Pyrite and organic-matter in Phanerozoic normal marine shales. Geochim. Cosmochim. Acta 50, 1967–1976.
Ralph, J.P., Graham, L.A., Catcheside, D.E.A., 1996. Extracellular oxidases and the transformation of solubilised low-rank coal by wood-rot fungi. Appl. Microbiol. Biotechnol. 46, 226–232.
Reinhard, C.T., Planavsky, N.J., Robbins, L.J., Partin, C.A., Gill, B.C., Lalonde, S. V., Bekker, A., Konhauser, K.O., Lyons, T.W., 2013. Proterozoic ocean redox and biogeochemical stasis. Proc. Natl. Acad. Sci. 110, 5357–5362.
Riebe, C.S., Kirchner, J.W., Finkel, R.C., 2004. Erosional and climatic effects on long-term chemical weathering rates in granitic landscapes spanning diverse climate regimes. Earth Planet. Sci. Lett. 224, 547–562.
Ronov, A.B., 1976. Volcanism, carbonate accumulation, life (Regularities of Glocal Geochemistry of Carbon). Geokhimiya 1252–1277.
Scott, C., Lyons, T.W., Bekker, A., Shen, Y., Poulton, S.W., Chu, X., Anbar, A.D., 2008. Tracing the stepwise oxygenation of the Proterozoic ocean. Nature 452, 456–459. doi:10.1038/nature06811
Siebert, C., Nagler, T.F., von Blanckenburg, F., Kramers, J.D., 2003. Molybdenum isotope records as a potential new proxy for paleoceanography. Earth Planet. Sci. Lett. 211, 159–171.
Siebert, C., Pett-Ridge, J.C., Opfergelt, S., Guicharnaud, R.A., Halliday, A.N., Burton, K.W., 2015. Molybdenum isotope fractionation in soils: Influence of redox conditions, organic matter, and atmospheric inputs. Geochim. Cosmochim. Acta 162, 1–24.
Sigman, D.M., Boyle, E.A., 2000. Glacial/interglacial variations in atmospheric carbon dioxide. Nature 407, 859–869.
Skidmore, M.L., Foght, J.M., Sharp, M.J., 2000. Microbial life beneath a high Arctic glacier. Appl. Environ. Microbiol. 66, 3214–3220.
Telling, J., Boyd, E.S., Bone, N., Jones, E.L., Tranter, M., MacFarlane, J.W., Martin, P.G., Wadham, J.L., Lamarche-Gagnon, G., Skidmore, M.L., Hamilton, T.L., Hill, E., Jackson, M., Hodgson, D.A., 2015. Rock comminution as a source of hydrogen for subglacial ecosystems. Nat. Geosci. 8, 851.
Torres, M.A., Moosdorf, N., Hartmann, J., Adkins, J.F., West, A.J., 2017. Glacial weathering, sulfide oxidation, and global carbon cycle feedbacks. Proc. Natl. Acad. Sci.
Torres, M.A., West, A.J., Li, G., 2014. Sulphide oxidation and carbonate dissolution as a source of CO2 over geological timescales. Nature 507, 346–349.
Tranter, M., Sharp, M.J., Lamb, H.R., Brown, G.H., Hubbard, B.P., Willis, I.C., 2002. Geochemical weathering at the bed of Haut Glacier d'Arolla, Switzerland - a new model. Hydrol. Process. 16, 959–993.

Turekian, K.K., Haven, N., Hans, K., Universitat, W.M. Der, 1961. Karl K. Turekian Dept. Geology, Yale University, New Haven, Conn. Karl Hans Wedepohl Mineralogische-Institut der Universitat, Gottingen, Germany Distribution of the Elements in Some Major Units of the Earth's Crust 175–192.

Voegelin, A.R., Naegler, T.F., Pettke, T., Neubert, N., Steinmann, M., Pourret, O., Villa, I.M., 2012. The impact of igneous bedrock weathering on the Mo isotopic composition of stream waters: Natural samples and laboratory experiments. Geochim. Cosmochim. Acta 86, 150–165.

Voegelin, A.R., Nägler, T.F., Beukes, N.J., Lacassie, J.P., 2010. Molybdenum isotopes in late Archean carbonate rocks: Implications for early Earth oxygenation. Precambrian Res. 182, 70–82.

Wadham, J.L., Bottrell, S., Tranter, M., Raiswell, R., 2004. Stable isotope evidence for microbial sulphate reduction at the bed of a polythermal high Arctic glacier. Earth Planet. Sci. Lett. 219, 341–355.

Wadham, J.L., Tranter, M., Skidmore, M., Hodson, A.J., Priscu, J., Lyons, W.B., Sharp, M., Wynn, P., Jackson, M., 2010. Biogeochemical weathering under ice: Size matters. Global Biogeochem. Cycles 24.

Walker, J.C.G., Hays, P.B., Kasting, J.F., 1981. A negative feedback mechanism for the long-term stabilization of Earth's surface temperature. J. Geophys. Res. Ocean. 86, 9776–9782.

Wang, Z.B., Ma, J.L., Li, J., Wei, G.J., Chen, X.F., Deng, W.F., Xie, L.H., Lu, W.J., Zou, L., 2015. Chemical weathering controls on variations in the molybdenum isotopic composition of river water: Evidence from large rivers in China. Chem. Geol. 410, 201–212.

Wasylenki, L.E., Anbar, A.D., Liermann, L.J., Mathur, R., Gordon, G.W., Brantley, S.L., 2007. Isotope fractionation during microbial metal uptake measured by MC-ICP-MS. J. Anal. At. Spectrom. 22, 905–910.

Wasylenki, L.E., Weeks, C.L., Bargar, J.R., Spiro, T.G., Hein, J.R., Anbar, A.D., 2011. The molecular mechanism of Mo isotope fractionation during adsorption to birnessite. Geochim. Cosmochim. Acta 75, 5019–5031.

West, A.J., 2012. Thickness of the chemical weathering zone and implications for erosional and climatic drivers of weathering and for carbon-cycle feedbacks. Geology 40, 811–814.

West, A.J., Galy, A., Bickle, M., 2005. Tectonic and climatic controls on silicate weathering. Earth Planet. Sci. Lett. 235, 211–228.

Wheat, C.G., Mottl, M.J., Rudnicki, M., 2002. Trace element and REE composition of a low-temperature ridge-flank hydrothermal spring. Geochim. Cosmochim. Acta 66, 3693–3705.

White, A.F., Blum, A.E., 1995. Effects of climate on chemical weathering in watersheds. Geochim. Cosmochim. Acta 59, 1729–1747.

White, A.F., Brantley, S.L., 2003. The effect of time on the weathering of silicate minerals: why do weathering rates differ in the laboratory and field? Chem. Geol. 202, 479–506.

Wille, M., Kramers, J.D., Nägler, T.F., Beukes, N.J., Schröder, S., Meisel, T., Lacassie, J.P., Voegelin, A.R., 2007. Evidence for a gradual rise of oxygen between 2.6 and 2.5Ga from Mo isotopes and Re-PGE signatures in shales. Geochim. Cosmochim. Acta 71, 2417–2435.

Zerkle, A.L., Scheiderich, K., Maresca, J.A., Liermann, L.J., Brantley, S.L., 2011. Molybdenum isotope fractionation by cyanobacterial assimilation during nitrate utilization and N(2)fixation. Geobiology 9, 94–106.

Chapter 2

Geochemical Methods

Sampling the Jollie River, eastern Southern Alps, New Zealand; October 2014

Summary: This chapter summarises the geochemical methods and developments in analytical techniques that facilitated the use of geochemical proxies in ***Chapters 3–5***.

Abstract

Geochemical analyses are essential to gaining a better understanding of how Earth surface processes impact on the cycling of elements (carbon, nutrients and metals) in the Critical Zone, from the atmosphere through to the hydrosphere and biosphere. In this research, specific elements were targeted in the dissolved products of chemical weathering and the solid products of erosion found in river waters, alongside the solid weathering materials found in soil horizons or transported amongst river suspended load and river bed materials. Relevant data derived from such materials include trace element concentrations (molybdenum, rhenium) acquired by Quadrupole – Inductively Coupled Plasma Mass Spectrometry (Q-ICP-MS, Thermo Scientific X-Series), molybdenum isotope compositions measured by Multiple Collector – Inductively Coupled Plasma Mass Spectrometry (MC-ICPMS, Thermo Neptune), major ion concentrations determined by Ion Chromatography (IC), total organic carbon and stable isotopes collected by Elemental Analyser – Isotope Ratio Mass Spectrometry (EA-IRMS, Thermo Scientific Delta V Advantage) and radiocarbon contents measured by Accelerator Mass Spectrometry (AMS). This chapter summarises the methods and developments in laboratory techniques that facilitated the acquisition of these data. Information regarding the development and refinement of chemical purification techniques for elemental and isotope analysis, including column design and calibration, the dissolution of materials for elemental and isotope analysis, double spike design and calibration, and isotope dilution techniques is provided. This includes a comparison of Re concentration data from river waters quantified by isotope dilution versus direct calibration techniques. Analytical uncertainties and the robustness of the data, including data reproducibility and precision from standard and sample replicates, are also considered.

2.1 Introduction

There have been considerable advances in Inductively Coupled Plasma Mass Spectrometer (ICP-MS) technology since the first measurements on river waters were made over two decades ago (e.g. Balaram, 1995; Gaillardet et al., 2003; Laborda et al., 2016; Misra et al., 2014; Wysocka and Vassileva, 2017). This has made it feasible to apply different methods to quantify trace element concentrations and isotope compositions, depending on the required measurement precision, the demands on sample mass, the available sample processing time, and the consideration of laboratory procedural blanks. In this thesis, geochemical method development has focussed on achieving accurate and precise rhenium (Re) and molybdenum (Mo) concentration data and Mo isotope measurements in a range of geological samples, with particular focus on river waters.

Dissolved Re concentrations in river water ($[Re]_{diss}$) are presented in ***Chapters 3–5***. Previous work has established that $[Re]_{diss}$ in natural river waters is low and typically in the range of 4.7 ± 0.2 pmol L^{-1} to 25.4 ± 1.2 pmol L^{-1} (or 0.88 to 4.73 pg g^{-1}) (Colodner et al., 1993a; Dalai et al., 2002; Hilton et al., 2014; Miller et al., 2011; Rahaman et al., 2012). The approach with the shortest sample processing time, lowest laboratory blank contribution and smallest sample volume required, is the direct measurement of $[Re]_{diss}$ by a Quadrupole – Inductively Coupled Mass Spectrometer (Q-ICP-MS) or High Resolution – ICP-MS (HR-ICP-MS). Depending on the instrumentation and tuning, it can be possible to resolve $[Re]_{diss}$ precisely at the pg g^{-1} level. The challenge with direct measurements, however, is the use of appropriate internal and external standards for re-calibration, and the instrument background to sample measurement ratio. Standard addition Q-ICP-MS is a refinement on the direct calibration method and although it increases sample demand, it can attain a high precision for a small sample volume (Hilton et al., 2014). Alternative methods include the use of anion exchange column chemistry to pre-concentrate Re by removing the bulk of the sample matrix (e.g. Pearce et al., 2009) and quantifying the column yield can allow for accurate sub-pg g^{-1} $[Re]_{diss}$ measurements (Hilton et al., 2014).

Isotope dilution (ID) ICP-MS is an approach that has been widely used to determine Re concentration in solid materials (e.g. Cumming et al., 2014; Selby and Creaser, 2003) and it is also possible to use it for water analysis (Miller et al., 2011; Pearce et al., 2009). Typically, a ^{185}Re enriched spike is added to a sample prior to column chemistry and the isotope ratio of the sample is then measured by an ICP-MS or a Thermal Ionization Mass Spectrometer (TIMS). This approach has several benefits: i) it allows an internal blank correction; ii) it does not require a 100% column yield; and iii) a higher analytical precision can be achieved, compared to a direct calibration approach. However, this method does require a greater sample mass.

In addition to Re, a trace element studied in detail in this research is molybdenum (Mo). Molybdenum concentrations and isotope ratios in a range of geological materials are presented in ***Chapter 5***. In river waters, Mo concentrations are typically higher than Re (e.g. major global rivers have $[Mo]_{diss}$ values of 0.45–59 nmol L^{-1} *cf.* $[Re]_{diss}$ values of 1.14–74 pmol L^{-1} in those same rivers; Miller et al., 2011). Therefore, although the general considerations described above for Re do also apply, there are not the same analytical challenges. In this research, focus is placed on accurately measuring the Mo isotope composition in a range of water samples and sediments collected from river catchments in New Zealand, Iceland and Canada. The measurement of Mo isotope ratios has become more routine over the last decade (Kendell et al., 2017), but there are still challenges with regard to the double spike methodology and reporting of data, which are outlined in this chapter.

The purpose of this chapter is to summarise the major methodological development steps taken during this research. Measurements of internal and external standards are provided to demonstrate precision and accuracy. For details on the selection of field sites and the specific sampling strategy and protocol required for collecting and processing river water, soil, suspended sediment and soils in Iceland, Canada and New Zealand in the field, readers are referred to ***Chapters 3–5***.

2.2 Direct calibration method for quantifying Re concentration

2.2.1 Overview

In this research, the direct calibration method was employed as a starting point to examine the general variability in $[Re]_{diss}$ between samples from a single location and amongst different localities. All river water samples were subsequently reanalysed by Isotope Dilution (ID) ICP-MS if enough sample was available (see section 2.3). However, the direct approach can yield precise and accurate data, so a full summary of the methods is provided here.

For the direct calibration method, several standard solutions with known concentrations are prepared, which cover the range of concentrations expected in sample solutions. Here, a stock of synthetic standard with $[Re]_{diss}$ = 1000 µg g^{-1} (ICP-MS tuning solution: Romil Cambridge 3%) was diluted and prepared in HNO_3 (Teflon double distilled) and deionised H_2O (18 mΩ) for introduction to the Q-ICP-MS (Thermo Fisher Scientific X-Series II). According to previous data on $[Re]_{diss}$ and $[Mo]_{diss}$ in river waters (Miller et al., 2011), a typical standard concentration range required for the analysis of Re and Mo concentrations in water samples will cover the range 0–50 pg g^{-1} and 0.01–1 ng g^{-1} for these elements, respectively. A calibration line is fitted to the measured data using a least-squares regression analysis (Figure 2.1). By comparison to the calibration line

acquired, [Re] and [Mo] concentrations in samples can be quantified using a linear model (Equation 2.1).

Equation 2.1 $[Re] = m \times CPS + c$

where [Re] (or [Mo]) is the sample concentration in pg g^{-1} or pmol L^{-1}, CPS is the measured instrumental counts per second, *m* is the gradient between these variables as defined by the standard solutions, and *c* is an intercept, that can be free to vary or set to 0. In our analyses, *c* was allowed to vary. The concentrations of standards are defined and an instrumental blank correction is contained within the calibration curve.

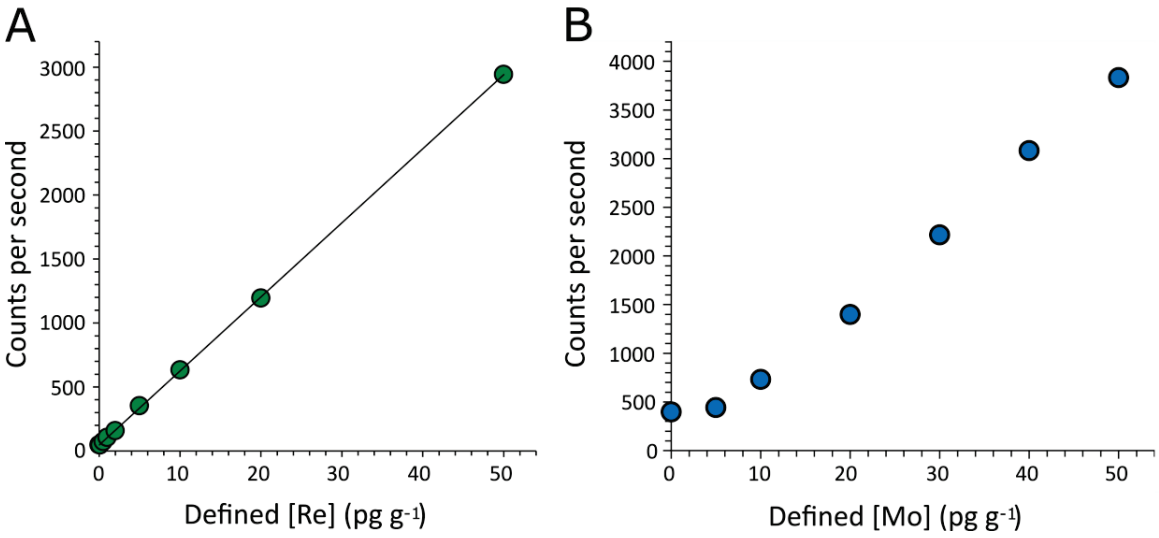

Figure 2.1 Examples of standard calibration lines generated by a direct calibration method on the Q-ICP-MS for Re and Mo. A. Re concentration calibration line. The counts per second generated are illustrated as a function of the specified Re concentration. **B.** Mo concentration calibration line. The counts per second generated are illustrated as a function of the specified Mo concentration. This calibration line indicates tailing at the low concentrations.

2.2.2 Sample introduction to Q-ICP-MS (Thermo X Series II)

Samples were generally acidified prior to the direct calibration analysis to yield a ~3% HNO_3 matrix. The purpose of acidification is to: (1) coat the inside of the vials with H^+ ions to reduce metal ion adsorption; and (2) to create a sample matrix similar to that of the standards prepared using HNO_3 diluent. Samples were introduced to the instrument using a glass Meinhard nebuliser and a cyclonic spray chamber.

For Re and Mo concentrations quantified by direct calibration using the Q-ICP-MS auto-sampler, data acquisition times were designed to be long enough to ensure that the counting statistics obtained were adequate for the elemental concentration range expected. The timings used were as follows: an uptake delay of ~90 s before analysis; an analysis time of 24 s (20 ms per Mo isotope

and 40 ms per Re isotope over 50 measurement cycles that were completed twice); and a wash out time of 180 s. This gave a total measurement time of ~5 min per sample. Prior to analysis, the instrument was optimised with a daily performance solution to confirm mass calibration, instrument sensitivity and to evaluate oxide and double charge species generation. For Re, the concentration data collected was calibrated using ^{187}Re because this Re isotope has the highest abundance and few elemental interferences ($^{171}Yb^{16}O$, ^{187}Os). Generally, the instrumental blank on ^{187}Re for dionized water at 3% HNO_3 was ~2–78 CPS, with the 20 pg g^{-1} synthetic Re standard typically yielding ~ 1340–1460 CPS. For Mo, the concentration data collected was calibrated using ^{98}Mo. The instrumental blank on ^{98}Mo for dionized water at 3% HNO_3 was ~2–4600 CPS, with typical values of ~80 pg g^{-1}. The 20 pg g^{-1} Mo synthetic standard typically yielded ~471,600–564,200 CPS.

2.2.3 Quantification of blanks

Following sample collection, Re can be introduced unintentionally into samples via several routes. However, previous work has quantified HNO_3 as the major contributor to the Re procedural contamination (Birck et al., 1997). To test the Re background, or blank, a careful assessment of acid dissolution procedures, the choice of reagents and cleaning procedures was carried out. Samples were prepared in the metal-free clean laboratories at Durham University, which are fitted with a High efficiency particulate air (HEPA) filtered air supply and laminar flow work stations to minimise contamination. Water (>18 mΩ) treated with a Milli-Q water system (Millipore Co.) was used both in chemistry and for pre-rinsing all beakers and vials. PFA Savillex® containers used for sample dry down and purification were cleaned by HCl-HNO_3 acid refluxing to remove any remaining residues from previous samples.

Several tests on reagent purity and the background Re concentration were also performed. By way of example, four different types of blank that were prepared to evaluate the controls on the background Re concentration are shown in Figure 2.2A. Two of these blanks contained HNO_3 and two contained deionized water, and these were prepared in cleaned (acid leach) and non-cleaned centrifuge tubes. The four blanks were run in a random sequence so that if any instrument oscillation occurred, each set of blanks was not all clustered on a particular fall or rise in Re concentration. They were also measured in pairs so that only the first measurement of any pair would be subject to any potential carry over from a previous sample.

The majority of the measurable Re blank was found to come from the HNO_3 and there was no apparent effect of differential cleaning methods (Figure 2.2A), supporting previous work on measuring Re in complex sample matrices (Birck et al., 1997). A sample of 3% Teflon double distilled HNO_3 acid prepared in the clean lab by sub-boiling and distillation in PFA stills showed a

factor of two lower Re counts, compared with its trace analysis 'commercial' grade HNO_3 (Romil SPA) counterpart. Consequently, Teflon double-distilled acids were used in standard preparation and for acidifying samples because of the anticipated low concentrations of Re in river waters. A more detailed experiment testing the leaching of centrifuge tubes with deionized or dilute HNO_3 prior to analysis also indicated this process had little effect on the background Re concentration and therefore it was considered an unnecessary precursor to future analyses (Figure 2.2B).

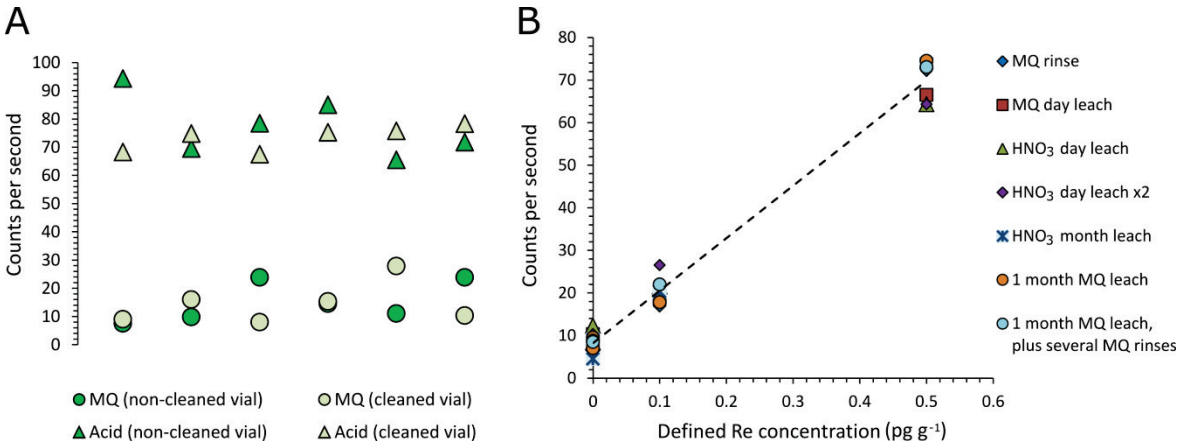

Figure 2.2 Assessment of the main background Re contributor. A. Counts per second (CPS) of Re in 3% HNO_3 versus deionised water (MQ) water are compared in cleaned and non-cleaned centrifuge tubes. Re concentrations are elevated in acid (HNO_3) relative to Milli-Q water with little effect of cleaning being apparent. **B.** Response of counts per second in blank and low concentration standards to different cleaning procedures. The calibration lines generated using centrifuge tubes cleaned by different methods show no clear relationship with the method used, implying that cleaning the centrifuge tubes has negligible impact on the resultant counts detected.

Combined Re and Mo standards were often used for generating calibration lines and determining both Re and Mo abundance in river waters. The 1000 µg g^{-1} Mo stock solution (ICP-MS tuning solution: Romil Cambridge 3%) was tested to determine its Re abundance. Standards containing different concentrations of Mo (in this case 0.01 ng g^{-1}, 0.1 ng g^{-1}, 0.5 ng g^{-1} and 1 ng g^{-1}) were prepared and run on the Q-ICP-MS. The counts per second generated were very low for Re and indistinguishable from the blank across all standard concentrations, emphasizing that the Mo stock contains negligible Re and was suitable for combined standards. If Re were to have been coming from the Mo ICP-MS tuning solution, then a higher concentration standard would have shown the greatest deviation from a calibration line, but this was not the case.

2.2.4 Inter- and Intra-run instrument stability

During an analytical run, instrument response can fluctuate due to the presence of sample matrix and electrical noise (Jarvis, 1997). Therefore, wherever possible, samples were analysed in order of increasing matrix. In addition, as a general rule, samples from rivers predicted to be rich in petrogenic organic carbon (OC_{petro}) based on knowledge of local bedrock geology, and therefore

thought to have the highest Re concentrations, were run towards the end of an analytical session to minimise the risk of artificially increasing the detected signal through carry over effects. Replicate analyses of standard solutions and samples were used to monitor changes in the analyte signal throughout an analytical session, at intervals of approximately 5–10 samples. Figure 2.3 illustrates the precision of Re and Mo concentration measurements in a single run for a standard in the middle of the calibration range. Although there is no systematic error, the values reported vary by up to ~11% from the calibration line, indicating that variations can occur during an analytical session at these very low concentrations (~5 pg g^{-1}). The data suggest that Re tends to reproduce better than Mo. Furthermore, when a typical calibration line for Mo is considered (Figure 2.1B) we find that the detection limits for Mo are higher than for Re with a tailing in the calibration line occurring at lower concentrations for Mo. Nevertheless, the natural abundance of Mo in river waters is typically ~100 times greater than that of Re.

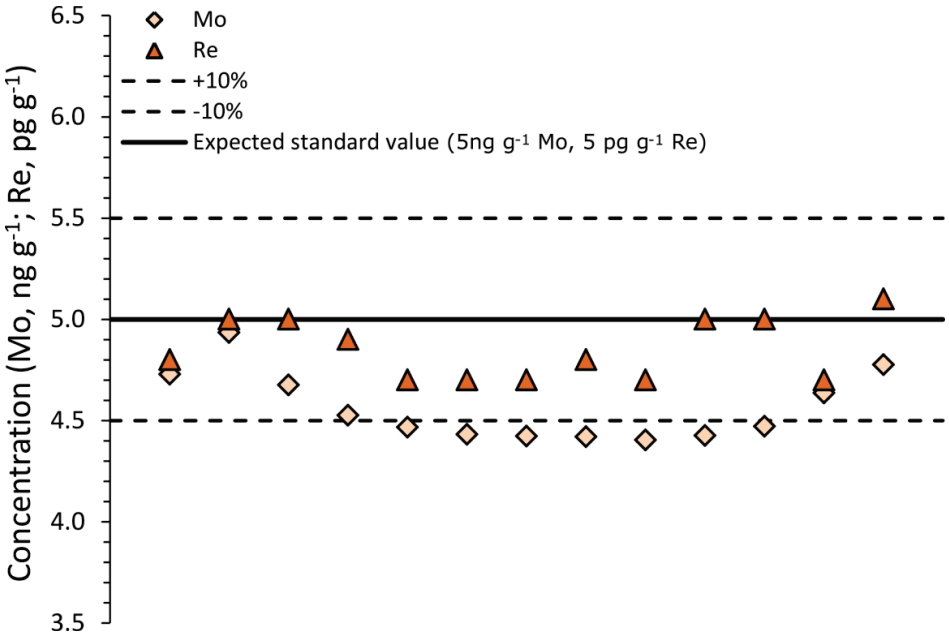

Figure 2.3 Precision of analyses on the Q-ICP-MS. Reproducibility of Re and Mo standards during a single analytical run on the Q-ICP-MS (X-Series) for a 5 pg g^{-1} standard solution.

The random instrument and procedural uncertainties, which may be introduced in sample preparation, were evaluated by processing replicate and duplicate samples. Replicate samples were run during the same analytical session while duplicate data were collected several months apart. When we consider these data, we find that the replicates are more similar to each other than the duplicate data are (Figure 2.4). This suggests that there is a greater drift in the sensitivity of the instrument over time or that variability in the calibration lines amongst analytical sessions can create biases in the data, which are only apparent when data from different sample batches are compared. These considerations, in part, gave rise to an investigation exploring isotope dilution methods for quantifying $[Re]_{diss}$ at low concentrations (sections 2.2.5.3 and 2.3).

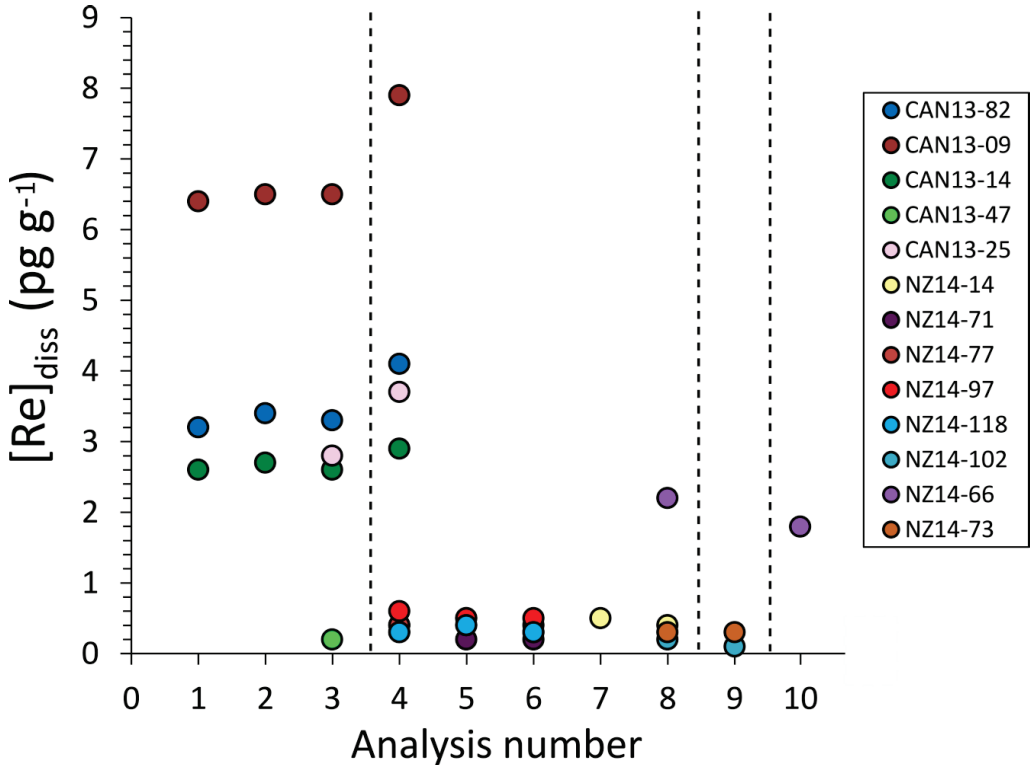

Figure 2.4 Reproducibility of sample Re data in replicate and duplicate analyses. Dashed lines separate different analytical sessions. Sample names are provided on alongside.

2.2.5 Improving the precision of $[Re]_{diss}$ measurements

2.2.5.1 Refining the direct calibration method

The Re data from the direct calibration method indicate that concentrations of Re are often at the sub- pg g^{-1} level in the sampled river waters; particularly those sampled in the Southern Alps, New Zealand, and Iceland. This makes analysis challenging by direct Q-ICP-MS methods, which sacrifice precision and accuracy (Figure 2.3). To improve the data quality, there are refinements that can be made to the direct Q-ICP-MS method. These include matrix matching the standard solutions and adjusting mass spectrometer peripheries. With regards to the latter, the sample and skimmer cones and the introduction system can be used specifically for water samples with a typically low matrix; in contrast to instruments being used to analyse rock-digestions. In addition, here, a Thermo Fisher X-Series II Q-ICP-MS was used but newer generations of Q-ICP-MS (e.g. Thermo Fisher iCAP, Agilent 7900) have lower detection limits and may allow for more precise (better than 5%) sub- pg g^{-1} measurements.

Alternatively, the precision of direct calibration $[Re]_{diss}$ data can be improved by doping samples with a known quantity of an element that does not occur at high concentrations in nature; a technique called internal standardisation. Any recorded fluctuations in the concentration of the doping element over an analytical session can then be monitored and attributed to instrument oscillation. A correction can be applied according to the oscillation observed. The doping element

should ideally be monoisotopic, to minimise elemental interferences, yield maximum mass sensitivity, and have an ionisation efficiency/ energy similar to those of the elements being analysed. Elements typically used for doping include Indium and Yttrium.

2.2.5.2 Standard addition method

When natural concentrations of elements in samples are low, an alternative method to direct measurements by Q-ICP-MS is standard addition. This method involves adding a standard with a known concentration of the element of interest to samples in order to increase the total concentration of that element. The resultant element concentration should then fall within the optimum calibration range and exceed machine detection limits. This method also reduces the problem of matrix effects. Although this method was not used for quantifying Re abundance in the samples used in this research, other published studies bearing Re data that are discussed within ***Chapters 3–5*** do take advantage of this technique (e.g. Hilton et al., 2014).

2.2.5.3 Isotope Dilution

For this research project, the approach taken to optimise precision and accuracy was to collect and process larger water samples by isotope dilution methods, which are known to give data with a higher precision (Anbar et al., 1992; Colodner et al., 1993b; Miller et al., 2011) than our initial direct calibration methods. This method is discussed in detail in section 2.3.

2.3 Isotope dilution and column chemistry development for [Re] analysis in river waters

2.3.1 Overview

The separation and pre-concentration of Re prior to analysis using column chemistry coupled with isotope dilution was explored as a means to lower the detection limits possible and to confirm the precision of analyses (Figure 2.5). The majority of the Re abundance data presented in ***Chapters 3–5*** was processed by combining isotope dilution with an anion-exchange mini-column chemistry method (Cumming et al., 2013).

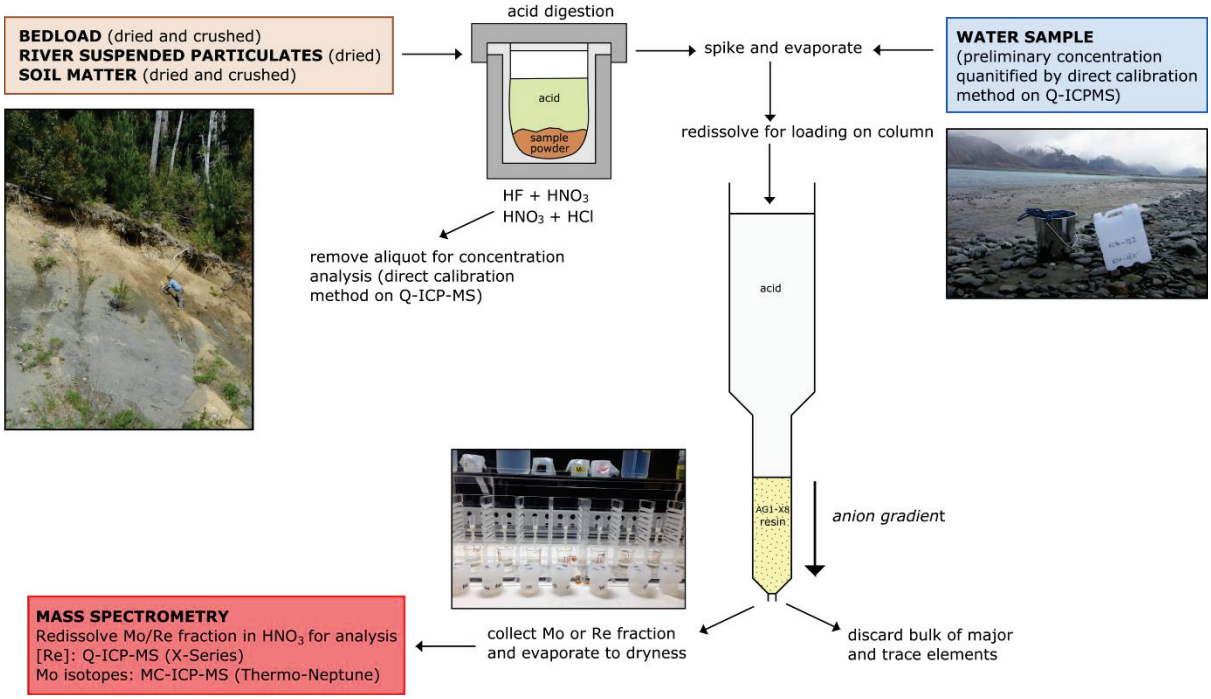

Figure 2.5 Summary of the methodology used to separate and pre-concentrate Re and Mo for elemental and isotope analyses. Water and sediment samples collected in the field were spiked and passed through an anion exchange resin before the element concentration or isotope composition of interest were quantified on a mass spectrometer.

Isotope dilution works by measuring the change in the ratio of signal intensities for two selected isotopes of an element after the addition of a known quantity of spike, which is enriched in one of the isotopes (Gill, 1997). Typically, the spike is enriched in a rare isotope, meaning that the measured isotope ratios are much larger than the natural abundance. For the analysis of Re concentrations in water samples, the isotope dilution method involved spiking samples with a ^{185}Re enriched spike (e.g. Pearce et al., 2009). The aim was to achieve a spike-sample mix ratio between 1.5–2.5, which would provide the best precision and accuracy. The spike volume required was defined according to the sample Re concentrations determined by the direct calibration method (section 2.2). Typically, between 30 and 500 mL of each river water sample was doped with the ^{185}Re tracer solution and evaporated to dryness before column chemistry. Two spike solutions were used: the first was used for low concentration samples and had a ^{185}Re concentration of 2.86×10^{-12} pmol g^{-1} and a ^{185}Re/^{187}Re ratio of 37.67; the second was used for spiking higher concentration samples and had a ^{185}Re concentration ratio of 2.10×10^{-9} nmol g^{-1} and a ^{185}Re/^{187}Re ratio of 28.94. Isotope dilution is advantageous relative to the direct calibration method as it can compensate for partial loss of Re during sample preparation, provided that the loss occurs after chemical equilibrium of the spike with the sample water. It is also not affected by sample matrix effects or drift in the instrument calibration.

2.3.2 Column chemistry to separate and purify samples

The Re separation and purification procedure involved concentrating sample Re in a smaller volume of solution and removing the bulk of the dissolved solids that would otherwise elevate the background signal and cause interferences (Figure 2.5). Purification also minimises the variation in instrumental mass bias arising from matrix differences between the sample and standard solutions (Kendall et al., 2017; Lu et al., 2017; Pearce et al., 2009). Chromatographic separation works by attracting different solute ion species to varying degrees to the active sites on a resin, usually loaded in a column that can be made of plastic, Teflon or glass. Carrier solutions (eluants) migrate down the column at different rates. The column design, type of resin, and reagents used determine how long an element of interest is retained on the resin. Here, 0.5 mL of Bio-Rad AG® 1-X8 (200–400 mesh) Eichrom anion exchange resin was used in a 1 mL Poly-Prep® column to pre-concentrate the Re and to remove sample matrix. The purification procedure involved the sequential use of three solutions (0.2M HNO_3, 0.2M HCl and 6M HNO_3) for loading, washing and collecting the Re fraction. These acid molarities were based on previous work using similar columns (Morgan et al., 1991; Selby and Creaser, 2001). In detail, 0.5 mL of anion exchange resin was first cleaned on each column with 1 mL of 8M HNO_3 and preconditioned with 1 mL of 0.2M HNO_3. Samples were loaded onto the preconditioned columns in 0.5 mL of 0.2M HNO_3, after which the column was rinsed with 3 mL of 0.2M HNO_3. The columns were then washed with 2 mL of 0.2M HCl and 0.25 mL 6M HNO_3. The pure Re fraction was recovered from the bottom of the column in acid cleaned PMP beakers during elution by 2.5 mL of 6M HNO_3 and evaporated to dryness. Other solutes that were eluted in earlier fractions were discarded. Teflon labware was cleaned between samples by soaking in aqua regia (a 2:1 mixture of HNO_3 and HC1) for 1 day, followed by heating to 180ºC in MQ, H_2O_2 and 8M HNO_3, each for 1 day.

The column chemistry method used for Mo isotope work (section 2.6.2; ***Chapter 5***) has previously been described as a method to simultaneously extract Re (Pearce et al., 2009). To explore this further, the 'Mo isotope columns' were calibrated by passing a 10 μg mL^{-1} Re solution through the columns and successive eluted fractions were collected. Elemental Re concentrations were determined for all calibration aliquots (0.5 mL) using the Q-ICP-MS and an elution curve was generated (Figure 2.6). Quantitative recovery of Re from the column was confirmed by assessing the yields of Re: 99% of the Re was collected between aliquots 12 and 17, with an overall yield of approximately 80%. Eight Re abundance data quantified for New Zealand river water samples were measured using this method. However, the mini-column method outlined above was faster and used for the majority of samples.

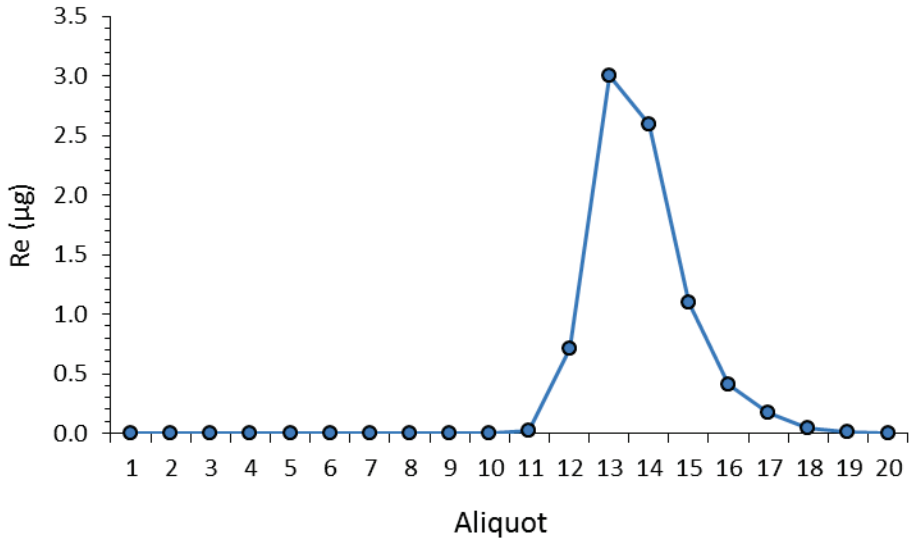

Figure 2.6 Column calibration for Re abundance. Re elution curve from the columns used primarily for Mo isotope work identifies the aliquots over which Re is eluted. The volume of each aliquot was 0.5 mL. The elution curve indicates that 99% of the Re was collected between aliquots 12 and 17.

2.3.3 Q-ICP-MS conditions, standard solutions and sample replicates

The Re isotope composition of the purified Re aliquots was determined in a 0.8M HNO_3 medium using a Thermo Scientific X-Series Q-ICP-MS at Durham University. Samples were run manually with an analytical time of 120 ms per analysis (20 ms on each Re isotope, which was measured three times) and there were a total of 20 analyses per sample. There was a minimum of a 30 s delay before uptake but the total wash out time varied depending on the previous sample concentration and was operated manually. An acid blank (3.5% HNO_3) was run in between each sample to monitor the background Re concentration. A 1 ng g^{-1} Re standard prepared in 3.5% HNO_3 was run prior to all samples to quantify the natural abundance ratio of $^{185}Re/^{187}Re$. The measured difference in $^{185}Re/^{187}Re$ values for the Re standard solution and the accepted $^{185}Re/^{187}Re$ value (0.5974: Gramlich et al., 1973) was used for mass fractionation correction of the Re sample data. Isotope dilution data can be sensitive to the natural abundance ratios of ^{185}Re and ^{187}Re that are calibrated in each analytical session using a non-spiked 1 ng g^{-1} solution standard, and may vary with background machine variation. All data were blank corrected. The column blank was measured as 1.05 ± 0.51 pg (±1 SD, n = 14), which is <0.5% of the typical sample mass of Re and similar to published methods (e.g. Dalai et al., 2002). Therefore, the blank had no discernible effect on the measured Re concentration of samples. Analytical uncertainties on the determined Re abundance were determined by full error propagation of the uncertainties in Re mass spectrometry measurements, blank abundance and isotope compositions, spike calibrations and the reproducibility of standard Re isotope values.

The long-term reproducibility of $[Re]_{diss}$ was also quantified by isotope dilution of the river water standard 'SLRS-5', which is an external standard. Although this standard is not certified for

$[Re]_{diss}$, previous analyses have reported a value of 66 ± 12 pg g^{-1} (Yeghicheyan et al., 2013). The reason for the relatively large uncertainty in this published value is because $[Re]_{diss}$ was only measured by two laboratories. Measurements at SARM Nancy are reported as 66 ± 3 pg g^{-1} (Yeghicheyan et al., 2013), but there is a need for more inter-laboratory comparisons in a wider analysis of SLRS-5. The isotope dilution method used here returned a long-term mean $[Re]_{diss}$ = 59.8 ± 1.7 pg g^{-1} (n = 12, ±2 SE) (Figure 2.7). This is in agreement with the reported value of 66 ± 12 pg g^{-1} (Yeghicheyan et al., 2013); confirming accuracy and also providing improved constraint on the composition of SLRS-5.

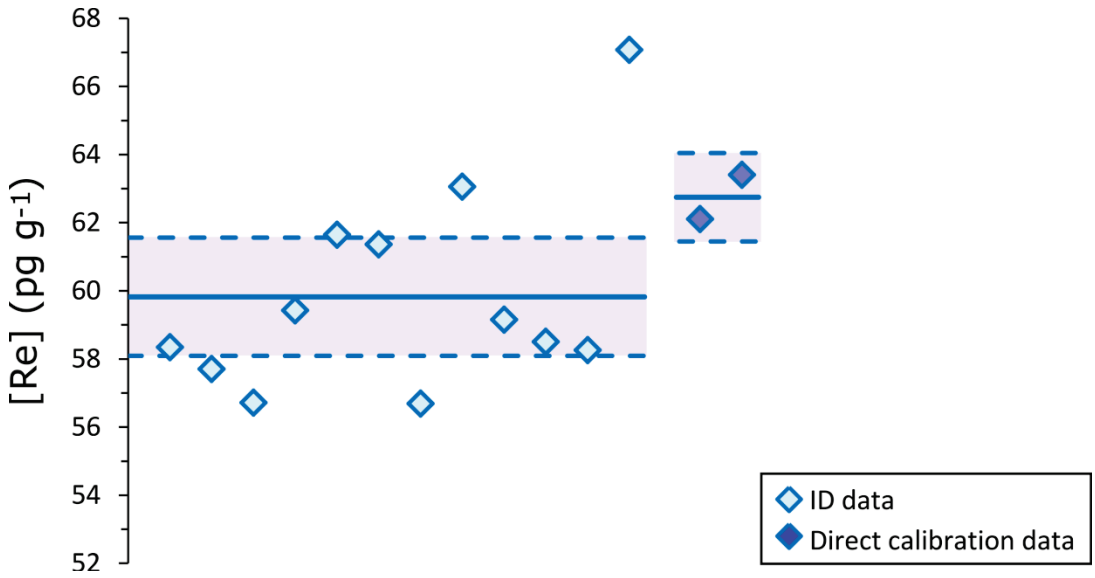

Figure 2.7 Reproducibility of the SLRS-5 standard by isotope dilution (ID) and direct calibration methods. The solid lines represent the mean for the two techniques and the dashed lines are ±2 SE on the mean.

In addition to the SLRS-5 standard, several Canadian water samples were processed in duplicate using the isotope dilution technique (Figure 2.8). This was partly to assess data reproducibility via this method, but also to evaluate data reliability as some of these Canadian samples appeared to have poorer agreement with the direct calibration Re data than observed in previous sample batches. Nevertheless, duplicate analyses of these data indicated that both full analytical procedures were in close agreement to a 1:1 relationship. The reproducibility of $[Re]_{diss}$ data in the Canadian river waters and the SLRS-5 standard demonstrate that the analytical procedure can be applied reliably to a wide range of geological water types.

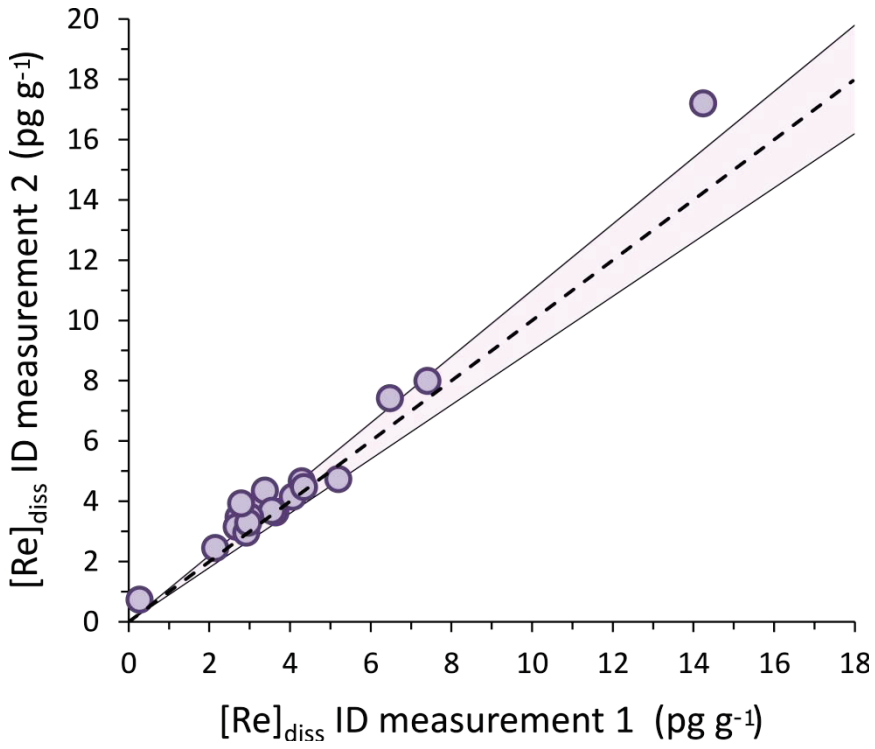

Figure 2.8 Reproducibility of Re abundance data quantified by isotope dilution (ID). Dashed line is a 1:1 line. The shaded envelope indicates ±10% deviation from the 1:1 line.

2.3.4 Comparison between direct Q-ICP-MS and ID Q-ICP-MS

Repeat measurements using both the direct Q-ICP-MS (calibration curve) and isotope dilution Q-ICP-MS techniques were made to assess the longer-term reproducibility and precision of these independent methods. This analysis includes river water data from New Zealand, Canada and Iceland, which span a large range of Re concentrations. Figure 2.9 and Figure 2.10 illustrate how the $[Re]_{diss}$ measurements by isotope dilution compare to the Re concentrations quantified by direct calibration across all concentrations (Figure 2.9) and the lower concentrations (Figure 2.10). In Figure 2.10, two columns types are indicated: the first column type was used for the majority of ID Re measurements and was a 1 mL Poly-Prep® column (section 2.3.2); the second type was a 10 mL column generally used in Mo isotope work (section 2.6.2). The results demonstrate general agreement between direct calibration and ID methods, particularly when Re concentrations are >1 pg g^{-1} and the data show close agreement to a 1:1 line. There is some suggestion that the New Zealand $[Re]_{diss}$ data quantified by direct Q-ICP-MS are higher than data quantified by isotope dilution, although the Canadian data is in closer agreement.

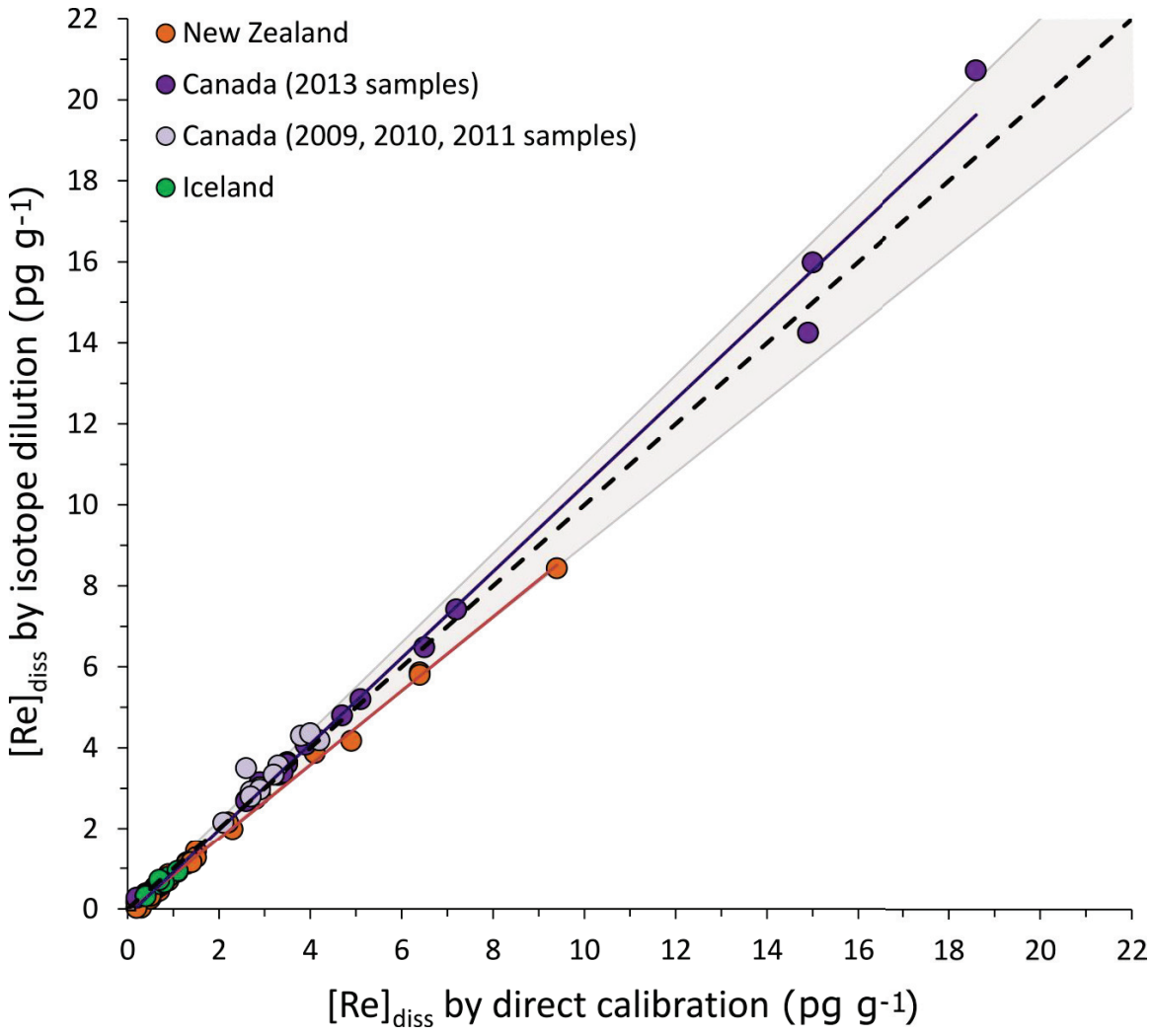

Figure 2.9 Comparison between $[Re]_{diss}$ data quantified using the direct calibration method and isotope dilution methods. The full range of concentrations quantified are separated according to sampling locality. Dashed line is a 1:1 line, with ±10% deviations from this line indicated within the shaded band. The orange line is the linear best fit for the New Zealand samples ($r^2 = 0.997$). The purple line is the linear best fit for the Canada (2013) samples ($r^2 = 0.993$).

At lower Re concentrations, there is a more systematic offset between the direct and isotope dilution $[Re]_{diss}$ measurements (Figure 2.10). The isotope dilution method produces values that are consistently ~30% lower than those quantified by the direct calibration method. This could imply that the direct method over-estimates Re concentrations when values are close to instrument detection limits. This may reflect the fact that blanks in the direct calibration method are up to ~50% of the Re concentration present in the low concentration samples. In contrast, the isotope dilution technique has column blanks that are typically <1% of the total sample mass used and all of the data are blank corrected. In addition, the differential matrix of major ions in river water (e.g. Na^{2+}, Ca^{2+}, SO_4^{2-}) may result in some of the differences observed between the measurement accuracy of $[Re]_{diss}$ measured by direct Q-ICP-MS and that via isotope dilution ICP-MS, and some of the observed differences between analytical runs (Figure 2.4). Therefore, when sample concentrations are low, particularly below ~0.5 pg g^{-1}, purifying and concentrating the Re prior to

analysis using column chemistry, coupled with isotope dilution, is the preferred technique for acquiring optimum precision, unbiased by background.

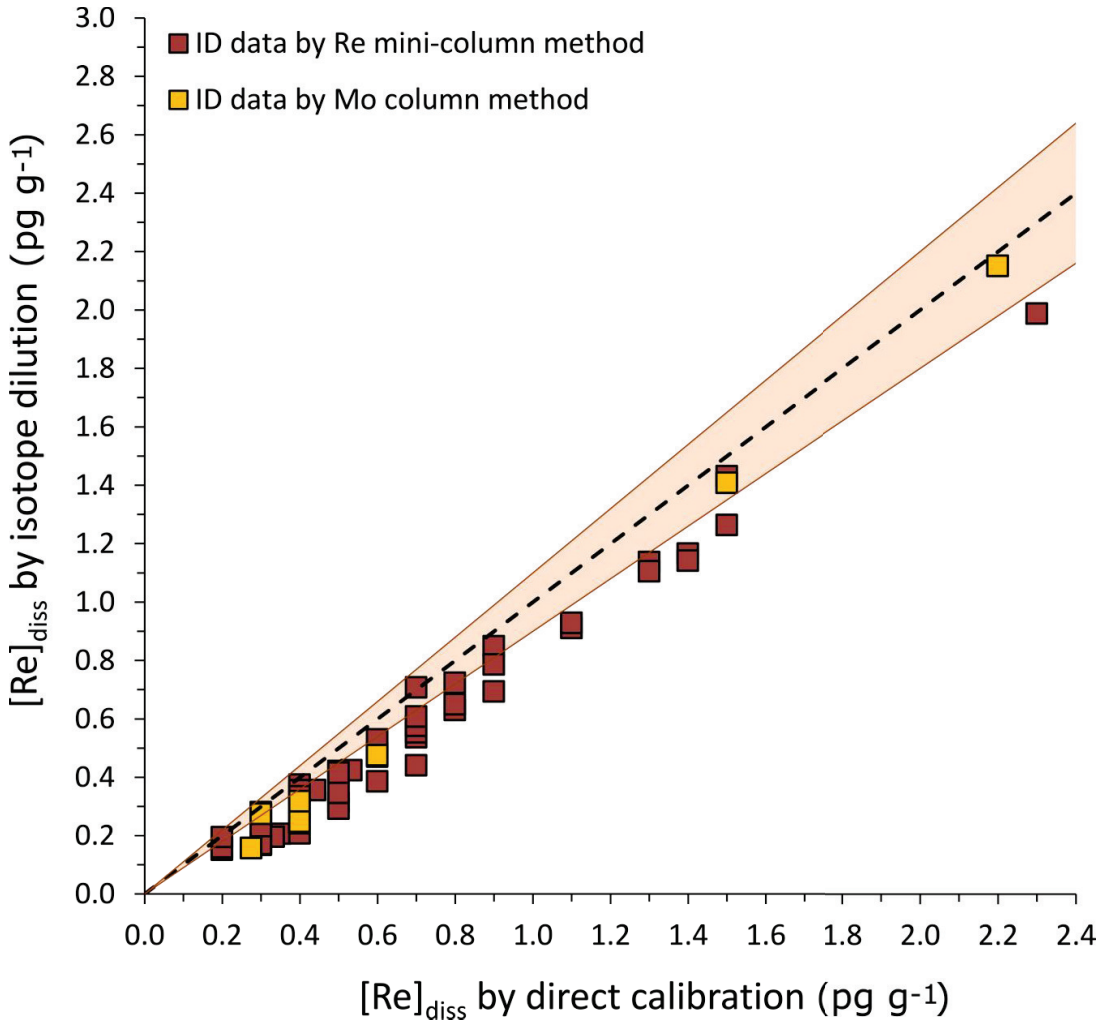

Figure 2.10 Comparison between Re abundance data in river waters quantified using the direct calibration method and isotope dilution methods at low Re concentrations. Data from the two column types are indicated. Red squares include data from New Zealand and Iceland; orange squares are data from New Zealand. Re concentration quantified by the direct calibration are systematically higher that those quantified by isotope dilution. Dashed line indicates a 1:1 relationship, and ±10% deviations from this line are indicated within the shaded band.

2.4 Re concentration in solid samples by isotope dilution

Measurement of [Re] in solid samples is more routine (e.g. Cumming et al., 2014; Rooney et al., 2012; Selby and Creaser, 2003) than for river waters (Miller et al., 2011) because concentrations are typically in the ng g^{-1} range. In this research, surface soil, weathered colluvium and river bed materials were ground to fine powders prior to acid digestion to generate integrated bulk samples. An aliquot of laboratory sand was run in the zirconium disc mill and the swing mill was washed with soap and water and rinsed with ethanol between samples. For Re concentration analysis, a known weight of sediment powder (~0.05–0.5 g) was doped with a known amount of ^{185}Re spike solution and digested in a 2:1 HF-HNO_3 mix (9 mL) for 24 hours at 120ºC and then evaporated.

The dried sample was further digested in a 2:1 mix of HNO_3-HCl (3 mL) for 24 h at 120ºC, and then evaporated. The Re was isolated and purified using a NaOH-acetone solvent extraction methodology (Cumming et al., 2013). In summary, 5 mL NaOH was added to the digested sediment, well mixed and transferred to a 15 mL centrifuge tube. Acetone (5 mL) was then added to the NaOH-sample mix to extract Re from the sample-NaOH solution. The mixture was agitated for 10 minutes and centrifuged for 15 minutes before the Re-bearing acetone was pipetted off and transferred to a Teflon beaker to evaporate at 70ºC. The Re isotope composition of the purified Re aliquots was determined in a 0.8M HNO_3 medium using a Thermo Scientific X-Series Q-ICP-MS. Data reproducibility were assessed by processing samples in duplicate. The very close agreement between duplicate sample data (Figure 2.11) indicates that sample heterogeneity in powdered aliquots is minimal and that the analytical procedure is effective in isolating sample Re.

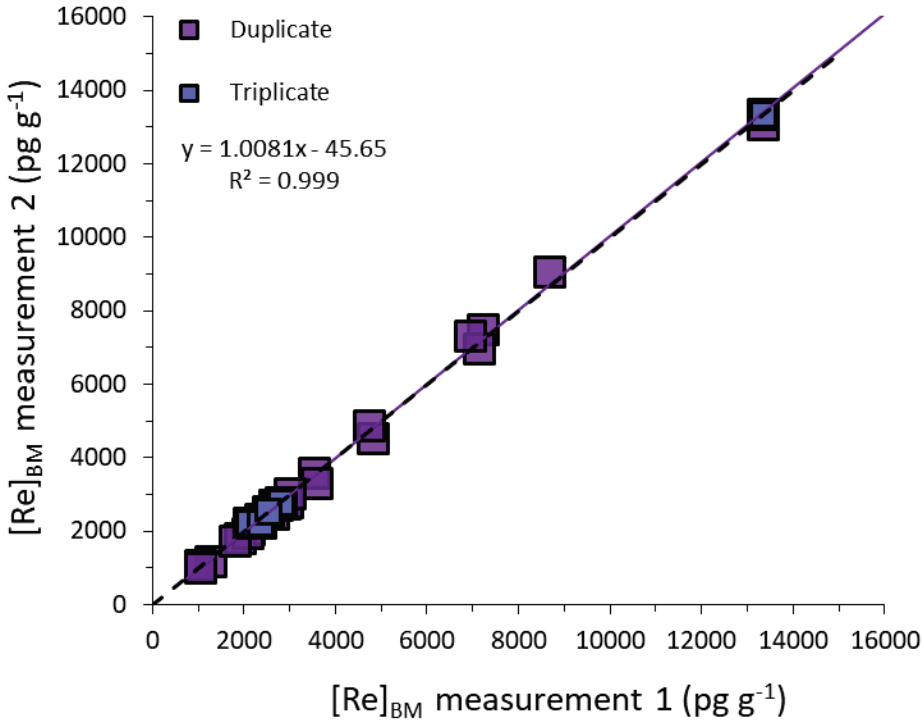

Figure 2.11 Reproducibility of Re abundance data in solid samples quantified by isotope dilution–ICP-MS. Dashed line is a 1:1 line and sample reproducibility is better than 8%, even with blank issues in some sample batches.

High and low concentration Re-bearing reference materials, Bush Creek (SBC-1) and SCO-1 shales respectively, were processed alongside sample runs to validate the accuracy and reproducibility of our Re data. The Re concentration in the Bush Creek (SBC-1) reference material was determined to be 10,090 ± 101 pg g^{-1} (±1 SD, n = 6) and the Re concentration in the SCO-1 reference material is 1085 ± 68 pg g^{-1} (±1 SD, n = 6). Variability in data across analytical runs is shown in Figure 2.12. The Re concentration values generated in our analyses are in agreement with published data on SCO-1 analysed by isotope dilution ICP-MS using an on-line chromatographic

matrix separation after acid digestion in a high pressure asher: 1050 pg g^{-1} (Meisel and Moser, 2004). The long-term in-house (Durham University) reproducibility of the Bush Creek (SBC-1) reference material by CrO_3-H_2SO_4 dissolution and Negative Thermal Ionisation Mass Spectrometry (N-TIMS) analysis (Selby and Creaser, 2003) is 10,331.9 ± 236.9 pg g^{-1}, n = 25, ± 1SD (Selby, 2017; *unpublished data*). We find that SCO-1 has more variability than Bush Creek, which may reflect the lower concentration of this standard and the lower precision at the lower concentrations: data show 10% deviation on the published value for this standard, *cf.* 2% for the Bush Creek reference material (Figure 2.12). Alternatively, the SCO-1 reference material may have greater heterogeneity, which has not been overcome using the aliquant amount.

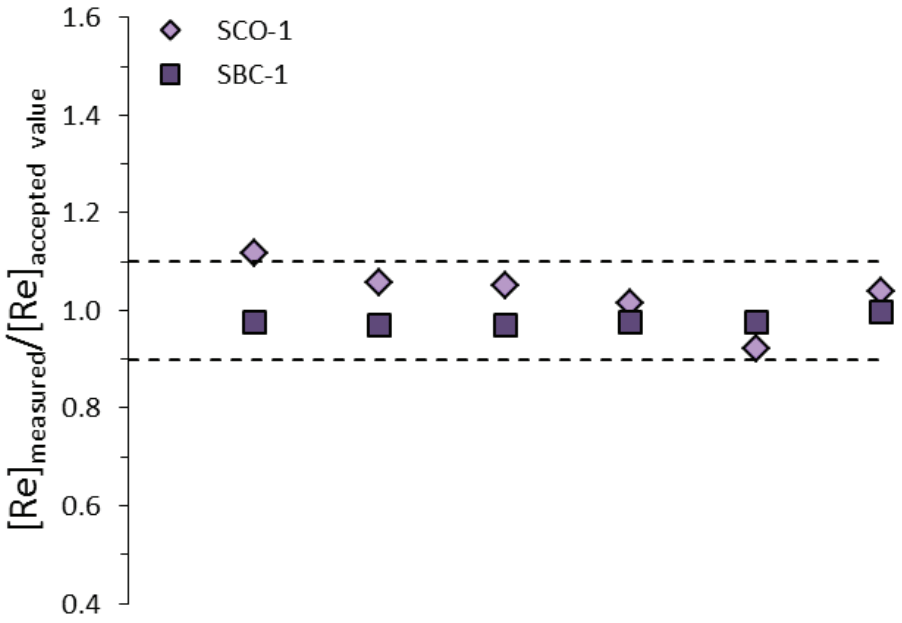

Figure 2.12 Reproducibility of Re abundance data quantified by isotope dilution – ICP-MS in reference materials. The standards' Re concentration data are normalised to published data (SCO-1: Meisel and Moser, 2004) or long-term in-house measurements (SBC-1: Selby, 2017; *unpub. data*) and indicate that the reproducibility is <3% for the SBC-1 standard and ~10% for the SCO-1 standard. Dashed lines are ±10%.

Blanks from the digestion protocol ranged from 1–80 pg g^{-1} (n = 19), with typical values between 2 and 8 pg g^{-1} (n = 16). Where blanks were high, full-analysis replicates produced data in agreement to within 5% (Figure 2.11), confirming that these blanks were representative of the analysis but had minimal effect on data accuracy. As for the water analyses, all data were corrected for mass fractionation and blank contributions.

2.5 Molybdenum abundance analysis

2.5.1 Water samples

Molybdenum concentrations in the dissolved river loads were determined by direct calibration against a pure Romil Mo standard diluted to between ~0.1–20 ng g^{-1} in 0.5M HNO_3 to form solutions with a concentration range comparable to that observed in samples (see section 2.2.1, in

analogy to Re). The Mo concentrations of samples processed for their Mo isotope composition were also determined for a second time by ID Multi Collector – ICP-MS (MC-ICP-MS) and agree with the direct calibration data to within 12% (Figure 2.13). In general, the concentrations generated by direct calibration on the Q-ICP-MS were used in the water data analyses (***Chapter 5***), to enable consistency in the comparison across all samples. However, where the accuracy of the numbers was important to the interpretation (Figure 5.12), the ID MC-ICP-MS data were used alongside the $\delta^{98/95}$Mo data collected on the same sample aliquots.

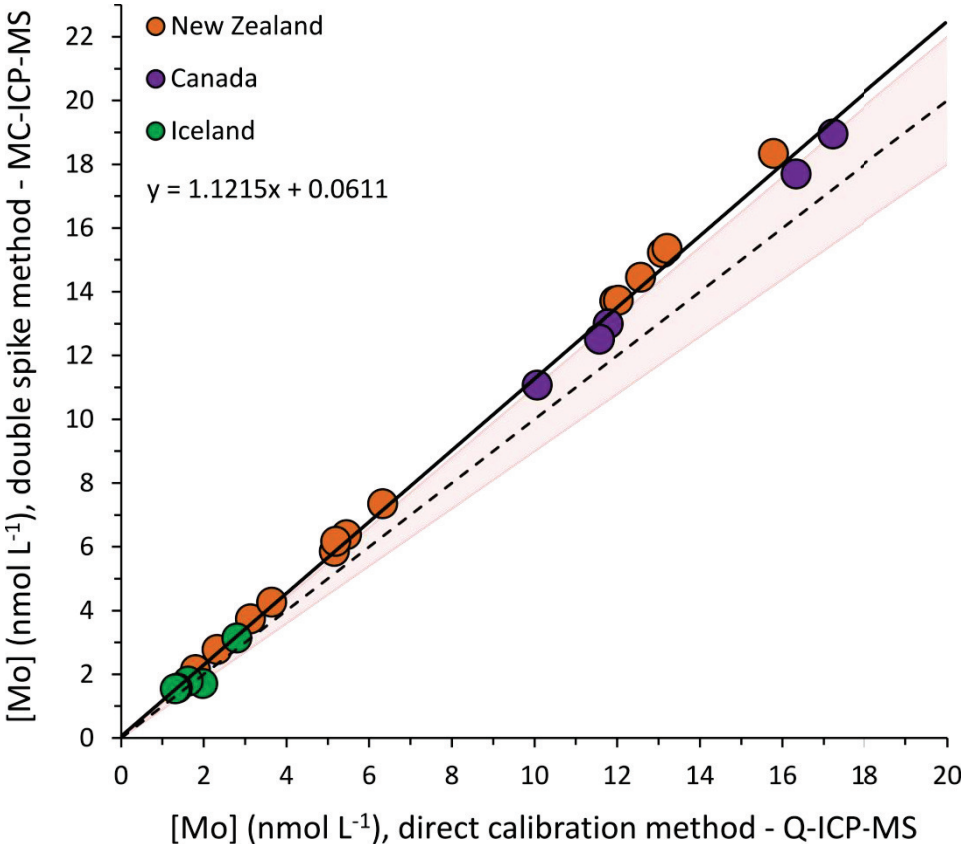

Figure 2.13 Agreement between Mo concentration data for water samples quantified using isotope dilution and MC-ICP-MS versus a direct calibration method and Q-ICP-MS. Data for all study sites (New Zealand, Canada and Iceland) are shown and are compared to a 1:1 agreement, indicated by the dashed line. The shaded band indicates ±10% deviations from the 1:1 line. The solid black line shows the best fit to the data from all catchments (linear regression equation is given on plot).

Confidence in these values was confirmed by the accuracy and reproducibility of the concentration of the BHVO-1 basalt and IAPSO seawater reference materials defined by this method. The BHVO-1 produced a mean [Mo] value of 1.00 ± 0.05 µg g^{-1} (n = 21, ±2 SD), which compares well to published data of [Mo] = 1.02 ± 0.10 µg g^{-1} (n = 10, 95% confidence) generated by isotope dilution thermal ionisation mass spectrometry (ID-TIMS) (Wieser et al., 2007). The IAPSO seawater reference material produced a mean [Mo] = 10.9 ± 0.51 ng g^{-1} (n = 5, ±2 SE), which is in agreement with published values of 10 and 11 ng g^{-1} (Greber et al., 2012). The agreement between the duplicate analyses of BHVO-1 and IAPSO is shown in Figure 2.14.

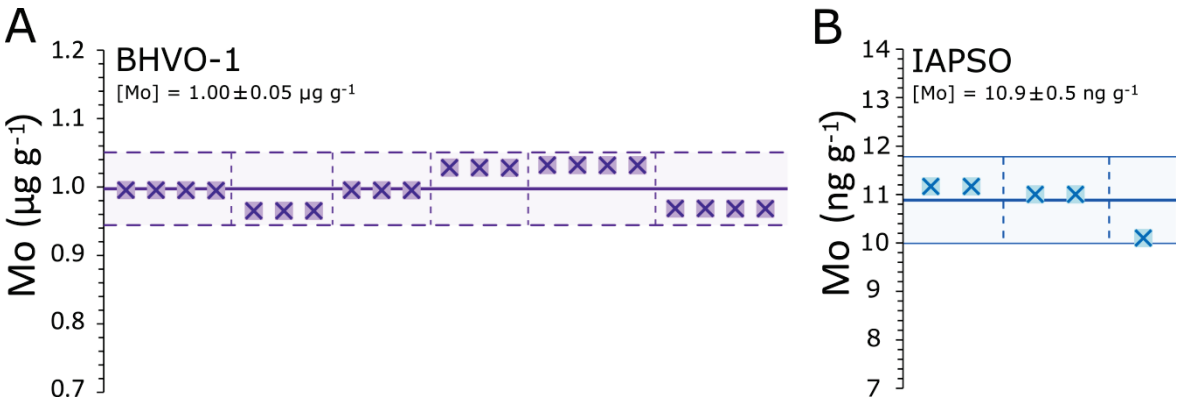

Figure 2.14 Mean and long-term reproducibility of Mo concentration quantified by isotope dilution for reference materials. A. BHVO-1 basalt reference material. Thick purple line shows the mean value. **B.** IAPSO seawater reference material. Thick blue line shows the mean value. Shaded areas represent ±2 SD on the mean. Vertical dashed lines separate analytical sessions.

2.5.2 Solid samples

Before digesting bedload and soil materials to assess their Mo concentration, these sediments were first powdered using a zirconium disc mill, in an analogous way to the preparation protocol for Re analysis in solid samples (section 2.4). Homogenising bedload samples by crushing allowed an integrated bulk Mo composition to be generated. The powdered solid samples (surface soil, weathered colluvium, river bed materials) and suspended particulates (non-powdered) were then digested in a 2:1 mix of concentrated HF-HNO_3 (6 mL) for 72 hours at 120ºC and evaporated. The dried sample was further digested in a 2:1 mix of concentrated HNO_3-HCl (4.5 mL) for 48 h at 120ºC, and evaporated, and then 3 mL of 16M HNO_3 followed by 5 mL of 6M HCl was added. After the solution was evaporated, the residue was re-dissolved in 10 mL of 1M HCl and a small aliquot (0.5 mL) was extracted for concentration analyses. These initial Mo concentration data were used to provide an indication of the spike volume required for Mo isotope analysis (based on a 1:1 spike-sample ratio; see section 2.6).

The Mo concentrations of spiked sample aliquots that were processed through column chemistry for isotope measurements were also quantified using isotope dilution by MC-ICP-MS (Thermo-Neptune). The Mo concentration is provided as an output of the spike deconvolution method (Rudge et al., 2009). These concentration data can be compared to the concentrations quantified in non-spiked sample aliquots by Q-ICP-MS (Figure 2.15A and 2.15B). The agreement between the two methods is considerably reduced for the solid samples than is observed for the waters (Figure 2.13), suggesting that matrix effects have a strong effect on data quality for the solid material. For this reason, direct Q-ICP-MS measurements of [Mo] for solid samples are not recommended unless the samples have been passed through a column to remove sample matrix.

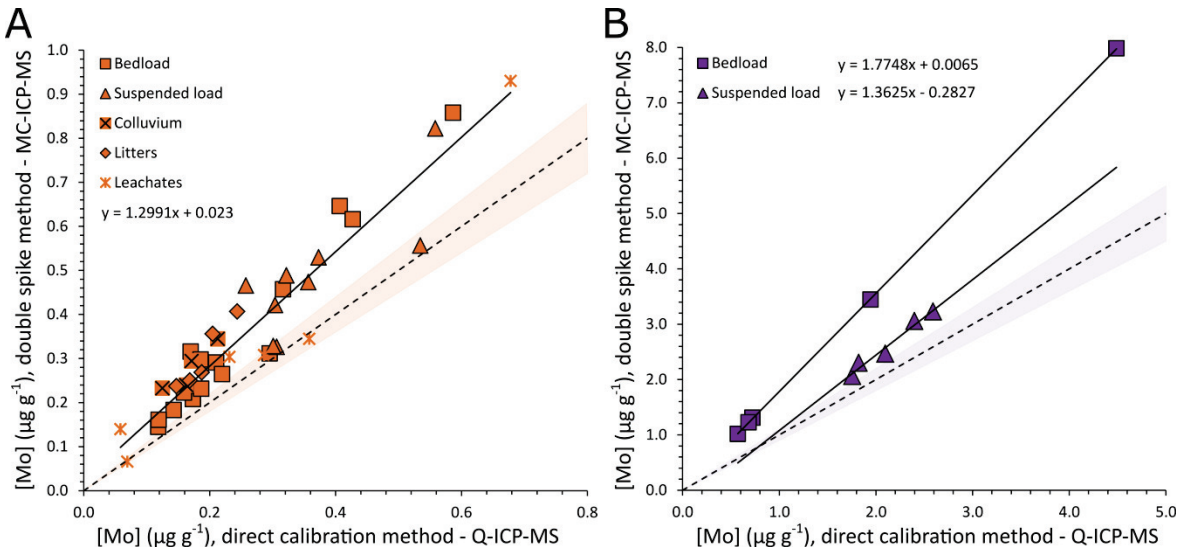

Figure 2.15 Agreement between Mo concentration data for solid samples quantified using Q-ICP-MS and MC-ICP-MS. A. Data for New Zealand samples. Data are compared to a 1:1 line, indicated by the dashed line. The shaded band indicates ±10% deviations from the 1:1 line. The solid black line shows the best fit to the data from all catchments for all sample types (linear regression equation is given on plot). **B.** Data for Canada samples. Data are compared to a 1:1 line, indicated by the dashed line. The shaded band indicates ±10% deviations from the 1:1 line. The solid black lines show the best fits to the data for the suspended sediments and bedload samples (linear regression equations are given on the plot).

The data quantified by MC-ICP-MS following the removal of sample matrix by column chemistry were used for the discussion of solid sample Mo concentrations (***Chapter 5***). The agreement between the duplicate analyses of solid samples is shown in Figure 2.16 and for most samples reproducibility was better than 5%.

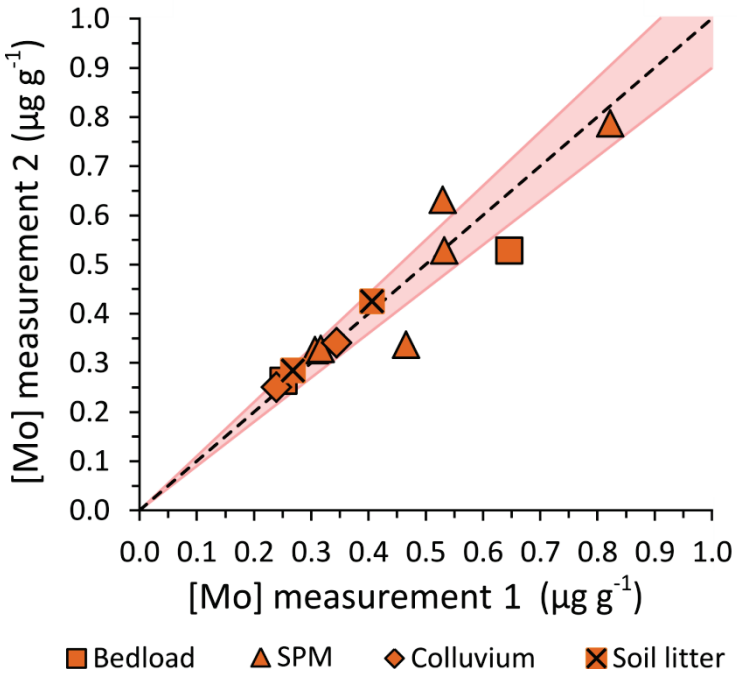

Figure 2.16 Agreement between duplicate solid sample Mo concentration data. Full procedural duplicates for a range of sediment samples from the western Southern Alps are compared against a 1:1 line. The ±10% fits to the 1:1 dashed line are indicated within the shaded band.

2.6 Molybdenum Stable Isotopes

2.6.1 Overview

Chapter 5 aims to accurately determine the atomic abundance ratio of Mo isotopes in river waters, soils, river suspended particulates and river bed materials. Previous research has established the convention of measuring ^{98}Mo and ^{95}Mo for a variety of reasons that consider isotope abundance, mass dependent fractionation and instrumental interferences (Kendell et al., 2017). Molybdenum stable isotope fractionation is conventionally reported in delta notation ($\delta^{98/95}$Mo) for ^{98}Mo/^{95}Mo ratios, in parts-per-thousand relative to a reference solution (Equation 2.2).

Equation 2.2 $$\delta^{98/95}\mathrm{Mo}_{\mathrm{sample}} = \left[\left(\frac{^{98/95}\mathrm{Mo}_{\mathrm{sample}}}{^{98/95}\mathrm{Mo}_{\mathrm{NIST-3134}}}\right) - 1\right] \times 1000$$

The NIST SRM (National Institute of Standards and Technology Standard Reference Material) 3134 standard has been proposed to serve as the zero-delta reference material for Mo isotopes (Goldberg et al., 2013; Greber et al., 2012). By bracketing analyses of samples by this standard, which is run under the same instrumental conditions, we can evaluate and correct for any systematic instrumental drift. Importantly, this correction relies on the assumption that instrumental mass bias has a constant drift during analysis and does not vary systematically between samples and standards. However, because the samples are double spiked, we have an independent way of correcting for instrument mass bias.

In this study, the $\delta^{98/95}$Mo value of the NIST SRM 3134 standard is assigned a value of 0‰. However, to enable direct comparison to older published data, which may have been normalised to other in-house Mo reference materials, or reported using the ^{97}Mo/^{95}Mo ratio, it may be necessary to scale data accordingly. The scaling required for inter-laboratory data comparison can vary (Goldberg et al., 2013) but, typically, the required correction to convert between $\delta^{98/95}$Mo normalised to NIST = 0‰ and many published data will be to subtract 0.25‰ (Nägler et al., 2014).

2.6.2 Column chemistry and Mo double spike

For isotope analysis of all sample types, Mo was first separated and purified using anion exchange chromatography. Sample solutions were passed through a column packed with an anion exchange resin (Bio-Rad AG1-X8), following the method used by Siebert et al. (2001), Pearce et al. (2009) and Nagai and Yokoyama (2016). As outlined for Re (section 2.3.1–2.3.2), purification helps to eliminate variation in instrumental mass bias arising from matrix differences between the sample and standard solutions. It also minimises elemental interferences; in this case Zirconium interferes on Mo masses 92, 94 and 96 and Ruthenium interferes on masses 96, 98 and 100 (Willbold et al., 2016). Although Mo isotopes are known to fractionate during the elution stage of the anion

exchange system, we correct for this fractionation by mixing and equilibrating the sample Mo with a double spike prior to purification (Pearce et al., 2009; Willbold et al., 2016).

The spike used consists primarily of the isotopes ^{97}Mo and ^{100}Mo in the proportions of 40% and 56%, respectively. The Mo concentration of the spike is 2.0281 μg g^{-1}. The spike isotopes follow the same fractionation law as the ^{98}Mo and ^{95}Mo isotopes that are of interest, and allow for $\delta^{98/95}$Mo data to be obtained. Doping samples with the double spike solution allows the fractionation that occurs during chemical separation and mass spectrometry to be corrected for. Therefore, the chemical separation technique can focus primarily on purification rather than on optimum yield.

The protocol for preparing the anion exchange resin for Mo isotope work first involved de-fining the resin by rinsing it with Milli-Q water, allowing it to settle and decanting off the fine material. Successive rinses with the following acids were then carried out: 6M HCl, 8M HNO_3 and 1M HCl. After the resin was loaded onto the columns it was pre-cleaned with 10 mL 2M NH_4NO_3 + 2M NH_4OH and 10 mL 8M HNO_3 twice before the column chemistry method was continued. For water samples, the resin could be used multiple times and for solid samples it was generally re-used 2–3 times.

For river waters, between 30 and 500 mL of the water was doped with a known amount of the ^{97}Mo-^{100}Mo double spike solution to achieve a combined Mo mass of ~100 ng, with a spike-sample mix ratio of 1:1. The chemistry was modified from that described by Pearce et al. (2009). In brief, the spiked water sample was evaporated to dryness before being re-dissolved in 5 mL 0.5M HCl for loading on to the column. The columns were pre-cleaned with 20 mL 8M HNO_3, 10 mL 6M HCl, 10 mL 1M HCL, 5 mL 1M HF and 10 mL 3M HNO_3, and preconditioned with 5 mL 0.5M HCl. The sample was loaded on to 2 mL of AG 1-X8 anion exchange resin in 5 mL 0.5M HCl, and the bulk matrix was washed through with 5 mL 0.5M HCl, 10 mL HCl + 1M HF, 8 mL 4M HCl and 12 mL 1M HF. The Mo was finally eluted in 12 mL 3M HNO_3. The columns were part-cleaned for subsequent chemistry with 20 mL 8M HNO_3 and 5 mL 1M HCl and stored in 0.5M HCl.

For the solid samples, the chemistry method closely follows that presented in Willbold et al. (2016). The columns were pre-cleaned with 10 mL 0.5M HCl, 10 mL 2M NH_4NO_3 + 2M NH_4OH, 10 mL 8M HNO_3, 5 mL 1M HF and 10 mL 0.5M HCl. The columns were then preconditioned in 3 mL 3M HCl. After concentration checks, the remaining 1M HCl solution from the digestion process (section 2.5.2) was spiked, before being evaporated and brought up in 4.75 mL of 3M HCl for loading. Immediately prior to loading, 0.25 mL of ascorbic acid was also added to the samples to oxidise Fe from Fe^{2+} to Fe^{3+} and enhance removal of Fe adsorbed to the resin matrix. The

volume of anion exchange resin used was 1 mL. A bulk wash with 3 mL 3M HCL followed. A 13 mL mixture consisting of 0.5M HCl + 0.5% H_2O_2 was then added to the columns in 1 mL aliquots for the first 3 mL, and 5 mL aliquots for the final 10 mL, to elute residual Fe. Zinc was then eluted in 10 mL 1M HF. The Mo aliquot was collected in 12 mL of 1M HCl in acid cleaned Teflon beakers. The columns were part-cleaned for subsequent chemistry with 20 mL 8M HNO_3 and stored in 0.5M HCl. The total procedural blanks for processing Mo in this study ranged from 0.1–1.7 ng g^{-1} with a mean blank [Mo] = 0.75 ± 0.51 ng g^{-1} (n = 16, ±1 SD).

2.6.3 Mo isotope ratio measurements by MC-ICP-MS

Molybdenum isotope measurements were made using a Thermo-Fischer Neptune multi-collector inductively coupled plasma mass spectrometer (MC-ICP-MS) in the Arthur Holmes Geochemistry Laboratory, Durham University. Samples were introduced to the instrument using an Aridus II desolvator and a Savillex PFA20 nebuliser at 150–200 ng g^{-1} concentration in 0.5M HNO_3. The uptake rate was ~35 µl min^{-1} and the maximum sensitivity was ~400 V (µg $g^{-1})^{-1}$. Measurements were made in low resolution mode using X-cones and static collectors. Analyses consisted of 50 cycles of 4 s integrations. Prior to each analysis there were 5 minutes of washout and a blank acid (0.5M HNO_3) was measured prior to each sample. The cup configuration was as follows: $L_4 = {}^{91}Zr$, $L_3 = {}^{92}Mo$, $L_2 = {}^{94}Mo$, $L_1 = {}^{95}Mo$, $C = {}^{96}Mo$, $H_1 = {}^{97}Mo$, $H_2 = {}^{98}Mo$, $H_3 = {}^{99}Ru$ and $H_4 = {}^{100}Mo$.

The data were deconvolved using IsoSpike, an add-in to IGOR Pro (Paton et al., 2011). Isospike is a double-spiked inversion software based on the method of Creech and Paul (2015), which uses algebraic equations presented in Rudge et al. (2009). The blank baseline subtraction was carried out using a step forward integration and in general, the last 60 s of data were used. However, the raw imported data were first assessed for any anomalies; for example errors can arise as a consequence of partial nebulizer blocks and any affected integrations must be removed manually. Raw ^{92}Mo, ^{94}Mo, ^{96}Mo and ^{100}Mo intensities were corrected for isobaric interferences using measured ^{91}Zr and ^{99}Ru data. Although instrumental mass bias is large (+17‰/amu), and exceeds the variability found in nature (~1‰/amu), it is very stable over time (Kendall et al., 2017). Therefore, a correction for mass-bias by standard-sample bracketing is possible. Here, NIST 3134 was used as the bracketing standard (section 2.6.1) and sample data were corrected based on the performance of this standard every session using linear interpolation between individual NIST 3134 measurements made every 1–2 unknowns.

The long-term $\delta^{98/95}Mo$ machine reproducibility was determined by measurement of an in-house Romil standard run under the same instrumental conditions, which gave $\delta^{98/95}Mo$ = 0.046 ± 0.029‰ (n = 99, ±2 SD). The long term reproducibility of the IAPSO seawater reference material is $\delta^{98/95}Mo$ = 2.07 ± 0.06‰ (n = 5, ±2 SD) (Figure 2.17), which is indistinguishable from the mean

of published values (2.08 ± 0.10‰; Goldberg et al., 2013). Full procedural duplicate analyses on two water analyses provided data in agreement to <0.02‰ and these data were averaged and reported with the ±2 SD error on the mean value in ***Chapter 5***. Duplicate analyses on 12 sediment samples produced data in agreement to within 0.1‰, with a mean difference of 0.025‰. The long-term reproducibility on the BHVO-1 basalt reference material processed in each analysis is $\delta^{98/95}$Mo = 0.19 ± 0.04‰ (n = 21, ±2 SD) (Figure 2.17). Sample reproducibility for the solid samples is shown in Figure 2.18: all samples fall within their ±2 SD error of the 0.05‰ fits of the 1:1 line.

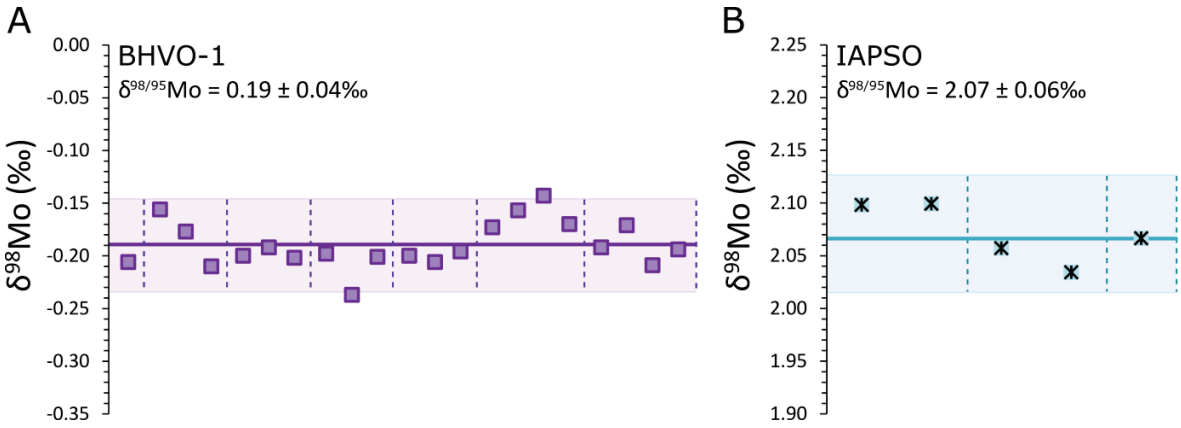

Figure 2.17 Long-term reproducibility of standards used in Mo isotope analyses. A. BHVO-1. Thick purple line shows the mean value. **B.** IAPSO seawater salinity reference material. Thick blue line shows the mean value. The ±2 SD errors on the long-term mean replicate values are indicated within the shaded bands. The ±2 SE analytical error on an individual measurement is smaller than the point size. Separate analytical sessions are marked with dashed vertical lines.

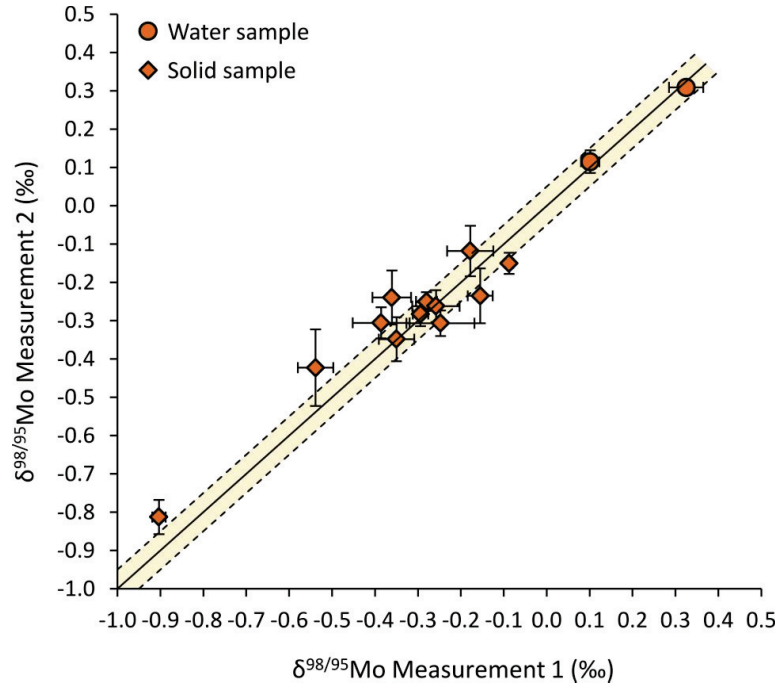

Figure 2.18 Agreement between duplicate $\delta^{98/95}$Mo data for water and solid samples. Full procedural duplicates for a range of sediment samples are compared against a 1:1 line. The fits to the 1:1 line, indicated by dashed lines, are for 0.05‰ deviations, which is the long term reproducibility on the BHVO-1 standard. Error bars indicated for measurements are ±2 SD on replicate runs of each individual sample.

2.7 Molybdenum sequential extraction experiment

Molybdenum cycling in surface weathering environments is known to be strongly influenced by adsorption to Fe-Mn (oxyhydr)oxides (Anbar et al., 2001; Arnold et al., 2004; Siebert et al., 2003). Therefore, a sequential extraction procedure was adapted to examine the role of this adsorption in the study catchments. Two suspended sediment samples from the western Southern Alps were subjected to two sequential extractions. The first extraction consisted of leaching with 10% acetic acid (HAc, Ultrapure). The HAc was intended to remove loosely bound exchangeable Mo (Chan and Hein, 2007; Wimpenny et al., 2010) and Mo present in carbonates (Henkel et al., 2016). The second extraction involved leaching with 2M HCl, to allow Mo that is more tightly bound to Fe and Mn oxyhydroxide-oxide residues to be removed from the particulates (Chan and Hein, 2007; Wimpenny et al., 2010; Siebert et al., 2015). Mo present within easily reducible and poorly crystalline Fe (and Mn) hydroxides and oxyhydroxides should be extracted by HCl leaching (Henkel et al., 2016; Siebert et al., 2015; Wiederhold et al., 2007). Organic matter is not thought to be extracted in the HAc or HCl leaches. Prior studies suggest the need for an additional leaching agent, such as H_2O_2, to extract Mo associated with the oxidizable fraction (e.g. Siebert et al., 2015). However, we cannot rule out the possibility that some organically-bound Mo may be leached by HCl, in analogy to the behaviour of Fe in HCl (Wiederhold et al., 2007).

Approximately 1g of suspended load particulates from a glacial catchment (Fox: sample NZ14-86; see ***Chapter 3*** and ***5*** for details on sampling location) and a catchment with glaciers confined to headwaters (Cook: sample NZ14-69) were each mixed with 40 mL of ultrapure HAc in capped beakers. The mixtures were then agitated in an ultrasonic water bath for 45 min, after which the particles were allowed to settle over 24 h. The supernatants were pipetted off with acid-cleaned pipette tips. The remaining residues were subsequently dissolved in distilled 2M HCl and the solutions agitated in an ultrasonic water bath for 45 min, after which they were placed on a hotplate at 70°C for 2 h. The final residues were left to settle over 24 h and then the supernatants were pipetted off. The extractable fractions are referred to as the HAc-leachable fractions and the HCl-leachable fractions (***Chapter 5***). The supernatants corresponding to both the HAc-leachable fractions and the HCl-leachable fractions were evaporated to dryness and dissolved in 0.5M HNO_3 for Mo abundance and isotope analyses.

2.8 Other analyses

2.8.1 Major ion and elemental concentrations

Concentration analyses on major elements were designed to characterise the overall composition of the samples (homogenised as powders in the case of bedload samples) and are bulk analyses. Major elements are present at concentrations exceeding 1% by mass and constitute the main minerals of

the sediments or ions within water samples. In river water samples, major ions were analysed by Ion Chromatography (IC). Lethbridge-03 is a certified reference material collected from Lethbridge, Alberta, in 2003 that was processed alongside samples to confirm the accuracy of the results. For the New Zealand samples (***Chapter 3***), the HCO_3^- concentration was estimated using the Total Alkalinity, temperature and pH (measured in the field) input into CO2SYS (Lewis and Wallace, 1998). The charge balance of dissolved cations ($TZ^+ = Na^+ + K+, 2Mg^{2+} +2Ca^{2+}$) and dissolved anions ($TZ^- = Cl^- + HCO_3^- + 2SO_4^{2-}$) was determined ($[TZ^+ - TZ^-]/[TZ^+ + TZ^-]$) as a measure of data quality (Jacobson et al., 2003). This was 11% across all samples, which is within the combined uncertainty and similar to previous work in this location (Jacobson et al., 2003).

For samples collected from Canada (***Chapter 4***), major and trace element (other than Re) concentrations in the river sediment samples were measured, respectively, by ICP-AES and ICP-MS at the SARM (Service d'Analyse des Roches et des Minéraux, INSU facility, Vandoeuvre-les-Nancy, France). Our Canadian study also took advantage of published data on the major ion chemistry of the samples collected between 2009 and 2011 that have been described previously (Dellinger, 2013) and supplemented our major ion analyses on the dissolved load of the 2013 samples collected by IC at Durham University.

2.8.2 Total organic carbon and stable isotopes

In river bed materials, suspended load sediments, surface soils and weathered colluvium, the organic carbon concentration ([OC], %) was measured following a 0.2M HCl leach protocol (Galy et al., 2007), which was tested on samples to ensure full removal of detrital carbonates (Figure 2.19). In this method, a powdered sediment sample of ~0.5 g was added to a 50 mL glass beaker with 15 mL of 0.2M HCl, covered with a watch glass and placed on a hotplate at ~70ºC for ~4 hours. After 4 hours, the supernatent was pipetted off and 50 mL of deionised H_2O was added to each sample. Once each sample had fully settled (overnight), the deionised H_2O was pipetted off and discarded. Finally, ~40 mL of deionised H_2O was added to each sample and the samples were transferred to an oven to dry down at 80ºC. The sample weight before and after this procedure was quantified. This leach method was tested with different acid molarities using the sample CAN13-02, to ensure full removal of detrital carbonates: the acid concentrations used were 0.1M, 0.2M, 0.3M, 0.5M, 0.75M and 1M HCl.

Aliquots of samples were combusted and the concentration of organic carbon, [OC], and the stable isotope composition of OC, $\delta^{13}C$ in ‰, were determined using a Costech elemental analyser coupled to a Thermo Scientific Delta V Advantage isotope ratio mass spectrometer (EA-IRMS) at Durham University. Corrections for procedural and instrument blanks were applied and the result normalized to the composition of international standards, reported relative to the Vienna Pee Dee

Belemnite (VPDB) with a precision of 0.2‰. Data reproducibility was assessed by processing sample replicates and full analysis duplicates (Figure 2.20). High precision was achieved on replicate analyses and duplicate data also fell within 1.5% of a 1:1 line.

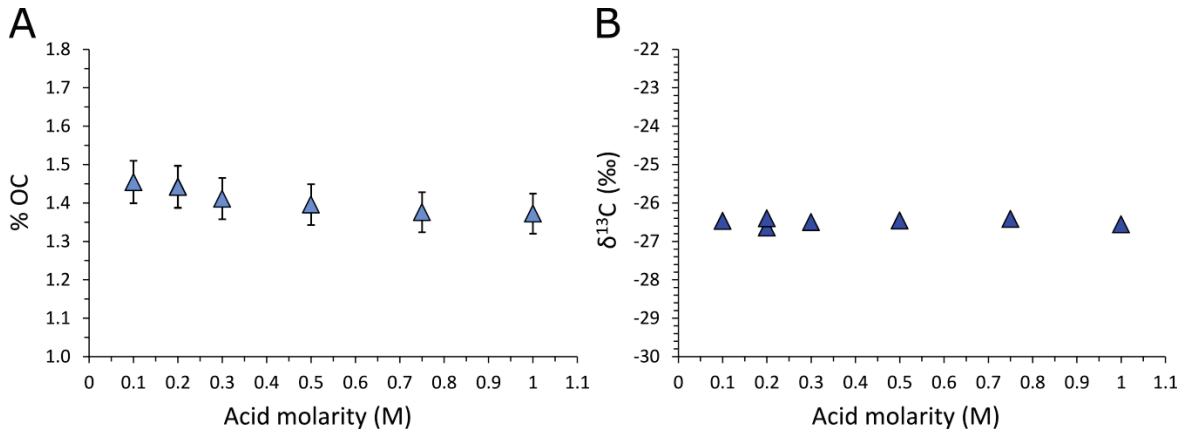

Figure 2.19 The effect of acid molarity on % total OC and $\delta^{13}C$. A. Patterns in quantified %OC at different acid molarities. The mean standard deviation on the mean of duplicate analyses was 3.8% and this error is indicted here. **B.** Patterns in quantified $\delta^{13}C$ at different acid molarities. The mean standard deviation on the mean of duplicate analyses is smaller than the symbol size. At all acid strengths, the %OC and $\delta^{13}C$ quantified are invariant, indicating full removal of inorganic carbon in each case.

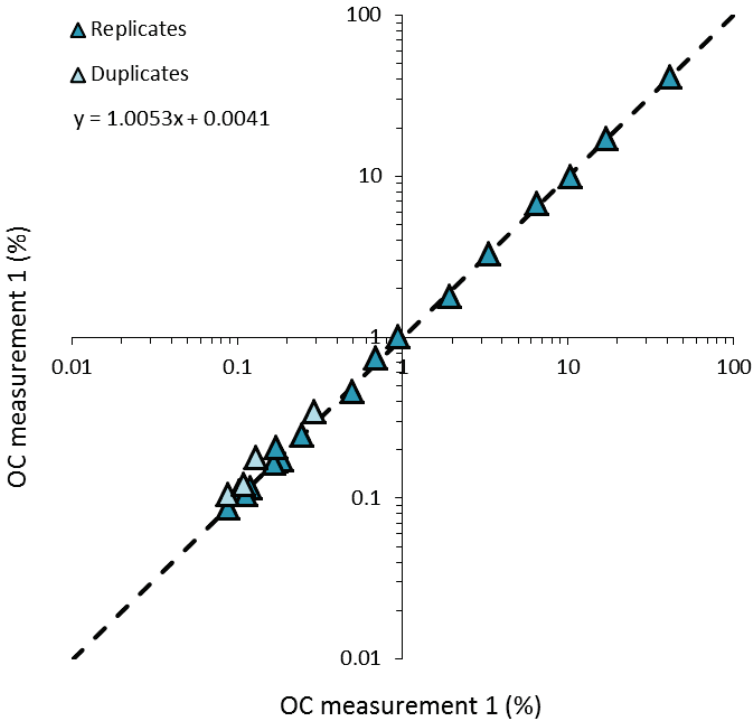

Figure 2.20 OC replicate and duplicate analyses. The trend line through the replicate data matches a 1:1 line indicating very high precision on replicate analyses. Duplicate data fall within 1.5% of the 1:1 line.

2.8.3 Radiocarbon activity of organic carbon

The radiocarbon activity of organic matter, reported as the Fraction Modern (F_{mod}) was measured following carbonate removal in four colluvium samples and two soil litters collected in New Zealand (***Chapter 3***) by Accelerator Mass Spectrometry (AMS) at the University of California Irvine facility, following graphitization. Sample preparation background was subtracted based on measurements of ^{14}C free coal processed through the full protocol. For Canadian samples, the particulate organic carbon composition, including the OC percentage and the radiocarbon activity, from suspended sediment and bed material samples collected in 2010 and 2011 were taken from published work (Hilton et al., 2015).

2.9 Summary

This research has successfully applied a range of geochemical techniques to quantify the chemical characteristics of river waters, river sediments and soils in the mountainous river catchments of New Zealand, the Mackenzie River Basin, Canada, and Iceland. Data acquired include major element data, total organic carbon and its isotopes, Re concentration, Mo concentration and Mo isotope composition.

The key points to summarise in relation to the coming ***Chapters 3*** to ***5*** are that two procedures capable of measuring Re concentrations in river water samples have been assessed. During the development of the aims and objectives of this research, $[Re]_{diss}$ in natural river water samples were measured by the direct calibration method from the study locations in New Zealand, Canada and Iceland (see ***Chapters 3–5***). This method proved to be most suited for quantifying Re abundance when concentrations exceed ~0.5–1.0 pg g^{-1} and it is worthy of future development due to the small demands on sample size and sample preparation time. The second method used isotope dilution combined with a Re extraction and purification technique involving anion-exchange column chemistry. This process demands more sample, consumables, and time, but it was found to improve precision and yield accurate results across a wide range of concentrations. The two techniques were found to agree closely across a wide range of concentrations, but there was a tendency for the direct calibration data to be offset to higher values at the lower Re concentrations. This may reflect the bias of quantifying concentrations close to machine detection limits. The first analyses of $[Re]_{diss}$ by ID Q-ICP-MS for the river water standard SLRS-5 are provided. They agree with published inter-laboratory comparisons, and provide a more precise value for this reference material (59.8 ± 1.7 pg g^{-1}, n = 12, ±2 SE). For solid samples, a NaOH-acetone extraction technique may be used with isotope dilution to quantify Re concentrations to a precision of <1%. Analyses of total digests for two contrasting rock certified and in house standards (SCO-1 and SCB-1) confirmed the accuracy of the methodology.

For Mo, there was a general agreement between concentrations of Mo in river water samples quantified by direct calibration Q-ICP-MS and a double spike – column chemistry MC-ICP-MS method (to within ~12%). The Mo concentrations in solid samples were most accurately quantified as an output of the double spike isotope dilution method, alongside Mo isotope measurements on the same sample aliquots; this was confirmed by accurate IAPSO and BHVO-1 data quantified by this method. The Mo isotope composition of samples was determined using previously published double spike and column chemistry methods, and returned a long-term precision of ~0.05‰ on the reference materials IAPSO and BHVO-1.

2.10 References

Anbar, A.D., Creaser, R.A., Papanastassiou, D.A., Wasserburg, G.J., 1992. Rhenium in seawater: Confirmation of generally conservative behavior. Geochim. Cosmochim. Acta 56, 4099–4103.

Anbar, A.D., Knab, K.A., Barling, J., 2001. Precise determination of mass-dependent variations in the isotopic composition of molybdenum using MC-ICPMS. Anal. Chem. 73, 1425–1431.

Arnold, G.L., Anbar, A.D., Barling, J., Lyons, T.W., 2004. Molybdenum isotope evidence for widespread anoxia in mid-proterozoic oceans. Science. 304, 87–90.

Balaram, V., 1995. Developments and trends in inductively coupled plasma mass spectrometry and its influence on the recent advances in trace element analysis. Curr. Sci. 69, 640–649.

Birck, J.L., Roy Barman, M., Capmas, F., 1997. Re-Os isotopic measurements at the femtomole level in natural samples. Geostand. Newsl. 21, 19–27.

Chan, L.H., Hein, J.R., 2007. Lithium contents and isotopic compositions of ferromanganese deposits from the global ocean. Deep. Res. Part Ii-Topical Stud. Oceanogr. 54, 1147–1162.

Colodner, D., Sachs, J., Ravizza, G., Turekian, K., Edmond, J., Boyle, E., 1993. The geochemical cycle of rhenium: a reconnaissance. Earth Planet. Sci. Lett. 117, 205–221.

Colodner, D.C., Boyle, E.A., Edmond, J.M., 1993. Determination of Rhenium and Platinum in Natural Waters and Sediments, and Iridium in Sediments by Flow Injection Isotope Dilution Inductively Coupled Plasma Mass Spectrometry. Anal. Chem. 65, 1419–1425.

Creech, J.B., Paul, B., 2015. IsoSpike: Improved double-spike inversion software. Geostand. Geoanalytical Res. 39, 7–15.

Cumming, V.M., Poulton, S.W., Rooney, A.D., Selby, D., 2013. Anoxia in the terrestrial environment during the late Mesoproterozoic. Geology 41, 583–586.

Cumming, V.M., Selby, D., Lillis, P.G., Lewan, M.D., 2014. Re–Os geochronology and Os isotope fingerprinting of petroleum sourced from a Type I lacustrine kerogen: Insights from the natural Green River petroleum system in the Uinta Basin and hydrous pyrolysis experiments. Geochim. Cosmochim. Acta 138, 32–56.

Dalai, T.K., Singh, S.K., Trivedi, J.R., Krishnaswami, S., 2002. Dissolved rhenium in the Yamuna River System and the Ganga in the Himalaya: Role of black shale weathering on the budgets of Re, Os, and U in rivers and CO_2 in the atmosphere. Geochim. Cosmochim. Acta 66, 29–43.

Dellinger, M., 2013. Apport des isotopes du lithium et des éléments alcalinsà la compréhension des processus d'altération chimiqueet de recyclage sédimentaire. École Dr. Des Sci. La Terre.

Gaillardet, J., Viers, J., Dupré, B., 2003. Trace elements in river waters. Treatise on geochemistry 5, 605.

Galy, V., Bouchez, J., France-Lanord, C., 2007. Determination of total organic carbon content and delta C-13 in carbonate-rich detrital sediments. Geostand. Geoanalytical Res. 31, 199–207.

Gill, R., 1997. Modern Analytical Geochemistry: an introduction to quantitative chemical analysis techniques for Earth, environmental and materials scientists. Addison Wesley Longman.

Goldberg, T., Gordon, G., Izon, G., Archer, C., Pearce, C.R., McManus, J., Anbar, A.D., Rehkämper, M., 2013. Resolution of inter-laboratory discrepancies in Mo isotope data: an intercalibration. J. Anal. At. Spectrom. 28, 724.

Gramlich, J.W., Murphy, T.J., Garner, E.L., Shields, W.R., 1973. Absolute isotopic abundance ratio and atomic weight of a reference sample of rhenium. J. Res. Natl. Bur. Stand. Sect. A Phys. Chem. 77A, 691.

Greber, N.D., Siebert, C., Nägler, T.F., Pettke, T., 2012. $\delta^{98/95}$Mo values and Molybdenum Concentration Data for NIST SRM 610, 612 and 3134: Towards a Common Protocol for Reporting Mo Data. Geostand. Geoanalytical Res. 36, 291–300.

Henkel, S., Kasten, S., Poulton, S.W., Staubwasser, M., 2016. Determination of the stable iron isotopic composition of sequentially leached iron phases in marine sediments. Chem. Geol. 421, 93–102.

Hilton, R.G., Gaillardet, J., Calmels, D., Birck, J.-L., 2014. Geological respiration of a mountain belt revealed by the trace element rhenium. Earth Planet. Sci. Lett. 403, 27–36.

Hilton, R.G., Galy, V., Gaillardet, J., Dellinger, M., Bryant, C., O'Regan, M., Grocke, D.R., Coxall, H., Bouchez, J., Calmels, D., 2015. Erosion of organic carbon in the Arctic as a geological carbon dioxide sink. Nature 524, 84-U162.

Jacobson, A.D., Blum, J.D., Chamberlain, C.P., Craw, D., Koons, P.O., 2003. Climatic and tectonic controls on chemical weathering in the New Zealand Southern Alps. Geochim. Cosmochim. Acta 67, 29–46.

Jarvis, K.E., 1997. Inductively coupled plasma-mass spectrometry. Mod. Anal. Chem. An introdu, 171–187.

Kendall, B., Dahl, T.W., Anbar, A.D., 2017. the Stable Isotope Geochemistry of Molybdenum. Rev. Mineral. Geochemistry 82, 683–732.

Laborda, F., Bolea, E., Jiménez-Lamana, J., 2016. Single particle inductively coupled plasma mass spectrometry for the analysis of inorganic engineered nanoparticles in environmental samples. Trends Environ. Anal. Chem. 9, 15–23.

Lewis and D. W. R. Wallace, E., 1998. Program Developed for CO_2 System Calculations ORNL/CDIAC.

Lu, D., Zhang, T., Yang, X., Su, P., Liu, Q., Jiang, G., 2017. Recent advances in the analysis of non-traditional stable isotopes by multi-collector inductively coupled plasma mass spectrometry. J. Anal. At. Spectrom. 32, 1848–1861.

Meisel, T., Moser, J., 2004. Platinum-Group Element and Rhenium Concentrations in Low Abundance Reference Materials. Geostand. Geoanalytical Res. 28, 233–250.

Miller, C.A., Peucker-Ehrenbrink, B., Walker, B.D., Marcantonio, F., 2011. Re-assessing the surface cycling of molybdenum and rhenium. Geochim. Cosmochim. Acta 75, 7146–7179.

Misra, S., Owen, R., Kerr, J., Greaves, M., Elderfield, H., 2014. Determination of δ^{11}B by HR-ICP-MS from mass limited samples: Application to natural carbonates and water samples. Geochim. Cosmochim. Acta 140, 531–552.

Morgan, J.W., Golightly, D.W., Dorrzapf, A.F., 1991. Methods for the separation of rhenium, osmium and molybdenum applicable to isotope geochemistry. Talanta 38, 259–265.

Nagai, Y., Yokoyama, T., 2016. Molybdenum isotopic analysis by negative thermal ionization mass spectrometry (N-TIMS): effects on oxygen isotopic composition. J. Anal. At. Spectrom. 31, 948–960.

Nägler, T.F., Anbar, A.D., Archer, C., Goldberg, T., Gordon, G.W., Greber, N.D., Siebert, C., Sohrin, Y., Vance, D., 2014. Proposal for an International Molybdenum Isotope Measurement Standard and Data Representation. Geostand. Geoanalytical Res. 38, 149–151.

Paton, C., Hellstrom, J., Paul, B., Woodhead, J., Hergt, J., 2011. Iolite: Freeware for the visualisation and processing of mass spectrometric data. J. Anal. At. Spectrom. 26, 2508.

Pearce, C.R., Cohen, A.S., Parkinson, I.J., 2009. Quantitative Separation of Molybdenum and Rhenium from Geological Materials for Isotopic Determination by MC-ICP-MS. Geostand. Geoanalytical Res. 33, 219–229.

Rahaman, W., Singh, S.K., Shukla, A.D., 2012. Rhenium in Indian rivers: Sources, fluxes, and contribution to oceanic budget. Geochemistry, Geophys. Geosystems 13.

Rooney, A.D., Selby, D., Lewan, M.D., Lillis, P.G., Houzay, J.P., 2012. Evaluating Re-Os systematics in organic-rich sedimentary rocks in response to petroleum generation using hydrous pyrolysis experiments. Geochim. Cosmochim. Acta 77, 275–291.

Rudge, J.F., Reynolds, B.C., Bourdon, B., 2009. The double spike toolbox. Chem. Geol. 265, 420–431.

Selby, D., Creaser, R.A., 2003. Re-Os geochronology of organic rich sediments: an evaluation of organic matter analysis methods. Chem. Geol. 200, 225–240.

Selby, D., Creaser, R.A., 2001. Re-Os geochronology and systematics in molybdenite from the endako porphyry molybdenum deposit, British Columbia, Canada. Econ. Geol. 96, 197–204.

Siebert, C., Nagler, T.F., Kramers, J.D., 2001. Determination of molybdenum isotope fractionation by double-spike multicollector inductively coupled plasma mass spectrometry. Geochemistry, Geophys. Geosystems 2, 1032.

Siebert, C., Nagler, T.F., von Blanckenburg, F., Kramers, J.D., 2003. Molybdenum isotope records as a potential new proxy for paleoceanography. Earth Planet. Sci. Lett. 211, 159–171.

Wiederhold, J.G., Teutsch, N., Kraemer, S.M., Halliday, A.N., Kretzschmar, R., 2007. Iron isotope fractionation in oxic soils by mineral weathering and podsolization. Geochim. Cosmochim. Acta 71, 5821–5833.

Wieser, M.E., De Laeter, J.R., Varner, M.D., 2007. Isotope fractionation studies of molybdenum. Int. J. Mass Spectrom. 265, 40–48.

Willbold, M., Hibbert, K., Lai, Y.J., Freymuth, H., Hin, R.C., Coath, C., Vils, F., Elliott, T., 2016. High-Precision Mass-Dependent Molybdenum Isotope Variations in Magmatic Rocks Determined by Double-Spike MC-ICP-MS. Geostand. Geoanalytical Res. 40, 389–403.

Wimpenny, J., James, R.H., Burton, K.W., Gannoun, A., Mokadem, F., Gíslason, S.R., 2010. Glacial effects on weathering processes: New insights from the elemental and lithium isotopic composition of West Greenland rivers. Earth Planet. Sci. Lett. 290, 427–437.

Wysocka, I., Vassileva, E., 2017. Method validation for high resolution sector field inductively coupled plasma mass spectrometry determination of the emerging contaminants in the open ocean: Rare earth elements as a case study. Spectrochim. Acta - Part B At. Spectrosc. 128, 1–10.

Yeghicheyan, D., Bossy, C., Bouhnik Le Coz, M., Douchet, C., Granier, G., Heimburger, A., Lacan, F., Lanzanova, A., Rousseau, T.C.C., Seidel, J.-L., Tharaud, M., Candaudap, F., Chmeleff, J., Cloquet, C., Delpoux, S., Labatut, M., Losno, R., Pradoux, C., Sivry, Y., Sonke, J.E., 2013. A Compilation of Silicon, Rare Earth Element and Twenty-One other Trace Element Concentrations in the Natural River Water Reference Material SLRS-5 (NRC-CNRC). Geostand. Geoanalytical Res. 37, 449–467.

Chapter 3

Mountain glaciation drives rapid oxidation of rock-bound organic carbon

Fox glacier and river in the western Southern Alps, New Zealand; September2014

Summary: Dissolved rhenium fluxes reveal that mountain glaciation can triple the CO_2 released during oxidative weathering of organic carbon in rocks.

A version of this chapter has been published in *Science Advances 3 (10), 2017*.

The paper is co-authored by Robert G. Hilton[1], David Selby[2], Chris J. Ottley[2], Darren R. Gröcke[2], Murray Hicks[3] and Kevin W. Burton[2]

Affiliations: [1]Department of Geography, Durham University, Durham, DH1 3LE, UK.
[2]Department of Earth Sciences, Durham University, Durham, DH1 3LE, UK.
[3]National Institute of Water and Atmospheric Research Ltd (NIWA), Christchurch, New Zealand.

A copy of this paper is provided in the appendix.

Abstract

Over millions of years, the oxidation of organic carbon contained within sedimentary rocks is one of the main sources of carbon dioxide to the atmosphere, yet the controls on this emission remain poorly constrained. We use rhenium to track the oxidation of rock-bound organic carbon in the mountain catchments of New Zealand, where high rates of physical erosion expose rocks to chemical weathering. Oxidative weathering fluxes are two to three times higher in catchments dominated by valley glaciers and exposed to frost-shattering processes, compared to those with less glacial cover; a feature that we also observe in mountain catchments globally. Consequently, we show that mountain glaciation can result in an atmospheric carbon dioxide source during weathering and erosion, as fresh minerals are exposed for weathering in an environment with high oxygen availability. This provides a counter-mechanism against global cooling over geological timescales.

3.1 Introduction

The exposure of organic matter in rocks to oxidative weathering at Earth's surface releases carbon dioxide (CO_2) to the atmosphere from long-term (>10^6 years) storage in the lithosphere and consumes atmospheric oxygen (O_2) (Petsch, 2014; Berner and Canfield, 1989; FranceLanord and Derry, 1997). The global CO_2 emissions from the oxidation of rock-derived organic carbon (petrogenic OC, OC_{petro}) are estimated to be 40–100 Mt C yr^{-1} (Petsch, 2014). Over million year (geological) timescales, this represents the main source of atmospheric CO_2 alongside volcanism and metamorphism (Berner and Canfield, 1989; FranceLanord and Derry, 1997; Petsch, 2014, Berner and Caldeira, 1997), and plays a role in setting atmospheric O_2 concentrations (Berner and Canfield, 1989; Stolper et al., 2016). Geological CO_2 emissions are removed from the atmosphere by chemical weathering of silicate minerals by carbonic acid coupled to carbonate precipitation (Maher and Chamberlain, 2014; Berner and Caldeira, 1997), and the burial of recently photosynthesized OC (FranceLanord and Derry, 1997; Hayes et al., 1999). These atmospheric CO_2 drawdown mechanisms are regulated by erosion, temperature and runoff and are thought to stabilize CO_2 concentrations and global climate (Maher and Chamberlain, 2014). However, we have little understanding of the factors controlling OC_{petro} oxidation rate (Petsch et al., 2000; Hilton et al., 2014; Petsch, 2014) and hence how millennial-scale changes in climate (Zachos et al., 2001) might modify this major CO_2 emission.

Chemical weathering of OC_{petro} proceeds as surficial gases and fluids permeate through sedimentary rocks, oxidizing organic matter and releasing CO_2 (Petsch, 2014). The kinetics of OC_{petro} weathering appear to be ~10 times faster than the kinetics of silicate mineral weathering (Chang and Berner, 1999). Faster reaction kinetics imply that shorter fluid residence times are

required to reach chemical equilibrium and maximize weathering fluxes during OC_{petro} oxidation (Maher and Chamberlain, 2014), compared to acid-hydrolysis silicate weathering (West, 2012; Maher and Chamberlain, 2014). When considered together with the high concentrations of O_2 in the present day atmosphere, weathering models suggest that the OC_{petro} oxidation rate is set by the mineral supply rate in most locations globally (Bolton et al., 2006). Microorganisms may also be important facilitators of OC_{petro} oxidation (Petsch et al., 2001). On the basis of these observations we propose that mountain glaciation could significantly enhance OC_{petro} oxidation rates due to a combination of physical and biogeochemical factors: i) frost-cracking and abrasive glacial grinding processes, which produce fine sediment with more surface area in an environment with high water availability (Hales and Roering, 2009; Anderson, 2005); ii) lower vegetation and soil cover that can increase the availability of O_2 to exposed bedrock and in deeper soil horizons; and iii) the activity of microorganisms catalysing weathering, both subglacially and during primary ecological succession on moraines (Petsch et al., 2001; Bardgett et al., 2007; Tranter et al., 2002; Wadham et al., 2004). Previous work has suggested that sulfide oxidation is enhanced subglacially (Tranter et al., 2002; Jacobson et al., 2003). If OC_{petro} oxidation rates also increase, CO_2 release may be highest during periods of repeated mountain glaciation over millennia (Herman et al., 2013) and may provide a mechanism to counter cooling trends in Earth's climate over timescales of 100 kyr to millions of years.

Here, we examine the potential for mountain glaciation to increase OC_{petro} oxidation rates. We focus on the mountain catchments of the western Southern Alps, New Zealand, where lithological contrasts are relatively small along-strike of the Alpine Fault (Hilton et al., 2008), but glacial coverage is variable (NSIDC, 2016) (Figure 3.1). Previous work has suggested that high silicate weathering rates (Jacobson et al., 2003; Lyons et al., 2005) are facilitated by rapid soil production (Larsen et al., 2014) and mineral supply by bedrock landslides (Emberson et al., 2016). Here, we assess the rates of oxidative weathering and the role of mountain glaciers using river water and sediment samples from 13 catchments (section 3.2). We also collected samples from two catchments in the eastern Southern Alps that host glaciers, but have lower physical erosion rates, and from the Waipaoa River in North Island, which has a high erosion rate but no glaciers (Lyons et al., 2005). In addition, we compile measurements from mountain catchments draining OC_{petro}-bearing sedimentary rocks in North America (Yukon and Mackenzie) and Asia (Taiwan rivers, Ganges and Brahmaputra) (Hilton et al., 2014; Miller et al., 2011).

To assess and quantify OC_{petro} oxidation rates, we measured the concentration of the redox sensitive trace element rhenium (Re) in river waters ($[Re]_{diss}$), river bed materials ($[Re]_{BM}$) and weathered colluvium and surface soils on hillslopes ($[Re]_{COL}$) using isotope dilution and inductively coupled plasma mass spectrometry (ICP-MS). The close association of Re and OC_{petro} in sedimentary rocks

(Selby and Creaser, 2003) and the solubility of Re upon oxidation during weathering (Colodner et al., 1993) (present as the soluble perrhenate oxyanion, ReO_4^-, in soils and rivers with pH values between 5.5 and 9.5) have led previous studies to suggest that Re can trace OC_{petro} oxidation (Petsch, 2014; Hilton et al., 2014; Jaffe et al., 2002; Dalai et al., 2002). For river catchments with similar runoff and bedrock composition, the dissolved Re concentration, $[Re]_{diss}$, has been shown to reflect the relative rate of oxidative weathering (Hilton et al., 2014). The dissolved Re discharge (mol yr^{-1}) or dissolved Re yield (mol km^{-2} yr^{-1}) provides a more direct means to quantify the oxidative weathering rate (Petsch, 2014; Hilton et al., 2014; Jaffe et al., 2002; Dalai et al., 2002). It has been used to estimate the associated CO_2 emissions by OC_{petro} oxidation when the Re to OC_{petro} ratio of the rocks undergoing weathering has been characterized (Hilton et al., 2014). The main uncertainties in the use of the Re proxy derive from the following: i) as a soluble element, Re may be mobilized more effectively during weathering than the CO_2 derived from OC_{petro} oxidation (Jaffe et al., 2002); ii) Re may be hosted in silicate and sulfide minerals (Miller et al., 2011); and iii) graphitic OC_{petro} is less susceptible to oxidation (Galy et al., 2008).

3.2 Materials and Methods

3.2.1 Sample collection

Samples were collected from 13 catchments in the western Southern Alps, which drain to the west of the main divide, two draining the eastern Southern Alps to the east of the main divide and the Waipaoa River in North Island, New Zealand (Figure 3.1, Tables 3.1, 3.2 and 3.3). Together, these catchments allowed us to examine the dual roles of physical erosion rate (Hilton et al., 2014) and glacial coverage on OC_{petro} weathering. The Southern Alps is a steep mountain belt built by transpression along the Alpine Fault. The western flank has a temperate climate, with a high erosion rate driven by orographic precipitation, exceeding 8 m yr^{-1}, steep slopes and bedrock landslides, which expose OC_{petro} in meta-sedimentary rocks (Hovius et al., 1997). Previous work has documented high rates of silicate and carbonate weathering in the western Southern Alps (Jacobson et al., 2003; Lyons et al., 2005). Erosion dominates the denudation, with the largest percentage of chemical denudation occurring in the Haast catchment (5%: Lyons et al., 2005). Along the western Southern Alps, the metamorphic grade varies perpendicular to the Alpine Fault strike, but the sedimentary protolith is similar in all catchments and the OC_{petro} content ranges from ~0.1 to ~0.2% (Hilton et al., 2008; Nibourel et al., 2015). In contrast, there are significant differences in glacial coverage including two catchments with large valley glaciers (Waiho and Fox) and some frontal catchments with minimal glacial coverage (e.g. Waitangitaona). The eastern Southern Alps is also dominated by glacial processes but experiences lower precipitation (< 2 m yr^{-1}), lower rates of bedrock landsliding (Hales and Roering, 2009) and slower long-term exhumation rates (Tippett and Kamp, 1993). As a result, the chemical denudation rates are also lower (Jacobson

and Blum, 2003). The Waipaoa River in North Island, New Zealand, drains lower metamorphic grade OC_{petro}-bearing sedimentary rocks at high erosion rates but lacks glacial influence (Leithold et al., 2006; Gomez et al., 2003).

To assess OC_{petro} oxidation in the western Southern Alps, we sampled the dissolved products of chemical weathering, weathered colluvium on hillslopes, and relatively un-weathered river bed materials of sand and finer grade. River waters (n = 51) were collected from the centre of river channels at their surface. Catchments were sampled 2–6 times over 1 month (14/09/14 – 03/10/14) at variable flow to examine the hydrological variability of dissolved ions released from chemical weathering (Maher, 2011). Water samples were decanted to sterile plastic containers prior to filtration through 142 mm diameter, 0.2 μm polyethersulfone (PES) filters within a day of collection and stored in acid-cleaned low-density polyethylene (LDPE) bottles. Alkalinity measurements were made by Gran titration on an aliquot of filtered water. All water samples intended for cation and Re analysis were acidified in the field to pH ~2 (Dalai et al., 2002; Hilton et al., 2014) with an unacidified aliquot kept for anion analyses. Two 250 mL rainwater samples were collected over 10 h periods (Table 3.1).

In the western Southern Alps, soils are thin and weathering profiles are often poorly developed (Larsen et al., 2014). Landslide-derived colluvium is an important locus of weathering (Emberson et al., 2016). Therefore, to characterize Re and OC_{petro} behaviour in the weathering zone, we collected ~500 cm^3 sized bulk samples of weathered colluvium at discrete depths between 10 and 70 cm below the soil surface at three sites on the forested hillslopes of Alex Knob, which drains to the Docherty Creek catchment. We also collected surface soil samples from the upper 3 cm that comprised a mixture of litter and mineral soil (n = 5) using a metal trowel and transferred samples to sterile plastic bags (Table 3.2).

River bed material samples (n = 31) were also collected to help constrain the composition of unweathered materials (Hilton et al., 2014) (Tables 3.2 and 3.3). Samples were taken from channel edges or from bank deposits that were taken to represent the sand to silt fraction deposited on the river bed during recent flow regimes, and transferred to sterile plastic bags. River water samples and bed materials were also collected from the eastern Southern Alps and Waipaoa River using these methods (Table 3.1 & Table 3.3).

3.2.2 Geochemical analyses

Dissolved rhenium concentrations in river water samples, ($[Re]_{diss}$, pmol L^{-1}), were measured by isotope dilution – quadrupole ICP-MS (Q-ICP-MS) in conjunction with anion-exchange column chemistry to pre-concentrate and purify Re. Between 30 and 500 mL of the water samples were

doped with a known amount of tracer solution consisting of enriched ^{185}Re and evaporated to dryness, with the dried sample dissolved in HNO_3 prior to anion-exchange column chemistry.

Solid samples (surface soil, weathered colluvium and river bed materials) were ground to a fine powder prior to acid digestion to generate an integrated bulk sample. Homogenizing bedload samples permitted an assessment of the average Re composition of the rocks at the catchment-scale for each river because fluvial transit times are short. A known weight of powder (~0.5 g) was doped with a known amount of ^{185}Re spike and digested in a 6:3 HF-HNO_3 mix (9 mL) for 24 hours at 120ºC and then evaporated. The dried sample was further digested in a 2:1 mix of HNO_3-HCl (3 mL) for 24 h at 120ºC, and then evaporated. Rhenium was isolated and purified using a NaOH-acetone solvent extraction methodology (Cumming et al., 2013).

The Re isotope composition of the purified Re aliquots were determined in a 0.8M HNO_3 medium using a Thermo Fischer Scientific X-Series Q-ICP-MS at Durham University. The procedural blank was ~1% of the lowest concentration samples. Uncertainties in the Re abundance were determined by error propagation of uncertainties in Re mass spectrometry measurements, blank abundance and isotope compositions, spike calibrations and reproducibility of standard Re isotope values. Repeat analyses of $[Re]_{diss}$ in a river water standard, SLRS-5, gave a concentration of 59.8 ± 1.7 pg g^{-1} (n = 12, ±2 SE), in agreement with the previously reported value of 66 ± 12 pg g^{-1} (Yeghicheyan et al., 2013).

Major ion concentrations in water samples were analysed by ion chromatography. Cation and anion standards and a certified reference standard (Lethbridge-03) were run to validate the analytical results. The HCO_3^- concentration was estimated using the total alkalinity, temperature, and pH (measured in the field) data inputted to CO2SYS (Lewis, 1998). The charge balance of dissolved cations ($TZ^+ = Na^+ + K+, 2Mg^{2+} + 2Ca^{2+}$) and dissolved anions ($TZ^- = Cl^- + HCO_3^- + 2SO_4^{2-}$) was determined ($[TZ^+ - TZ^-]/[TZ^+ + TZ^-]$) as a measure of data quality (Jacobson et al., 2003). This was 11% across all samples, within the combined uncertainty and similar to previous work in this location (Jacobson et al., 2003).

In river bed materials, surface soils, and weathered colluvium, the organic carbon concentration ([OC], %) was measured following a 0.2M HCl leach protocol (Galy et al., 2007), which was tested on samples from this location to ensure full removal of detrital carbonates. Aliquots of samples were combusted and the concentration and stable isotope composition of OC ($\delta^{13}C$, ‰) were determined using a Costech elemental analyser coupled to a Thermo Fischer Scientific Delta V Advantage isotope ratio mass spectrometer (EA-IRMS) at Durham University. Corrections for procedural and instrument blanks were applied and the result normalized to the composition of

international standards (reported relative to the Vienna Pee Dee Belemnite (VPDB) with a precision of 0.2‰). The radiocarbon activity (reported as the Fraction Modern, F_{mod}) was measured on four colluvium samples and two soil litters by Accelerator Mass Spectrometry (AMS) at the University of California, Irvine Keck Carbon Cycle facility, following graphitization. Sample preparation background was subtracted based on measurements of ^{14}C free coal processed through the full protocol (Table 3.2).

3.2.3 Quantification of OC_{petro} oxidation rate and its uncertainty

To convert the dissolved Re flux to an estimate of CO_2 release (Equation 3.1), there are known uncertainties related to the behaviour of Re and OC_{petro} during weathering (Hilton et al., 2014; Petsch, 2014). The main uncertainties in this setting are as follows: (i) because Re is a soluble element, oxidative weathering may mobilize Re more effectively during early soil formation, meaning that some Re measured in river waters does not correspond to release of CO_2 at the weathering site (Jaffe et al., 2002); (ii), partly related to (i), some dissolved Re may come from sulfide and silicate minerals (Hilton et al., 2014; Miller et al., 2011); and (iii) graphitic OC_{petro} may not be susceptible to oxidation and remain in the soil (Galy et al., 2008; Bouchez et al., 2010). Regarding point (i) and (ii), soils from Taiwan suggest congruent dissolution of Re and loss of OC_{petro} can occur during weathering of young, thin soils (Hilton et al., 2014). On a soil profile on OC_{petro} rich shale from Ohio (Jaffe et al., 2002), Re-depletion reaches 100% in the most highly weathered soil, whereas OC_{petro} loss is ~70% (Table 3.2). The data from weathered colluvium in the western Southern Alps are more consistent with the Ohio Shale than Taiwan. For point (iii), graphite is present in rocks within a kilometre of the Alpine Fault making up almost 50% of the OC (Nibourel et al., 2015), and its measured abundance decreases to small amounts ~10–20 km from the Alpine Fault (Beyssac et al., 2016).

To account for and quantify the uncertainties on the CO_2 flux estimate we used a Monte Carlo simulation. This includes uncertainty on the dissolved Re flux (section 3.3.3), the measured variability in $[OC]_{BM}/[Re]_{BM}$, and the assumptions (i), (ii) and (iii) above. For each catchment (area = A km^2), we used ±2 SE on the mean for the $[Re]_{diss}$ and the $[OC]_{BM}/[Re]_{BM}$ ratio. To account for the relative mobility of Re and OC_{petro} during weathering (Jaffe et al., 2002), we defined f_C as the ratio between the percentage loss of OC_{petro} in soil compared to bedrock and the percentage loss of Re in soil compared to bedrock. We also use this term to account for any Re derived from non-OC_{petro} sources. Based on published work, we varied f_C from 0.5 to 1 (Hilton et al., 2014; Jaffe et al., 2002). To account for the presence of graphite which may not be oxidised, we varied the fraction of OC_{petro} as graphite ($f_{graphite}$) from 0.5 to 0, informed by measurements from the study location (Nibourel et al., 2015). The CO_2 oxidation flux, J_{CO2} (gC km^{-2} yr^{-1}) was then calculated using Equation 3.1.

Equation 3.1 $$J_{CO2} = J_{Re} \times ([OC]_{BM}/[Re]_{BM}) \times f_C \times (1 - f_{graphite})$$

The Monte Carlo simulation was run 100,000 times for each catchment, with a 'full probability' distribution for each variable. We report the median value ±1 standard deviation range. This reflects the present state of knowledge of the Re-proxy for OC_{petro} oxidation. Future work should seek to refine this approach and reduce the uncertainties, for a better understanding of f_C and $f_{graphite}$. By doing so it may be possible to quantify catchment scale fluxes using Re measurements more widely (Petsch, 2014).

3.2.4 Quantification of glacier cover using the World Glacier Inventory

The relative importance of glacial processes in the catchments of the western Southern Alps was quantified using glacier locations and areas from the World Glacier Inventory (NSIDC, 2016). The total sum of glacier area (km^2) was quantified for each catchment using ArcGIS, with flow routing algorithms to isolate drainage areas (Table 3.4). In the global dataset, published estimates were used.

3.2.5 Biospheric OC erosion and burial

Previous work has estimated the erosion rate of biospheric OC in catchments of the western Southern Alps (Hilton et al., 2008). To estimate how this contributes to CO_2 drawdown, we required an estimate of the burial efficiency of OC. Based on a recent global compilation (Galy et al., 2015), the sediment yield to an offshore basin plays an important role in setting the burial efficiency of OC. This is because sediment accumulation rate is a first order control on OC burial efficiency in many marine environments (Blair and Aller, 2012). Using the sediment yield of ~6,000–10,000 t km^{-2} yr^{-1} for the western Southern Alps (Hilton et al., 2008), the burial efficiency would be predicted to be from ~40% to 100% based on the global dataset (Galy et al., 2015). A high burial efficiency would be consistent with the very high preservation potential of terrestrial palynomorphs offshore from the western Southern Alps (Ryan et al., 2016). To provide a conservative estimate of biospheric OC burial, we used the lowest value in this range (40%) and multiplied the erosional export flux (Hilton et al., 2008) by the OC burial efficiency to estimate CO_2 drawdown by biospheric OC erosion.

3.3 Results

3.3.1 River bed materials

The mean organic carbon (OC) weight percentage in river bed materials, $[OC]_{BM}$, from the western Southern Alps is 0.13 ± 0.01 wt. % (n = 31, ±2 SE) and the mean stable carbon isotope composition is $\delta^{13}C$ = -22.5 ± 0.6‰ (n = 31, ±2 SE). For comparison, the $[OC]_{BM}$ values are lower

than those in Taiwan (Hilton et al., 2014) but more than double those measured in the Himalaya (Galy et al., 2008). The mean values of river bed materials are similar to previous measurements from this location (Hilton et al., 2008; Nibourel et al., 2015) and to the mean of bedrock values in the western Southern Alps, [OC] = 0.15 ± 0.05 wt. % and $\delta^{13}C$ = -21.1 ± 1.1‰ (n = 11, ±2 SE) (Hilton et al., 2008), suggesting that they are dominated by OC_{petro}, with minor inputs from biospheric OC generated by recent photosynthesis by C3 plants ($\delta^{13}C$ ~ -28‰). The river bed materials have less variability in their average composition when compared to bedrock, which likely reflects the integration of OC_{petro}-bearing sediment from landslides and mass wasting processes, which can erode OC_{petro} from large areas of the catchment (Hovius et al., 1997; Reusser and Bierman, 2010). The river sediments downstream are a mixture of these inputs (Hilton et al., 2008). Although the river bed materials have a slightly lower OC concentration than bedrock in the mountain belt, they are indistinguishable within the variability in the means and can therefore provide a robust method to assess the catchment-averaged bedrock composition (Galy et al., 2008; Hilton et al., 2008; Dellinger et al., 2014). This is consistent with findings in other erosive settings where bedrock landslides excavate deep into the landscape, tap into unweathered rock, and supply it to rivers in the sand-silt-clay fraction of river sediments (Hilton et al., 2011).

The mean Re concentration in river bed materials, $[Re]_{BM}$, is 118 ± 21 pg g^{-1} (n = 31, ±2 SE) (Table 3.3). Although this Re concentration is low for sedimentary rocks (Dubin and Peucker-Ehrenbrink, 2015), it is in line with the low $[OC]_{BM}$ in the western Southern Alps and consistent with organic matter being a dominant host of Re in sediments (Selby and Creaser, 2003). The mean $[Re]_{BM}/[OC]_{BM}$ ratio is 0.9 ± 0.2 × 10^{-7} g g^{-1} (n = 31, ±2 SE) and there is no systematic variability along-strike of the Alpine Fault (that is, no variability with latitude and longitude).

3.3.2 Weathered colluvium

Samples of weathered colluvium collected from hillslopes in the western Southern Alps are examined for loss of OC_{petro} and Re (Table 3.2). In the Docherty Creek catchment, which neighbours the Waiho River, weathered colluvium has a low mean $[Re]_{COL}$ = 29 ± 6 pg g^{-1} (n = 4, ±2 SE), compared to local river bed materials downstream (NZ14-90, $[Re]_{BM}$ = 112 pg g^{-1}). Soil litter samples are also depleted in Re (Table 3.2). This is expected if Re loss occurs during oxidative weathering. The mean OC content of the colluvium, $[OC]_{COL}$ = 1.2 ± 0.3 wt. % (n = 4, ± 2SE), is higher than that of the local river bed materials (NZ14-90, $[OC]_{BM}$ = 0.21 wt. %). However, organic matter in the colluvium has a stable isotope composition (mean $\delta^{13}C$ = -25.9 ± 0.4‰) and radiocarbon activity (reported as fraction modern, F_{mod} = 0.80 ± 0.09) that are very different from the expected rock inputs (NZ14-90; $\delta^{13}C$ = -21.2‰, and expected F_{mod} ~ 0). The values suggest an important contribution from biospheric OC in these samples (Hilton et al., 2008).

To assess the OC_{petro} content of the weathered colluvium samples and to account for OC derived from recent productivity (biospheric OC), we adopted a mixing analysis based on observations of $\delta^{13}C$ and F_{mod} values. The ^{14}C activity of sedimentary rocks is generally considered to be below the analytical background, i.e. $F_{mod} = 0$, and thus is distinct from modern biospheric OC ($F_{mod} \sim 1$) and degraded soil of ~1000 years old (F_{mod} ~0.9). The $\delta^{13}C$ of OC_{petro} in the Southern Alps is ^{13}C-enriched ($\delta^{13}C$ ~ -21 to -22‰) compared to the terrestrial biosphere (dominated by C3 plants) (Hilton et al., 2008).

The stable isotope composition of an element shown against the reciprocal of its concentration can reveal mixing trends, or processes that alter the concentration and fractionate isotopes. Surface soil litters are OC-rich and ^{13}C-depleted, and they describe a linear trend between $\delta^{13}C_{org}$ and 1/[OC], albeit one that only describes ~40% of the variability in the data (Supplementary Figure 3.1A). This is consistent with the degradation of plant-derived OC in surface soils, loss of OC and enrichment in ^{13}C. In contrast, the weathered colluvium samples define a different linear trend, which we interpret as a mixture of degraded biospheric organic matter (originally derived from the surface soil) with ^{13}C-enriched, OC-poor material from the sedimentary rocks (Supplementary Figure 3.1B). The intercept of these two trends implies that the degraded soil OC has a value of -26.8 ± 0.8‰ (propagating the 95% uncertainty bounds on the linear trends).

The weathered colluvium samples are also ^{14}C-depleted (Supplementary Figure 3.1B), which is consistent with OC_{petro} addition. The samples can be described by a linear trend between F_{mod} and $\delta^{13}C_{org}$ that intercepts biospheric and petrogenic OC (Supplementary Figure 3.1B). Using the 'degraded soil' $\delta^{13}C_{org}$ value (Supplementary Figure 3.1A) and the trend defined by the samples, we estimated the F_{mod} of the biospheric OC in these samples as $F_{mod} = 0.93 \pm 0.36$. These values and their uncertainties were used in a two component end member mixing model (Leithold et al., 2006) to quantify the fraction of OC_{petro} (f_{petro}) and the corresponding $[OC]_{petro}$ ($f_{petro} \times [OC]$) (Table 3.1). The high $[OC]_{COL}$ of these samples and the relatively low OC_{petro} content of rocks in this mountain range (Hilton et al., 2008), together with the observation that century aged biospheric OC is important in these New Zealand soils (Supplementary Figure 3.1), result in uncertainty on the absolute OC_{petro} contents. Additional aging of biospheric OC would act to reduce the F_{mod} of the biospheric OC. We therefore calculated an upper bound on the $[OC_{petro}]$ and a lower bound on the loss of OC_{petro} during weathering. The weathered colluvium samples had an average $[OC_{petro}] = 0.15 \pm 0.06\%$ (n = 4, ±2 SE), which is lower than that of the local river bed materials in this catchment $[OC]_{BM} = 0.21\%$ (Table 3.2). The data are consistent with OC_{petro} loss during weathering on hillslopes. The coupled loss of Re and OC_{petro} during chemical weathering supports previous measurements on soil from the Ohio Shale (Table 3.2) (Jaffe et al., 2002), the Himalaya (Pierson-

Wickmann et al., 2002) and Taiwan (Hilton et al., 2014). The weathered colluvium from New Zealand and published soil data show that Re is generally more mobile during OC_{petro} weathering, and so we account for this when estimating the OC_{petro} weathering rate using the dissolved Re flux.

3.3.3 River waters

The major dissolved ions in rivers draining the western Southern Alps (Ca^{2+}, Mg^{2+}, Na^{+} and K^{+}) characterize the overall weathering processes and reflect a source rock comprising meta-sedimentary silicate rocks hosting trace carbonate minerals (Supplementary Figure 3.2A). The water measurements from this study in 2014 are consistent with sampling campaigns in 1998, 1999 and 2000 (Lyons et al., 2005; Jacobson et al., 2003). Notably, all sampling campaigns find higher relative HCO_3^- and Ca^{2+} concentrations in the heavily glaciated Fox and Waiho rivers (Supplementary Figure 3.2A), which probably reflects the higher susceptibility of carbonate minerals to acid hydrolysis reactions in these catchments. The overlap of the datasets collected from different years, seasons and flow regimes (Supplementary 3.2A and 3.2B) suggests that spatial patterns in dissolved ion composition are retained despite the potential for seasonal and flood-event scale variability (Maher, 2011).

The $[Re]_{diss}$ values in the western Southern Alps rivers range from 0.81 to 11.55 pmol L^{-1}, with a mean $[Re]_{diss}$ = 3.05 ± 0.69 pmol L^{-1} (n = 51, ±2 SE) (Table 3.1). There is distinct variability between different catchments (Figure 3.1), with the Waiho and Fox catchments having the highest mean $[Re]_{diss}$ values throughout the sampling period. Mean $[Re]_{diss}$ is not correlated with $[Re]_{BM}$ in the western Southern Alps, suggesting that the bedrock geology does not set the spatial pattern in $[Re]_{diss}$. When all the data are considered together, the catchment-averaged $[Re]_{diss}$ is correlated with the proportion of area covered by glaciers upstream (Figure 3.1B, r^2 = 0.87, P < 0.001, n = 13).

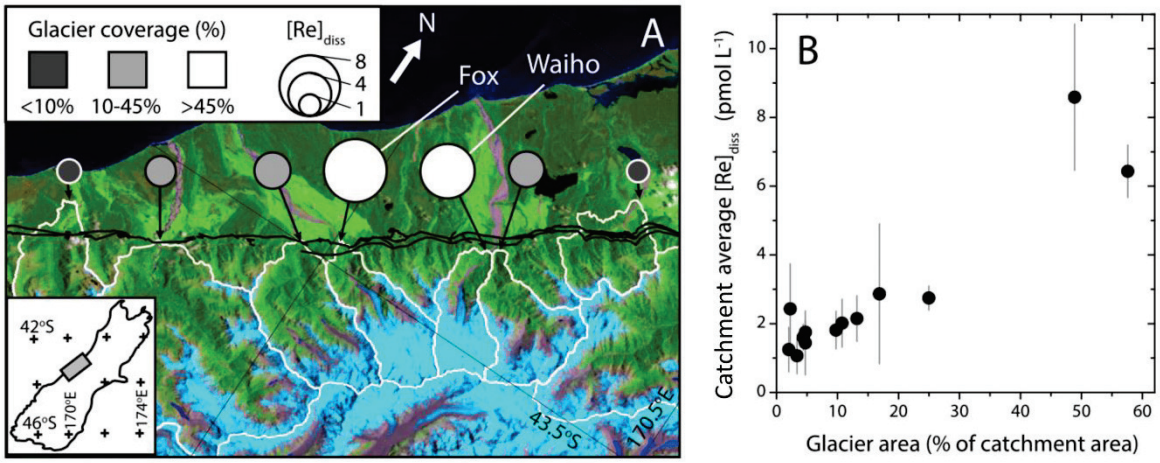

Figure 3.1 The western Southern Alps, New Zealand. A. Catchments for the central part of the study area where glacier area varies most, with catchment boundaries marked in white. The black line is the Alpine Fault trace. Image is Landsat ETM (Enhanced Thermatic Mapper) (31/12/2002) shown to illustrate glacial coverage. The catchment averaged dissolved rhenium concentration, $[Re]_{diss}$ (pmol L^{-1}), is shown as the circle size and the shading reflects the percentage catchment area with glaciers (NSIDC, 2016). Inset shows the location of the study area on South Island, New Zealand. **B.** Positive relationship between catchment averaged $[Re]_{diss}$ and the percentage of the catchment area covered by glaciers (n = 13, $r^2 = 0.87$, $P < 0.001$). Grey whiskers are ±2 SE on the mean $[Re]_{diss}$ values.

The $[Re]_{diss}$ values are generally low compared to those measured in river waters globally (Miller et al., 2011) and in rivers draining meta-sedimentary rocks in Taiwan, which have values ranging from ~5–25 pmol L^{-1} (Hilton et al., 2014). However, when $[Re]_{diss}$ values are normalized to the concentration of Re in river bed materials, $[Re]_{BM}$ (Hilton et al., 2014; Dellinger et al., 2014; Galy et al., 2008), the values are more similar to those in Taiwan. In the western Southern Alps, catchments dominated by river erosion and bedrock landslides (that is, not by glacial erosion processes) have a mean $[Re]_{diss} = 1.92 \pm 0.76$ pmol L^{-1} and mean $[Re]_{BM} = 105 \pm 20$ pg g^{-1}, giving a $[Re]_{diss}/[Re]_{BM} = 3.4 \pm 1.4 \times 10^{-3}$ (pg g^{-1} / pg g^{-1}), which is slightly higher than those measured in Taiwan, where the average $[Re]_{diss}/[Re]_{BM}$ is $3.3 \pm 0.5 \times 10^{-3}$. The two mountain belts have comparable physical erosion rates (Lyons et al., 2005; Hilton et al., 2014), suggesting that Re mobility is similar between the sites despite the contrasts in bedrock geology. The $[Re]_{diss}/[Re]_{BM}$ values are more than double in the Waiho and Fox catchments that host valley glaciers and have extensive glacial coverage.

3.3.4 Dissolved Re flux

To estimate oxidative weathering yields, we quantified the dissolved Re yield (mol km^{-2} yr^{-1}) in catchments where we have annual water discharge estimates (Hicks et al., 2011). These are in the Hokitika, Whataroa, Haast and Waiho rivers (Tables 3.4 and 3.5). Our river water samples from 2014 cover a relatively narrow dynamic range in water flow especially in the glacial catchment (~ 0.5 times to 1.5 times mean flow values), but do not show significant dilution at higher flow (Supplementary Figure 3.2C and Table 3.5). This suggests that the annual water discharge (Q_{annual},

m^3 yr^{-1}) (Hicks et al., 2011) and our mean $[Re]_{diss}$ for each large catchment can together provide a reliable estimate of dissolved Re flux. To assess the role of seasonal and/or inter-annual variability, we plot our major ion data (e.g. Ca^{2+}) alongside daily water discharge (Q_w, m^3 s^{-1}) for the Whataroa and Hokitika catchments and compare this to published data from 1998–1999 (Lyons et al., 2005) and 2000–2001 (Jacobson et al., 2003) (Supplementary Figure 3.2B). The broad consistency in ion concentrations and ion ratios suggest that annual and seasonal variability may be of second order importance when compared to contrasts between different catchments.

To assess in more detail whether the average of the ion concentrations collected at low Q_w may overestimate the dissolved ion flux, if ions are diluted at high flow (Maher, 2011), we compared the flux calculated using an average concentration method, to that calculated by a rating curve method (taking into account dilution) using published datasets from the study location (Lyons et al., 2005). For these data, the average measured $[Ca^{2+}]$ multiplied by the mean annual runoff returns a Ca^{2+} flux of 4.21×10^8 mol yr^{-1} for the Hokitika River. If we model the $[Ca^{2+}]$-Q_w relationship (Supplementary Figure 3.2B) as a power law rating curve (Tipper et al., 2006) and apply it to the daily Q_w data from 1971–2015, the annual Ca^{2+} flux = 4.39×10^8 mol yr^{-1}. The methods agree within 4%, with the average concentration method slightly underestimating flux. In comparison, for the SO_4^{2-} flux, which also shows dilution with Q_w in published data (Lyons et al., 2005), the difference in estimated fluxes is 3%. Assuming similar dilution trends for $[Re]_{diss}$ as for $[Ca^{2+}]$ and $[SO_4^{2-}]$, which is suggested based on the available data (Supplementary Figure 3.2C), results in a <5% underestimation of flux. While longer-time series sampling would be informative for tracking the dissolved ion source and linking it to hydrological pathways (Tipper et al., 2006; Maher, 2011), an average concentration with an accuracy of within ~5% is adequate for calculating the Re flux. Rainwater and hydrothermal water samples (Table 3.1) have very low $[Re]_{diss}$ (<0.2 pmol L^{-1}) so no correction is made to the Re flux from these inputs.

3.3.5 Global compilation

Published data are compiled from catchments around the world that allow for a comparison to our findings in New Zealand (Table 3.6). The required data are as follows: i) dissolved Re concentration, $[Re]_{diss}$; ii) catchment-averaged bedrock Re composition, an indication of which is provided by $[Re]_{BM}$; iii) annual water discharge, to estimate dissolved Re yield; and iv) suspended sediment yield as a proxy of physical erosion rate (Miller et al., 2011; Hilton et al., 2014; Hilton et al., 2008; Hicks et al., 2011; Korup, 2004; Jacobson et al., 2003; Dadson et al., 2003; Galy et al., 2015; Dornblaser and Striegl, 2009). We also add new measurements of river water and bed material samples from the Jollie and Hooker catchments draining the eastern Southern Alps, the Waipaoa River in North Island, New Zealand, and the Yukon River and Mackenzie River, Canada, which we collected using similar methods. We estimate the dissolved Re yield for each of these

sites and account for variability in the bedrock geology by normalizing the Re yield to the measured $[Re]_{BM}$. We quantify the upstream area covered by glaciers from published work, or by using the World Glacier Inventory as we do for the western Southern Alps (see section 3.2.4). We find dissolved Re yield (normalized by $[Re]_{BM}$) increases with increasing annual suspended sediment yields across the dataset (Figure 3.2), supporting previous work from Taiwan (Hilton et al., 2014). However, catchments with mountain glaciation upstream of the sampling locations (where glaciers cover >1% of the area) have a higher dissolved Re yield for a given suspended sediment yield (Figure 3.2).

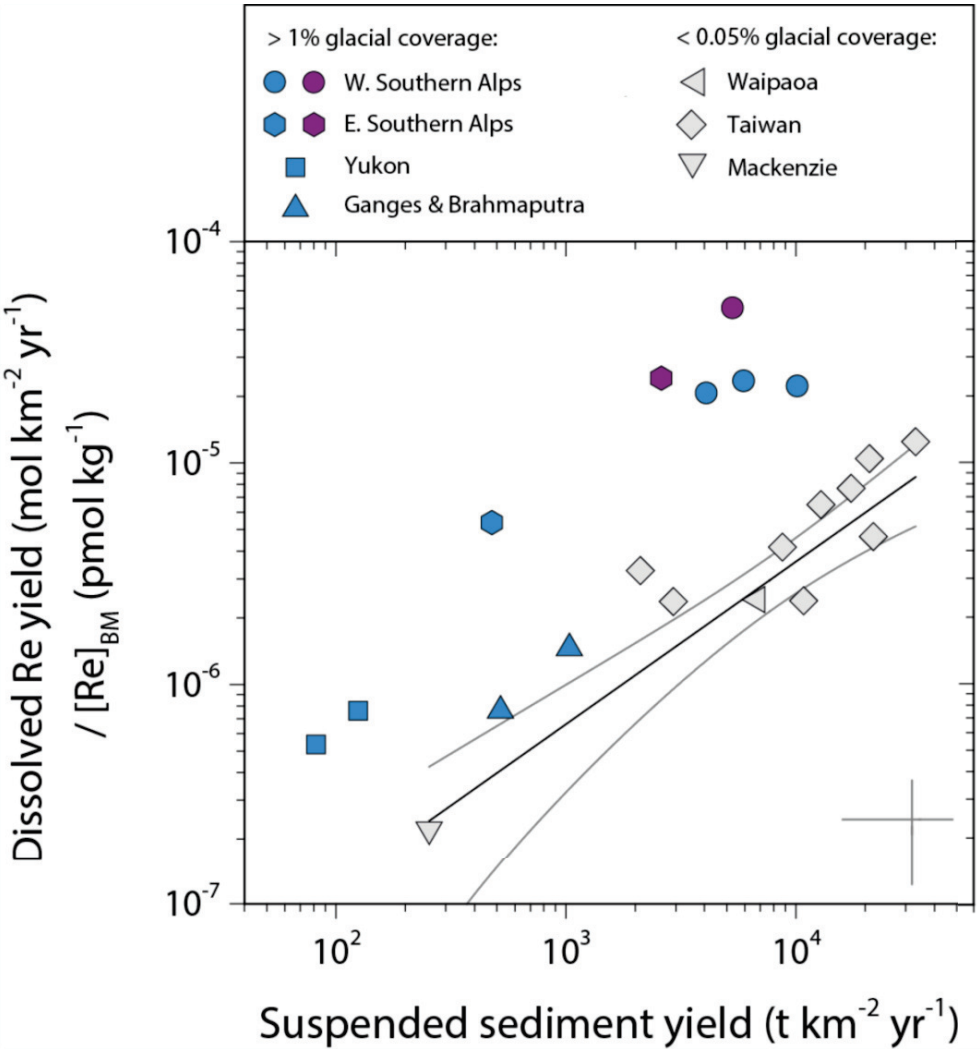

Figure 3.2 Dissolved rhenium (Re) yield in mountain catchments around the world draining sedimentary rocks as a function of suspended sediment yield. Dissolved Re yields (mol km^{-2} yr^{-1}) have been normalized to river bed material Re concentration ($[Re]_{BM}$, pmol kg^{-1}) to account for lithological variability between catchments (Table 3.6). Grey whiskers show ±50% of the values. Grey symbols represent catchments with <0.05% of their area covered by glaciers, with the power law best fit to data shown by the black line and the 95% confidence intervals shown in grey ($y = (4.1 \pm 3.4 \times 10^{-9})x^{(0.7 \pm 0.1)}$, $r^2 = 0.82$, $P < 0.001$, n = 12). Blue symbols represent catchments with glaciers covering >1% of the catchment area and purple symbols represent catchments with the highest coverage of glaciers (>40%). Rhenium data for the Southern Alps, Waipaoa, and Yukon catchments come from this study; for the Yukon, data are also from Miller et al., 2011; for the Mackenzie the data come from Miller et al., 2011; for Taiwan, data are from Hilton et al., 2014; and for the Ganges and Brahmaputra catchments, data are from Miller et al., 2011.

3.4 Discussion

The erosion rates in the western Southern Alps are high (4,000–10,000 t km^{-2} yr^{-1}), and comparable to those in Taiwan (Hilton et al., 2014; Lyons et al., 2005). The similarity in Re mobility between these settings agrees with the notion that high erosion rates can enhance oxidative weathering of OC_{petro} and the release of Re to the dissolved load of rivers (Hilton et al., 2014). This probably reflects the rapid soil formation in the western Southern Alps (Larsen et al., 2014) and is consistent with an important role of bedrock landslides for exposing bedrock clasts in landslide deposits and focusing hydrological pathways in landslide scars (Emberson et al., 2016). In the global data compilation, we find that suspended sediment yield (a proxy for physical erosion rate) is correlated with dissolved Re yield (Figure 3.2). This suggests that OC_{petro} oxidation is supply limited in many locations, as predicted by the relatively fast kinetics of OC_{petro} oxidation and the high atmospheric O_2 concentrations at present (Chang and Berner, 1999; Bolton et al., 2006). This contrasts with acid-hydrolysis weathering of silicate minerals, which is thought to be kinetically limited at the high erosion rates experienced in mountain belts (West, 2012; Maher and Chamberlain, 2014). The implication is that for catchments underlain by sedimentary rocks, increased erosion may result in less effective CO_2 drawdown by silicate weathering, whereas CO_2 release by oxidative weathering of OC_{petro} continues to increase (Figure 3.3).

In the western Southern Alps, we find that glacial cover is a major control on the average $[Re]_{diss}$ measured in catchments (Figure 3.1). This is not only the case for the catchments with large valley glaciers (the Waiho and Fox: Figure 3.1A): glacial processes appear to enhance oxidative weathering to some degree in all catchments. Although this may seem to conflict with the idea that OC_{petro} oxidation in mountains is already supply limited (Hilton et al., 2014), there are characteristics of glacial catchments that mean that for the same physical erosion rate, oxidation rate may be further enhanced. These include: i) physical mechanisms that increase effective surface area (Anderson, 2005; Hales and Roering, 2009); and ii) biogeochemical mechanisms that increase O_2 availability and the competitiveness of microbial communities (Bardgett et al., 2007). Physical mechanisms include glacial abrasion (Anderson, 2005), which can supply large quantities of fine material for weathering within the glacial system and in the deposited moraines. Our data show no evidence for the dilution of $[Re]_{diss}$ concentrations downstream in the Fox and Waiho catchments, suggesting that water seeping from moraines has a similar $[Re]_{diss}$ to the river water (Table 3.1) and that moraines are important loci for oxidative weathering reactions. At higher elevations on steep rock walls, freeze/thaw cycles and frost cracking driven by sustained sub-zero temperatures and water availability in the porous bedrock can also increase the supply of fresh, fine material to O_2 in the air and water (Hales and Roering, 2009). Biogeochemical factors work in parallel, with limited vegetation and soil development in glacial catchments resulting in less demand for oxygen by heterotrophic respiration (Bardgett et al., 2007). Oxygen should therefore be able to penetrate

deeper into exposed rock surfaces (Chang and Berner, 1999; Bolton et al., 2006). Microbial communities also facilitate OC_{petro} oxidation (Petsch, 2014; Petsch et al., 2001) and these are known to be active both sub-glacially (Tranter et al., 2002; Wadham et al., 2004) and in moraines colonized by organisms during primary succession (Bardgett et al., 2007).

The mechanisms described here are not unique to catchments of the western Southern Alps, but should operate wherever mountain glaciation occurs on OC_{petro}-bearing rocks. In the glaciated eastern Southern Alps catchments, erosion rates are lower than those in the western Southern Alps (Jacobson et al., 2003; Hales and Roering, 2009; Lyons et al., 2005) and so lower OC_{petro} oxidation rates may be expected (Hilton et al., 2014). However, when compared to catchments with similar erosion rates in unglaciated Taiwan, the glaciated catchments have higher dissolved Re yields (Figure 3.2). The glacier-free Waipaoa River data are consistent with the data from Taiwan. When we examine larger rivers draining OC_{petro}-bearing sedimentary rocks (Table 3.6), we find that a global pattern starts to emerge. Erosion rate is a first order control on oxidative weathering rate (dissolved Re yield), but catchments hosting glaciers (>1% of the catchment area, e.g. Yukon, Brahmaputra, Ganges, Southern Alps New Zealand) have dissolved Re yields that are up to three times greater for a given erosion rate than catchments with very low glacial coverage, regardless of the basin area (Figure 3.2).

The dissolved Re yield can be used to estimate the CO_2 oxidation yield, J_{CO2} (gC km^{-2} yr^{-1}), by OC_{petro} oxidation (Petsch, 2014; Hilton et al., 2014; Jaffe et al., 2002; Dalai et al., 2002). There must be good constraint on the Re to OC ratio of the sedimentary rocks and the behaviour of Re and OC_{petro} during weathering. In the western Southern Alps, the river bed materials provide an estimate of catchment-averaged [Re] and [OC_{petro}] and their compositions are similar to measured bedrocks. The weathered colluvium confirms coupled Re and OC_{petro} loss (Supplementary Figure 3.1, Table 3.2) (Petsch, 2014; Hilton et al., 2014; Dalai et al., 2002). To quantify the CO_2 release, the dissolved Re yield in grams (J_{Re}, g km^{-2} yr^{-1}) is combined with the $[OC]_{BM}$:$[Re]_{BM}$ (g g^{-1}) (Equation 3.1).

We correct the estimated CO_2 release to account for the relative mobility of Re and OC_{petro} during weathering in soils, with f_C being the ratio between percentage loss of OC_{petro} in soil versus percentage loss of Re in soil. This factor also accounts for the role of sulfide and silicate minerals as trace sources of dissolved Re (Hilton et al., 2014; Miller et al., 2011). On the basis of the published data from soils (Hilton et al., 2014; Jaffe et al., 2002; Pierson-Wickmann et al., 2002) and our measurements from the western Southern Alps (Table 3.3), f_C is expected to be <1 but >0.5. To account for the presence of graphite that may not be oxidised, we vary the fraction of OC_{petro} as graphite ($f_{graphite}$) from 0 to 0.5, informed by measurements from the study location

(Nibourel et al., 2015). The CO_2 oxidation flux, J_{CO2} (gC km^{-2} yr^{-1}), is calculated using a Monte Carlo simulation to account for these uncertainties (section 3.2.3).

In the western Southern Alps, catchments with limited glacial coverage are estimated to release 14 $^{+9}/_{-5}$ tC km^{-2} yr^{-1} (Whataroa) by OC_{petro} oxidation using the Re proxy (Table 3.4). These are similar to OC_{petro} oxidation yields estimated in Taiwan where erosion rates are similar (Hilton et al., 2014). This suggests that the Re proxy is producing consistent results at the catchment-scale. The Re derived estimate of CO_2 flux from OC_{petro} oxidation for the glaciated Waiho catchment is approximately double, at 30 $^{+20}/_{-11}$ tC km^{-2} yr^{-1}. These values are similar to seasonal measurements of soil respiration in a primary succession on sedimentary rocks exposed by recent glacial retreat in Svalbard (~10–24 tC km^{-2} yr^{-1}, based on monthly averaged data) (Bekku et al., 2004), but lower than typical rates of soil respiration in mineral soils that contain non-rock derived organic matter (Hicks Pries et al., 2017). Although the uncertainties on the CO_2 fluxes are relatively large based on our current understanding of Re and OC_{petro} mobility, the difference between the glaciated catchments and the other catchments is larger than these uncertainties (Table 3.4).

In catchments where mountain glaciers are confined to headwaters, the Re derived estimates of CO_2 release do not negate CO_2 drawdown by silicate weathering (~2–10 tC km^{-2} yr^{-1}; Lyons et al., 2005) and by erosion and sedimentary burial of biospheric OC (~40 tC km^{-2} yr^{-1}; Hilton et al., 2008) (Figure 3.3). In stark contrast, the doubling of the OC_{petro} oxidation rate in the Waiho catchment converts it into a net CO_2 source during erosion and weathering (Figure 3.3). At present, the Waiho and Fox rivers drain less than 5% of the sampled area (Figure 3.1), so the enhanced glacial contribution to CO_2 fluxes from OC_{petro} oxidation has a modest influence across the mountain belt. However, under more heavily glaciated conditions the Southern Alps would be primed to act as a CO_2 source. Accelerated OC_{petro} oxidation driven by the physical and biogeochemical mechanisms that we have identified may have increased CO_2 emissions (Figure 3.3). The heavily glaciated western Southern Alps catchments indicate that biospheric OC erosion and burial will also decrease as glacial cover increases. In addition, at high erosion rates and high rates of mineral supply, silicate weathering rates are very sensitive to temperature and runoff (West, 2012; Maher and Chamberlain, 2014) and cooler temperatures may decrease rates of CO_2 drawdown (Figure 3.3).

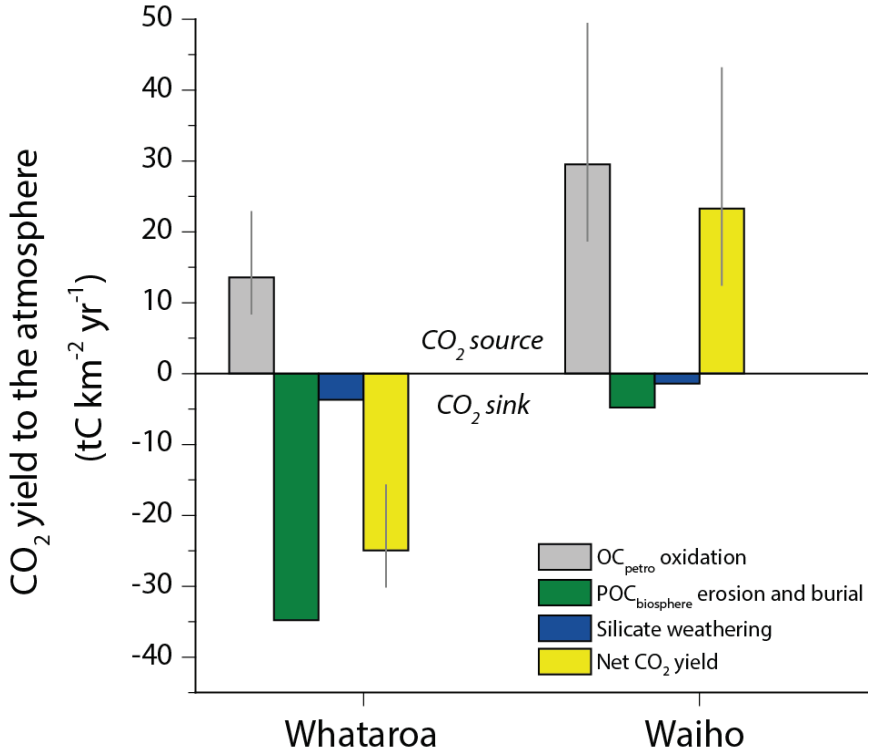

Figure 3.3 Net carbon balance due to erosion and weathering in the western Southern Alps. Two catchments with contrasting glacial coverage area are shown: the Whataroa (9.7% glacier coverage) and the Waiho (57.6% glacier coverage). The CO_2 release to the atmosphere by OC_{petro} weathering (this study, from dissolved rhenium measurements) is shown alongside the CO_2 drawdown by erosion and burial of biospheric particulate organic carbon ($POC_{biosphere}$) (Hilton et al., 2008) and silicate weathering (Lyons et al., 2005; Jacobson et al., 2003).

3.5 Wider implications

The global CO_2 emissions by OC_{petro} oxidation remain to be better quantified. Nevertheless, they are probably as large as those from volcanic degassing (Petsch, 2014). To evaluate the strength of this feedback in glaciated mountain belts for counteracting global cooling, and for potentially having the capacity to end a glaciation, both the OC_{petro} presence and abundance in glaciated mountain ranges must be taken into account. By way of example, the Himalaya have the potential to be a key site for CO_2 fluxes by OC_{petro} oxidation, because they host OC_{petro} bearing Tethyan Sedimentary Series shales at high altitudes. Furthermore, around the world rocks containing OC_{petro} have been subject to repeated mountain glaciation throughout the Late Cenozoic. Enhanced OC_{petro} oxidation in locations such as the Rockies, the Andes and the European Alps (Herman et al., 2013) could have driven these sites to operate as important CO_2 sources, and O_2 sinks, during sustained periods of global cooling and glaciation over 10^4 to $>10^6$ yr (Stolper et al., 2016). OC_{petro} oxidation could act in tandem with transient CO_2 emissions from enhanced sulfide oxidation, and weathering of carbonate minerals by sulfuric acid, during glaciation (Torres et al., 2017). It may also help explain the apparent limit to CO_2 minima in the latter part of the Cenozoic (Galbraith and Eggleston, 2017). At this time, falling temperatures should have encouraged the development of glaciers at sub-tropical latitudes and rapid rates of OC_{petro} oxidation in association. The additional

removal of O_2 from the atmosphere and release of CO_2 by OC_{petro} oxidation under this cooling climate should have served as a poignant forcing in the climate system. Although the global fluxes are difficult to quantify from the available data (Figure 3.2), enhanced OC_{petro} oxidation associated with more extensive glacial erosion processes is consistent with the ~2% decline in atmospheric O_2 recorded in ice cores over the last 800,000 years (Stolper et al., 2016). If the decline in atmospheric O_2 results from changes in OC burial versus OC_{petro} oxidation alone, it implies a net CO_2 release of ~3×10^{11} moles yr^{-1}, or ~3–4 Mt C yr^{-1} (Stolper et al., 2016). This corresponds to only a modest (~6%) increase in global OC_{petro} oxidation rates (Petsch, 2014) over this period in which the duration and intensity of glaciation increased (Herman et al., 2013). We propose that the link between OC_{petro} weathering and mountain glaciation offers a previously unrecognized feedback between climate and the carbon cycle where increased CO_2 emissions act to counter further global cooling during the Late Cenozoic.

3.6 Summary

Petrogenic organic carbon oxidation generates a significant source of CO_2 that is released to the atmosphere and it plays an important role in Earth's long-term carbon cycle. Dissolved rhenium fluxes allow the oxidation of OC_{petro} in sedimentary rocks and the associated CO_2 emissions to be tracked and quantified. In the western Southern Alps, we find that catchments with glaciers confined to headwaters experience CO_2 emissions that are comparable to the magnitude of carbon sequestered during the weathering of silicate minerals coupled to carbonate precipitation (Whataroa: 14 $^{+9}/_{-5}$ tC km^{-2} yr^{-1}). However, in stark contrast, we find that the presence of valley glaciers in catchments that are otherwise comparable drives enhanced rates of CO_2 release by OC_{petro} oxidation: Re fluxes are tripled by 2–3 times relative to the less glaciated catchments (Waiho: 30 $^{+20}/_{-11}$ tC km^{-2} yr^{-1}). We propose three mechanisms that may be important for explaining this trend. The first is a physical mechanism, whereby the generation of fine sediment particles with a reactive surface area for oxidation is increased by the presence of valley glaciers, due to the abrading and grinding processes associated with glacier movement. The second and third mechanisms are tied to biological processes. Limited soil and vegetation cover in glacial catchments should lower the demand for oxygen by the biosphere, meaning that more O_2 is available for bedrock weathering. In addition, the action of microbial activity, both sub-glacially and in moraine deposits, may facilitate the oxidation of OC_{petro} in glacial environments. In the western Southern Alps, we calculate that the increased CO_2 emissions by OC_{petro} oxidation in catchments with valley glaciers turn the net carbon budget in these sites into a net CO_2 source. We also demonstrate a global link between elevated dissolved Re fluxes and the presence of glaciers in mountain catchments around the world. Consequently, this could imply that during times of global cooling the development of glaciers in mountainous areas could buffer global climate change: as CO_2 emissions rise increased radiative forcing should return the planet to a warmer state.

3.7 Supplementary Figures

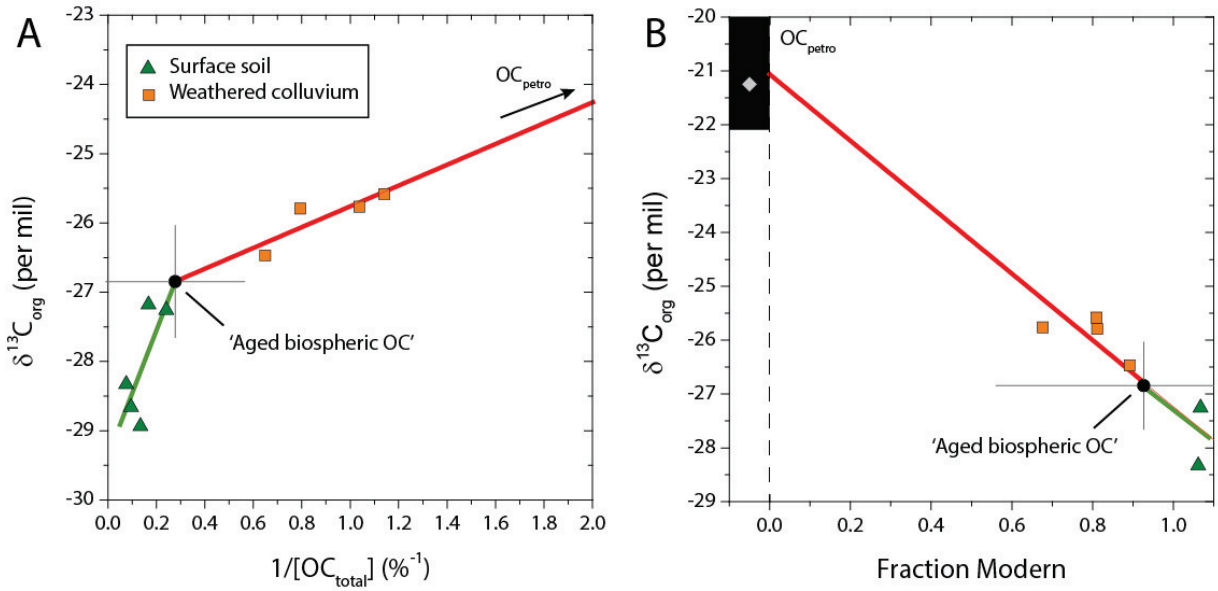

Supplementary Figure 3.1 Weathered colluvium from the western Southern Alps. A. The inverse of organic carbon concentration ($1/[OC_{total}]$) versus the stable isotope composition of organic carbon ($\delta^{13}C_{org}$) for bulk surface soils (triangles) and weathered colluvium (squares). Green line shows linear trend through surface soils (r^2 = 0.38). Red line shows linear trend (r^2 = 0.62) through weathered materials. The intersection of these linear trends suggests the presence of aged biospheric OC in the weathered colluvium, mixing with OC_{petro}. **B.** The radiocarbon activity of samples reported as the Fraction Modern versus $\delta^{13}C_{org}$ (as per A). Black box indicates range of OC_{petro} composition based on published measurements (Hilton et al., 2008) and grey diamond is a river bed material sample downstream of the sampling site. Linear trend through samples (r^2 = 0.73) suggests mixing of biospheric OC and OC_{petro}. The aged biospheric end member used in the mixing analysis is shown as a black circle.

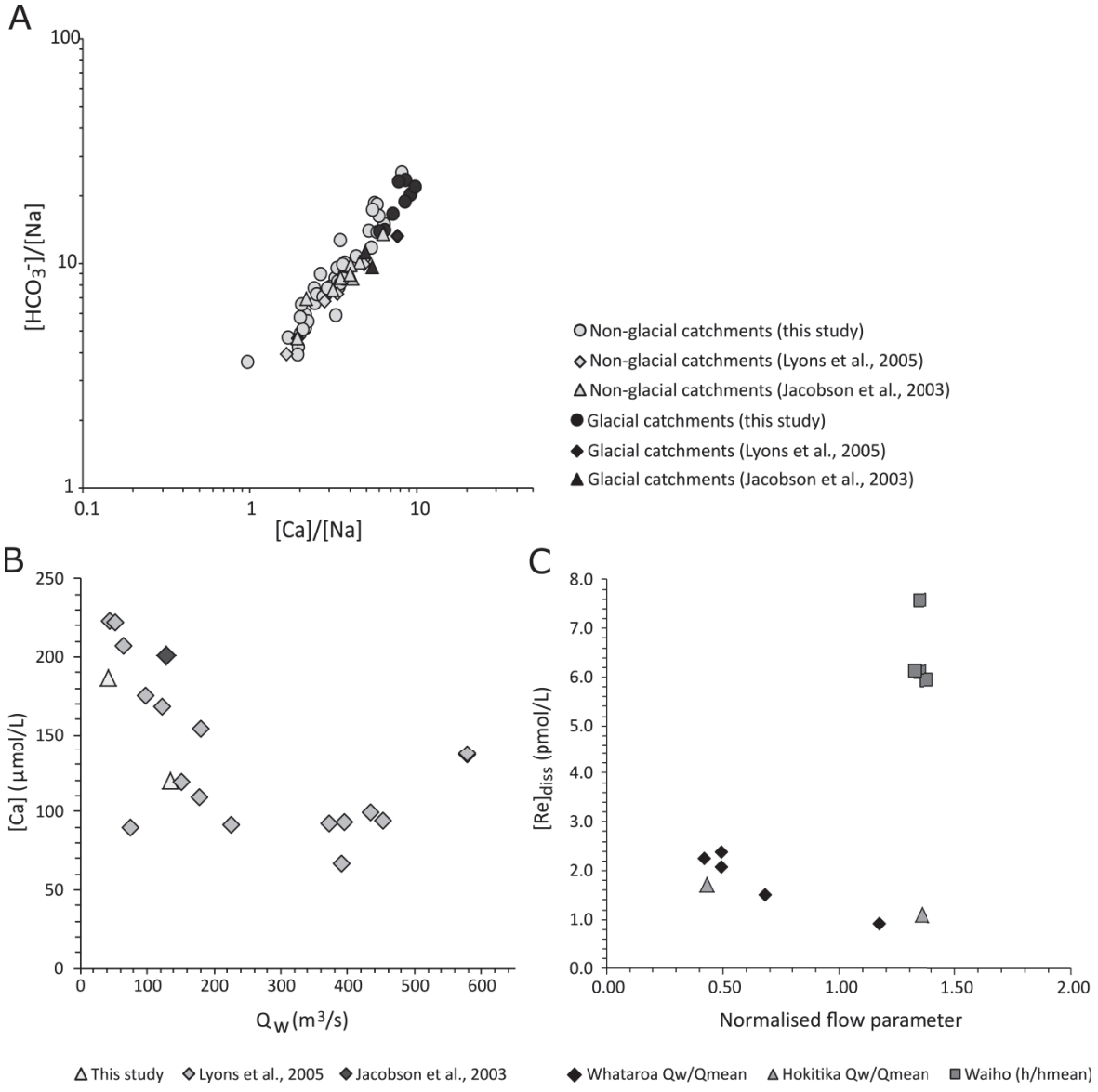

Supplementary Figure 3.2 Dissolved major ion concentrations in the western Southern Alps. A. Positive correlation between $[HCO_3^-]/[Na]$ and [Ca]/[Na] reflects the congruent release of bicarbonate and calcium during chemical weathering. The ion concentrations in the catchments of the Southern Alps from this study (circles) are shown relative to published data from the Southern Alps (diamonds and triangles: Jacobson et al., 2003; Lyons et al., 2005). The patterns reflect increased rates of carbonate weathering reactions in the western Southern Alps; this is particularly true for catchments hosting valley glaciers (black symbols). Note the consistency between the new and published data. Units are mol:mol. **B.** Daily water discharge at time of sampling (Q_w, $m^3\ s^{-1}$) versus $[Ca^{2+}]$ for the Hokitika River for samples from this study (2014, triangles) alongside published data (grey diamonds) from 1999-2000 (Jacobson et al., 2003; Lyons et al., 2005). **C**. River flow versus $[Re]_{diss}$ in the Hokitika, Whataroa and Waiho catchments where active stream gauge data is available for 2014. The daily water discharge (m^3/s) on sample collection days (Q_w) for the Hokitika and Whataroa catchments has been normalized to the long-term mean average flow (Q_{mean}) from 1971–2015. An inverse relationship between Q_w/Q_{mean} and $[Re]_{diss}$ reflects a dilution trend. For the Waiho, stage height (h) is normalized to the long-term mean stage height (h_{mean}) from 1983–2015 and did not co-vary during the sampling period.

3.8 Data Tables

Table 3.1 | Major ion and rhenium concentration data for water samples from the Southern Alps, New Zealand.

Region	Catchment	Collection date	Sample ID	Latitude (degrees S)	Longitude (degrees E)	pH	T (°C)	Na^+ (µmol L^{-1})	K^+ (µmol L^{-1})	Mg^{2+} (µmol L^{-1})	Ca^{2+} (µmol L^{-1})	F^- (µmol L^{-1})	Cl^- (µmol L^{-1})	SO_4^{2-} (µmol L^{-1})	$[Re]_{diss}$ (pmol L^{-1})	Total Alkalinity (µmol L^{-1})	HCO_3^- (µmol/L^{-1})
Western Southern Alps	Hokitika	14/09/2014	NZ14-14	42.89427	171.13238	8.52	8.8	66.09	15.13	11.93	162.25	1.05	35.83	25.88	1.91	448.74	441.23
		14/09/2014	NZ14-16	42.88324	171.15501	8.52	11.2	101.30	29.49	17.70	216.75	2.11	47.11	34.30	2.26	613.55	603.33
		14/09/2014	NZ14-18	42.95557	171.01666	8.36	8.4	57.83	25.38	13.99	186.50	1.58	31.31	32.74	1.70	506.08	500.14
		14/09/2014	NZ14-20	42.74549	171.00066	8.20	11.3	83.48	32.05	22.22	178.25	1.58	53.88	29.62	1.54	435.44	431.71
		26/09/2014	NZ14-77	44.23183	169.23164	8.31	8.3	47.39	20.00	9.47	119.25	0.53	34.70	21.83	1.10	349.79	346.01
		26/09/2014	NZ14-79	42.74551	171.00058	8.06	9.6	67.83	25.38	14.40	135.75	1.05	46.83	22.14	1.11	394.47	392.02
	Wanganui	15/09/2014	NZ14-22	43.16322	170.62808	8.14	8.9	259.57	37.18	11.52	251.50	4.21	217.21	74.84	2.88	953.97	947.28
		15/09/2014	NZ14-24	43.03586	170.44994	8.34	9.9	116.52	51.28	23.05	352.50	2.11	67.14	67.66	2.53	929.75	919.50
		16/09/2014	NZ14-40	43.15522	170.62608	8.14	6.4	53.91	19.49	7.00	130.25	1.05	59.52	41.47	1.69	423.24	420.21
		26/09/2014	NZ14-81	43.15533	170.62608	7.98	8.3	56.09	23.85	7.82	159.50	0.53	40.34	30.25	1.50	409.83	407.74
	Poerua	15/09/2014	NZ14-26	43.20627	170.521	8.43	7.5	31.74	42.82	9.47	257.75	1.05	28.21	89.18	3.73	817.79	806.89
		15/09/2014	NZ14-28	43.13449	170.48598	8.21	9.9	46.96	50.51	12.76	263.00	1.05	43.44	80.14	3.38	882.78	875.46
		16/09/2014	NZ14-37	43.15672	170.50438	7.74	8	71.74	31.79	13.58	139.50	0.53	85.19	31.49	1.47	306.17	305.26
		26/09/2014	NZ14-82	43.15686	170.50215	7.92	8.8	46.09	32.56	9.05	132.00	0.53	44.85	25.88	1.14	347.07	345.50
	Whataroa	15/09/2014	NZ14-30	43.29351	170.41246	8.02	8.4	80.43	20.51	13.99	304.50	1.58	34.70	63.61	2.07	724.52	720.62
		15/09/2014	NZ14-32	43.16091	10.3768	7.73	10.7	118.26	49.49	33.74	513.25	2.11	60.37	58.93	2.37	1279.62	1276.09
		16/09/2014	NZ14-41	43.28552	170.40111	8.21	6.4	60.00	15.13	9.88	204.00	1.05	36.39	35.86	1.51	478.83	474.85
		26/09/2014	NZ14-83	43.28552	170.40121	8.04	7.5	43.04	13.59	7.00	150.00	0.53	29.34	24.63	0.90	352.54	350.47
		02/10/2014	NZ14-110	43.28548	170.40146	8.25	8.4	80.87	21.03	14.81	298.00	1.58	35.54	60.18	2.23	740.78	734.09
	Waitangitaona	16/09/2014	NZ14-34	43.28241	170.30812	8.20	7	58.26	30.00	14.81	129.75	1.05	50.21	31.81	1.33	326.60	323.85
		26/09/2014	NZ14-84	43.2822	170.30545	7.86	8	41.30	23.08	8.64	80.00	0.53	37.52	14.97	0.81	163.05	162.35
	Waiho	16/09/2014	NZ14-44	43.44185	170.17308	8.43	2	37.83	63.59	33.33	323.75	1.05	23.41	193.02	6.11	907.41	895.67
		16/09/2014	NZ14-47	43.41813	170.1806	8.48	3.8	53.48	88.97	52.26	493.50	1.05	26.80	192.08	7.56	1111.19	1095.06
		27/09/2014	NZ14-91	43.41808	170.18065	8.26	4.4	45.65	90.51	48.97	446.00	0.53	22.85	165.89	5.94	1017.08	1008.03

Region	Catchment	Collection date	Sample ID	Latitude (degrees S)	Longitude (degrees E)	pH	T (°C)	Na^+ (µmol L^{-1})	K^+ (µmol L^{-1})	Mg^{2+} (µmol L^{-1})	Ca^{2+} (µmol L^{-1})	F^- (µmol L^{-1})	Cl^- (µmol L^{-1})	SO_4^{2-} (µmol L^{-1})	$[Re]_{diss}$ (pmol L^{-1})	Total Alkalinity (µmol L^{-1})	HCO_3^- (µmol/L^{-1})
		02/10/2014	NZ14-107	43.61212	169.85655	8.34	4.1	57.83	88.72	55.56	491.50	1.05	21.16	198.63	6.13	1108.85	1097.08
	Callery	16/09/2014	NZ14-48	43.39675	170.18344	8.43	5.4	74.78	35.90	22.22	398.00	1.05	26.23	94.79	2.55	893.73	881.98
		27/09/2014	NZ14-93	43.39678	170.18346	8.35	6.9	45.65	24.87	13.99	264.75	1.05	25.11	90.12	2.59	851.34	841.88
		02/10/2014	NZ14-108	43.39725	170.18408	8.42	6.8	58.70	29.74	17.28	317.75	1.05	24.82	115.06	3.09	1032.27	1018.96
	Waiho/ Callery confluence	02/10/2014	NZ14-109	43.3933	170.18042	8.43	6.5	77.39	52.56	32.51	447.75	1.05	26.23	134.39	4.55	1085.42	1071.15
		27/09/2014	NZ14-87	43.44046	170.07457	8.29	9.4	71.30	68.97	29.63	368.75	2.11	52.75	131.90	4.89	1011.23	1001.30
		27/09/2014	NZ14-89	43.38486	170.13333	8.05	9.5	63.04	28.21	20.99	128.25	1.05	51.90	21.52	1.46	418.76	416.23
	Fox	18/09/2014	NZ14-63	43.49958	170.05521	8.62	1.1	56.52	105.13	58.85	441.00	1.05	20.59	266.29	10.67	1344.86	1318.48
		18/09/2014	NZ14-66	43.48704	170.02962	8.52	3.3	112.61	144.10	92.18	722.75	1.58	32.16	274.09	11.55	1620.05	1594.56
		19/09/2014	NZ14-68	43.48704	170.02956	8.94	4.2	80.87	121.28	58.02	482.00	1.05	44.85	148.74	6.26	1178.01	1130.72
		27/09/2014	NZ14-85	43.48598	170.02983	8.31	3.6	76.52	115.64	63.79	549.25	1.05	27.64	190.83	7.68	1289.69	1276.97
		27/09/2014	NZ14-86			8.67	1.1	50.87	111.79	57.20	463.00	0.53	19.18	178.98	6.78	1058.14	1034.81
	Cook	19/09/2014	NZ14-69	43.49912	169.9653	8.48	6.4	51.74	28.46	16.87	174.25	0.53	47.95	41.78	1.85	437.93	431.27
		29/09/2014	NZ14-98	43.49902	169.96536	8.31	7.8	57.83	51.03	32.92	369.25	1.05	28.49	92.92	3.88	881.77	872.77
	Karangarua	19/09/2014	NZ14-71	43.57515	169.8051	8.18	7.3	45.65	19.49	10.29	91.00	0.00	41.75	16.84	0.84	224.44	222.56
		29/09/2014	NZ14-97	43.57513	169.8051	8.05	9.2	49.13	28.21	17.28	171.25	1.05	31.31	52.70	2.28	627.92	624.25
		30/09/2014	NZ14-100	43.63503	169.95711	8.02	9.1	53.91	25.13	32.92	319.75	1.05	20.87	64.86	2.97	885.29	880.54
		01/10/2014	NZ14-103	43.62964	169.94629	7.88	6.6	45.65	38.97	17.28	121.25	0.53	26.80	32.43	1.86	411.52	409.89
		01/10/2014	NZ14-105	43.61212	169.89484	8.05	8.1	77.39	36.41	28.40	257.00	1.05	30.18	57.37	2.84	743.74	739.47
		03/10/2014	NZ14-111	43.57394	169.80774	7.99	7	47.83	24.36	15.23	139.25	0.53	30.47	28.69	1.30	375.08	373.14
	Paringa	19/09/2014	NZ14-73	43.71198	169.49315	7.95	8	43.91	21.54	8.23	91.25	0.53	41.18	16.53	0.93	224.44	223.31
		29/09/2014	NZ14-94	43.71133	169.49055	8.14	9.2	56.09	35.90	16.05	183.75	1.05	35.83	35.55	1.57	333.51	331.00
	Makawhio (Jacob's river)	29/09/2014	NZ14-95	43.57327	169.67892	7.71	9.5	56.52	34.36	17.70	155.50	1.05	38.65	34.92	1.91	401.82	400.71
		03/10/2014	NZ14-112	43.57354	169.67828	7.50	7.2	38.70	17.18	8.23	65.50				0.98	181.56	181.26
		19/09/2014	NZ14-75	43.85398	169.05496	8.09	8.6	59.57	21.54	20.99	220.50	1.05	37.80	34.30	2.01	605.68	601.82
		03/10/2014	NZ14-113	43.85398	169.05486	8.00	8.4	57.39	19.74	19.75	205.75	1.05	34.98	32.74	1.45	570.51	567.54
		03/10/2014	NZ14-114	44.03936	169.37927	8.02	7.3	46.52	7.44	18.93	169.50	1.05	17.49	27.44	1.80	402.20	399.98

Region	Catchment	Collection date	Sample ID	Latitude (degrees S)	Longitude (degrees E)	pH	T (°C)	Na^+ (µmol L^{-1})	K^+ (µmol L^{-1})	Mg^{2+} (µmol L^{-1})	Ca^{2+} (µmol L^{-1})	F^- (µmol L^{-1})	Cl^- (µmol L^{-1})	SO_4^{2-} (µmol L^{-1})	$[Re]_{diss}$ (pmol L^{-1})	Total Alkalinity (µmol L^{-1})	HCO_3^- (µmol/L^{-1})
	Hydrothermal	30/09/2014	NZ14-102	43.62964	169.94629	7.02	55.5	17508.70	712.82	184.36	742.25	48.42	4761.64	0.94	0.11	22415.40	22398.17
	Rainwater	15/09/2014	NZ14-RW1	43.389672	170.183759			55.65	3.08	4.94	5.50				0.16		
	Rainwater	02/10/2014	NZ14-RW2	43.389672	170.183759			60.00	3.08	4.53	2.75				0.15		
Eastern Southern Alps	Hooker	04/10/2014	NZ14-116	43.69284	170.09869	8.39	2.1	30.87	11.28	16.46	169.25	0.53	8.74	74.21	0.91	524.72	518.39
	Hooker	04/10/2014	NZ14-117	43.69269	170.09903	8.29	4.1	48.26	15.64	28.81	279.75	0.53	11.00	72.03	1.24	655.22	648.90
	Tasman	04/10/2014	NZ14-118	43.70715	170.17097	8.43	3.2	67.39	17.44	15.23	240.75	0.53	7.33	82.32	1.05	547.35	540.10
	Jollie	05/10/2014	NZ14-120	43.86295	170.1756	8.24	8.4	58.70	7.44	14.40	129.75	1.05	9.31	27.44	0.86	356.91	353.61
	Hooker, Jollie and Tasman confluence	05/10/2014	NZ14-122	43.99801	170.19449	8.31	7.7	42.61	9.49	10.29	129.50	1.05	8.74	45.53	1.05	482.13	477.07

Table 3.2 | Re and OC_{petro} in weathered colluvium.

[a]Radiocarbon activity as Fraction Modern. [b]fraction of organic carbon present as petrogenic organic carbon, determined from mixing analysis (see Materials and Methods). [c]petrogenic organic carbon concentration. *f_{petro} assumed to be 1 based on the % [OC] and the stable isotope composition of river bed materials in New Zealand, which are similar to those measured in bedrocks of the mountain belt. **f_{petro} assumed to be 1 in the absence of F_{mod} measurements (based on sampling methodology and type). nd = not determined.

Site	Sample ID	Lat. (°S)	Long. (°E)	Sample type	Ref.	$[OC_{total}]$ %	$\delta^{13}C_{org}$ (per mil)	F_{mod} [a]	f_{petro} [b]	UCIAMS Publication Code	$[OC_{petro}]$ % [c]	[Re] (pg g^{-1})
Alex Knob, Doherty Creek, New Zealand	NZ14-54	43.40796	170.16727	Weathered colluvium	this study	1.26	-25.8	0.81 ± 0.001	0.13 ± 0.05	178308	0.16 ± 0.06	36.1 ± 0.3
	NZ14-55	43.40602	170.16171	Weathered colluvium	this study	1.54	-26.5	0.89 ± 0.001	0.05 ± 0.02	178310	0.07 ± 0.03	31.4 ± 0.2
	NZ14-56	43.40602	170.16171	Weathered colluvium	this study	0.88	-25.6	0.81 ± 0.001	0.13 ± 0.05	178311	0.11 ± 0.04	23.7 ± 0.2
	NZ14-59	43.40596	170.16115	Weathered colluvium	this study	0.96	-25.8	0.68 ± 0.001	0.26 ± 0.10	178313	0.25 ± 0.10	24.2 ± 0.2
	Average of weathered colluvium (n = 4)										*0.15*	*28.8*
	NZ14-57	43.40596	170.16115	Surface soil	this study	4.16	-27.3	1.07 ± 0.002	nd	178312		24.7 ± 0.2
	NZ14-58	43.40596	170.16115	Surface soil	this study	5.97	-27.2	nd	nd			21.3 ± 0.2
	NZ14-60	43.40596	170.16115	Surface soil	this study	13.24	-28.3	1.06 ± 0.002	nd	178314		52.0 ± 0.4
	NZ14-61	43.40909	170.16335	Surface soil	this study	10.48	-28.7	nd	nd			27.0 ± 0.2
	NZ14-62	43.41448	170.15887	Surface soil	this study	7.44	-28.9	nd	nd			21.7 ± 0.2
	NZ14-90	43.38486	170.13333	Local river bed material	this study	0.21	-21.2	nd	1*			111 ± 1
Ohio Shale, US	244			Weathered rock	(*30*)	1.75	nd	nd	1**		1.75	890
	245			Weathered rock	(*30*)	1.46	nd	nd	1**		1.46	850
	246			Weathered rock	(*30*)	4.29	nd	nd	1**		4.29	17700
	Average of weathered rock (n = 3)										*2.50*	*6480*
	247			Rock	(*30*)	7.30	nd	nd	1**		7.30	89400
	248			Rock	(*30*)	5.95	nd	nd	1**		5.95	115600
	249			Rock	(*30*)	7.13	nd	nd	1**		7.13	74500
	250			Rock	(*30*)	7.80	nd	nd	1**		7.80	81100
	251			Rock	(*30*)	6.75	nd	nd	1**		6.75	78000
	Average of rock (n = 5)										*6.99*	*87720*

Table 3.3 | River bed materials.

Catchment	Sample ID	Date	Latitude (deg. S)	Longitude (deg. E)	$[Re]_{BM}$ (pg g^{-1})	$[OC]_{BM}$ %	$\delta^{13}C$ (‰)
Hokitika	NZ14-15	14/09/2014	42.89427	171.13438	104.9	0.08	-25.2
Hokitika	NZ14-17	14/09/2014	42.88324	171.15501	51.3	0.09	-22.2
Hokitika	NZ14-19	14/09/2014	42.95557	171.01666	87.2	0.11	-24.1
Hokitika	NZ14-21	14/09/2014	42.74549	171.00066	71.6	0.17	-23.3
Hokitika	NZ14-78	26/09/2014	44.23183	169.23164	109.9	0.17	-22.9
Hokitika	NZ14-80	26/09/2014	42.74551	171.00058	73.4	0.12	-23.5
Wanganui	NZ14-23	15/09/2014	43.16322	170.62808	77.8	0.08	-23.6
Wanganui	NZ14-25	15/09/2014	43.03586	170.44994	53.1	0.08	-24.6
Poerua	NZ14-27	15/09/2014	43.20627	170.52100	94.4	0.10	-21.1
Poerua	NZ14-29	15/09/2014	43.13449	170.48598	107.9	0.14	-20.8
Poerua	NZ14-38	16/09/2014	43.15672	170.50438	81.1	0.17	-20.5
Whataroa	NZ14-31	15/09/2014	43.29351	170.41246	236.2	0.10	-24.3
Whataroa	NZ14-33	15/09/2014	43.16091	170.37680	47.4	0.14	-23.2
Whataroa	NZ14-42	16/09/2014	43.29319	170.41313	76.9	0.12	-23.3
Waitangitaona	NZ14-35	16/09/2014	43.28241	170.30812	251.5	0.18	-20.8
Callery	NZ14-49	16/09/2014	43.39675	170.18344	66.2	0.08	-25.7
Waiho	NZ14-45	16/09/2014	43.44185	170.17308	177.4	0.10	-23.1
Waiho	NZ14-92	27/09/2014	43.41808	170.18065	103.7	0.11	-23.0
Waikupa	NZ14-88	27/09/2014	43.44046	170.07457	125.2	0.16	-20.2
Docherty Creek	NZ14-90	27/09/2014	43.38486	170.13333	111.9	0.21	-21.2
Fox	NZ14-64	18/09/2014	43.49958	170.05521	241.2	0.13	-20.7
Fox	NZ14-65	18/09/2014	43.49958	170.05521	172.1	0.13	-20.6
Fox	NZ14-67	19/09/2014	43.48704	170.02962	235.7	0.19	-20.3
Cook	NZ14-70	19/09/2014	43.49912	169.96530	113.9	0.18	-21.7
Karangarua	NZ14-72	19/09/2014	43.57515	169.80510	76.1	0.17	-22.8
Karangarua	NZ14-101	30/09/2014	43.63503	169.95711	74.5	0.11	-23.1

Catchment	Sample ID	Date	Latitude (deg. S)	Longitude (deg. E)	$[Re]_{BM}$ (pg g^{-1})	$[OC]_{BM}$ %	$\delta^{13}C$ (‰)
Karangarua	NZ14-104	01/10/2014	43.62964	169.94629	190.8	0.18	-20.7
Karangarua	NZ14-106	01/10/2014	43.61212	169.89484	132.1	0.16	-22.2
Makawhio (Jacob's River)	NZ14-96	29/09/2014	43.57327	169.67892	93.2	0.14	-21.7
Paringa	NZ14-74	19/09/2014	43.71198	169.49315	99.2	0.11	-23.4
Haast	NZ14-76	19/09/2014	43.85398	169.05496	116.7	0.13	-24.3
Hooker Glacier	NZ14-115	04/10/2014	44.03936	169.37926	72.5	0.06	-27.0
Tasman River	NZ14-119	04/10/2014	43.70715	170.17097	82.1	0.06	-26.9
Jollie River	NZ14-121	05/10/2014	43.86295	170.17560	67.6	0.06	-25.9

Table 3.4 | Western Southern Alps catchment average data and dissolved rhenium yield estimates.

*Glaciers identified from the World Glacier Inventory (NSIDC, 2016). **from Hicks et al. (2011) & Jacobson and Blum (2003). ***Determined using Equation 1.

Catchment	Drainage area (km^2)	Average $[Re]_{diss}$ ($pmol\ L^{-1}$)	Number glaciers*	Total glacier area* (km^2)	Glacier coverage in catchment* (%)	Water discharge ($g\ yr^{-1}$)**	$[Re]_{BM}/[OC]_{BM}$ ($g\ g^{-1}$)	OC_{petro} oxidation rate ($tC\ km^{-2}\ yr^{-1}$)***
Hokitika	349	1.60 ± 0.37	65	15.2	4.4	2.3E+15	7.3E-08 ± 2.4E-08	$15\ ^{+7}/_{-5}$
Wanganui	344	2.15 ± 0.66	73	45.4	13.2			
Poerua	136	2.43 ± 1.31	7	3.1	2.3			
Whataroa	454	1.81 ± 0.54	139	44.2	9.7	3.6E+15	1.1E-07 ± 6.1E-08	$14\ ^{+9}/_{-5}$
Waitangitaona	72	1.07 ± 0.52	12	2.4	3.4			
Callery	95	2.75 ± 0.35	21	23.6	25.0			
Waiho	67	6.43 ± 0.76	9	38.6	57.6	4.0E+14	1.3E-07 ± 7.7E-08	$30\ ^{+20}/_{-11}$
Fox	92	8.59 ± 2.13	10	45.2	48.9			
Cook	131	2.87 ± 2.03	17	22.1	16.9			
Karangarua	363	2.02 ± 0.69	84	39.0	10.7			
Makawhio	129	1.25 ± 0.65	23	2.6	2.0			
Paringa	226	1.44 ± 0.93	18	10.7	4.7			
Haast	1312	1.75 ± 0.33	226	62.3	4.7	9.7E+15	9.0E-08 ± 3.8E-08	$15\ ^{+8}/_{-5}$

Table 3.5 | Hydrological data for catchments with river gauging stations.

*Values for the Waiho catchment refer to the stage height and are reported in units of metres.

Catchment	Average Q_w 1971-2015 (m^3/s)	Average Q_w Sept 2014 (m^3/s)	Average Q_w 2014 (m^3/s)	Q_w on days of collection (m^3/s)	Date of collection	Daily discharge (Q_w) / Mean discharge (Q_w mean)	[Re] (pmol L^{-1})
Whataroa	129.07	51.49	129.10	63.95	15/09/2014	0.50	2.07
				63.95	15/09/2014	0.50	2.37
				88.06	16/09/2014	0.68	1.51
				151.41	26/09/2014	1.17	0.90
				54.44	02/10/2014	0.42	2.23
Hokitika	99.64	52.39	105.44	42.95	14/09/2014	0.43	1.70
				135.35	26/09/2014	1.36	1.10
Waiho*	4931*	6495*	6850*	6635*	16/09/2014	1.35*	6.11
				6635*	16/09/2014	1.35*	7.56
				6787*	27/09/2014	1.38*	5.94
				6543*	02/10/2014	1.33*	6.13

Table 3.6 | Catchment-averaged rhenium measurements from rivers draining sedimentary rocks in mountain catchments globally.

River	Area (km^2)	Suspended sediment yield ($t\ km^{-2}\ yr^{-1}$)	Ref.	Glacier area (%)	Ref.	Average $[Re]_{diss}$ ($pmol\ L^{-1}$)	n	Ref.	$[Re]_{BM}$ ($pmol\ kg^{-1}$)	n	Ref.	Runoff ($mm\ yr^{-1}$)	Ref.	Dissolved Re yield ($mol\ km^{-2}\ yr^{-1}$)	Dissolved Re yield ($mol\ km^{-2}\ yr^{-1}$) / $[Re]_{BM}$ ($pmol\ kg^{-1}$)
Mackenzie	1712738	254	(Galy et al., 2015)	<0.05%	(Tank et al., 2012)	16.20	7	(Miller et al., 2011)	13130	3	This study	179	(Miller et al., 2011)	2.90E-03	2.21E-07
Taimarli	190	2105	(Dadson et al., 2003)	<0.05%	(NSIDC, 2016)	5.63	1	(Hilton et al., 2014)	3965	3	(Hilton et al., 2014)	2300	(Dadson et al., 2003)	1.30E-02	3.27E-06
Upper Chenyoulan	205	2927	(Dadson et al., 2003)	<0.05%	(NSIDC), 2016)	4.69	1	(Hilton et al., 2014)	3965	3	(Hilton et al., 2014)	2000	(Dadson et al., 2003)	9.38E-03	2.37E-06
Waipaoa	1570	6797	(Hicks et al., 2011)	<0.05%	(NSIDC, 2016)	31.31	2	This study	9044	1	This study	697	(Hicks et al., 2011)	2.18E-02	2.41E-06
Chenyoulan	367	8719	(Dadson et al., 2003)	<0.05%	(NSIDC, 2016)	8.70	3	(Hilton et al., 2014)	3965	3	(Hilton et al., 2014)	1900	(Dadson et al., 2003)	1.65E-02	4.17E-06
Laonung	853	10785	(Dadson et al., 2003)	<0.05%	(NSIDC, 2016)	4.99	1	(Hilton et al., 2014)	3965	3	(Hilton et al., 2014)	1900	(Dadson et al., 2003)	9.47E-03	2.39E-06
Hsiukuluan	249	12851	(Dadson et al., 2003)	<0.05%	(NSIDC, 2016)	10.29	1	(Hilton et al., 2014)	3965	3	(Hilton et al., 2014)	2500	(Dadson et al., 2003)	2.57E-02	6.49E-06
Wulu	639	17371	(Dadson et al., 2003)	<0.05%	(NSIDC, 2016)	13.86	3	(Hilton et al., 2014)	3965	3	(Hilton et al., 2014)	2200	(Dadson et al., 2003)	3.05E-02	7.69E-06
Yenping	476	19118	(Dadson et al., 2003)	<0.05%	(NSIDC, 2016)	12.98	1	(Hilton et al., 2014)	3965	3	(Hilton et al., 2014)	2100	(Dadson et al., 2003)	2.73E-02	6.88E-06
Hualien	1506	20850	(Dadson et al., 2003)	<0.05%	(NSIDC, 2016)	19.75	2	(Hilton et al., 2014)	3965	3	(Hilton et al., 2014)	2100	(Dadson et al., 2003)	4.15E-02	1.05E-05
Chihpen	166	21687	(Dadson et al., 2003)	<0.05%	(NSIDC, 2016)	7.69	1	(Hilton et al., 2014)	3965	3	(Hilton et al., 2014)	2400	(Dadson et al., 2003)	1.85E-02	4.66E-06
Liwu	435	33103	(Dadson et al., 2003)	<0.05%	(NSIDC, 2016)	20.63	6	(Hilton et al., 2014)	3965	3	(Hilton et al., 2014)	2400	(Dadson et al., 2003)	4.95E-02	1.25E-05
Ganga	1033052	519	(Galy et al., 2015)	1	(Immerzeel and Bierkens, 2010)	3.90	1	(Miller et al., 2011)	2446	2	(Pierson-Wickmann et al., 2000)	477	(Miller et al., 2011)	1.86E-03	7.61E-07
Yukon at Pilot	831400	82	(Dornblaser and Striegl, 2009)	1.1	(Tank et al., 2012)	13.40	7	(Miller et al., 2011)	6353	1	(Huh et al., 2004)	254	(Dornblaser and Striegl, 2009)	3.40E-03	5.35E-07
Yukon at Dawson	264179	125	(Brabets et al., 2000)	>1.1	(Tank et al., 2012)	16.86	1	This study	5741	1	This study	259	(Dornblaser and Striegl, 2009)	4.36E-03	7.59E-07
Jollie	140	476	(Hicks et al., 2011)	1.7	(NSIDC, 2016)	0.86	1	This study	363	1	This study	2285	(Hicks et al., 2011)	1.95E-03	5.39E-06
Brahmaputra	595000	1034	(Galy et al., 2015)	3.1	(Immerzeel and Bierkens, 2010)	4.40	3	(Miller et al., 2011)	2589	2	(Pierson-Wickmann et al., 2000)	857	(Miller et al., 2011)	3.77E-03	1.46E-06

River	Area (km^2)	Suspended sediment yield ($t\ km^{-2}\ yr^{-1}$)	Ref.	Glacier area (%)	Ref.	Average $[Re]_{diss}$ ($pmol\ L^{-1}$)	n	Ref.	$[Re]_{BM}$ ($pmol\ kg^{-1}$)	n	Ref.	Runoff ($mm\ yr^{-1}$)	Ref.	Dissolved Re yield ($mol\ km^{-2}\ yr^{-1}$)	Dissolved Re yield ($mol\ km^{-2}\ yr^{-1}$) / $[Re]_{BM}$ ($pmol\ kg^{-1}$)
Hokitika	349	5918	(Hicks et al., 2011)	4.4	(NSIDC, 2016)	1.60	6	This study	446	6	This study	6535	(Hicks et al., 2011)	1.05E-02	2.35E-05
Haast	1312	4072	(Hicks et al., 2011)	4.7	(NSIDC, 2016)	1.75	3	This study	627	1	This study	7412	(Hicks et al., 2011)	1.30E-02	2.07E-05
Whataroa	454	10136	(Hicks et al., 2011)	9.7	(NSIDC, 2016)	1.81	5	This study	645	3	This study	7923	(Hicks et al., 2011)	1.44E-02	2.23E-05
Hooker	107	2596	(Hicks et al., 2011)	41.4	(NSIDC, 2016)	1.24	1	This study	415	2	This study	8111	(Hicks et al., 2011)	1.00E-02	2.42E-05
Waiho	67	5300	(Jacobson et al., 2003)	57.6	(NSIDC, 2016)	6.43	4	This study	755	2	This study	5900	(Jacobson et al., 2003)	3.80E-02	5.03E-05

3.9 References

Anderson, S. P., 2005. Glaciers show direct linkage between erosion rate and chemical weathering fluxes. Geomorphology 67, 147–157.

Bardfett, R. D., Richter, A., Bol, R., Garnett, M. H., Bäumler, R., Xu, X., Lopez-Capel, E., Manning, D. A., Hobbs, P. J. & Hartley, I. R., 2007. Heterotrophic microbial communities use ancient carbon following glacial retreat. Biology Letters 3, 487–490.

Bekku, Y. S., Kume, A., Masuzawa, T., Kanda, H., Nakatsubo, T. & Koizumi, H., 2004. Soil respiration in a high arctic glacier foreland in Ny-Alesund, Svalbard. Polar bioscience 17, 36–46.

Berner, R. A. & Caldeira, K., 1997. The need for mass balance and feedback in the geochemical carbon cycle. Geology 25, 955–956.

Berner, R. A. & Canfield, D. E., 1989. A new model for atmospheric oxygen over Phanerozoic time. American Journal of Science 289, 333–361.

Beyssac, O., Cox, S. C., Vry, J. & Herman, F., 2016. Peak metamorphic temperature and thermal history of the Southern Alps (New Zealand). Tectonophysics 676, 229–249.

Blair, N. E. & Aller, R. C., 2012. The Fate of Terrestrial Organic Carbon in the Marine Environment. In: Carlson, C. A. & Giovannoni, S. J. (eds.) Annual Review of Marine Science, Vol 4.

Bolton, E. W., Berner, R. A. & Petsch, S. T., 2006. The weathering of sedimentary organic matter as a control on atmospheric O_2: II. Theoretical modeling. American Journal of Science 306, 575–615.

Bouchez, J., Beyssac, O., Galy, V., Gaillardet, J., France-Lanord, C., Maurice, L. & Moreira-Turcq, P., 2010. Oxidation of petrogenic organic carbon in the Amazon floodplain as a source of atmospheric CO_2. Geology 38, 255–258.

Brabets, T. P., Wang, B. & Meade, R. H., 2000. Environmental and hydrologic overview of the Yukon River basin, Alaska and Canada. Water-Resources Investigations Report.

Chang, S. B. & Berner, R. A., 1999. Coal weathering and the geochemical carbon cycle. Geochimica et Cosmochimica Acta 63, 3301–3310.

Colodner, D., Sachs, J., Ravizza, G., Turekian, K., Edmond, J. & Boyle, E., 1993. The Geochemical Cycle of Rhenium - A Reconnaissance. Earth and Planetary Science Letters 117, 205–221.

Cumming, V. M., Poulton, S. W., Rooney, A. D. & Selby, D., 2013. Anoxia in the terrestrial environment during the late Mesoproterozoic. Geology 41, 583–586.

Dadson, S. J., Hovius, N., Chen, H., Dade, W. B., Hsieh, M.-L., Willett, S. D., Hu, J.-C., Horng, M.-J., Chen, M.-C., Stark, C. P., Lague, D. & Lin, J.-C., 2003. Links between erosion, runoff variability and seismicity in the Taiwan orogen. Nature 426, 648–651.

Dalai, T. K., Singh, S. K., Trivedi, J. R. & Krishnaswami, S., 2002. Dissolved rhenium in the Yamuna River System and the Ganga in the Himalaya: Role of black shale weathering on the budgets of Re, Os, and U in rivers and CO_2 in the atmosphere. Geochimica Et Cosmochimica Acta 66 29–43.

Dellinger, M., Gaillardet, J., Bouchez, J., Calmels, D., Galy, V., Hilton, R. G., Louvat, P. & France-Lanord, C., 2014. Lithium isotopes in large rivers reveal the cannibalistic nature of modern continental weathering and erosion. Earth and Planetary Science Letters 401, 359–372.

Dornblaser, M. M. & Striegl, R. G., 2009. Suspended sediment and carbonate transport in the Yukon River Basin, Alaska: Fluxes and potential future responses to climate change. Water Resources Research 45.

Dubin, A. & Peucker-Ehrenbrink, B., 2015. The importance of organic-rich shales to the geochemical cycles of rhenium and osmium. Chemical Geology 403, 111–120.

Emberson, R., Hovius, N., Galy, A. & Marc, O., 2016. Chemical weathering in active mountain belts controlled by stochastic bedrock landsliding. Nature Geoscience 9, 42–45.

France-Lanord, C. & Derry, L. A., 1997. Organic carbon burial forcing of the carbon cycle from Himalayan erosion. Nature 390, 65–67.

Galbraith, E.D., Eggleston, S., 2017. A lower limit to atmospheric CO_2 concentrations over the past 800,000 years. Nat. Geosci. 10, 295.

Galy, V., Beyssac, O., France-Lanord, C. & Eglinton, T., 2008. Recycling of Graphite During Himalayan Erosion: A Geological Stabilization of Carbon in the Crust. Science 322, 943–945.

Galy, V., Bouchez, J. & France-Lanord, C., 2007. Determination of total organic carbon content and delta C-13 in carbonate-rich detrital sediments. Geostandards and Geoanalytical Research 31, 199–207.

Galy, V., Peucker-Ehrenbrink, B. & Eglinton, T., 2015. Global carbon export from the terrestrial biosphere controlled by erosion. Nature 521, 204.

Gomez, B., Trustrum, N. A., Hicks, D. M., Roger, K. M., Page, M. J. & Tate, K. R., 2003. Production, storage, and output of particulate organic carbon: Waipaoa River basin, New Zealand. Water Resources Research 39.

Hales, T. C. & Roering, J. J., 2009. A frost "buzzsaw" mechanism for erosion of the eastern Southern Alps, New Zealand. Geomorphology 107, 241–253.

Hayes, J. M., Strauss, H. & Kaufman, A. J., 1999. The abundance of C-13 in marine organic matter and isotopic fractionation in the global biogeochemical cycle of carbon during the past 800 Ma. Chemical Geology 161, 103–125.

Herman, F., Seward, D., Valla, P. G., Carter, A., Kohn, B., Willett, S. D. & Ehlers, T. A., 2013. Worldwide acceleration of mountain erosion under a cooling climate. Nature 504, 423.

Hicks, D. M., Shankar, U., McKerchar, A. I., Basher, L., Lynn, I., Page, M. & Jessen, M., 2011. Suspended sediment yields from New Zealand rivers. Journal of Hydrology (Wellington North) 50, 81–142.

Hicks Pries, C. E., Castanha, C., Porras, R. & Torn, M. S., 2017. The whole-soil carbon flux in response to warming. Science 2.

Hilton, R. G., Gaillardet, J., Calmels, D. & Birck, J.-L., 2014. Geological respiration of a mountain belt revealed by the trace element rhenium. Earth and Planetary Science Letters 403, 27–36.

Hilton, R. G., Galy, A. & Hovius, N., 2008. Riverine particulate organic carbon from an active mountain belt: Importance of landslides. Global Biogeochemical Cycles 22.

Hilton, R. G., Galy, A., Hovius, N., Horng, M.-J. & Chen, H., 2011. Efficient transport of fossil organic carbon to the ocean by steep mountain rivers: An orogenic carbon sequestration mechanism. Geology 39, 71–74.

Hovius, N., Stark, C. P. & Allen, P. A., 1997. Sediment flux from a mountain belt derived by landslide mapping. Geology 25, 231–234.

Huh, Y., Birck, J. L. & Allegre, C. J., 2004. Osmiurn isotope geochemistry in the Mackenzie River basin. Earth and Planetary Science Letters 222, 115–129.

Immerzeel, W. W. & Bierkens, M. F. P., 2010. Seasonal prediction of monsoon rainfall in three Asian river basins: the importance of snow cover on the Tibetan Plateau. International Journal of Climatology 30, 1835–1842.

Jacobson, A. D. & Blum, J. D., 2003. Relationship between mechanical erosion and atmospheric CO_2 consumption in the New Zealand Southern Alps. Geology 31, 865–868.

Jacobson, A. D., Blum, J. D., Chamberlain, C. P., Craw, D. & Koons, P. O., 2003. Climatic and tectonic controls on chemical weathering in the New Zealand Southern Alps. Geochimica Et Cosmochimica Acta 67, 29–46.

Jaffe, L. A., Peucker-Ehrenbrink, B. & Petsch, S. T., 2002. Mobility of rhenium, platinum group elements and organic carbon during black shale weathering. Earth and Planetary Science Letters 198, 339–353.

Korup, O., 2004. Landslide-induced river channel avulsions in mountain catchments of southwest New Zealand. Geomorphology 63, 57–80.

Larsen, I. J., Almond, P. C., Eger, A., Stone, J. O., Montgomery, D. R. & Malcolm, B., 2014. Rapid Soil Production and Weathering in the Southern Alps, New Zealand. Science 343, 637–640.

Leithold, E. L., Blair, N. E. & Perkey, D. W., 2006. Geomorphologic controls on the age of particulate organic carbon from small mountainous and upland rivers. Global Biogeochemical Cycles 20.

Lewis, E., & Wallace, D. W. R., 1998. Program Developed for CO_2 System Calculations. ORNL/CDIAC-105.

Lyons, W. B., Carey, A. E., Hicks, D. M. & Nezat, C. A., 2005. Chemical weathering in high-sediment-yielding catchments, New Zealand. Journal of Geophysical Research-Earth Surface, 110.

Maher, K., 2011. The role of fluid residence time and topographic scales in determining chemical fluxes from landscapes. Earth and Planetary Science Letters 312, 48–58.

Maher, K. & Chamberlain, C. P., 2014. Hydrologic Regulation of Chemical Weathering and the Geologic Carbon Cycle. Science 343, 1502–1504.

Miller, C. A., Peucker-Ehrenbrink, B., Walker, B. D. & Marcantonio, F., 2011. Re-assessing the surface cycling of molybdenum and rhenium. Geochimica Et Cosmochimica Acta 75, 7146–7179.

Nibourel, L., Herman, F., Cox, S. C., Beyssac, O. & Lavé, J., 2015. Provenance analysis using Raman spectroscopy of carbonaceous material: A case study in the Southern Alps of New Zealand. Journal of Geophysical Research: Earth Surface 120, 2056–2079.

National Snow and Ice Data Center. 2016. World Glacier Inventory. http://nsidc.org/.

Petsch, S. T., 2014. Weathering of organic carbon, Elsevier.

Petsch, S. T., Berner, R. A. & Eglinton, T. I., 2000. A field study of the chemical weathering of ancient sedimentary organic matter. Organic Geochemistry 31, 475–487.

Petsch, S. T., Eglington, T. I. & Edwards, K. J., 2001. C-14-dead living biomass: Evidence for microbial assimilation of ancient organic carbon during share weathering. Science 292, 1127–1131.

Pierson-Wickmann, A.-C., Reisberg, L. & France-Lanord, C., 2002. Behavior of Re and Os during low-temperature alteration: Results from Himalayan soils and altered black shales. Geochimica et Cosmochimica Acta 66, 1539–1548.

Pierson-Wickmann, A. C., Reisberg, L. & France-Lanord, C., 2000. The Os isotopic composition of Himalayan river bedloads and bedrocks: importance of black shales. Earth and Planetary Science Letters 176, 203–218.

Reusser, L. J. & Biermann, P. R., 2010. Using meteoric 10Be to track fluvial sand through the Waipaoa River basin, New Zealand. Geology 38, 47–50.

Ryan, M. T., Newnham, R. M., Dunbar, G. B., Vandergoes, M. J., Rees, A. B. H., Neil, H., Callard, S. L., Alloway, B. V., Bostock, H., Hua, Q. & Anderson, B. M., 2016. Exploring the source-to-sink residence time of terrestrial pollen deposited offshore Westland, New Zealand. Review of Palaeobotany and Palynology 230, 37–46.

Selby, D. & Creaser, R. A., 2003. Re-Os geochronology of organic rich sediments: an evaluation of organic matter analysis methods. Chemical Geology 200, 225–240.

Stolper, D. A., Bender, M. L., Dreyfus, G. B., Yan, Y. & Higgins, J. A., 2016. A Pleistocene ice core record of atmospheric O_2 concentrations. Science 353, 1427–1430.

Tank, S. E., Raymond, P. A., Striegl, R. G., McClelland, J. W., Hoomes, R. M., Fiske, G. J. & Peterson, B. J., 2012. A land-to-ocean perspective on the magnitude, source and implication of DIC flux from major Arctic rivers to the Arctic Ocean. Global Biogeochemical Cycles 26.

Tipper, E. T., Bickle, M. J., Galy, A., West, A. J., Pomies, C. & Chapman, H. J., 2006. The short term climatic sensitivity of carbonate and silicate weathering fluxes: Insight from seasonal variations in river chemistry. Geochimica Et Cosmochimica Acta 70, 2737–2754.

Tippett, J. M. & Kamp, P. J. J., 1993. Fission-track analysus of the Late Cenozoic vertical kinematics of continental Pacific crust, South Island, New Zealand. Journal of Geophysical Research-Solid Earth 98, 16119–16148.

Torres, M. A., Moosdorf, N., Hartmann, J., Adkins, J. F. & West, A. J., 2017. Glacial weathering, sulfide oxidation, and global carbon cycle feedbacks. Proceedings of the National Academy of Sciences.

Tranter, M., Sharp, M. J., Lamb, H. R., Brown, G. H., Hubbard, B. P. & Willis, I. C., 2002. Geochemical weathering at the bed of Haut Glacier d'Arolla, Switzerland - a new model. Hydrological Processes 16, 959–993.

Wadham, J. L., Bottrell, S., Tranter, M. & Raiswell, R., 2004. Stable isotope evidence for microbial sulphate reduction at the bed of a polythermal high Arctic glacier. Earth and Planetary Science Letters 219, 341–355.

West, A. J., 2012. Thickness of the chemical weathering zone and implications for erosional and climatic drivers of weathering and for carbon-cycle feedbacks. Geology 40, 811–814.

Yeghicheyan, D., Bossy, C., Bouhnik LE Coz, M., Douchet, C., Granier, G., Heimburger, A., Lacan, F., Lanzanova, A., Rousseau, T. C. C., Seidel, J.-L., Tharaud, M., Candaudap, F., Chmeleff, J., Cloquet, C., Delpoux, S., Labatut, M., Losno, R., Pradoux, C., Sivry, Y. & Sonke, J. E., 2013. A Compilation of Silicon, Rare Earth Element and Twenty-One other Trace Element Concentrations in the Natural River Water Reference Material SLRS-5 (NRC-CNRC). Geostandards and Geoanalytical Research 37, 449–467.

Zachos, J., Pagani, M., Sloan, L., Thomas, E. & Billups, K., 2001. Trends, rhythms, and aberrations in global climate 65 Ma to present. Science 292, 686–693.

Chapter 4

Erosion and weathering drive net CO_2 drawdown in the Mackenzie River Basin over geological time

Mackenzie River at Tsiigetchic; June 2017 (Photo credit: Mathieu Dellinger)

Summary: Dissolved river rhenium fluxes constrain the rate of oxidative weathering of petrogenic organic carbon in the Mackenzie River Basin to be 0.4 tC km^{-2} yr^{-1}, yet the Mackenzie River catchment carbon budget remains a net carbon sink under the present climate state.

A version of this chapter will be submitted to Earth and Planetary Science Letters.

The paper will be co-authored by, Robert G. Hilton[1], Mathieu Dellinger[1], David Selby[2], Ed Tipper[3], Valier Galy[4], Jérôme Gaillardet[5], Damien Calmels[6], Chris J. Ottley[2] and Kevin W. Burton[2].

Affiliations: [1]Department of Geography, Durham University, Science Laboratories, South Road, Durham, DH1 3LE, UK
[2]Department of Earth Sciences, Durham University, Science Laboratories, South Road, Durham, DH1 3LE, UK
[3]Department of Earth Sciences, University of Cambridge, UK
[4]Woods Hole Oceanographic Institute, Woods Hole, USA
[5]Institute de Physique du Globe, Paris, France
[6]Université Paris-Sud, Orsay, France

Abstract

The exposure of organic carbon in rocks to oxidative weathering can release carbon dioxide (CO_2) to the atmosphere and consume atmospheric oxygen (O_2). Alongside volcanism, metamorphism, and the weathering of carbonate minerals by sulfuric acid, this is a major source of atmospheric CO_2 over million year timescales. The balance between CO_2 release during the oxidation of sedimentary rocks and CO_2 drawdown by silicate weathering, carbonate weathering, and organic carbon burial sets the net carbon budget during weathering and erosion. However, the rates of rock-derived organic carbon (petrogenic organic carbon, OC_{petro}) oxidation remain poorly constrained in river catchments. Here, we utilize the relationship between organic carbon and rhenium in rocks, and their behaviour during oxidative weathering, to quantify CO_2 release by OC_{petro} oxidation in the Mackenzie River Basin, Canada. We have measured the dissolved rhenium in river waters ($[Re]_{diss}$) and examined the Re and OC_{petro} content of erosion and weathering products in river sediments. Sampling took place between 2009 and 2013 and was focussed at gauging stations along the Mackenzie River and its main tributaries (Liard, Peel and Arctic Red), alongside tributaries of the Peel River. The data indicate that variations in $[Re]_{diss}$ at an individual location are relatively minor between sample years, but they do reveal a dilution trend with increasing water discharge in the Mackenzie River at Tsiigehtchic. The proportion of $[Re]_{diss}$ derived from OC_{petro}, is evaluated by dissolved [Re]/[Na] and [Re]/[SO_4] ratios alongside compiled measurements from silicate, sulfide and OC_{petro} phases. This approach suggests that >85% of the $[Re]_{diss}$ is derived from OC_{petro} in the main river channels. Using the $[Re]_{diss}$ flux, we estimate that the modern-day CO_2 emission driven by OC_{petro} weathering is 0.38 $^{+0.10}/_{-0.09}$ tC km^{-2} yr^{-1} for the Mackenzie River at Tsiigehtchic, and 0.79 $^{+0.23}/_{-0.19}$ tC km^{-2} yr^{-1} , 0.66 $^{+0.19}/_{-0.16}$ tC km^{-2} yr^{-1} and 0.84 $^{+0.23}/_{-0.20}$ tC km^{-2} yr^{-1} for the Peel, Arctic Red and Liard catchments, respectively. When combined with the silicate and carbonate weathering rates and the sedimentary burial of biospheric organic carbon constrained by prior work, these data suggest that the upper part of the Mackenzie River Basin presently acts as a CO_2 sink of ~1.2 tC km^{-2} yr^{-1} as a result of the carbon transfers by weathering and erosion.

4.1 Introduction

Erosion and weathering transfer carbon between the atmosphere and lithospheric storage on geological timescales (10^4–10^6 years). The net carbon balance between carbon dioxide (CO_2) sequestration, occurring through silicate weathering by carbonic acid coupled to carbonate precipitation (Ebelmen, 1845; Gaillardet et al., 1999) and the burial of biospheric organic carbon (Berner, 1982; FranceLanord and Derry, 1997), versus CO_2 release during volcanism (Marty and Tolstikhin, 1998), carbonate weathering by sulphuric acid (Calmels et al., 2007; Torres et al., 2014) and the oxidation of rock-derived organic carbon (Petsch, 2014), governs atmospheric CO_2 concentrations (Berner and Caldeira, 1997). The organic carbon and sulphur cycles also set atmospheric O_2 concentrations over geological timescales (Berner and Canfield, 1989; Bolton et

al., 2006). Although the chemical denudation of silicate rocks has been studied in detail (e.g. Berner and Maasch, 1996; Gaillardet et al., 1999; Walker et al., 1981), the field-based quantification of oxidative weathering of rock-derived organic carbon (petrogenic OC, OC_{petro}) remains limited to mountain river catchments in Taiwan (Hilton et al., 2014) and New Zealand (***Chapter 3***, Horan et al., 2017), the floodplains of the Beni River in the Amazon Basin (Bouchez et al., 2014, 2010) and the Ganges and Yamuna Rivers (Dalai et al., 2002; Galy et al., 2008a). Nonetheless, the global CO_2 emissions from OC_{petro} oxidation are estimated to be 40–100 Mt C yr^{-1} (Petsch, 2014), which is similar to the CO_2 drawdown by chemical weathering of silicate minerals by carbonic acid (Gaillardet et al., 1999; Moon et al., 2014). Better quantification of these CO_2 sources is necessary to assess the geological carbon budgets during weathering and erosion, and to evaluate how long-term changes in tectonics and climate influence atmospheric CO_2 (Pagani et al., 2009).

Mountain river catchments are thought to be important sites for oxidative weathering (Calmels et al., 2007; Hilton et al., 2014) because high rates of physical erosion, typically in the order of 10^3–10^4 t km^{-2} yr^{-1}, can rapidly supply OC_{petro} and sulphides (e.g. pyrite) to oxic surface waters and the atmosphere. They are also important locations where climate-weathering feedbacks operate because reactions are not supply limited (Maher and Chamberlain, 2014; West, 2012; West et al., 2005). When sedimentary rocks are exposed at the Earth's surface in mountain belts, the CO_2 released during weathering and erosion can be large (Hilton et al., 2014; Torres et al., 2016), and may negate the CO_2 sinks by silicate weathering and the burial of recently fixed organic carbon (Horan et al., 2017; Torres et al., 2014). Other features of mountainous topography may result in enhanced rates of OC_{petro} oxidation, including orographic precipitation, high rates of soil formation (Larsen et al., 2014), bedrock landsliding (Emberson et al., 2016), and the combination of glacial and periglacial processes at higher elevations (Horan et al., 2017).

Here, we quantify carbon fluxes during weathering and erosion in the Mackenzie River Basin, north west Canada, which is a major supplier of water, sediment and carbon from land to sea (Carson et al., 1998; Hilton et al., 2015; Holmes et al., 2002; Macdonald et al., 1998; McClelland et al., 2016; Millot et al., 2003). The basin is dominated by Palaeozoic sedimentary rocks (Millot et al., 2003) and previous work has quantified CO_2 drawdown by the erosion and marine burial of biospheric OC (Hilton et al., 2015), silicate weathering (Gaillardet et al., 1999; Millot et al., 2003) and the transient flux of CO_2 released during weathering of carbonate minerals by sulfuric acid (Calmels et al., 2007). In addition to providing a type example of a sedimentary-rock dominated basin (Dellinger et al., 2014), the Mackenzie River allows us to evaluate OC erosion and weathering in Arctic environments, complementing findings of previous studies that focused on

catchments at lower latitudes (Bouchez et al., 2010; Galy et al., 2008a; Hilton et al., 2014; Horan et al., 2017).

To track chemical weathering, we assess the products of chemical reactions in the dissolved load of rivers (Gaillardet et al., 1999; Jacobson et al., 2003; Meybeck, 1987; West et al., 2005). To evaluate the oxidative weathering of OC_{petro} over the river catchment scale, we measure dissolved rhenium (Re) concentrations at multiple sites along the Mackenzie River and its tributaries. Rhenium is considered to be a suitable proxy for determining OC_{petro} oxidation because it is found in close association with OC_{petro} in sedimentary rocks (Selby and Creaser, 2003). When rocks are exposed to chemical weathering, soils developed on OC-rich rocks indicate that Re loss tracks the OC_{petro} loss (Jaffe et al., 2002; Pierson-Wickmann et al., 2002). Similar observations have been made in rocks with lower OC_{petro} contents in active mountain belts (Hilton et al., 2014; Horan et al., 2017). Rhenium becomes soluble upon oxidation (Colodner et al., 1993a) and it is possible to track oxidative weathering by measuring this element in the dissolved load of rivers (Dalai et al., 2002). River networks integrate hydrological sources and chemical reaction products, providing a landscape-scale perspective of weathering processes and fluxes (Gaillardet et al., 1999; Maher and Chamberlain, 2014). If both the dissolved Re flux and the content of Re and OC_{petro} in the rocks undergoing weathering are known, it is possible to quantify the absolute rate of OC_{petro} oxidation (Hilton et al., 2014). Uncertainties in the use of the Re proxy include the possibility that phases other than OC_{petro}, including sulfides and silicate minerals, may supply Re to the dissolved load during weathering (Colodner et al., 1993a; Dalai et al., 2002). Therefore, we assess the relative input of Re from different sources using elemental ratios from dissolved weathering products and solid phases to better constrain the CO_2 release during OC_{petro} oxidation. The CO_2 budgets we calculate bear implication for atmospheric CO_2 concentrations and global climate over geological timescales.

4.2 Materials and methods

4.2.1 Setting

The Mackenzie River Basin (Figure 4.1) spans an upstream area of 1.78×10^6 km^2 at the river delta and is the largest point source of sediment to the Arctic Ocean (Holmes et al., 2002), organic carbon in particulate form (Hilton et al., 2015) and the second largest input of dissolved solids (Calmels et al., 2007). It drains the Rocky and Mackenzie Mountains in north west Canada. From west to east, the Rockies, the interior platform (plains), and the Canadian Shield, which are composed of Precambrian granitic basement, define the basin (Reeder et al., 1972). The basin geology comprises 68.3% sedimentary rocks (Palaeozoic clastics and carbonates) including the carbonate platform in the central part, the carbonaceous shales of the interior plain and the Rockies,

which are mainly composed of carbonate, dolomitic limestone and shale (Wheeler et al., 1996). The sedimentary rocks host organic carbon, with OC_{petro} concentrations inferred from the radiocarbon content of river bed material samples that are typically between 0.1–0.3 wt. %, but are higher (0.6 wt. %) in the Peel catchment (Hilton et al., 2015). Approximately one-third (29.2%) of the basin drains non-sedimentary rocks, including granitic rock outcropping in the Rockies and 2.5% of evaporate units in the plains (Beaulieu et al., 2011; Millot et al., 2003).

Weathering of sedimentary rocks dominates the dissolved ion loads in the Mackenzie River (Calmels et al., 2007; Millot et al., 2002) with 38% of the HCO_3^- flux derived from silicate weathering, and 62% from carbonate weathering (Calmels et al., 2007). Of the carbonate weathering HCO_3^- flux, 15% is derived from carbonic acid-driven weathering and 85% from sulphuric acid (via sulphide oxidation) driven weathering (Calmels et al., 2007). For the Mackenzie River at Tsiigehtchic (1,680,000 km^2), the associated CO_2 drawdown by silicate weathering is estimated to be 3.63×10^4 mol km^{-2} yr^{-1} (Gaillardet et al., 1999) or 0.44 t C km^{-2} yr^{-1}. The carbonate weathering rate reported by Gaillardet et al. (1999) was a CO_2 drawdown of 14.4×10^4 mol yr^{-1}, or 1.73 t C km^{-2} yr^{-1}, assuming weathering by carbonic acid. However, subsequent work has shown a large proportion of this flux derives from weathering of carbonate by sulfuric acid (Calmels et al., 2007), with a release of 6.2×10^4 mol km^{-2} yr^{-1}, or 0.74 t C km^{-2} yr^{-1} (Torres et al., 2014). The modern day erosion and export of biospheric organic carbon eroded from soils and vegetation ($OC_{biosphere}$) has been estimated for the upper part of the basin draining north of the Great Slave Lake, which acts as a sediment trap for particulates eroded from upstream (Carson et al., 1998). Over this 774,200 km^2 area, the erosion of $OC_{biosphere}$ is estimated to be $2.9\ ^{+1.7}/_{-1.1}$ t C km^{-2} yr^{-1} at the Delta head (Hilton et al., 2015) with a burial efficiency of >65% in the Beaufort Sea (Hilton et al., 2015; Vonk et al., 2015). An additional flux of OC_{petro} in the solid load, which has not been oxidised, is $0.6\ ^{+0.2}/_{-0.2}$ t C km^{-2} yr^{-1} (Hilton et al., 2015).

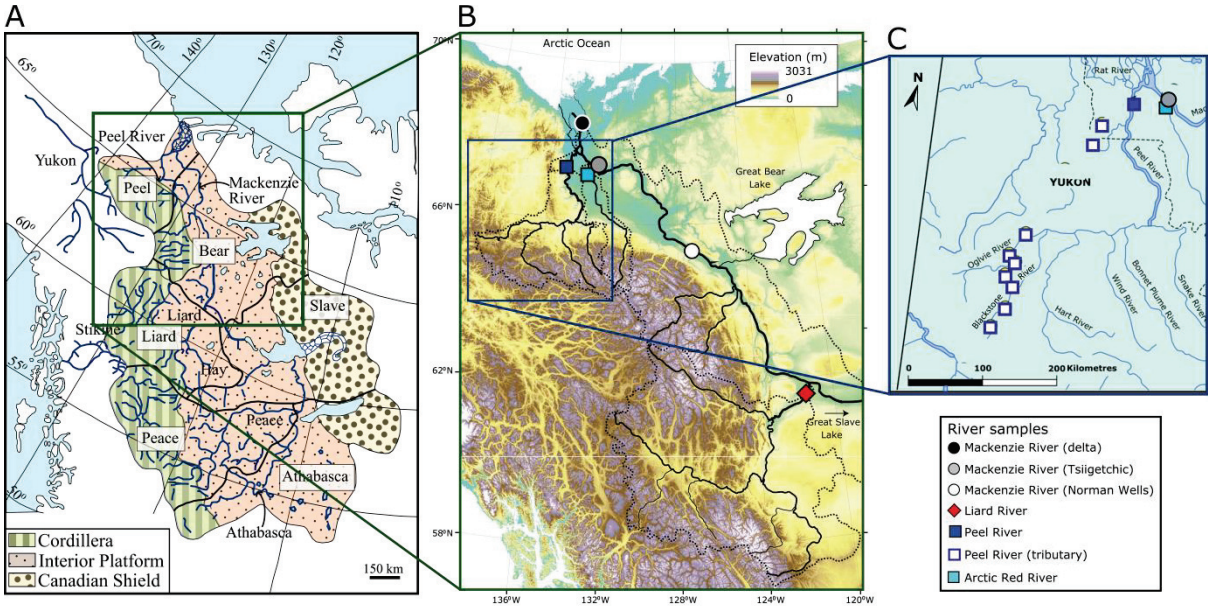

Figure 4.1 The Mackenzie River Basin. A. Main lithological sub-divisions (Cordillera, Interior Platform and Canadian Shield) and the major sub-basins (Peel, Bear, Liard, Slave, Peace and Athabasca) of the Mackenzie River Basin (modified from Millot et al., 2003). **B.** Location of river sampling within the Mackenzie River Basin (modified from Hilton et al., 2015). **C.** Inset of the Peel catchment showing the tributaries of the Peel sampled in 2013.

4.2.2 Samples

River samples were collected in July 2009, September 2010, May/June 2011 and July 2013. They capture periods of high stage and falling stage, when the majority of water and sediment is exported by the Mackenzie River; as outlined in Hilton et al. (2015). Three locations on the main channel of the Mackenzie River were sampled: the Environment Canada gauging stations at Tsiigehtchic (2009–2011, 2013), the Middle Delta (2010, 2011, 2013) and the main stem at Norman Wells (2010). The main tributaries upstream of the Great Slave Lake, which is an effective sediment trap for materials entering from the lower latitude Rockies (Carson et al., 1998), were sampled: these include the Liard (2009–2011), the Peel (2009–2011, 2013) and the Arctic Red (2009–2011, 2013) rivers. In addition, tributaries of the Peel River (including the Ogilvie and Blackstone rivers) were sampled in 2013.

Sample materials include the dissolved products of chemical weathering and the solid products of weathering and erosion carried in suspended load and by river bed materials. River sediment depth-profiles were collected at the main sampling locations to allow the full range of erosion products from these large river systems to be assessed (Bouchez et al., 2014, 2011; Dellinger et al., 2014; Galy et al., 2008b; Hilton et al., 2015; Lupker et al., 2011). These depth profiles take advantage of the hydro-dynamic sorting of particles, with a dominant recovery of quartz-rich sediment at the base of the profile, and more clay-rich sediments closer to the surface (Dellinger et al., 2014; Hilton et al., 2015). In addition, channel depth, water velocity and instantaneous water discharge

were measured by two or more transects at each sampling site (Figure 4.1), using an Acoustic Doppler Current Profiler (ADCP Rio Grande 600 kHz). At the major sampling sites, each depth profile was collected at a point where flow velocity and acoustic backscatter contrasts suggest hydrodynamic sorting. Each water sample (7–8 litres) was transferred into a clean bucket and stored in sterilized plastic bags. In the upper Peel River tributaries, depth sampling was not possible and surface suspended sediments were collected. Each bag was first weighed to determine the sampled volume, before being filtered within 24 h using pre-cleaned filter units through 0.2 μm polyethersulfone (PES) filters and stored in acid-cleaned LDPE bottles (Hilton et al., 2015). All water samples intended for cation and Re analysis were acidified in the field to pH ~2 following published methods (Dalai et al., 2002; Hilton et al., 2014) and an un-acidified aliquot was kept for anion analyses. River alkalinity was determined shortly after filtration by Gran Titration on an aliquot of filtered water. Suspended sediment was immediately rinsed from the filters using filtered river water and transferred into clean amber-glass vials.

To help constrain the composition of the least weathered portion of the river load, river bed materials were collected at the base of the depth transects from a boat, using a metal bucket as a dredge, and decanted to a sterile bag (Dellinger et al., 2014; Hilton et al., 2015). In addition, river bank deposits (June 2009 and 2013) were collected from fresh material close to the channel. All sediments were freeze-dried upon return to laboratories within two weeks, weighed and powdered in an agate mill.

4.2.3 Rhenium concentration

Dissolved Re concentrations in the river water samples, $[Re]_{diss}$, were measured by isotope dilution. A tracer solution enriched in ^{185}Re was added to 30–100 mL of the water at a volume that would achieve a spike:sample mix ratio between 1.5 and 2.5. The spiked sample was evaporated to dryness. Anion-exchange column chemistry was then used to pre-concentrate the Re and to remove sample matrix. In brief, the sample was loaded onto 0.5 mL of AG1-X8 (200–400 mesh) Eichrom resin in 0.2 M HNO_3, rinsed with 3 mL of 0.2M HNO_3, washed with 2 mL of 0.2M HCl and eluted to cleaned PMP beakers in 2.5 mL 6M HNO_3. The purified eluted residues were analysed by quadrupole inductively-coupled-plasma mass spectrometry (Thermo Scientific X-Series Q-ICP-MS) in 0.8M HNO_3. The measured difference in $^{185}Re/^{187}Re$ values for the Re standard solution and the accepted $^{185}Re/^{187}Re$ value (0.5974: Gramlich et al., 1973) was used for mass fractionation correction of the Re sample data. All data were blank corrected. The full procedural blank was 1.35 ± 0.56 pg (±1 SD, n = 5), which is less than 0.5% of the typical sample mass of Re and similar to published methods (Dalai et al., 2002; Meisel and Moser, 2004). Uncertainties in the determined Re abundance were calculated by full error propagation of uncertainties in Re mass spectrometer measurements, blank abundance and isotope compositions, spike calibrations and reproducibility of

standard Re isotope values. Analysis of $[Re]_{diss}$ in a river water standard, SLRS-5, produced a value of 59.8 ± 1.7 pg g^{-1} (n = 12, ±2 SE), in agreement with the previously reported value of 66 ± 12 pg g^{-1} (Yeghicheyan et al., 2013).

For Re concentration measurement in sediments, solid samples were first crushed into fine powders using a zirconium disc mill to achieve an integrated bulk sample. Next, approximately 0.05 g of each bedload and suspended load sample was doped with a known amount of the ^{185}Re tracer solution and digested in a 6:3 concentrated HF-HNO_3 mix (9 mL) for 24 hours at 120ºC and then evaporated. The dried sample was further digested in a 2:1 mix of concentrated HNO_3-HCl (3 mL) for 24 h at 120ºC, and then evaporated to dryness. The rhenium was isolated and purified using a NaOH-acetone solvent extraction methodology (Cumming et al., 2013). The Re isotope composition of the purified Re aliquots were then determined in a 0.8M HNO_3 medium using a Thermo Scientific X-Series Q-ICP-MS. As for the water analyses, all data were corrected for mass fractionation and blank contributions.

Blanks from the digestion protocol ranged from 1–80 pg g^{-1} (n = 19), with typical values between 2 and 8 pg g^{-1} (n = 16); this equates to <0.2% of a typical sample concentration (~3000 pg g^{-1}). Where blanks were high, full-analysis replicates produced data in agreement to within 5%, confirming that these blanks were representative of the analysis but had minimal effect on data accuracy. Bush Creek (SBC-1) and SCO-1 standards are used for determining trace element abundance, and may be used as a research material for Re. The Re concentration in the Bush Creek standard was quantified to be 10,090 ± 82 pg g^{-1} (±2 SE, n = 6) and the Re concentration in the SCO-1 standard is 1085 ± 55 pg g^{-1} (±2 SE, n = 6). These values are in agreement with published data on SCO-1 (1050 pg g^{-1}: Meisel and Moser, 2004) and the long-term in-house reproducibility of the Bush Creek standard by Cr-H_2SO_4 dissolution and Negative Thermal Ionisation Mass Spectrometry (N-TIMS) analysis (10,331.9 ± 236.9 pg g^{-1}, n = 25, ±1 SD) (Selby and Creaser, 2003).

4.2.4 Major ion and elemental concentrations

Major ion concentrations in water samples were analysed by Ion Chromatography. Cation and anion standards and a certified reference standard (Lethbridge-03) were run to validate the analytical results. Major and trace element (other than Re) concentrations in the river sediment samples were measured, respectively, by ICP-AES and ICP-MS at the SARM (Service d'Analyse des Roches et des Minéraux, INSU facility, Vandoeuvre-les-Nancy, France). In river bed materials and suspended load sediments, the organic carbon concentration ([OC], %) was measured following a 0.2M HCl leach protocol (Galy et al., 2007), which was tested on samples from this location to ensure full removal of detrital carbonates. Aliquots of samples were combusted and the

concentration and stable isotope composition of OC ($\delta^{13}C$, ‰) was determined using a Costech elemental analyser coupled to a Thermo Scientific Delta V Advantage isotope ratio mass spectrometer (EA-IRMS). Corrections for procedural and instrumental blanks were applied and the result normalized to the composition of international standards (reported relative to the VPDB, with a precision of 0.2‰).

4.2.5 Additional data

This study takes advantage of published data on particulate organic carbon (POC), including the organic carbon (OC) percentage, $\delta^{13}C$, and the radiocarbon activity, reported as Fraction Modern (F_{mod}), from suspended sediment and river bed material samples collected in 2010 and 2011 (Hilton et al., 2015). The major ion chemistry of the samples collected between 2009 and 2011 has been described previously (Dellinger, 2013) and supplements our major ion analyses on the dissolved load of the 2013 samples.

4.3 Results

4.3.1 Bulk weathering characteristics

To deduce oxidative weathering reactions in the context of bulk chemical weathering variability, the concentrations of major ions in the dissolved load and sediments of the rivers were studied (Table 4.1). Concentrations of Ca^{2+}, Mg^{2+}, Na^{+}, and SO_4^{2-} are helpful for characterizing the overall weathering processes (Gaillardet et al., 1999) and we use mixing diagrams with Na normalised molar ratios in order to evaluate the main lithologies that are being weathered (Figure 4.2). Following Millot et al. (2003), all Na data has been corrected for any cyclic input of ocean-derived Na input by precipitation, based on the conservative behaviour of chlorine, and is given as Na*; where [Na]* = [Na] - 0.85[Cl].

Overall, data from the dissolved phase of the main river channels indicate that this basin is characterized by sedimentary silicate rocks hosting trace carbonate minerals. The major ion chemistry of the 2009–2011 dissolved load samples (Dellinger, 2013) correlates closely with the major ion data from the 2013 dissolved load samples and previous measurements from the Mackenzie River Basin (Millot et al., 2003). Similarities in these data suggest that broad spatial patterns in dissolved ion compositions are maintained, although there may be potential for seasonal and flood-event scale variability. Rivers that have low Na normalised ratios ($[HCO_3^-]$/[Na*], [Mg]/[Na*] and [Ca]/[Na*]) reflect waters draining predominantly silicate rocks, and this is true of the main channel of the Mackenzie River, sampled at Tsiigetchic and the delta. Some spatial variability is apparent across the Mackenzie River Basin, however, and tributaries feeding the Peel River show a wide range in chemical composition. The samples from the Engineer Creek and Rock

River tributaries have high [Ca]/[Na*], $[HCO_3^-]$/[Na] and [Mg]/[Na*], suggesting that carbonate weathering is important in these catchments. Sulfate concentrations are also elevated in all of the Peel tributaries (Mean $[SO_4^{2-}]$ = 1691 ± 454 μmol L^{-1} (n = 11, ±2 SE), relative to the main channel Mackenzie (Mean $[SO_4^{2-}]$ = 396 ± 74 μmol L^{-1} (n = 4, ±2 SE). The oxidative weathering of sulfide minerals generates sulfuric acid that can subsequently weather carbonate minerals and has been shown previously in the basin (Calmels et al., 2007). The high reaction kinetics of sulfide oxidation and carbonate weathering, compared with silicate weathering, can help to explain the relative enrichment in Ca, Mg and HCO_3^- in the Peel River catchment.

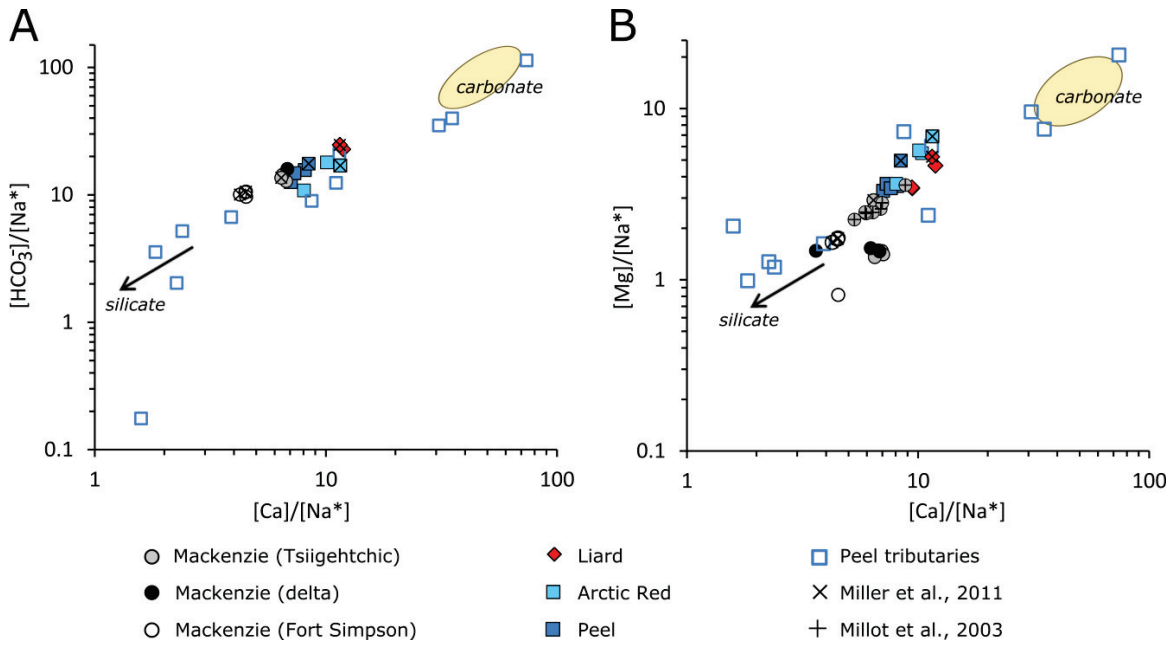

Figure 4.2 Bulk weathering characteristics in the Mackenzie River Basin revealed by major dissolved ion ratios. The ion ratios of sites in the Mackenzie River Basin sampled in 2009-2013 are shown, with main stem sites as circles (Mackenzie River at the delta – black circles, Tsiigehtchic – grey circles and Fort Simpson – white circle) and large tributaries (Peel – dark blue squares; Arctic Red – light blue squares; Liard – diamonds). Open blue squares are smaller tributaries of the Peel sampled in 2013. Published data are marked by X (Millot et al., 2003) or + (Miller et al., 2011) for **A.** $[HCO_3^-]$/[Na*] versus [Ca]/[Na*] and **B.** [Mg]/[Na*] versus [Ca]/[Na*]. Na* is Na corrected for the cyclic Na component. Units are mol:mol. The relative positions of silicate and carbonate endmembers is indicated (Gaillardet et al., 1999). Note the consistency between the new and published data.

4.3.2 Dissolved rhenium

The concentrations of dissolved Re, $[Re]_{diss}$, in the Mackenzie River Basin range from 1.46–85.7 pmol L^{-1} across the sample set (Table 4.1), but there is much less variability at a given sample location. In the main stem of the Mackenzie River at Tsiigetchic, the mean $[Re]_{diss}$ = 16.3 ± 1.1 pmol L^{-1} (n = 4, ±2 SE) and at the delta, the mean $[Re]_{diss}$ = 17.5 ± 2.7 pmol L^{-1} (n = 3, ±2 SE). At Norman Wells, only one sample is available, with $[Re]_{diss}$ = 11.5 pmol L^{-1} (± 0.69%, ±2 SE analytical uncertainty). The Liard, Peel and Arctic Red catchments have slightly higher mean $[Re]_{diss}$ concentrations. These are 21.9 ± 2.7 pmol L^{-1} (n = 3, ±2 SE) for the Liard River, 19.0 ± 4.8 pmol L^{-1} (n = 4, ±2 SE) in the Peel River and 18.2 ± 4.9 (n = 3, ±2 SE) in the Arctic Red River.

The greatest variation in $[Re]_{diss}$ is observed in the tributaries feeding the Peel River. Engineer Creek has a mean $[Re]_{diss}$ of 85.7 ± 14.4 pmol L^{-1} (n = 3, ±2 SE), which is the highest concentration measured across the Mackenzie River Basin. In contrast, a tributary to the Peel River (sampled at 67.13862ºN, 136.00302ºW) has the lowest measured $[Re]_{diss}$ in the basin, at just 1.46 pmol L^{-1} (±1.3%, ±2 SE analytical uncertainty). $[Re]_{diss}$ values for the Mackenzie River Basin fall towards the more concentrated end of published data from global rivers (4.7 ± 0.2 pmol L^{-1} to 25.4 ± 1.2 pmol L^{-1}: Colodner et al., 1993b; Dalai et al., 2002; Hilton et al., 2014; Miller et al., 2011; Rahaman et al., 2012).

To understand the distribution in $[Re]_{diss}$, we examine dissolved ion ratios to assess the source of Re (Dalai et al,. 2002). Dissolved Re concentrations show a broad positive correlation with the sum of dissolved ∑cations (Supplementary Figure 4.1), where ∑Cations = [Na]* + [K] + [Ca] + [Mg] (r^2 = 0.6). This provides an indication that both Re and major cations are released to the rivers in roughly the same proportion throughout the basin during chemical weathering. However, considering that the Mackenzie and its tributaries drain different sub-basins with their own characteristic lithologies, some scatter is expected.

4.3.3 Dissolved rhenium flux

Catchment hydrographs for the Peel and Mackenzie Rivers show that water discharge, Q_w m^3 s^{-1}, peaks in May following ice break up (Figure 4.3A and 4.3B) and the samples collected here cover a range in Q_w. Our new data and published data (Miller et al., 2011) from the Mackenzie River Tsiigehtchic show that $[Re]_{diss}$ is reduced with increasing water discharge (Q_w) (Figure 4.3C). A constant weathering input of Re would be diluted if there is an increase in runoff derived from precipitation, with waters entering the river from more rapid hydrological pathways with lower residence times in the weathering zone at higher Q_w (Maher, 2011; Tipper et al., 2006). At Tsiigehtchic, the relationship between $[Re]_{diss}$ and Q_w is well described by a power law function (r^2 = 0.7), where $[Re] = 32.2Q_w^{-0.075}$. This relationship can be used to estimate $[Re]_{diss}$ from gauged measurements of daily discharge from the Mackenzie River (Environment Canada data, accessed online, 10/05/17). Weathering fluxes are calculated as the product of discharge and element concentration, and we use the predictions of Re abundance to estimate total annual dissolved Re flux over the time period 2009–2013. This method predicts that the dissolved Re fluxes are similar between 2009 and 2013; varying from 4637–5309 mol yr^{-1}.

For the Liard and Arctic Red rivers, we do not have enough data at low Q_w to define a relationship between Q_w and $[Re]_{diss}$ and to calculate dissolved Re fluxes by this method. For these stations, we can estimate dissolved Re flux using long-term average annual Q_w and the mean measured $[Re]_{diss}$. To constrain the error associated with estimates of Re flux derived from average annual discharge

calculated over the years 2009–2013 and the average $[Re]_{diss}$ versus the Re flux calculated by the modelled power-law relationship, we assess the discrepancy between these results for the Mackenzie River at Tsiigehtchic. The approaches agree to within 10%, suggesting that an average method provides a reasonably accurate reflection of the dissolved Re flux through time in this catchment (Supplementary Figure 4.2A).

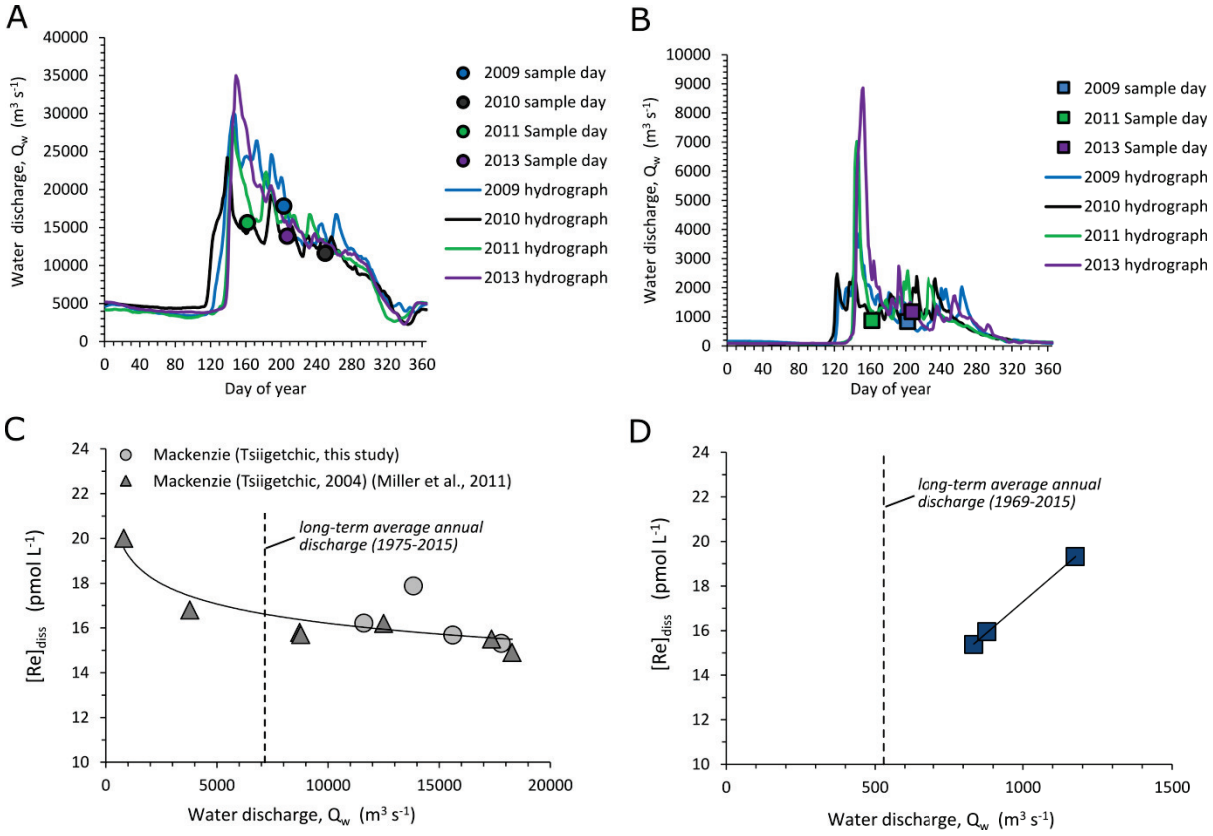

Figure 4.3 Relationship of dissolved Re concentration ($[Re]_{diss}$) with water discharge, Q_w (m^3 s^{-1}). A. Hydrographs for the Mackenzie River at Tsiigehtchic over the sampling years 2009, 2010, 2011 and 2013. Water discharge (m^3 s^{-1}) at the time of sampling (ADCP measurement) in each year is indicated by the circles. **B.** As part A. but for the Peel River from 2009, 2011 and 2013. **C.** $[Re]_{diss}$ versus water discharge in the Mackenzie River indicating a dilution trend. Grey triangles are data collected by Miller et al. (2011) on samples from the Mackenzie River sampled in March, June, July and August 2004. Samples from this study were collected in July 2009, September 2010, June 2011 and July 2013. The long-term average annual discharge (1972–2015) is shown by the vertical dashed line. The trend line is a power law (r^2 = 0.7). **D.** As part C. but for the Peel River. The trend line fitted is linear (r^2 = 1.00). The long-term average annual discharge (1969–2015) is shown by the vertical dashed line.

The $[Re]_{diss}$ data from the Peel suggest a positive linear relationship with water discharge (Figure 4.3D). This could reflect the fast reaction kinetics of the OC_{petro} oxidation (Chang and Berner, 1999), which can keep pace with the short contact time between surface runoff and rocks at high discharges. Alternatively, it could reflect groundwater concentrated in solutes and Re being flushed out at high discharges. In part, the difference between the Mackenzie and Peel catchments may be a reflection of catchment area: the Peel River drains 70,600 km^2; compared with 1,680,000 km^2 drained by the Mackenzie. As a result, $[Re]_{diss}$ may be more sensitive to changes in discharge in the

Peel River because it is not buffered across a wide catchment area. It is possible that $[Re]_{diss}$ may follow a power law relationship at the lower Q_w in the Peel River or be relatively chemostatic (Maher, 2011), although the available data do not constrain this (Figure 4.3D). To be consistent, we report dissolved Re fluxes for all catchments as calculated using an average annual Q_w and the average $[Re]_{diss}$ from our measurements.

4.3.4 River bed materials and suspended sediments

The rhenium concentrations in river sediments from across the basin are assessed to understand the nature of the source material and the extent of weathering (Table 4.2). We also measured the organic carbon content of river sediments to characterize the association between organic carbon and Re and their behaviours during river transit of the solid phase. Radiocarbon measurements allow us to quantify the contribution of OC_{petro} versus biospheric OC in river sediments (Hilton et al., 2015) and can be used to establish the [Re]/[OC] of the source rocks.

To the south of the basin, in the Liard catchment, the Re concentration in river bed materials, $[Re]_{BM}$, is 1405 pg g^{-1} and 862 pg g^{-1}, which is similar to published data: 1932 pg g^{-1} (Huh et al., 2004). The $[Re]_{BM}$ in the main channel of the Mackenzie River at Tsiigetchic is 740 pg g^{-1} and 747 pg g^{-1}. Concentrations downstream at the Mackenzie delta are more than double this at 2020 ± 591 pg g^{-1} (n = 5, ±2 SE). The higher concentrations in the delta coincide with the additional contribution of sediments from the Peel and Arctic Red catchments (Carson et al., 1999; Carson et al., 1998). Huh et al. (2004) find a $[Re]_{BM}$ = 5019 pg g^{-1} in the Arctic Red and $[Re]_{BM}$ = 3922 pg g^{-1} in the Peel. Here, in the Arctic Red catchment we measure $[Re]_{BM}$ of 3380 pg g^{-1} and 4099 pg g^{-1}, and in the Peel mainstem the mean $[Re]_{BM}$ = 4473 ± 1842 pg g^{-1} (n = 4, ±2 SE). Much greater variability in $[Re]_{BM}$ is found in the tributaries feeding the Peel River, where $[Re]_{BM}$ varies from 1050 pg g^{-1} in the West Blackstone River to 321,459 pg g^{-1} in the Ogilvie River.

In the main channels, the Re concentration in the suspended particulate matter, $[Re]_{SPM}$, ranges from 1805 pg g^{-1} (Mackenzie River at delta) to 7214 pg g^{-1} (Arctic Red). On a per catchment basis, the mean $[Re]_{SPM}$ is low in the Liard (2613 ± 295 pg g^{-1}: n = 4, ±2 SE) and the Mackenzie River at Tsiigetchic (2368 ± 360 pg g^{-1}: n = 5, ±2 SE) and the delta (2708 ± 531 pg g^{-1}: n = 6, ±2 SE) compared with the Arctic Red (7180 ± 70 pg g^{-1}: n = 2, ±2 SE) and Peel rivers (4167 ± 700 pg g^{-1}: n = 4, ±2 SE). The patterns in Re abundance suggest that the Re composition of the suspended material tracks that of the bedload.

To assess the patterns of Re abundance in the river sediments, across both suspended load sorted with water depth and the river bed materials, we examine the [Al]/[Si] ratio (Figure 4.4), which is correlated with the medium grain size (Dellinger, 2013) and thus is a proxy for grain size in this

basin (Dellinger, 2013; Dellinger et al., 2014). River bed materials have the lowest [Al]/[Si] ratios, while suspended sediments possess higher [Al]/[Si] ratios. In general, the decrease in [Al]/[Si] reflects a greater contribution of quartz and a coarsening of the river sediments (increase in the size of the 50th and 90th percentile of the grain size distributions). It is also informative to normalize the [Re] to the aluminium concentration, [Al], as this ratio provides an indication of the extent of [Re] dilution by quartz, carbonate and organic matter (Bouchez et al., 2012; Dellinger et al., 2014). In addition, aluminium is generally considered to be immobile, so it remains in weathering residues and can offer some insight into whether Re has been lost from the solid load during weathering (Bouchez et al., 2012). Alongside Re, Na is established as one of the most mobile elements during chemical weathering (Gaillardet et al., 2003), however it is largely sourced from inorganic minerals, mainly feldspars (Priyadarshi, 2005). It should rarely be incorporated into secondary weathering products and its distribution in the river SPM should be carried by the least weathered mineral phases (Dellinger et al., 2014). We therefore plot [Na]/[Al] against [Al]/[Si] to help evaluate the behaviour of Re in the context of the behaviour of another mobile element, but one sourced from dominantly inorganic phases. The river sediments define a hyperbolic relation between [Na]/[Al] and [Al]/[Si], with data from the Mackenzie and Liard Rivers described by a mixing hyperbola, which is distinct to the Peel and Arctic Red rivers. In contrast, [Re]/[Al] does not show this distribution with [Al]/[Si], suggesting a very different behaviour in the water column as a function of grainsize (Figure 4.4).

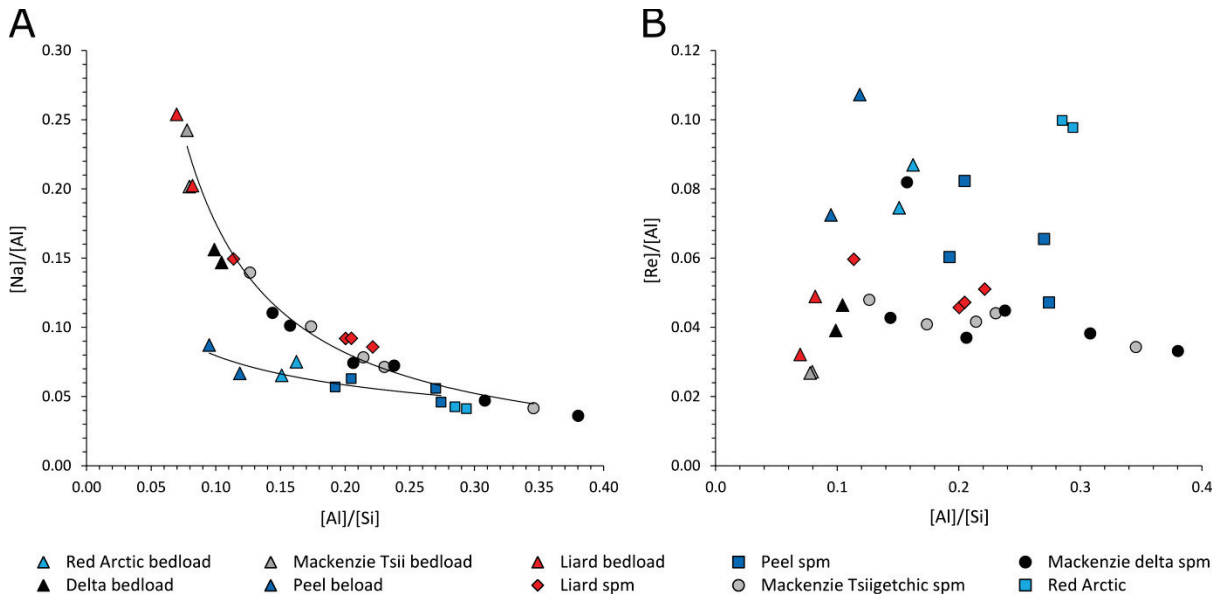

Figure 4.4 Composition of river sediments (suspended load and river bed materials) as a function of [Al]/[Si] ratio. A. [Na]/[Al] ratios are negatively correlated with [Al]/[Si], which is a proxy for grain size (Dellinger, 2013). The Liard River and main Mackenzie River show similar behaviour, described by a power law (black line), similar to that observed in other large river basins (Bouchez et al., 2011).The Peel and Arctic Red rivers have lower [Na]/[Al] in the coarsest components. **B.** [Re]/[Al] ratios are not well correlated with grain size for the same catchments, indicating that Re is not sorted in the water column. This is true of all catchments. Uncertainties are smaller than the symbol size.

The total organic carbon concentration, [OC], of river bed material samples, $[OC]_{BM}$, in the Mackenzie, Liard and Peel catchments has been quantified previously (Hilton et al., 2015). The Mackenzie and Liard have similar values of $[OC]_{BM}$ at 0.16% and 0.14%, respectively, while the Peel has a higher $[OC]_{BM}$ = 0.75%. River suspended load samples are also similar in terms of their $[OC]_{SPM}$ in the Liard and Mackenzie catchments. We combine data from Hilton et al. (2015) with our own data on samples collected in 2013 and find that the mean $[OC]_{SPM}$ for the Liard is 1.48 ± 0.04% (n = 4, ±2 SE), compared to 1.48 ± 0.08% (n = 4, ±2 SE) at the Mackenzie (Tsiigehtchic) and 1.60 ± 0.47 % (n = 4, ±2 SE) at the delta. In the Peel and Arctic Red river catchments, the $[OC]_{SPM}$ is higher, with mean values of 2.09 ± 0.2% (n = 4, ±2 SE) and 2.06 ± 0.22% (n = 2, ±2 SE), respectively. The [OC] of river bank samples are, in general, similar to the suspended load at these sites. At the delta, the mean [OC] of 3 bank samples is 1.48 ± 0.87% (n = 3, ±2 SE), which is indistinguishable from the suspended load samples. In the Peel, one bank sample is comparable to the suspended load, with a [OC] of 1.4%, but a second sample enriched in woody debris has a much higher [OC] of 19.4%.

The stable carbon isotope composition of organic carbon in the river sediments provides an indication of the contribution of organic matter sources. The river bed material samples have low isotope values relative to suspended sediments, with an overall mean across the Liard, Peel, and Mackenzie delta of $\delta^{13}C$ = -28.1 ± 0.1‰ (n = 3, ±2 SE) (Hilton et al., 2015). Previous work has suggested that these sediments are dominated by OC_{petro} based on their radiocarbon activity (Hilton et al., 2015). The $\delta^{13}C$ values are similar to bedrocks outcropping in the Mackenzie Mountains (Johnston et al., 2012). In contrast, the suspended load samples are ~1.5‰ heavier, with a combined average of -26.5 ± 0.05‰ (n = 15, ±2 SE) for the Liard and Mackenzie (delta and Tsiigetchic), and a combined average of -26.8 ± 0.07‰ (n = 6, ±2 SE) for the Peel and Arctic Red rivers (Hilton et al., 2015). The remarkable homogeneity of $\delta^{13}C$ in the suspended load samples (Hilton et al., 2015) is a feature not seen in other large rivers (Bouchez et al., 2014; Galy et al., 2008b). The woody-debris rich bank material from the Peel catchment has a $\delta^{13}C$ value of -26.9‰, which is within the variability of the suspended sediment. In the Peel River catchment, the river sediments in the tributaries show the greatest variability in $\delta^{13}C$. At Engineer Creek, samples have values of -7.8‰, -18.3‰ and -28.9‰. The high sulfate content of the dissolved load in this catchment combined with the isotopically heavy values of the river sediments probably reflects microbial activity associated with redox cycling of iron and sulfur and preferentially extracting ^{12}C for metabolic processes; thereby leaving behind a residue enriched in ^{13}C (Wadham et al., 2004). Elsewhere, the river sediments from the Peel tributaries are more similar to bed materials in the Peel mainstem, with a mean $\delta^{13}C$ = -28.1 ± 1.17‰ (n = 8, ±2 SE). The Ogilvie tributary has the lowest $\delta^{13}C$, with values of -28.3 ‰ and -31.4‰, again highlighting the local variability apparent within the Peel catchment (Supplementary Figure 4.3).

Considering the $\delta^{13}C$ of the river sediments in the context of [Re]/[OC] ratios is informative for interpreting whether the organic carbon is derived from a petrogenic or biospheric source. In the Liard catchment, the mean [Re]/[OC] of the suspended sediments is $1.77 \pm 0.22 \times 10^{-7}$ g g^{-1} (n = 4, ±2 SE), compared with 6.03×10^{-7} g g^{-1} in the river bed material. In the Mackenzie at Tsiigehtchic, the mean [Re]/[OC] of the suspended sediments is similar to the Liard at $1.60 \pm 0.28 \times 10^{-7}$ g g^{-1} (n = 5, ±2 SE) and the bed material has [Re]/[OC] = 4.67×10^{-7} g g^{-1}. In the delta, the mean [Re]/[OC] of the suspended sediments is $1.75 \pm 0.24 \times 10^{-7}$ g g^{-1} (n = 6, ±2 SE) compared with 3.40×10^{-7} g g^{-1} in the bed material. The Peel River sediments bear similarity to the delta, having mean [Re]/[OC] in the suspended load of $2.01 \pm 0.42 \times 10^{-7}$ g g^{-1} (n = 5, ±2 SE) and 3.31×10^{-7} g g^{-1} in the bed material. The [Re]/[OC] of the Peel River bank material, which was enriched in wood, is notably lower than any other sample, 0.36×10^{-7} g g^{-1}. When plotted against [Re]/[OC], the $\delta^{13}C$ data shows a distribution whereby the suspended sediments all sit at low [Re]/[OC] and high $\delta^{13}C$ and the bed materials have more variability in [Re]/[OC], but all have lower $\delta^{13}C$ (Supplementary Figure 4.3).

4.4 Discussion

To determine whether the Mackenzie River Basin is a source or sink for CO_2 as a consequence of erosion and weathering, the remaining unknown is the rate of OC_{petro} oxidation. Here we use Re to examine this process and quantify fluxes. To do so, we first assess the source of dissolved Re as suggested by dissolved ion ratios, and then turn to the solid residue of erosion and weathering carried in the suspended load and at the river bed. Having better constrained the source and behaviour of Re and its link to OC_{petro}, we then seek to quantify weathering fluxes and estimate the CO_2 release from OC_{petro} oxidation.

4.4.1 Insights on the source of dissolved rhenium

Sedimentary rocks dominate the Mackenzie River Basin and its weathering regime (Millot et al., 2003). The waters draining these rocks are characterized by a chemical signature that depends on the chemical composition of the bedrock. To assess the contribution of the dissolved Re flux that derives from OC_{petro} oxidation we need to understand the relative contribution of Re from its main sources. These are thought to be organic matter, sulphide and silicate minerals, with carbonate minerals thought to contain negligible Re in their inorganic structure (Dalai et al., 2002; Miller et al., 2011). To do this, we use the elemental ratios [Re]/[Na*] and [Re]/[SO_4^{2-}]. Dissolved riverine Na concentrations, $[Na^*]_{diss}$, primarily reflect patterns in silicate weathering (Gaillardet et al., 1999), while dissolved riverine SO_4^{2-} concentrations, $[SO_4^{2-}]_{diss}$, in the Mackenzie are dominated by the oxidative weathering of sulfides (Calmels et al., 2007). Therefore, by quantifying [Re]/[Na*] and [Re]/[SO_4^{2-}] ratios in the river waters with knowledge of the endmember compositions, we can account for inputs of Re from silicate and sulfide minerals.

To define the elemental ratios of the endmembers, we first compile published measurements of Re, Na and S concentrations made on specific lithologies and individual minerals. For the silicate endmember, we find similar [Re]/[Na] and [Re]/[S] ratios for bulk mantle xenoliths (Bodinier, 1988; Pearson et al., 2004; Reisberg and Lorand, 1995), a spinel-lherzolite (Burton et al., 1999) and a basalt sample we collected in Iceland (Table 4.3). Other basalt samples also have similar [Re]/[Na] ratios (Burton et al., 2002). To constrain the [Re]/[Na] and [Re]/[S] ratios in sulphides and sedimentary organic matter is more difficult because Na and S are not necessarily measured alongside Re. However, compiling available data shows that sulfides extracted from sedimentary rocks (Kelley et al., 2017; Norman et al., 2003; Sundby et al., 2004) usually have a lower [Re]/[S] ratio (0.00107 μmol mol^{-1}) and a slightly higher [Re]/[Na] (0.102 μmol mol^{-1}) than silicates (Table 4.3). For comparison, the modal [Re]/[S] ratio in pyrite samples measured by Miller et al. (2011) is 3×10^{-3}, which is similar to the mean [Re]/[S] ratio of these sulfides (1.2×10^{-3}). A set of organic rich coals, with [OC] >75%, highlight the Re enrichment expected for sedimentary organic matter (Cohen, 2004; Colodner et al., 1993b; Selby and Creaser, 2003), with high [Re]/[Na] = 280 ± 23 μmol mol^{-1} and [Re]/[S] = 1.17 ± 0.52 μmol mol^{-1}.

When plotted alongside the dissolved ion ratios, the endmember values from the literature can be used to define the variability observed (Figure 4.5). The combination of spot sampling of small Peel tributaries and time-series sampling of the main rivers indicates that differences in Re source can occur at small spatial scales. For the main rivers, we find that most samples plot in a similar place, suggesting that the main channels integrate dissolved products of weathering and the resulting element fluxes become more similar and also consistent over time. Published data from a sampling campaign in 2004 (Miller et al., 2011) confirm this observation because they are very similar to the 2009–2013 data (Figure 4.2). In the Peel catchment, the dissolution of sulfides appears to play a relatively greater role. Tributaries of the Peel show more variable ion ratios; for example the river water sample CAN13-48 has a particularly low [Re]/[Na]* and a $[Re]_{diss}/[SO_4^{2-}]_{diss}$ value that sits outside the mixing envelope defined by the endmembers.

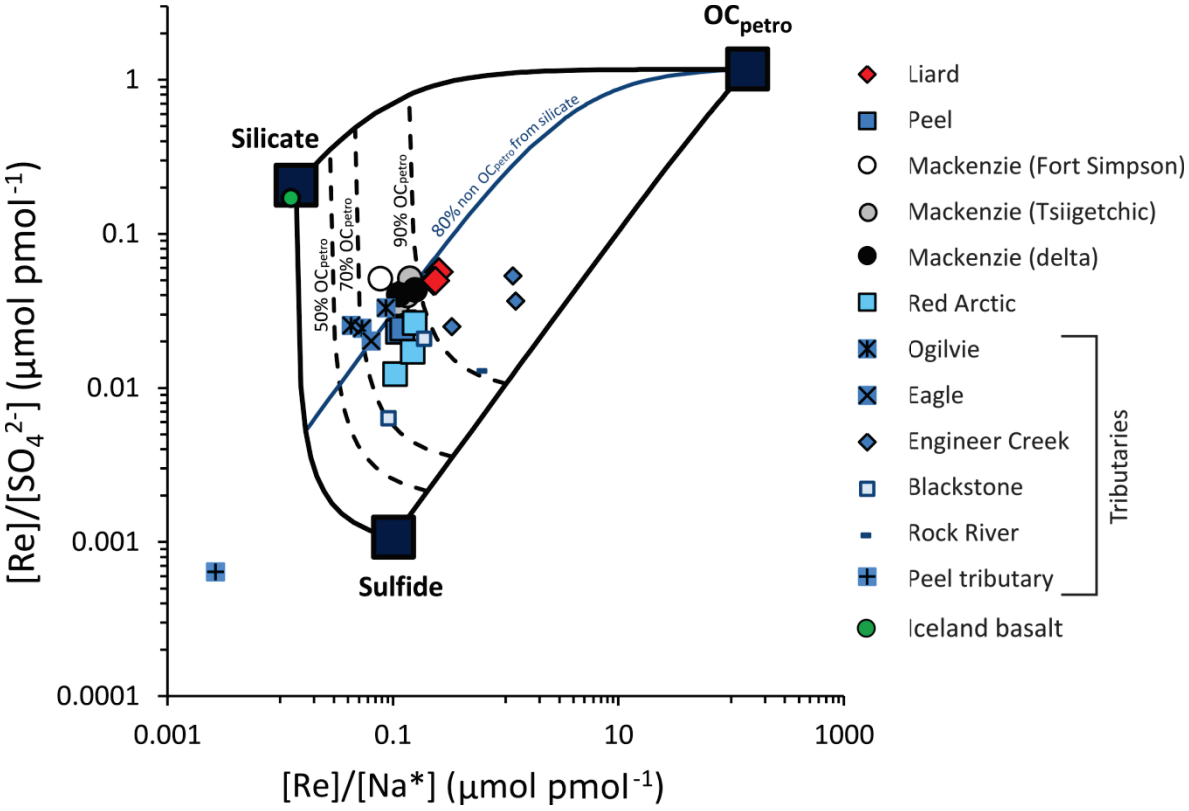

Figure 4.5 Mixing model to describe the minerals sourcing Re to the dissolved load. The ion ratios $[Re]/[SO_4^{2-}]$ and [Re]/[Na*] are used to define the endmember contributions from the mineral phases OC_{petro}, silicate and sulfides. The chemical composition of the river waters reflects a weathering contribution from these endmembers. Ion ratios are constrained using data on coals for OC_{petro} (Dai et al., 2015). Data for an Icelandic basalt (this study, green circle), bulk mantle xenoliths (Bodinier et al., 1988; Reisberg and Lorand, 1995; Pearson et al., 2004) and a spinel-lherzolite (Burton et al., 1999) are used to constrain the silicate endmember. A compilation of data from sedimentary rocks (Norman et al., 2003; Sundby et al., 2004; Kelley et al., 2017) are used for the sulfide endmember (Table 4.3). The endmember ratios imply that ~85% of the Re is derived from organic matter in the majority of sample locations. The $[Na]_{diss}$ concentrations were corrected for atmospheric contribution using $[Cl^-]$, giving $[Na^*]_{diss}$ (Millot et al., 2003). The percentage contribution of OC_{petro} is indicated with black dashed lines: 90%, 70% and 50%. The 80% contribution of silicate (20% sulfide) in the non-OC_{petro} contribution to $[Re]_{diss}$ is indicated by the blue line.

The element ratios in the solid samples from published sources can be used to estimate the contributions of Re to the dissolved load from silicates, sulfides and organic matter in rocks. This makes the assumption that the end member compositions here are representative, and that the release of Re from these sources is stoichiometric. An alternative approach to constrain the end member compositions is to use small tributaries that drain bedrock with less variability, which has the benefit of providing a more robust basis for these assumptions. As a starting point, using the literature values as endmembers and calculating the mixing domain, the samples from the main stem of the Mackenzie River Basin suggest that between 80% and 90% of the dissolved Re is sourced from OC_{petro} (Figure 4.4; section 4.8). The Liard River has a higher contribution from OC_{petro}, at ~90%. The Peel River has a higher contribution from sulfide derived Re, with a percentage of dissolved Re from OC_{petro} ~80%. However, the uncertainty on the exact compositions of the endmembers means that this approach provides only a semi-quantitative estimate of the Re

contribution from OC_{petro} oxidation. If instead we use the sulfate-rich tributary of the Peel to define the sulfide endmember composition ([Re]/[Na] = 0.0027 μmol mol^{-1} and [Re]/[SO_4^{2-}] = 0.00064 μmol mol^{-1}), the mixing model suggests >94% of the dissolved Re in all sample locations is derived from the OC_{petro} composition.

It is important to recognise that the endmember mixing model (Figure 4.5) has particularly poor constraint on the [Re]/[Na*] and [Re]/[S] composition of OC_{petro}. For example, not all of the OC_{petro} in the Mackenzie River Basin is likely to be present in the form of coal. Marine-derived sedimentary organic matter is likely to have a higher [S] and [Na] but similar [Re], with a resultant lower [Re]/[S] ratio than coal (e.g. Berner and Raiswell, 1984). This would act to shift the position of this source downwards in [Re]/[S]-[Re]/[Na] mixing space (Figure 4.5) and lower the estimated contribution of dissolved Re from OC_{petro}. Future work may also seek better to constrain the silicate endmember more precisely for this setting; for example by measuring the Re concentration of the Canadian Shield rivers to the south of the Mackenzie River Basin, which drain granitic rocks.

As a result of the uncertainty in the current endmember positions in Figure 4.5, it may be more appropriate to follow the approach of Galy and France-Lanord (1999) to calculate the relative contribution of OC_{petro} to the dissolved Re budget. In this approach, the concentration of Re in the river water ($[Re]_{diss}$) is considered to be the sum of Re sourced from OC_{petro}, silicate minerals, sulfide minerals and precipitation; assuming negligible anthropogenic, carbonate and evaporite contributions for the major rivers, and correcting for the cyclic contribution (Equation 4.1).

Equation 4.1 $$[Re]_{diss} = [Re]_{OCpetro} + [Re]_{silicate} + [Re]_{sulfide} + [Re]_{cyclic}$$

The proportion of Re derived from OC_{petro} oxidation is inferred to be the difference between the total Re budget in a given river water sample and the Re contribution from silicate, sulfide and precipitation. To calculate the contribution of Re from precipitation in a river water sample, we multiply the [Re]/[Cl] ratio in seawater by the [Cl]/[Re] ratio in the river water sample. To calculate the contribution of Re from silicate minerals, we approximate the composition [Re]/[Na] of silicate with the [Re]/[Na] ratio in the silicate endmember used in Figure 4.4 and multiply this by the [Na]/[Re] ratio in the sample. To calculate the contribution of Re from sulfide minerals, we multiply the [Re]/[SO_4^{2-}] ratio in the Peel tributary (sample CAN13-47) by the [SO_4^{2-}]/[Re] ratio in the sample. This Peel tributary has a very high [SO_4^{2-}] of 2289 μmol L^{-1}, suggesting very high rates of sulfide oxidation here and that this tributary may best describe the composition of the local sulphide endmember in the Mackenzie River Basin. In contrast, other Peel River tributaries, including the Rock, Engineer, and Blackstone rivers, have high [Re]/[Na] and mid-range [Re]/[SO_4^{2-}] and are more similar to the main stem sites.

This approach is advantageous because it does not require any previous knowledge of the composition of the OC_{petro} endmember, which is probably the greatest unknown in Figure 4.5. The model (Equation 4.1) is based on the following four assumptions: i) chloride is only derived from evaporites and from precipitation; ii) the dissolution of carbonate does not contribute to the dissolved sodium; iii) evaporite weathering yields only NaCl; and iv) sulfate is entirely derived from sulfide oxidation (Galy and France-Lanord, 1999). Nonetheless, as with the mixing model (Figure 4.5), this approach also indicates that the bulk of dissolved Re in the main channels is derived from OC_{petro} oxidation: the mean percentage of $[Re]_{diss}$ from OC_{petro} oxidation in the Liard, Peel, Mackenzie (Tsiigetchic), Mackenzie delta and Arctic Red is 93%, 85%, 87%, 86% and 86%, respectively. The Ogilvie, Eagle and Blackstone Rivers have a higher contribution of Re from sulfide minerals and a lower resultant contribution of Re from OC_{petro}: the greatest range is observed in the samples from the Ogilvie River (64–82%).

The high percentage of $[Re]_{diss}$ contributed by OC_{petro} in the Mackenzie River Basin is consistent with the notion that $[Re]_{diss}$ is primarily hosted in sedimentary organic matter (Cohen, 2004; Selby and Creaser, 2003) and that Re is released during the exposure and oxidation of OC_{petro} at Earth's surface (Jaffe et al., 2002). Therefore, OC_{petro} has a major influence on Re river chemistry relative to silicate and sulfide minerals. This observation probably relates to the fact that the kinetics of OC_{petro} weathering are ~10 times faster than those for silicate weathering (Chang and Berner, 1999) and that Re contents are lower in sulfides (Kelley et al., 2017; Sundby et al., 2004) than those found in organic matter (Dai et al., 2015; Selby and Creaser, 2003).

4.4.2 Source and behaviour of Re in river sediments

The relationship between [Na]/[Al] and [Al]/[Si] in river sediments (Figure 4.4) indicates that Na is sorted through the water column between the fine surface particles and the coarser river bed sediments. For Na, the reason for this is thought to be a combination of: i) the hydrodynamic behaviour of the primary mineralogical sources; and ii) Na mobility in the dissolved phase during weathering and the production of secondary minerals (Bouchez et al., 2011; Bouchez et al., 2012). In the Mackenzie River Basin, the weathering intensity is relatively low and the geochemistry of suspended sediments largely reflects erosion of unweathered bedrock, dominated by shales (Dellinger et al., 2014). This suggests that modern weathering processes are unlikely to play a major role in the evolution of [Na]/[Al] within the river sediments. Instead, the pattern can be explained by hydrodynamic sorting of particles based on their grain size, shape and relative density. In the coarse fraction, albite ($NaAlSi_3O_8$) can be an important mineral alongside quartz (Bouchez et al., 2011) and can explain the Na enrichment relative to Al in the coarser sediments with low [Al]/[Si] ratios (Figure 4.4A). In finer sediments (higher [Al]/[Si] ratios), phyllosilicate minerals become more important, and these are typically depleted in Na during their formation

during weathering in soils. In the Mackenzie River catchment, most of these minerals are recycled from eroded shales (Dellinger et al., 2014), and the Na depletion reflects multiple cycles of sedimentary rock weathering. The Peel and Arctic Red sediments sit below the trend outlined by data from the Mackenzie and Liard catchments. This is consistent with a lower proportion of igneous rocks upstream (Millot et al., 2003; Dellinger et al., 2014) and a lower input of feldspar to the river sediments.

In contrast, the [Re]/[Al] ratios in the river suspended load and bed materials are relatively invariant with [Al]/[Si] (Figure 4.4B). Given the behaviour of Na described herein (Figure 4.4A) and the recycling of sedimentary rocks into the modern weathering regime (Dellinger et al., 2014), contemporary weathering processes are unlikely to affect the [Re]/[Al] ratios. Therefore, the relatively constant [Re]/[Al] ratio as a function of grain size reflects the hydrodynamic behaviour of the Re host phase. It suggests that the Re host phases are found in roughly similar proportions throughout the river water column, regardless of the size of the particulates in which Re is present. The characteristics of OC_{petro}, including its relatively low density, and the observation that it is associated with both coarse minerals and phyllosilicates (Bouchez et al., 2010; Galy et al., 2008a), make OC_{petro} a candidate to be the major Re bearing component. The [Re]/[Al] ratio is higher in the Peel river sediments, which fits the notion that this basin has higher OC_{petro} concentrations compared to the main Mackenzie and Liard River (Hilton et al., 2015). This supports the suggestion of a strong affiliation between Re and OC_{petro} (Cohen, 2004; Jaffe et al., 2002; Selby and Creaser, 2003). If Re was predominantly sourced from sulfide minerals then we might expect an enrichment in Re in the bottom waters, where [Al]/[Si] is low, as sulfide minerals are typically dense. The fact that this does not occur, and also that the river with the highest sulfide contribution has the lowest concentration of dissolved Re, confirms that the weathering of sulfides appears to play a minor role in the weathering flux of Re, relative to OC_{petro}, in the Mackenzie River Basin.

4.4.3 Estimates of CO_2 fluxes via OC_{petro} oxidation

To estimate CO_2 emissions by OC_{petro} oxidation, the dissolved Re flux can be combined with the [Re]/[OC] of the bedrock undergoing weathering (Hilton et al., 2014; Jaffe et al., 2002; Petsch, 2014). Here, we refine this approach by following a similar method as Dalai et al. (2002), whereby we use dissolved ion ratios to constrain the fraction of dissolved Re derived from OC_{petro} weathering (Figure 4.5). Long-term average annual Q_w from gauging stations account for runoff variability that has been monitored over several decades. We calculate average annual Q_w for the Liard = 1944 $m^3\ s^{-1}$ (1972–2015), the Mackenzie at Tsiigetchic = 7156 $m^3\ s^{-1}$ (1972–2015), the Peel = 538 $m^3\ s^{-1}$ (1969–2015) and the Arctic Red = 124 $m^3\ s^{-1}$ (1968–2015) (Environment Canada, accessed online, 10/05/17). Annual Re fluxes are 250 ± 31 kg yr^{-1}, 684 ± 48 kg yr^{-1}, 60 ± 15 kg yr^{-1} and 13 ± 3.6 kg yr^{-1}, for the Liard, the Mackenzie at Tsiigetchic, the Peel, and the Arctic Red

catchments, respectively. The endmember mixing model (Figure 4.5) can be used as a first-order guide to the correction that is required to make the $[Re]_{diss}$ flux representative of OC_{petro} oxidation. River water samples from the main channels have >85% of $[Re]_{diss}$ derived from OC_{petro} oxidation, so we apply this correction to our estimates of Re flux.

In order to quantify the [Re]/[OC] ratio of the rocks in these catchments, we consider the [Re]/[OC] ratios of the river suspended sediments and the bed materials together with radiocarbon measurements on the organic matter, reported as the "Fraction Modern" (F_{mod}) (Hilton et al., 2015). The source rock in each catchment is defined as having $F_{mod} \sim 0$, because it is fully ^{14}C-depleted relative to background. We find that the river bed materials offer a good indication of the [Re]/[OC] of the source rock, as they have low ^{14}C content (low F_{mod}). Nevertheless, because F_{mod} values do exceed 0, the river bedloads must contain some biospheric organic carbon (Hilton et al., 2015) incorporated as the sediments were weathered and eroded upstream. The importance of biospheric OC is more pronounced in the suspended loads, which have high F_{mod} relative to the bedloads. The [Re]/[OC] of the suspended load samples is also lower than that of the bedloads, suggesting input of Re-poor organic-rich material in these samples. The [Re]/[OC] ratio of a wood rich sample in the Peel River is 3.58×10^{-8} g g^{-1}, which suggests that the patterns in the data can be explained by the mixing of OC sources – high [Re]/[OC] in sedimentary rocks, and low [Re]/[OC] in the live, oxygenated terrestrial biosphere (Figure 4.6). Organic carbon rich soil litters from other locations, such as Taiwan and New Zealand, have similar low [Re]/[OC] ratios; these are 1.3×10^{-9} and 9.5×10^{-9} g g^{-1}, respectively (Hilton et al., 2014; Horan et al., 2017).

By fitting linear trends through the F_{mod}-[Re]/[OC] data from the combination of bed materials and suspended loads, we can better constrain the average $[Re]/[OC_{petro}]$ composition of the sedimentary rocks in the basin. This approach yields an intercept on the [Re]/[OC] axis reflecting the [Re]/[OC] composition of the source rock, where $F_{mod} = 0$ (Figure 4.6). The combined linear regression for all catchments indicates a [Re]/[OC] ratio of $6.5\ ^{+2.75}/_{-1.25} \times 10^{-7}$ g g^{-1} (±95% confidence). This value agrees closely with published mean values of bedrocks from the Liard sub-catchment (Ross and Bustin, 2009), where average [Re]/[OC] ratios are 5.6×10^{-7} g g^{-1} for the Besa and Golata shales (Figure 4.6; Supplementary Figure 4.4). With more data, it may be possible to take this approach for each sampling catchment. The intercept on the F_{mod} axis provides an indication of the ^{14}C activity of the biosphere and with F_{mod} values of ~0.5 to 0.7 it is consistent with the erosion of aged soil organic carbon in the Mackenzie River Basin (Hilton et al., 2015).

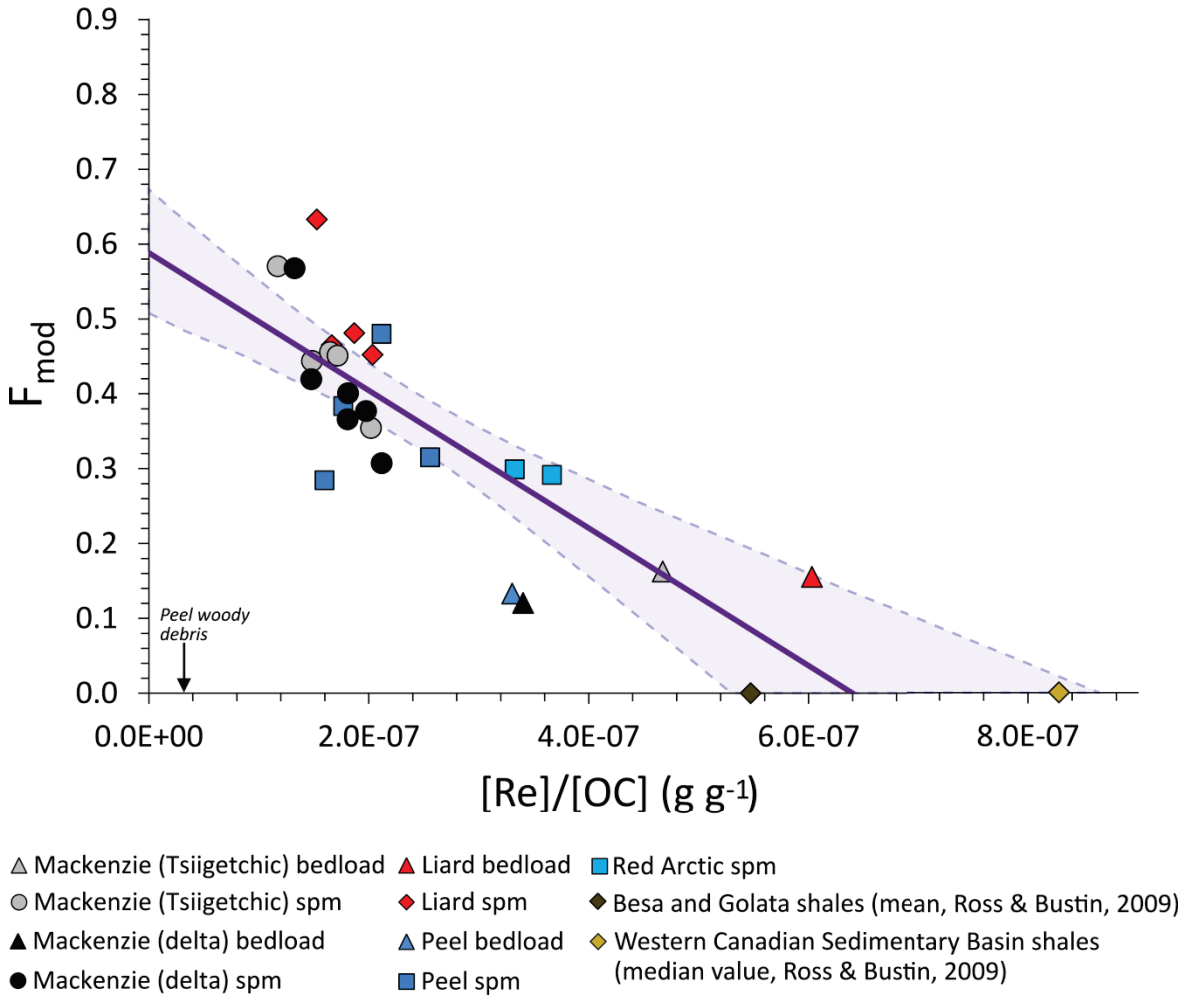

Figure 4.6 Model used to determine the [Re]/[OC] of the source rock. F_{mod} and [Re]/[OC] ratios for river suspended load (spm) and river bedloads are fitted with a linear trendline marked by the solid purple line. The low [Re]/[OC] ratio of a wood-rich bank sample collected from the Peel catchment is (3.58×10^{-8} g g^{-1}) is indicated; this reflects the high concentration of biospheric carbon in this sample. The *x* intercept provides an indication of [Re]/[OC_{petro}] in each of the catchments, where $F_{mod} = 0$. The ±95% confidence intervals are shown within the purple shaded band.

Together, the dissolved Re yield (J_{Re}, g km^{-2} yr^{-1}) and the $[Re]_{BM}$:$[OC]_{BM}$ (g g^{-1}) allow us to make an estimate of the CO_2 oxidation yield, J_{CO2} (gC km^{-2} yr^{-1}) by OC_{petro} oxidation (Equation 4.3). It is important to account for some decoupling of rhenium and organic carbon as a result of the solubility of Re upon oxidation, which could allow it to be mobilized more effectively during weathering relative to CO_2 (Jaffe et al., 2002). The effects of this potential decoupling are accounted for by the term f_C, which reflects the ratio between the percentage loss of OC_{petro} in soil versus that of Re. Based on published data from soils (Hilton et al., 2014; Horan et al., 2017; Jaffe et al., 2002; Pierson-Wickmann et al., 2002), this ratio is expected to be <1 but >0.5. We also use the f_C term to account for non-OC_{petro} derived Re. Uncertainty in the translation of a Re flux into a CO_2 flux can also arise if there is incomplete oxidation of organic carbon; for example graphitic OC_{petro} is less susceptible to oxidation (Galy et al., 2008a). To account for the presence of graphitic

carbon, which may not be oxidised, we vary the fraction of OC_{petro} as graphite ($f_{graphite}$) from 0.2 to 0, as high grade metamorphic rocks are not as common in the Mackenzie mountains and Rockies (Johnston et al., 2012), compared to Taiwan and the Southern Alps where this approach has been most recently applied (Beyssac et al., 2016, 2007). The CO_2 oxidation flux, J_{CO2} (gC km^{-2} yr^{-1}), is then calculated and a Monte Carlo simulation is used to account for these uncertainties following the approach of Horan et al. (2017).

Equation 4.3 $$J_{CO2} = J_{Re} \times ([OC_{petro}]_{BM}/[Re]_{BM}) \times f_C \times (1 - f_{graphite})$$

In the Mackenzie River catchment (based on $[Re]_{diss}$ fluxes at Tsiigetchic), we quantify CO_2 yields to be 0.38 $^{+0.10}/_{-0.09}$ tC km^{-2} yr^{-1}. In the Peel, Arctic Red and Liard catchments, we find CO_2 yields are higher when considered on a per unit area basis, at 0.79 $^{+0.23}/_{-0.19}$ tC km^{-2} yr^{-1}, 0.66 $^{+0.19}/_{-0.16}$ tC km^{-2} yr^{-1} and 0.84 $^{+0.23}/_{-0.20}$ tC km^{-2} yr^{-1}, respectively (Table 4.4). The river flux of unweathered OC_{petro} is ~0.6 $^{+0.2}/_{-0.2}$ tC km^{-2} yr^{-1} in the Mackenzie River, suggesting that the overall oxidative weathering makes up ~40% of the total OC_{petro} denudation.

To explain the differences in weathering yields between the catchments, we consider how the physical erosion rates vary between the catchments. Physical erosion is known to enhance the rate of oxidative weathering of organic carbon in rocks (Hilton et al., 2014), therefore we might expect $[Re]_{diss}$ and associated CO_2 fluxes in the Mackenzie River Basin to be governed by this parameter. We use published sediment yields (t km^{-2} yr^{-1}) as a measure of the physical erosion rate normalized by runoff. In the Mackenzie River catchment sediment yields are 124 t km^{-2} yr^{-1}, while the Peel, Liard and Arctic Red catchments experience sediment yields of 295 t km^{-2} yr^{-1}, 149 t km^{-2} yr^{-1} and 392 t km^{-2} yr^{-1}, respectively (Carson et al., 1998). These erosion rates are about a factor of ten lower than those recorded in active mountain belts, such as the western Southern Alps and Taiwan (Hilton et al., 2014; Horan et al., 2017). The calculations of atmospheric Re yields (tC km^{-2} yr^{-1}) are also an order of magnitude lower in the Mackenzie River Basin (Figure 4.7). In the overall relationship between Re and physical erosion, the data from the Mackenzie River Basin serve to strengthen the hypothesis that mountain belts erode rapidly accessible Re from a surficial weathering zone, where oxidation reactions are limited predominantly by mineral supply.

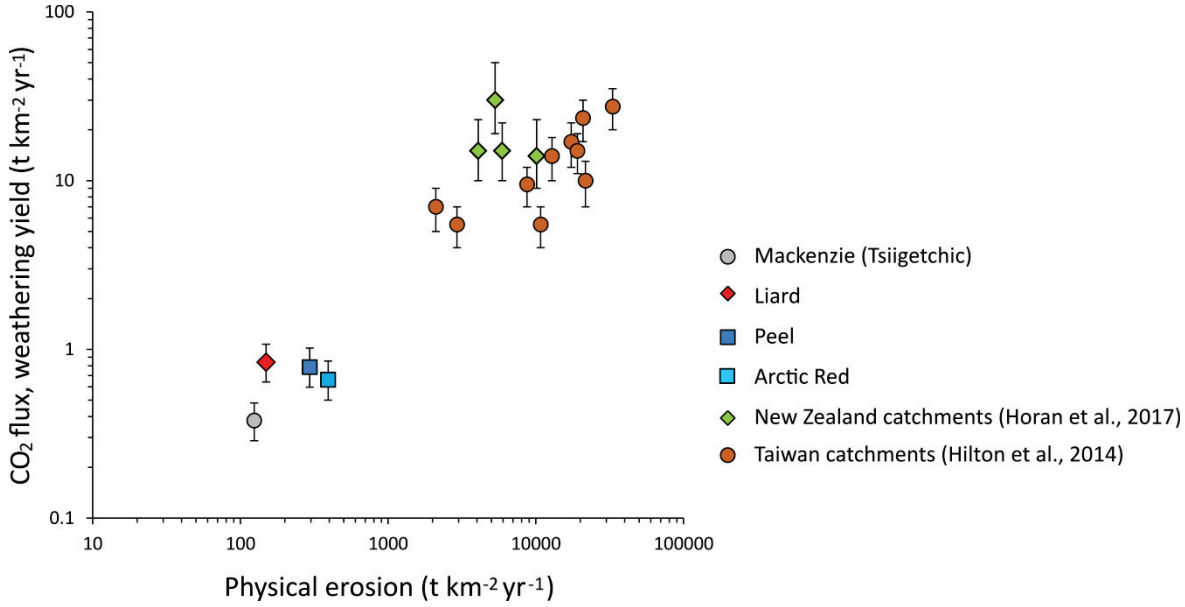

Figure 4.7 Dissolved rhenium (Re) yield in mountain catchments around the world draining sedimentary rocks as a function of suspended sediment yield. Physical erosion rates are quantified using decadal average suspended sediment concentration. Orange circles are from Taiwanese catchments (Hilton et al., 2014) and the green diamonds are from New Zealand catchments (Horan et al., 2017).

4.4.4 The net CO_2 budget of the Mackenzie River catchment

Examining the transfer of Re across the Mackenzie River Basin has allowed us to assess the rate and controls on OC_{petro} oxidation while also estimating, for the first time, the associated CO_2 release. In the Mackenzie River catchment we are able to combine our estimates of CO_2 flux from OC_{petro} oxidation ($0.38\ ^{+0.10}/_{-0.09}$ t km^{-2} yr^{-1}) with pre-existing data on biospheric organic carbon burial rates and silicate and carbonate weathering rates to calculate the net carbon budget. The silicate weathering CO_2 flux is ~0.4 tC km^{-2} yr^{-1} (Gaillardet et al., 1999) and, assuming a burial efficiency of 65%, the erosion and burial of biospheric organic carbon offshore is ~1.89 tC km^{-2} yr^{-1} (Hilton et al., 2015). The transient CO_2 release by sulfuric acid driven carbonate weathering is ~0.7 tC km^{-2} yr^{-1} (Calmels et al., 2007, re-calculated in Torres et al., 2014). The CO_2 drawdown by carbonate weathering by carbonic acid is 0.98 tC km^{-2} yr^{-1}, but this is often considered to be CO_2 neutral over timescales of 10^3–10^6 years when coupled to carbonate mineral precipitation (Gaillardet et al., 1999). Together, these data suggest that the Mackenzie River catchment has a net CO_2 budget that equates to a sink of $1.2\ ^{+0.33}/_{-0.30}$ tC km^{-2} yr^{-1} from the atmosphere (Figure 4.8).

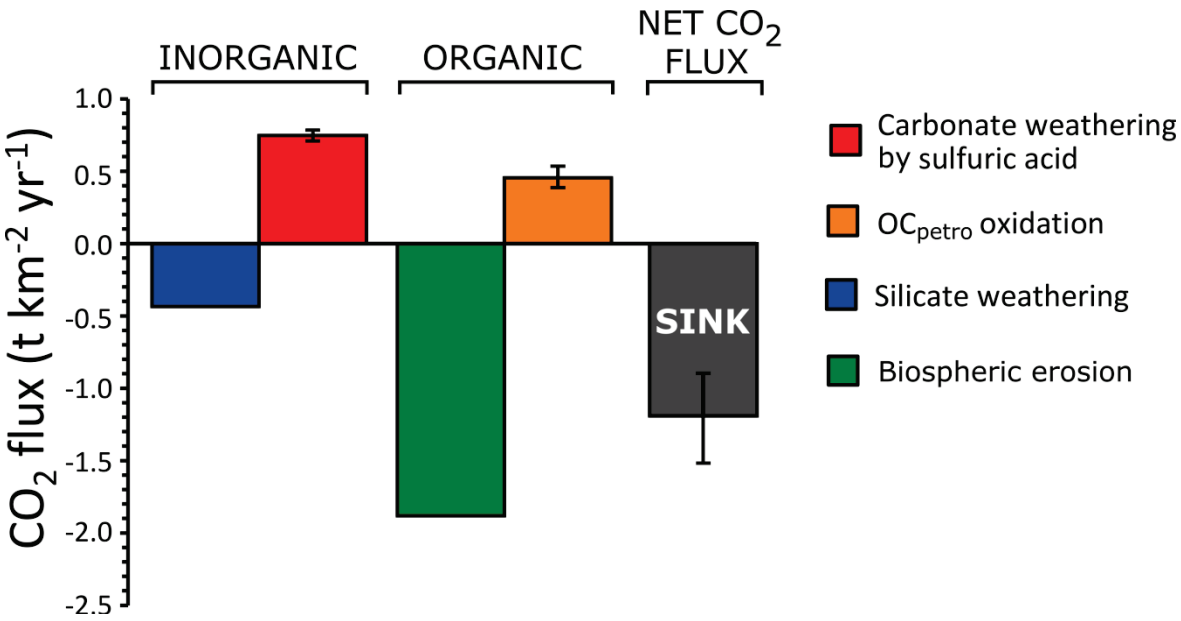

Mechanism	C flux (t km^{-2} yr^{-1})	Reference
Silicate weathering	-0.44	Gaillardet et al., 1999
Carbonate weathering	-0.98	Gaillardet et al., 1999
Carbonate weathering by sulfuric acid	0.75 (±0.04)	Calmels et al., 2007; Torres et al., 2014
Organic carbon burial	-1.89	Hilton et al., 2014
Petrogenic organic carbon oxidation	0.38 ($^{+0.10}/_{-0.09}$)	This study

Figure 4.8 Carbon cycle budget of the Mackenzie River catchment. The CO_2 flux derived from petrogenic organic carbon (OC_{petro}) oxidation calculated in this study is differenced from the transfer and burial of OC from the terrestrial biosphere ($OC_{biosphere}$) and silicate weathering (Hilton et al., 2015) and carbonate weathering by sulfuric acid (Calmels et al., 2007; Torres et al., 2014). The net carbon balance is a sink.

4.4.5 Global relevance of the OC budgets in the Mackenzie River Basin

Estimates of CO_2 flux from OC_{petro} oxidation are limited globally. Therefore, our understanding of the net carbon balance in mountainous catchments during weathering and erosion remains tentative. Current carbon flux estimates for non-glaciated mountainous regions in Taiwan (Hilton et al., 2014) and New Zealand (***Chapter 3***, Horan et al., 2017) trend toward net sinks. Although OC_{petro} oxidation counterbalances silicate weathering in each of these sites, the drawdown of CO_2 by biospheric organic carbon erosion tends to control the net carbon balance. This is also what we observe in the Mackenzie River Basin, where high erosion of OC from soils (Hilton et al., 2015) creates a significant carbon sink. In the Mackenzie River Basin, the CO_2 sourced from OC_{petro} oxidation is slightly higher than the CO_2 sequestered during the weathering of silicate minerals, but it is insufficient, even alongside the CO_2 released by carbonate weathering by sulfuric acid, to negate the large carbon sinks driven by biospheric organic carbon erosion, and silicate weathering

by carbonic acid. Consequently, under the current climate conditions, erosion and weathering act as a CO_2 sink via the organic and inorganic carbon cycles.

In mountain catchments subject to glaciation, carbon fluxes appear to be controlled to a lesser extent by biospheric organic carbon erosion. For example, in the western Southern Alps, the presence of valley and headwater glaciers triples estimates of CO_2 sourced from weathering of OC_{petro} and thereby converts the net carbon balance positive (***Chapter 3***, Horan et al., 2017). If we consider the implication of vast areas of the Mackenzie River Basin becoming glaciated, as would have occurred at the Last Glacial Maximum, then this region could have acted as an important CO_2 source. As biospheric carbon stocks diminish and OC_{petro} oxidation rates are simultaneously enhanced, an increased source of atmospheric CO_2 has the potential to buffer climate change in this basin over millions of years.

4.5 Conclusion

Elemental Re abundance is used to provide insight into the oxidative weathering reactions driving the release of CO_2 to the atmosphere from sedimentary organic matter in the Mackenzie River Basin. River water and sediment collected from 2009–2013 at sites on the main Mackenzie River and its tributaries are used to assess spatial and temporal patterns of chemical weathering and Re mobility. Limited loss of Re is observed in the river sediments, with Re appearing to be distributed evenly throughout the water column from the river bed through to the suspended load, regardless of the grain size. The low density of OC_{petro} makes it a plausible component as the major Re host. In the dissolved products of chemical weathering, we examine Re source (from silicate minerals, sulfides and OC_{petro}) using [Re]/[Na] and [Re]/[SO_4^{2-}] ion ratios. Based on endmember compositions from a literature compilation, we estimate that >85% of the dissolved Re is derived from OC_{petro} at the main channel sampling sites. The strong affiliation of Re with OC_{petro} confirms Re is a suitable proxy for tracking OC_{petro} weathering.

Dissolved Re flux measurements are used together with estimates of bedrock [Re]/[OC] to quantify CO_2 release by OC_{petro} oxidation. The [Re]/[OC] of the unweathered source rock is constrained using [Re]/[OC] and ^{14}C data from the river suspended sediments and bed materials. Potential errors in the Re flux derived from differences in the mobility of Re and CO_2 during weathering and the presence of graphitic carbon that is less susceptible to oxidation are assessed using a Monte Carlo Simulation. Using this method, we conclude that OC_{petro} oxidation is a significant source of CO_2 to the atmosphere in the Mackenzie River Basin, of $0.38\ ^{+0.10}/_{-0.09}$ tC km^{-2} yr^{-1}; comparable in magnitude to the atmospheric CO_2 that is sequestered by silicate weathering (Gaillardet et al., 1999). However, the absolute rates of this CO_2 emission in the Mackenzie River catchment are not sufficient to negate the estimated CO_2 drawdown by erosion of OC from the terrestrial biosphere

and during silicate weathering by carbonic acid. Therefore, the Mackenzie River catchment presently acts as a carbon sink, sequestering atmospheric CO_2 during weathering and erosion. The potency of this sink mainly depends on the ratio between OC_{petro} oxidation and biospheric carbon erosion and burial. We postulate that this may not have been constant over glacial–interglacial cycles, which will have impacted the net CO_2 budget of this large river basin.

4.6 Supplementary Figures

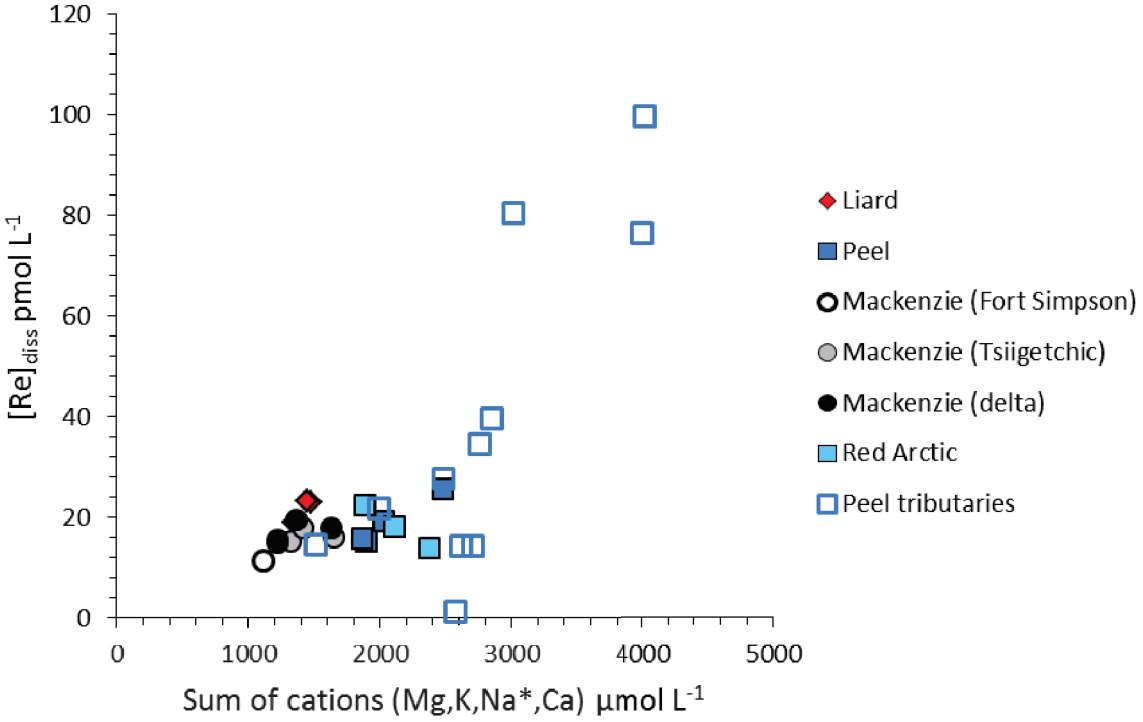

Supplementary Figure 4.1 Relationship between $[Re]_{diss}$ and ΣCations*. The positive correlation reflects the broadly consistent rate that Re and cations are released to the river dissolved load during chemical weathering. There is a tendency for the Arctic Red River, Peel River and Peel tributaries to have relatively higher Re and Cations* concentrations, which may reflect the higher physical erosion rates in these catchments relative to the Liard and Mackenzie catchments.

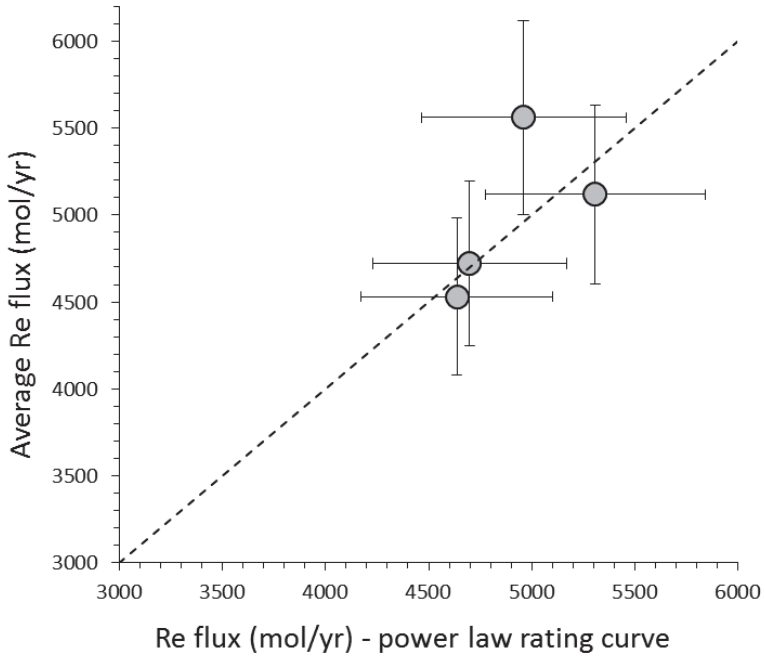

Supplementary Figure 4.2 Correspondence between $[Re]_{diss}$ flux calculated by a modelled relationship between $[Re]_{diss}$ and discharge versus average $[Re]_{diss}$ multiplied by average discharge over 2009–2013. Re flux calculated by a power-law model versus the average concentration method in the Mackenzie River (Tsiigetchic sampling locality). Error bars are ±10% deviations on the given value.

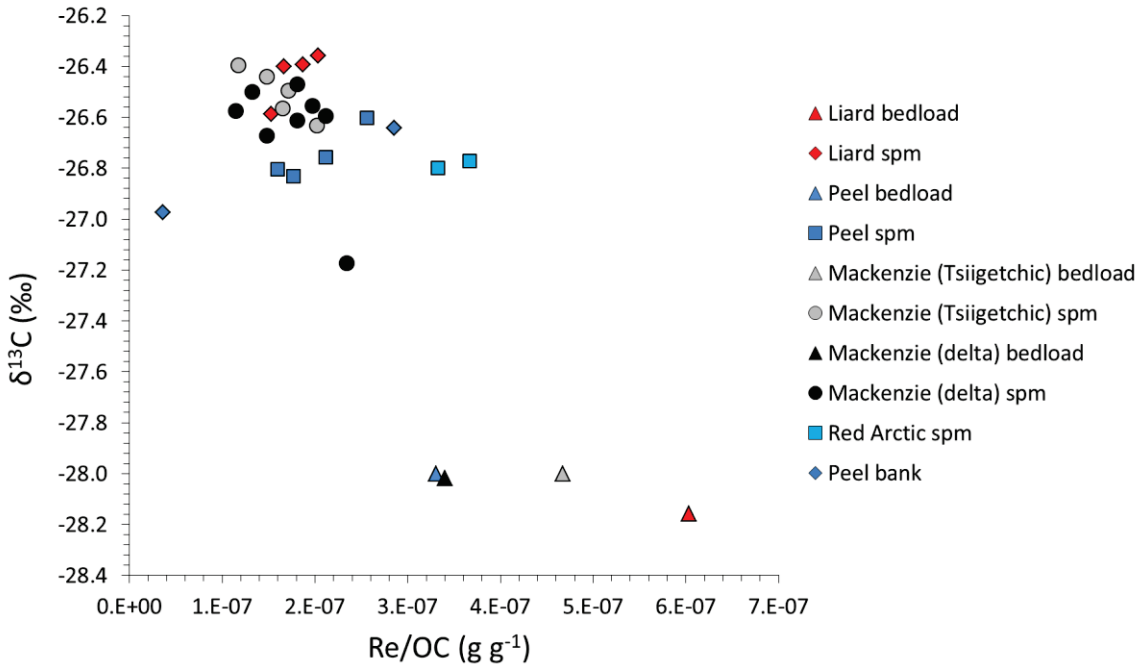

Supplementary Figure 4.3 Relationship between $\delta^{13}C$ and the [Re]/[OC] content of the river sediments. Bedload samples have low $\delta^{13}C$ and high [Re]/[OC], while suspended sediments (spm) are isotopically heavier and have lower [Re]/[OC] ratios.

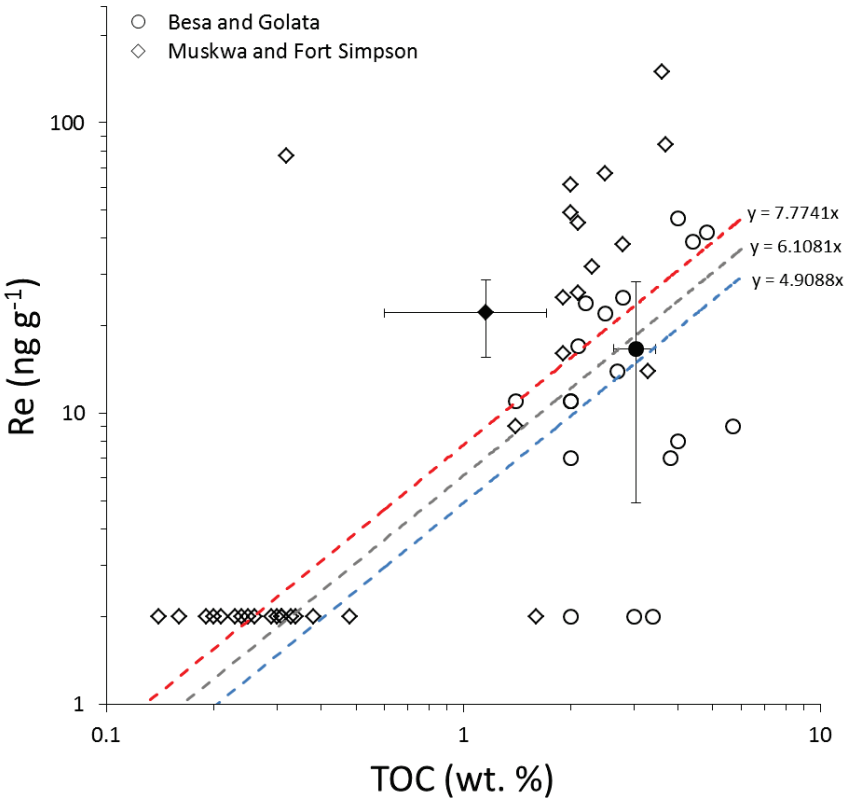

Supplementary Figure 4.4 Relationship between OC_{petro} concentration and Re concentration in the source rock. Data from the Mackenzie River Basin are considered alongside published data from western Canada (Ross and Bustin, 2010): data from the Besa and Golata sampling localities are marked as open circles with the mean as solid circle (±2 SE), while data from Muskwa and Fort Simpson are coded as open diamonds, with the mean as a filled diamond (±2 SE). For comparison, linear trend lines for the different catchments from our study are shown in red (Liard), grey (Mackenzie at Tsiigetchic) and blue (Peel) and these have gradients that reflect the Re/OC_{petro} content of the bed materials.

4.7 Data Tables

Table 4.1 | Major ion and rhenium concentration data for water samples from the Mackenzie River Basin

Sample name	Collection Date	River	Location	Latitude (deg. N)	Longitude (deg. W)	Water-depth (m)	pH	Temp. (°C)	Na* (µmol L^{-1})	K (µmol L^{-1})	Mg (µmol L^{-1})	Ca (µmol L^{-1})	F (µmol L^{-1})	Cl (µmol L^{-1})	SO_4 (µmol L^{-1})	Sr (µmol L^{-1})	Li (µmol L^{-1})	HCO_3^- (µmol L^{-1})	Re (pmol L^{-1})
CAN09-04	15/7/2009	Liard	Fort Simpson	61.8357	121.2851				74.18	14.35	378.63	881.28	4.31	8.83	337.68		0.49	1687.76	19.12
CAN10-46	13/9/2010	Liard	Fort Simpson	61.8234	121.2976				100.11	17.78	408.00	945.87	4.60	22.38	469.69		0.82		23.07
CAN10-48	13/9/2010	Liard	Fort Simpson	61.8230	121.2976				98.02	17.30	402.98	922.43	4.50	21.85	471.69		0.83		23.38
CAN09-39	21/7/2009	Peel	Fort MacPherson	67.3323	134.8688				138.50	14.48	622.60	1122.87	4.52	44.93	667.13		0.70	2162.91	15.37
CAN13-01	19/07/2013	Peel	Fort Macpherson	67.33448	134.87762	0	7.92	19.5	205.72	17.33	797.60	1451.19		42.22	966.90	3.03	0.56	2587.82	25.75
CAN13-81	26/07/2013	Peel	Fort Macpherson	67.33448	134.87762	3.5			159.04	12.68	690.40	1162.18		36.51	797.14	2.68	0.46	2350.30	19.31
CAN11-79	11/6/2011	Peel	Fort MacPherson						141.76	16.90	625.71	1080.20	3.75	48.15	705.17	1.39	0.79		15.94
CAN09-07	16.07.2009	Mackenzie	Fort Simpson	61.85104	121.27722				149.25	22.96	258.67	673.76	3.02	197.33	226.77		0.46	1438.94	11.54
CAN09-47	22/7/2009	Mackenzie	Tsiigehtchic	67.4584	133.7233				122.13	19.08	364.92	822.16	5.89	145.66	365.40		0.53	1564.45	15.30
CAN10-14	7/9/2010	Mackenzie	Tsiigehtchic	67.4580	133.7270				146.39	22.19	462.04	1020.98	5.38	196.66	461.04	2.12	0.63		16.21
CAN11-68	11/6/2011	Mackenzie	Tsiigehtchic						110.14	23.03	312.09	778.16	3.86	131.34	304.83	1.75	0.54		15.68
CAN13-82	26/07/2013	Mackenzie	Tsiigehtchic	67.45818	133.72734	5			133.59	19.23	398.33	868.36		188.97	451.03	3.28	0.32	1918.43	17.87
CAN13-65	24/07/2013	Mackenzie	Delta Middle Channel, Inuvik	68.41313	134.08893	6	8.04	16.9	123.64	18.29	384.71	842.04		163.42	454.22	3.20	0.30	1973.48	19.57
CAN10-26	8/9/2010	Mackenzie	Delta Middle Channel, Inuvik	68.4343	134.2222				158.76	21.74	460.50	991.26	4.21	167.38	444.51	2.34	0.73		17.90
CAN11-100	14/6/2011	Mackenzie	Delta Middle Channel, Inuvik						197.25	21.51	291.08	713.16				1.51	0.52		15.01
CAN09-50	22/7/2009	Arctic Red	Tsiigehtchic	67.4261	133.7787				143.35	21.68	570.39	1152.73	5.72	16.15	854.42		0.95	1552.23	22.46
CAN10-18	7/9/2010	Arctic Red	Tsiigehtchic	67.4396	133.7553				133.08	18.58	840.25	1382.91	4.52	23.55	1141.46	1.62	0.88		13.96
CAN13-83	26/07/2013	Arctic Red	Tsiigehtchic			0.3			120.48	15.54	759.36	1217.25		15.08	1057.73	2.75	0.49	2161.63	18.16
CAN13-09	20/07/2013	Ogilvie	First Demptser sight	65.71532	137.99249	0	8.1	12.1	400.80	12.16	776.69	1561.40		91.79	1051.88	3.61	1.57	2674.45	34.80
CAN13-12	20/07/2013	Ogilvie	Dempster Bridge	65.36131	138.17824	0	8.26	12.9	521.85	11.32	691.58	1249.46		73.13	1147.58	3.44	1.54	2702.91	27.92
CAN13-33i	22/07/2013	Ogilvie	Dempster	65.36216	138.30226	0	7.81	13.8	513.38	9.68	525.63	940.27		22.22	861.89	2.80	0.84	1818.83	21.88
CAN13-33ii	22/07/2013	Ogilvie	Dempster	65.36216	138.30226	0	7.81	13.8											

Sample name	Collection Date	River	Location	Latitude (deg. N)	Longitude (deg. W)	Water-depth (m)	pH	Temp. (°C)	Na* (µmol L^{-1})	K (µmol L^{-1})	Mg (µmol L^{-1})	Ca (µmol L^{-1})	F (µmol L^{-1})	Cl (µmol L^{-1})	SO_4 (µmol L^{-1})	Sr (µmol L^{-1})	Li (µmol L^{-1})	HCO_3^- (µmol L^{-1})	Re (pmol L^{-1})
			Bridge																
CAN13-05	19/07/2013	Eagle	Nr Eagle Plains	66.44326	136.71062	0	7.44	13.9	619.13	19.37	809.37	1401.04		19.33	1978.73	3.07	1.14	1256.21	39.83
CAN13-13	20/07/2013	Engineer Creek	Dempster Bridge	65.35699	123.29301	0	8.08	12.2	229.06	21.91	1210.06	2534.39		329.31	3070.56	7.69	4.48	2834.50	76.50
CAN13-29	22/07/2013	Upper Engineer Creek	Dempster	65.10129	138.35582	0	6.98	9.2	85.87	15.23	893.66	3019.72		37.71	1881.58	6.14	1.02	3412.29	99.89
CAN13-30	22/07/2013	Upper Engineer Creek (upstream Red Creek)	Dempster	65.17129	138.36353	0	6.99	10.3	65.61	12.89	902.38	2025.11		33.85	2202.97	4.58	0.97	2296.26	80.56
CAN13-14	20/07/2013	Blackstone	Dempster Bridge	64.60593	138.34065	0	7.77	10.6	155.83	12.75	1174.57	1353.20		5.31	2280.78	5.02	0.56	1394.00	14.40
CAN13-25	22/07/2013	West Blackstone	Dempster Bridge	64.83523	138.36215	0	7.75	11	77.50	12.24	529.57	886.71		12.17	710.71	2.55	0.17	1628.13	14.69
CAN13-45	23/07/2013	Rock	Dempster	66.91653	136.34325	0	7.89	9	25.50	8.60	690.98	1884.46		9.55	1124.15	3.42	0.13	2890.43	14.49
CAN13-47	23/07/2013	Unnamed	Dempster	67.13862	136.00302	0	6.97	9.3	546.51	21.17	1132.31	866.52		4.85	2288.50	2.96	0.45	95.77	1.46

Table 4.2 | Ion concentrations in river sediments

Sample ID	River	Location	Date	Latitude	Longitude	Sample type	Sample Water Depth (m)	Suspended Sediment Concentration (mg/L)	[OC total] (%)		δ13Corg (permil)		F_{mod}	Al (µg g^{-1})	Na (µg g^{-1})	Si (µg g^{-1})	Re (pg g^{-1})
CAN09-11	Liard	Fort Simpson	16/7/2009	61.8423	121.2957									28744	5816	350604	1405
CAN10-50	Liard	Fort Simpson	13/09/2010	61.8234	121.2976	BL	Thalweg	-	0.14	Hilton et al., 2014	-28.2	Hilton et al., 2014	0.155	26796	6803	384839	862
CAN11-05	Liard	Fort Simpson	04/06/2011	61.8234	121.2976	spm	3.5	542	1.51	Hilton et al., 2014	-26.4	Hilton et al., 2014	0.465	55058	5059	274805	2515
CAN10-46	Liard	Fort Simpson	13/09/2010	61.8234	121.2976	spm	4.8	492	1.49	Hilton et al., 2014	-26.6	Hilton et al., 2014	0.633	38265	5712	336460	2283
CAN11-03	Liard	Fort Simpson	04/06/2011	61.8234	121.2976	spm	6.5	490	1.43	Hilton et al., 2014	-26.4	Hilton et al., 2014	0.481	56524	5200	275974	2667
CAN11-07	Liard	Fort Simpson	04/06/2011	61.8234	121.2976	spm	0	438	1.47	Hilton et al., 2014	-26.4	Hilton et al., 2014	0.452	58509	5015	264288	2986
CAN09-41	Peel	Fort MacPherson	21/7/2009	67.3319	134.8691									40620	2708	342723	4356
CAN13-02	Peel	Fort Macpherson	19/07/2013	67.33448	134.8776	Bank			1.44	this study	-26.6	this study					4122
CAN13-03	Peel	Fort Macpherson	19/07/2013	67.33448	134.8776	Bank-wood			19.40	this study	-27.0	this study					6936
CAN10-03	Peel	Fort MacPherson	07/09/2010	67.3313	134.8656	spm	8.5	250	2.00	Hilton et al., 2014	-26.8	Hilton et al., 2014	0.383	58694	3338	305188	3538
CAN10-06	Peel	Fort MacPherson	07/09/2010	67.3313	134.8656	spm	0	101	2.24	Hilton et al., 2014	-26.8	Hilton et al., 2014	0.284	76053	3487	277376	3587
CAN10-07	Peel	Fort MacPherson	07/09/2010	67.3313	134.8656	BL	Thalweg	-	0.75	Hilton et al., 2014	-28.0	Hilton et al., 2014	0.133	34205	2982	360439	2478
CAN11-77	Peel	Fort MacPherson	11/06/2011	67.3313	134.8656	spm	6	325	2.27	Hilton et al., 2014	-26.8	Hilton et al., 2014	0.480	58519	3680	285790	4817
CAN11-79	Peel	Fort MacPherson	11/06/2011	67.3313	134.8656	spm	0	146	1.85	Hilton et al., 2014	-26.6	Hilton et al., 2014	0.315	72153	4028	267139	4729
CAN09-48	Mackenzie	Tsiigehtchic	22/7/2009	67.4494	133.7406									27225	5490	342499	740
CAN10-16	Mackenzie	Tsiigehtchic	07/09/2010	67.4530	133.7405	BL	Thalweg	-	0.16	Hilton et al., 2014	-28.0	Hilton et al., 2014	0.162	27913	6766	358803	747
CAN10-15	Mackenzie	Tsiigehtchic	07/09/2010	67.4530	133.7405	spm	0	231	1.42	Hilton et al., 2014	-26.6	Hilton et al., 2014	0.354	83833	3487	242552	2876
CAN11-65	Mackenzie	Tsiigehtchic	11/06/2011	67.4530	133.7405	spm	13	941	1.62	Hilton et al., 2014	-26.4	Hilton et al., 2014	0.570	39509	5512	312667	1894
CAN11-66	Mackenzie	Tsiigehtchic	11/06/2011	67.4530	133.7405	spm	10	445	1.40	Hilton et al., 2014	-26.4	Hilton et al., 2014	0.444	50607	5089	291446	2069
CAN11-67	Mackenzie	Tsiigehtchic	11/06/2011	67.4530	133.7405	spm	5	322	1.43	Hilton et al., 2014	-26.6	Hilton et al., 2014	0.456	56614	4436	264428	2357
CAN11-68	Mackenzie	Tsiigehtchic	11/06/2011	67.4530	133.7405	spm	0	291	1.54	Hilton et al., 2014	-26.5	Hilton et al., 2014	0.451	59948	4281	260268	2642
CAN13-62	Mackenzie	Delta Middle Channel	24/07/2013	68.41313	134.0889	Bank-0.5m			0.84	this study	-27.0	this study					1966
CAN13-63	Mackenzie	Delta Middle Channel	24/07/2013	68.41313	134.0889	Bank-1.0m			2.32	this study	-27.2	this study					2652
CAN13-64	Mackenzie	Delta Middle Channel	24/07/2013	68.41313	134.0889	Bank-1.5m			1.29	this study	-26.6	this study					2723

Sample ID	River	Location	Date	Latitude	Longitude	Sample type	Sample Water Depth (m)	Suspended Sediment Concentration (mg/L)	[OC total] (%)		δ13Corg (permil)		F_{mod}	Al (µg g^{-1})	Na (µg g^{-1})	Si (µg g^{-1})	Re (pg g^{-1})
CAN10-28	Mackenzie	Delta	09/09/2010	68.4092	134.0805	spm	19	513	1.42	Hilton et al., 2014	-26.7	Hilton et al., 2014	0.419	56947	4229	276161	2105
CAN10-27	Middle Channel	Inuvik	8/9/2010	68.4457	134.2135									32290	4740	309115	1498
CAN11-89	Mackenzie	Delta	13/06/2011	68.4092	134.0805	spm	8	240	1.54	Hilton et al., 2014	-26.5	Hilton et al., 2014	0.401	62302	4507	261837	2794
CAN10-29	Mackenzie	Delta	09/09/2010	68.4092	134.0805	spm	17	275	1.49	Hilton et al., 2014	-26.6	Hilton et al., 2014	0.377	77165	3635	250498	2949
CAN10-32	Mackenzie	Delta	09/09/2010	68.4092	134.0805	spm	0	162	1.42	Hilton et al., 2014	-26.6	Hilton et al., 2014	0.307	90608	3264	238298	3003
CAN10-38	Mackenzie	Delta	09/09/2010	68.4092	134.0805	BL	Thalweg	-	0.37	Hilton et al., 2014	-28.0	Hilton et al., 2014	0.120	32258	5037	326363	1261
CAN11-87	Mackenzie	Delta	13/06/2011	68.4092	134.0805	spm	20	848	2.71	Hilton et al., 2014	-26.5	Hilton et al., 2014	0.568	43895	4440	278898	3595
CAN11-88	Mackenzie	Delta	13/06/2011	68.4092	134.0805	spm	15	850	1.00	Hilton et al., 2014	-26.6	Hilton et al., 2014	0.366	42215	4662	293562	1805
CAN09-53	Arctic Red	Tsiigehtchic	22/7/2009	67.4261	133.7787									45330	2960	300177	3380
CAN10-20	Arctic Red	Tsiigehtchic	7/9/2010	67.4395	133.7530									47146	3539	290371	4099
CAN10-17	Arctic Red	Tsiigehtchic	07/09/2010	67.4394	133.7529	spm	6	123	2.17		-26.8		0.299	73830	3042	251246	7214
CAN10-19	Arctic Red	Tsiigehtchic	07/09/2010	67.4394	133.7529	spm	0	123	1.95		-26.8		0.291	71608	3042	251246	7145
CAN13-10	Ogilvie	Along Dempster	20/07/2013	65.56789	138.1782	Bank			0.90		-28.3	this study					11354
CAN13-11	Ogilvie	Along Dempster	20/07/2013	65.45345	138.2198	Bedrock -Lignite			3.29		-31.4	this study					321459
CAN13-07	Eagle River	Nr Eagle Plains	19/07/2013	66.44326	136.7106	Bank			1.48		-26.5	this study					4453
CAN13-28	Upper Engineer Creek	Dempster	22/07/2013	65.10129	138.3558	Bank			3.18		-7.8	this study					13315
CAN13-31	Upper Engineer Creek (upstream Red Creek)	Dempster	22/07/2013	65.17129	138.3635	Bank			1.35		-28.9	this study					13343
CAN13-32	Upper Engineer Creek (upstream Red Creek)	Dempster	22/07/2013	65.17129	138.3635	Bank (orange mat)			1.67		-18.3	this study					12618
CAN13-14	Blackstone	Dempster bridge	20/07/2013	64.60593	138.3407				2.92		-27.8	this study					25064
CAN13-15	Blackstone	Dempster bridge	20/07/2013	64.60593	138.3407	Bank			0.93		-26.8	this study					2488
CAN13-24	West Blackstone	Dempster bridge	22/07/2013	64.83523	138.3622	Bedload -dredge			0.29		-27.1	this study					1050
CAN13-44	Rock	Dempster	23/07/2013	66.91653	136.3433	Bank			1.12		-29.6	this study					8669
CAN13-48	Unnamed	Dempster	23/07/2013	67.13862	136.003	Bank			0.68		-27.5	this study					2737

Table 4.3 | Composition of Re sources compiled from the literature.

Sample type	Details	Reference	n	[Re]/[Na] (µmol/mol)	±SE		[Re]/[S] (µmol/mol)	±SE
Silicate minerals	Peridotite (massive and xenolith)	Pearson et al., 2004	47	0.0236	0.0038		0.2948	0.0485
Silicate minerals	Spinel-lherzolite	Burton et al., 1999	1	0.0038			0.1832	
Silicate minerals	Basalts	Burton et al., 2002	3	0.0039	0.0006			
Silicate minerals	Peridotites	Reisberg and Lorand, 1995	11	0.0256	0.0133	*	0.1785	0.0281
Silicate minerals	Icelandic basalt	This study	1	0.0125			0.1702	
			average	*0.0139*			*0.2067*	
Sulphide	Sedimentary sulphides	Sundby et al., 2004	44	0.1063	0.0113	**	0.0011	0.0001
Sulphide	Sedimentary sulphides (pyrite)	Kelley et al., 2017	3	0.0968	0.0157	**	0.001	0.0006
			average	0.1016			0.0011	
OC_{petro}	Coals and siliciclastic rocks	Dai et al., 2015	16	140.1	11.5		1.169	0.522

*Na data on corresponding samples from Bodinier et al. (1988)

**Assuming a mean [Na] of sulphides = 176 µmol g^{-1} (Norman et al., 2002) and mean [S] = 16670 µmol g^{-1}

Table 4.4 | Estimates of OC_{petro} oxidation

*This calculation takes account of the fraction of OC_{petro} that may be present as graphite and less susceptible to oxidation ($f_{graphite}$ = 0–0.2) and the potential decoupling between OC_{petro} and Re in the weathering zone (fc = 0.5–1).

River catchment	Area (km^2)	Runoff ($mm\ yr^{-1}$)	Discharge ($m^3\ s^{-1}$)	Ref.	Suspended sediment yield ($t\ km^{-2}\ yr^{-1}$)	Ref.	$[Re]_{diss}$ average ($pg\ g^{-1}$)	±SE	[Re]/[C] (g/g)	±SE	Ref.	CO_2 flux* ($t\ km^{-2}\ yr^{-1}$)	+ error	- error
Mackenzie	1680000	134	7156	Environment Canada long-term discharges	124	Carson 1998	3.03	0.11	7.25E-07	1.50E-07	This study	0.38	0.10	0.09
Peel	70600	240	538	Environment Canada long-term discharges	295	Carson 1998	3.56	0.44	7.25E-07	1.50E-07	This study	0.79	0.23	0.19
Arctic Red	18600	211	124	Environment Canada long-term discharges	392	Carson 1998	3.39	0.46	7.25E-07	1.50E-07	This study	0.66	0.19	0.16
Liard	275000	223	1944	Environment Canada long-term discharges	149	Carson 1998	4.07	0.25	7.25E-07	1.50E-07	This study	0.84	0.23	0.20

4.8 Appendix

Following the approach of Gaillardet et al. (1999) and others, the general form of the mixing equation to determine the relative contribution of the endmembers in Figure 4.5 is given by:

Equation 5.1A $$\left(\frac{X}{Re}\right)_{diss} = \sum \left(\frac{X}{Re}\right)_i \times \alpha_i(Re)$$

where i refers to the organic matter, sulfide and silicate source reservoirs and α_i is the mixing proportion of Re, where the sum of the $\alpha_i = 1$. Because of the uncertainty on the exact compositions of the endmembers (particularly for the sulfide and OC_{petro}) we use this approach to provide a semi-quantitative estimate of the Re contribution from weathering of OC_{petro}. To do this, we solve Equation 1 using the endmember compositions provided in Table 4.3.

4.9 References

Beaulieu, E., Goddéris, Y., Labat, D., Roelandt, C., Calmels, D., Gaillardet, J., 2011. Modeling of water-rock interaction in the Mackenzie basin: Competition between sulfuric and carbonic acids. Chem. Geol. 289, 114–123.

Berner, R.A., 1982. Burial of organic-carbon and pyrite sulfur in the modern ocean – its geochemical and environmental significance. Am. J. Sci. 282, 451–473.

Berner, R.A., Caldeira, K., 1997. The need for mass balance and feedback in the geochemical carbon cycle. Geology 25, 955–956.

Berner, R.A., Canfield, D.E., 1989. A new model for atmospheric oxygen over Phanerozoic time. Am. J. Sci. 289, 333–361.

Berner, R.A., Maasch, K.A., 1996. Chemical weathering and controls on atmospheric O_2 and CO_2: Fundamental principles were enunciated by J.J. Ebelmen in 1845. Geochim. Cosmochim. Acta 60, 1633–1637.

Berner, R. a, Raiswell, R., 1984. Geology C / S method for distinguishing freshwater from marine sedimentary rocks. Geological Society of America, 365–368.

Beyssac, O., Cox, S.C., Vry, J., Herman, F., 2016. Peak metamorphic temperature and thermal history of the Southern Alps (New Zealand). Tectonophysics 676, 229–249.

Beyssac, O., Simoes, M., Avouac, J.P., Farley, K.A., Chen, Y.-G., Chan, Y.-C., Goffé, B., 2007. Late Cenozoic metamorphic evolution and exhumation of Taiwan. Tectonics 26.

Bodinier, J.L., 1988. Geochemistry and petrogenesis of the Lanzo peridotite body, western Alps. Tectonophysics 149, 67–88.

Bolton, E.W., Berner, R.A., Petsch, S.T., 2006. The weathering of sedimentary organic matter as a control on atmospheric O_2: II. Theoretical modeling. Am. J. Sci. 306, 575–615.

Bouchez, J., Beyssac, O., Galy, V., Gaillardet, J., France-Lanord, C., Maurice, L., Moreira-Turcq, P., 2010. Oxidation of petrogenic organic carbon in the Amazon floodplain as a source of atmospheric CO_2. Geology 38, 255–258.

Bouchez, J., Gaillardet, J., Lupker, M., Louvat, P., France-Lanord, C., Maurice, L., Armijos, E., Moquet, J.-S., 2012. Floodplains of large rivers: Weathering reactors or simple silos? Chem. Geol. 332, 166–184.

Bouchez, J., Galy, V., Hilton, R.G., Gaillardet, J., Moreira-Turcq, P., Perez, M.A., France-Lanord,

C., Maurice, L., 2014. Source, transport and fluxes of Amazon River particulate organic carbon: Insights from river sediment depth-profiles. Geochim. Cosmochim. Acta 133, 280–298.

Bouchez, J., Lupker, M., Gaillardet, J., France-Lanord, C., Maurice, L., 2011. How important is it to integrate riverine suspended sediment chemical composition with depth? Clues from Amazon River depth-profiles. Geochim. Cosmochim. Acta 75, 6955–6970.

Burton, K.W., Gannoun, A., Birck, J.-L., Allègre, C.J., Schiano, P., Clocchiatti, R., Alard, O., 2002. The compatibility of rhenium and osmium in natural olivine and their behaviour during mantle melting and basalt genesis. Earth Planet. Sci. Lett. 198, 63–76.

Burton, K.W., Schiano, P., Birck, J.L., Allegre, C.J., 1999. Osmium isotope disequilibrium between mantle minerals in a spinel-lherzolite. Earth Planet. Sci. Lett. 172, 311–322.

Calmels, D., Gaillardet, J., Brenot, A., France-Lanord, C., 2007. Sustained sulfide oxidation by physical erosion processes in the Mackenzie River basin: Climatic perspectives. Geology 35, 1003–1006.

Carson Conly, F. M. and Jasper, J. N., M.A., 1999. Riverine sediment balance of the Mackenzie Delta, Northwest Territories, Canada. Hydrol. Process. 13, 2499–2518.

Carson J.N.; Conly, F.M.., M.A.. J., 1998. Magnitude and Sources of Sediment Input to the Mackenzie Delta, Northwest Territories, 1974-94. Arctic 51, 116–124.

Chang, S.B., Berner, R.A., 1999. Coal weathering and the geochemical carbon cycle. Geochim. Cosmochim. Acta 63, 3301–3310.

Cohen, A.S., 2004. The rhenium-osmium isotope system: applications to geochronological and palaeoenvironmental problems. J. Geol. Soc. London. 161, 729–734.

Colodner, D., Sachs, J., Ravizza, G., Turekian, K., Edmond, J., Boyle, E., 1993. The geochemical cycle of rhenium: a reconnaissance. Earth Planet. Sci. Lett. 117, 205–221.

Colodner, D.C., Boyle, E.A., Edmond, J.M., 1993. Determination of Rhenium and Platinum in Natural Waters and Sediments, and Iridium in Sediments by Flow Injection Isotope Dilution Inductively Coupled Plasma Mass Spectrometry. Anal. Chem. 65, 1419–1425.

Cumming, V.M., Poulton, S.W., Rooney, A.D., Selby, D., 2013. Anoxia in the terrestrial environment during the late Mesoproterozoic. Geology 41, 583–586.

Dai, S.F., Seredin, V. V, Ward, C.R., Hower, J.C., Xing, Y.W., Zhang, W.G., Song, W.J., Wang, P.P., 2015. Enrichment of U-Se-Mo-Re-V in coals preserved within marine carbonate successions: geochemical and mineralogical data from the Late Permian Guiding Coalfield, Guizhou, China. Miner. Depos. 50, 159–186.

Dalai, T.K., Singh, S.K., Trivedi, J.R., Krishnaswami, S., 2002. Dissolved rhenium in the Yamuna River System and the Ganga in the Himalaya: Role of black shale weathering on the budgets of Re, Os, and U in rivers and CO_2 in the atmosphere. Geochim. Cosmochim. Acta 66, 29–43.

Dellinger, M., 2013. Apport des isotopes du lithium et des éléments alcalinsà la compréhension des processus d'altération chimiqueet de recyclage sédimentaire. École Dr. Des Sci. La Terre.

Dellinger, M., Gaillardet, J., Bouchez, J., Calmels, D., Galy, V., Hilton, R.G., Louvat, P., France-Lanord, C., 2014. Lithium isotopes in large rivers reveal the cannibalistic nature of modern continental weathering and erosion. Earth Planet. Sci. Lett. 401, 359–372.

Ebelmen, J.J., 1845. Sur les produits de la décomposition desespèces minérales de la famille des silicates. Anna. Mines 7, 3–66.

Emberson, R., Hovius, N., Galy, A., Marc, O., 2016. Chemical weathering in active mountain belts controlled by stochastic bedrock landsliding. Nat. Geosci. 9, 42–45.

Environment Canada. Water Survey of Canada. <https://www.canada.ca/en/environment-climate-change/services/water-overview/quantity/monitoring/survey.html> (accessed 5.10.17).

FranceLanord, C., Derry, L.A., 1997. Organic carbon burial forcing of the carbon cycle from

Himalayan erosion. Nature 390, 65–67.

Gaillardet, J., Dupre, B., Louvat, P., Allegre, C.J., 1999. Global silicate weathering and CO_2 consumption rates deduced from the chemistry of large rivers. Chem. Geol. 159, 3–30.

Gaillardet, J., Viers, J., Dupré, B., 2003. Trace elements in river waters. Treatise on geochemistry 5, 605.

Galy, A., France-Lanord, C., 1999. Weathering processes in the Ganges-Brahmaputra basin and the riverine alkalinity budget. Chem. Geol. 159, 31–60.

Galy, V., Beyssac, O., France-Lanord, C., Eglinton, T., 2008a. Recycling of Graphite During Himalayan Erosion: A Geological Stabilization of Carbon in the Crust. Science. 322, 943–945.

Galy, V., Bouchez, J., France-Lanord, C., 2007. Determination of total organic carbon content and delta C-13 in carbonate-rich detrital sediments. Geostand. Geoanalytical Res. 31, 199–207.

Galy, V., France-Lanord, C., Lartiges, B., 2008b. Loading and fate of particulate organic carbon from the Himalaya to the Ganga-Brahmaputra delta. Geochim. Cosmochim. Acta 72, 1767–1787.

Gramlich, J.W., Murphy, T.J., Garner, E.L., Shields, W.R., 1973. Absolute isotopic abundance ratio and atomic weight of a reference sample of rhenium. J. Res. Natl. Bur. Stand. Sect. A Phys. Chem. 77A, 691.

Hilton, R.G., Gaillardet, J., Calmels, D., Birck, J.-L., 2014. Geological respiration of a mountain belt revealed by the trace element rhenium. Earth Planet. Sci. Lett. 403, 27–36.

Hilton, R.G., Galy, V., Gaillardet, J., Dellinger, M., Bryant, C., O'Regan, M., Grocke, D.R., Coxall, H., Bouchez, J., Calmels, D., 2015. Erosion of organic carbon in the Arctic as a geological carbon dioxide sink. Nature 524, 84-U162.

Holmes, R.M., McClelland, J.W., Peterson, B.J., Shiklomanov, I.A., Shiklomanov, A.I., Zhulidov, A. V., Gordeev, V. V., Bobrovitskaya, N.N., 2002. A circumpolar perspective on fluvial sediment flux to the Arctic ocean. Global Biogeochem. Cycles 16, 45-1-45–14.

Horan, K., Hilton, R.G., Selby, D., Ottley, C.J., Gröcke, D.R., Hicks, M., Burton, K.W., 2017. Mountain glaciation drives rapid oxidation of rock-bound organic carbon. Sci. Adv. 3.

Huh, Y., Birck, J.L., Allegre, C.J., 2004. Osmiurn isotope geochemistry in the Mackenzie River basin. Earth Planet. Sci. Lett. 222, 115–129.

Jacobson, A.D., Blum, J.D., Chamberlain, C.P., Craw, D., Koons, P.O., 2003. Climatic and tectonic controls on chemical weathering in the New Zealand Southern Alps. Geochim. Cosmochim. Acta 67, 29–46.

Jaffe, L.A., Peucker-Ehrenbrink, B., Petsch, S.T., 2002. Mobility of rhenium, platinum group elements and organic carbon during black shale weathering. Earth Planet. Sci. Lett. 198, 339–353.

Johnston, D.T., Macdonald, F.A., Gill, B.C., Hoffman, P.F., Schrag, D.P., 2012. Uncovering the Neoproterozoic carbon cycle. Nature 483, 320.

Kelley, K.D., Selby, D., Falck, H., Slack, J.F., 2017. Re-Os systematics and age of pyrite associated with stratiform Zn-Pb mineralization in the Howards Pass district, Yukon and Northwest Territories, Canada. Miner. Depos. 52, 317–335.

Larsen, I.J., Almond, P.C., Eger, A., Stone, J.O., Montgomery, D.R., Malcolm, B., 2014. Rapid Soil Production and Weathering in the Southern Alps, New Zealand. Science 343, 637–640.

Lupker, M., France-Lanord, C., Lave, J., Bouchez, J., Galy, V., Metivier, F., Gaillardet, J., Lartiges, B., Mugnier, J.-L., 2011. A Rouse-based method to integrate the chemical composition of river sediments: Application to the Ganga basin. J. Geophys. Res. Surf. 116.

Macdonald, R.W., Solomon, S.M., Cranston, R.E., Welch, H.E., Yunker, M.B., Gobeil, C., 1998. A sediment and organic carbon budget for the Canadian beaufort shelf. Mar. Geol. 144, 255–

273.

Maher, K., 2011. The role of fluid residence time and topographic scales in determining chemical fluxes from landscapes. Earth Planet. Sci. Lett. 312, 48–58.

Maher, K., Chamberlain, C.P., 2014. Hydrologic Regulation of Chemical Weathering and the Geologic Carbon Cycle. Science. 343, 1502–1504.

Marty, B., Tolstikhin, I.N., 1998. CO_2 fluxes from mid-ocean ridges, arcs and plumes. Chem. Geol. 145, 233–248.

McClelland, J.W., Holmes, R.M., Peterson, B.J., Raymond, P.A., Striegl, R.G., Zhulidov, A. V, Zimov, S.A., Zimov, N., Tank, S.E., Spencer, R.G.M., Staples, R., Gurtovaya, T.Y., Griffin, C.G., 2016. Particulate organic carbon and nitrogen export from major Arctic rivers. Global Biogeochem. Cycles 30, 629–643.

Meisel, T., Moser, J., 2004. Platinum-Group Element and Rhenium Concentrations in Low Abundance Reference Materials. Geostand. Geoanalytical Res. 28, 233–250.

Meybeck, M., 1987. Global chemical weathering of surficial rocks estimated from river dissolved loads. Am. J. Sci. 287, 401–428.

Miller, C.A., Peucker-Ehrenbrink, B., Walker, B.D., Marcantonio, F., 2011. Re-assessing the surface cycling of molybdenum and rhenium. Geochim. Cosmochim. Acta 75, 7146–7179.

Millot, R., Gaillardet, J., Dupre, B., Allegre, C.J., 2003. Northern latitude chemical weathering rates: Clues from the Mackenzie River Basin, Canada. Geochim. Cosmochim. Acta 67, 1305–1329.

Millot, R., Gaillardet, J., Dupre, B., Allegre, C.J., 2002. The global control of silicate weathering rates and the coupling with physical erosion: new insights from rivers of the Canadian Shield. Earth Planet. Sci. Lett. 196, 83–98.

Moon, S., Chamberlain, C.P., Hilley, G.E., 2014. New estimates of silicate weathering rates and their uncertainties in global rivers. Geochim. Cosmochim. Acta 134, 257–274.

Norman, M., Robinson, P., Clark, D., 2003. Major- and trace-element analysis of sulfide ores by laser-ablation ICP-MS, solution ICP-MS, and XRF: New data on international reference materials. Can. Mineral. 41, 293–305.

Pagani, M., Caldeira, K., Berner, R., Beerling, D.J., 2009. The role of terrestrial plants in limiting atmospheric CO_2 decline over the past 24 million years. Nature 460, 85-U94.

Pearson, D.G., Irvine, G.J., Ionov, D.A., Boyd, F.R., Dreibus, G.E., 2004. Re-Os isotope systematics and platinum group element fractionation during mantle melt extraction: a study of massif and xenolith peridotite suites. Chem. Geol. 208, 29–59.

Petsch, S.T., 2014. Weathering of organic carbon, 2nd ed, Treatise on Geochemistry . Elsevier.

Pierson-Wickmann, A.-C., Reisberg, L., France-Lanord, C., 2002. Behavior of Re and Os during low-temperature alteration: Results from Himalayan soils and altered black shales. Geochim. Cosmochim. Acta 66, 1539–1548.

Priyadarshi, N., 2005. Sodium in Natural Waters, in: Water Encyclopedia.

Rahaman, W., Singh, S.K., Shukla, A.D., 2012. Rhenium in Indian rivers: Sources, fluxes, and contribution to oceanic budget. Geochemistry, Geophys. Geosystems 13.

Reeder, S.W., Hitchon, B., Levinson, A.A., 1972. Hydrogeochemistry of the surface waters of the Mackenzie River drainage basin, Canada—I. Factors controlling inorganic composition. Geochim. Cosmochim. Acta 36, 825–865.

Reisberg, L., Lorand, J.P., 1995. Longevity of sub-continental mantle lithosphere from osmium isotope systematics in orogenic peridotite massifs. Nature 376, 159–162.

Ross, D.J.K., Bustin, R.M., 2009. Investigating the use of sedimentary geochemical proxies for paleoenvironment interpretation of thermally mature organic-rich strata: Examples from the Devonian-Mississippian shales, Western Canadian Sedimentary Basin. Chem. Geol. 260, 1–

19.

Selby, D., Creaser, R.A., 2003. Re-Os geochronology of organic rich sediments: an evaluation of organic matter analysis methods. Chem. Geol. 200, 225–240.

Sundby, B., Martinez, P., Gobeil, C., 2004. Comparative geochemistry of cadmium, rhenium, uranium, and molybdenum in continental margin sediments. Geochim. Cosmochim. Acta 68, 2485–2493.

Tipper, E.T., Bickle, M.J., Galy, A., West, A.J., Pomies, C., Chapman, H.J., 2006. The short term climatic sensitivity of carbonate and silicate weathering fluxes: Insight from seasonal variations in river chemistry. Geochim. Cosmochim. Acta 70, 2737–2754.

Torres, M.A., West, A.J., Clark, K.E., Paris, G., Bouchez, J., Ponton, C., Feakins, S.J., Galy, V., Adkins, J.F., 2016. The acid and alkalinity budgets of weathering in the Andes–Amazon system: Insights into the erosional control of global biogeochemical cycles. Earth Planet. Sci. Lett. 450, 381–391.

Torres, M.A., West, A.J., Li, G., 2014. Sulphide oxidation and carbonate dissolution as a source of CO_2 over geological timescales. Nature 507, 346–349.

Vonk, J.E., Giosan, L., Blusztajn, J., Montlucon, D., Pannatier, E.G., McIntyre, C., Wacker, L., Macdonald, R.W., Yunker, M.B., Eglinton, T.I., 2015. Spatial variations in geochemical characteristics of the modern Mackenzie Delta sedimentary system. Geochim. Cosmochim. Acta 171, 100–120.

Wadham, J.L., Bottrell, S., Tranter, M., Raiswell, R., 2004. Stable isotope evidence for microbial sulphate reduction at the bed of a polythermal high Arctic glacier. Earth Planet. Sci. Lett. 219, 341–355.

Walker, J.C.G., Hays, P.B., Kasting, J.F., 1981. A negative feedback mechanism for the long-term stabilization of Earth's surface temperature. J. Geophys. Res. Ocean. 86, 9776–9782.

West, A.J., 2012. Thickness of the chemical weathering zone and implications for erosional and climatic drivers of weathering and for carbon-cycle feedbacks. Geology 40, 811–814.

West, A.J., Galy, A., Bickle, M., 2005. Tectonic and climatic controls on silicate weathering. Earth Planet. Sci. Lett. 235, 211–228.

Wheeler, J O; Hoffman, P F; Card, K D; Davidson, A; Sanford, B V; Okulitch, A V; Roest, W.R., 1996. Geological map of Canada. Nat. Resour. Canada.

Yeghicheyan, D., Bossy, C., Bouhnik Le Coz, M., Douchet, C., Granier, G., Heimburger, A., Lacan, F., Lanzanova, A., Rousseau, T.C.C., Seidel, J.-L., Tharaud, M., Candaudap, F., Chmeleff, J., Cloquet, C., Delpoux, S., Labatut, M., Losno, R., Pradoux, C., Sivry, Y., Sonke, J.E., 2013. A Compilation of Silicon, Rare Earth Element and Twenty-One other Trace Element Concentrations in the Natural River Water Reference Material SLRS-5 (NRC-CNRC). Geostand. Geoanalytical Res. 37, 449–467.

Chapter 5

Controls on the molybdenum isotope fractionation during weathering and erosion in river catchments

Paringa River in the western Southern Alps, New Zealand; September 2014

Summary: The adsorption of isotopically light molybdenum to (oxyhyr)oxides appears to control the fraction and isotope composition of molybdenum remaining in river water.

A version of this chapter will be submitted to Geochimica et Cosmochimica Acta.

The paper will be co-authored by Alex J. M^{c}Coy-West[1], Robert G. Hilton[2], Chris Ottley[1], David Selby[1], and Kevin W. Burton[1]

Affiliations: [1]Department of Earth Sciences, Durham University, Durham, DH1 3LE, UK.

[2]Department of Geography, Durham University, Durham, DH1 3LE, UK.

Abstract

Molybdenum (Mo) isotopes can be used to investigate the weathering and redox reactions that control the composition of continental runoff and ultimately the long-term evolution of Mo isotopes in seawater. Here, we present measurements of $\delta^{98/95}$Mo for rivers in mountain catchments in the Southern Alps, New Zealand; the Mackenzie River Basin and the Yukon, north west Canada; and the Skaftá River, Iceland. These settings have contrasting lithologies, differing erosion rates and processes (glacial versus non-glacial), and variable extents of biological cover, which allow us to explore the potential controls on dissolved $\delta^{98/95}$Mo variability in rivers. To understand the processes involved, we have examined weathering products on hillslopes, river bed materials and river suspended sediments, alongside the dissolved products of weathering.

We observe large differences in the dissolved river $\delta^{98/95}$Mo composition across the different study sites that reflect the variability (~0.7‰) in the $\delta^{98/95}$Mo composition of the bedrock geology and the primary minerals sourcing Mo to the rivers. The Mo isotope composition of river waters varies between New Zealand ($\delta^{98/95}$Mo = 0.00 to 0.32‰), Iceland ($\delta^{98/95}$Mo = 0.26 to 0.47‰) and the Mackenzie and Yukon rivers ($\delta^{98/95}$Mo = 0.73 to 1.53‰). Molybdenum is sourced from sulfides, silicate minerals and petrogenic organic carbon (OC_{petro}) and their relative contribution to the dissolved river Mo budget is evaluated using [Mo]/[Na*] and [Mo]/[SO_4^{2-}] ion ratios found in pure mineral endmembers. We find that the bulk of dissolved Mo is derived from OC_{petro} in the Southern Alps and the main channels of the Mackenzie River Basin (>90%), with sulfides providing a slightly greater contribution to some of the smaller rivers in the south of the Mackenzie River Basin. In Iceland, dissolved Mo in the Skaftá River is derived predominantly from silicate minerals (~99%), with a minor role of sulfides also apparent.

In all of the river catchments, a shift towards heavier Mo isotope compositions in the dissolved load ($\Delta^{98/95}Mo_{diss\text{-}BM}$ = ~0.4–0.8‰) is observed, relative to the bed materials, which is independent of lithological variability and cannot be explained by primary mineral dissolution alone. Potential mechanisms that could drive this fractionation include atmospheric inputs, biological processes, secondary weathering reactions and the cycling of Mo by organic matter. However, we find that the $\delta^{98/95}$Mo composition of the river waters becomes heavier as the amount of Mo remaining in solution decreases, suggesting that isotopically light Mo is being removed from the dissolved load. In support of this hypothesis, the $\delta^{98/95}$Mo data from colluvium samples from hillslopes of the western Southern Alps are enriched in isotopically light Mo, by up to 0.9‰, relative to local river bed materials. The $\delta^{98/95}$Mo and Mo concentration data are most consistent with the adsorption of Mo on to Fe and Mn (oxyhydr)oxides being the primary driver of the observed fractionation, and the fractionation factors observed closely match those predicted by experimental modelling studies.

5.1. Introduction

The mobilisation and sequestration of molybdenum (Mo) in Earth's surface environments bears on our understanding of the weathering and redox reactions that control atmospheric gas concentrations (Arnold et al., 2004), biological processes (e.g. Barron et al., 2009) and the chemistry of rivers and oceans (Archer and Vance, 2008). Molybdenum cycling is relevant for interpreting the evolution of atmospheric O_2 and CO_2 as a result of its dynamic redox behaviour in surface environments (e.g. Bertine and Turekian, 1973; Morford and Emerson, 1999). For living organisms, Mo represents an essential micronutrient required by enzymes for catalysing reactions in carbon, sulfur and nitrogen metabolism. The largest flux of Mo to the World's oceans is thought to be from rivers, which are estimated to discharge ~3.1×10^8 mol yr^{-1} of Mo to the oceans (Miller et al., 2011); this is much larger than the ~0.2×10^8 mol yr^{-1} derived from hydrothermal systems (Kendall et al., 2017; Wheat et al., 2002) (***Chapter 1***, Figure 1.11). As such, the Mo isotope composition of river waters (reported as $\delta^{98/95}Mo = [(({}^{98}Mo/{}^{95}Mo)_{sample} / ({}^{98}Mo/{}^{95}Mo)_{NIST\text{-}3134}) - 1] \times 1000$ [‰]) places a fundamental boundary condition on the Mo isotope composition of the oceans (Archer and Vance, 2008; Pearce et al., 2010a)

Molybdenum is removed from seawater in sediments and this can induce an isotope fractionation that can vary depending on the redox state of the depositional environment. Under oxidising conditions, Mo is present in solution as the stable hexavalent oxyanion molybdate, MoO_4^{2-}. In this form, Mo is slowly removed from the water column through uptake into ferromanganese phases, such as magnetite, ferrihydrite, goethite and hematite minerals, which preferentially incorporate isotopically light Mo (Barling et al., 2001; Barling and Anbar, 2004; Goldberg et al., 2009; Miller et al., 2011; Wasylenki et al., 2011). Oxic sediments tend to show the largest Mo isotope fractionation, and their Mo isotope composition broadly scales with the degree of anoxia (Kendall et al., 2017). As a result of this fractionation, the modern oceans are the heaviest Mo reservoir on Earth (Kendall et al., 2017).

In contrast, Mo is readily removed from solution in anoxic-sulfidic waters with very little net isotope fractionation. In the presence of reduced sulfur, Mo forms oxothiomolybdate ions, $[MoO_4\text{-}xSx]^{2-}$, which are highly particle-reactive and thus are rapidly removed from solution (e.g. Barling et al., 2001; Bostick et al., 2003; Dahl et al., 2013; Helz et al., 1996). In euxinic settings, the reduced Mo fractionation means that the isotope composition of sediments is more similar to seawater, with some restricted marine basins implying quantitative Mo removal (e.g. Arnold et al., 2004; Barling et al., 2001; Neubert et al., 2008; Noordmann et al., 2015). These features have led to the use of Mo isotopes to understand palaeo-redox conditions in marine sediments from the geological record (e.g. Algeo and Lyons, 2006; Dean et al., 1999; Pearce et al., 2010b; Scott et al., 2008).

However, to interpret $\delta^{98/95}$Mo records from sediments requires knowledge of the processes that determine the Mo isotope composition of continental runoff (Dickson, 2017). Measurements of $\delta^{98/95}$Mo in the dissolved load of rivers display large variability from -0.1‰ to 2.15‰ (Archer and Vance, 2008). The degree to which this variability reflects the weathering source (i.e. $\delta^{98/95}$Mo of rocks being weathered) versus process (e.g. fractionation of Mo during weathering or cycling by the biosphere) still remains unclear (Neubert et al., 2011). When rocks are exposed to weathering reactions, Mo can be oxidised to the soluble MoO_4^{2-} anion, which coordinates weakly with other environmentally common ligands and tends to dominate aqueous speciation. In the form of the MoO_4^{2-} anion, Mo is susceptible to leaching from the soils (Arnorsson and Oskarsson, 2007; Gupta et al., 1997; Miller et al., 2011) and may be mobilised and transported through the hydrological network of a catchment, delivering dissolved Mo to rivers (Miller et al., 2011). Mo (VI) species are abundant over a range of Eh and pHs that span typical freshwater (and seawater) conditions (Kendell et al., 2017).

Sulfide minerals, such as diagenetic pyrite, and organic matter are thought to be major host phases of Mo in the Earth's crust (Raiswell and Plant, 1980) and they are generally enriched in heavy isotopes compared to silicate minerals (e.g. Voegelin et al., 2012). The dissolution of these easily oxidised phases will therefore yield higher $\delta^{98/95}$Mo values in river waters than would be expected from the dissolution of primary silicate minerals (Neubert et al., 2008; Neubert et al., 2011). Nevertheless, although dissolved river $\delta^{98/95}$Mo values can directly reflect the Mo isotope composition of the catchment lithology (Malinovsky et al., 2007; Neubert et al., 2011), elsewhere, isotope fractionation has been observed (Pearce et al., 2010a; Scheiderich et al., 2010) or inferred to explain larger isotope variability (Archer and Vance 2008). For instance, the discharge-weighted mean river $\delta^{98/95}$Mo (based on measurements from rivers making up 22% of global water discharge) is ~0.45‰ (Archer and Vance 2008). This is higher than the $\delta^{98/95}$Mo values of silicate rocks of the upper continental crust, which have a typical range of approximately $\delta^{98/95}$Mo = 0 to 0.15‰ (Greber et al., 2014; Voegelin et al., 2014; Willbold and Elliott, 2017), and implies significant Mo isotope fractionation has occurred between the bulk silicate crust and continental runoff. The fractionation of Mo isotopes may arise during the following processes: i) incongruent dissolution of primary minerals; ii) secondary clay mineral formation; iii) the development of iron (Fe) and manganese (Mn) (oxyhydr)oxides; iv) reactions associated with soil organic matter and redox processes; v) biological cycling; and vi) atmospheric inputs (Siebert, et al. 2015). The effects of these processes are only just beginning to be explored at the soil profile scale (Siebert et al., 2015; King et al., 2016) and the river catchment scale (e.g. Neubert et al., 2011; Voegelin et al., 2012), with little known about the Mo isotope composition of river suspended sediments (Siebert et al., 2015).

To better constrain the controls on the $\delta^{98/95}$Mo values of river waters, we have examined the Mo concentration and $\delta^{98/95}$Mo values in river dissolved loads ($\delta^{98/95}Mo_{diss}$), suspended particulate material ($\delta^{98/95}Mo_{SPM}$) and river bed materials ($\delta^{98/95}Mo_{BM}$), in addition to soil colluvium ($\delta^{98/95}Mo_{COL}$) and surface soil litter ($\delta^{98/95}Mo_{litter}$) samples that characterize Mo behaviour in the weathering zone of hillslopes. We have also evaluated the behaviour of Mo in relation to the element rhenium (Re), which is thought to be sourced from similar mineral phases to Mo (Peucker-Ehrenbrink and Hannigan, 2000) and also becomes soluble and mobile following weathering (as ReO_4^-) (Miller et al., 2011). However, in contrast to Mo, Re is thought to be rarely incorporated into secondary weathering products and terrestrial organic matter (Colodner et al. 1993). To assess the potential mechanisms driving Mo isotope fractionation in rivers we also undertook selective extractions on river suspended sediments, which allowed the $\delta^{98/95}$Mo values associated with different particulate phases to be interpreted.

Our investigation uses three locations with contrasting lithology, erosion rates and erosional processes (e.g. glacial versus non-glacial catchments). First, the rivers of the western Southern Alps, New Zealand, are considered. These rivers drain meta-sedimentary rocks with relatively uniform composition along strike of the Alpine Fault (Mortimer, 2004), but there is variability in glacial coverage, exposure of bare rock and temperate rainforest (Hall and Riggs, 2011; Hilton et al., 2008). Consequently, the western Southern Alps permit an assessment of the role that biological productivity and glacial processes may have on Mo mobilization and isotope fractionation within river catchments. Second, we consider samples from river catchments within the Mackenzie River Basin and the Yukon River, north-west Canada. Rivers there drain sedimentary rocks with higher organic matter and sulfide contents relative to the New Zealand catchments (Calmels et al., 2007; Hilton et al., 2015; Marsh et al., 2003; Mathez et al., 1995; Verplanck et al., 2008). Third, we assess samples from the glacial Skaftá River in Iceland that drains basaltic rock, to complement existing $\delta^{98/95}$Mo data from Iceland (Pearce et al., 2010a). Together, the catchments have allowed us to assess any common behaviour of $\delta^{98/95}$Mo isotopes with differences in lithology, erosion rate and biological cover. We will demonstrate that lithological differences can explain only some of the variability in the rivers across the studied sites, and that there is evidence for a further 0.4–0.8‰ offset between river waters and unweathered river sediments, which can be attributed to fractionation during weathering and transport; consistent with the complexation of Mo with (oxyhydr)oxides.

5.2. Methodology

5.2.1 Sample sites

The Southern Alps is a steep mountain belt built by transpression along the Alpine Fault and it has an uplift rate of 8–10 mm yr^{-1} (Tippett and Kamp, 1995). The western flank has a temperate climate, with a high erosion rate driven by orographic precipitation, exceeding 8 m yr^{-1}, steep slopes and bedrock landslides that expose meta-sedimentary rocks (Hovius et al., 1997; Jacobson et al., 2003). Along the western Southern Alps, the metamorphic grade varies perpendicular to the Alpine Fault strike, but the sedimentary protolith is similar in all catchments and the organic carbon content of the rocks ranges from ~0.1 to 0.2% (Hilton et al., 2008; Nibourel et al., 2015). Physical erosion rates vary from 4072 t km^{-2} yr^{-1} in the Haast catchment to 10,136 t km^{-2} yr^{-1} in the Whataroa catchment (Hicks et al., 2011). Chemical erosion yields range from 110 t km^{-2} yr^{-1} in the Hokitika catchment to 120 t km^{-2} yr^{-1} in the Whataroa catchment (Jacobson and Blum, 2003). However, there are significant differences in glacial coverage, including two catchments with large valley glaciers (Waiho and Fox) and a large area of exposed bare rock, contrasting with catchments of similar size but with <4% glacial coverage (e.g. Poerua, Waitangitaona, Makawhio) and developed temperate rainforest. River samples were collected from 13 major catchments in the western Southern Alps and two draining the eastern flank (Figure 5.1).

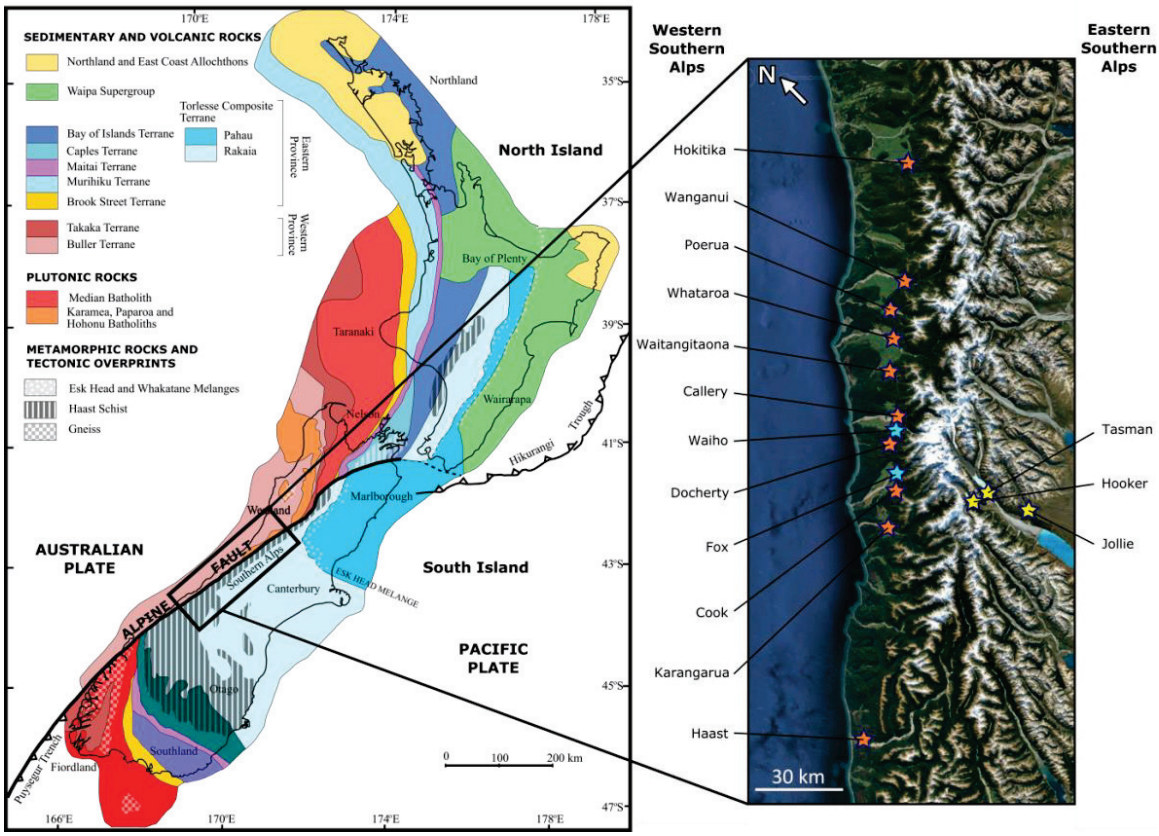

Figure 5.1 Geological map and sampling localities in New Zealand. Geological map is adapted from Mortimer et al. (2004). Inset indicates the main river catchments sampled in the Southern Alps.

The Mackenzie River Basin spans an area of 1.78×10^6 km^2 and drains the Rocky and Mackenzie Mountains (Rockies) in north west Canada. The basin geology comprises 68.3% sedimentary rocks (clastics and carbonates), including the carbonate platform in the central part, the carbonaceous shales of the interior plain and the Rockies, which are mainly composed of carbonate, dolomitic limestone and shale (Calmels et al., 2007; Millot et al., 2003; Reeder et al., 1972; Wheeler et al. 1996). The sedimentary rocks host organic carbon, with petrogenic organic carbon (OC_{petro}) concentrations that are typically between 0.1 and 0.3 wt. % organic carbon (OC), but can reach 0.6 wt. % locally in the Peel catchment (Hilton et al., 2015). There are 29.2% of non-sedimentary rocks in the basin, including the granitic rock outcropping in the Rockies and 2.5% of evaporites in the plains (Beaulieu et al., 2011; Millot et al., 2003). Five key localities from across the basin were included in a Mo isotope analysis. Two sampling localities were along the main channel of the Mackenzie River, at the Environment Canada gauging stations Tsiigehtchic and the Middle Delta. In addition, the Peel River and its tributary, the Ogilvie River, which join the Mackenzie River between Tsiigetchic and the Middle Delta were assessed (Figure 5.2). The Yukon River, sampled at Dawson to the south west of Mackenzie River Basin, was also included as an example of a river where glacial and periglacial processes operate in headwaters over rocks that are relatively enriched in sulfide and organic carbon, compared to the Southern Alps (Marsh et al., 2003; Verplanck et al., 2008; Mathez et al., 1995). The physical erosion rate in the Canadian catchments is variable: the average annual suspended sediment yields for the Mackenzie (Tsiigetchic) and Peel catchments are 124 t km^{-2} yr^{-1} and 294 t km^{-2} yr^{-1}, respectively (Carson and Conly, 1998). In the Yukon catchment (at Dawson) physical erosion rates are 125 t km^{-2} yr^{-1} (Brabets et al., 2000).

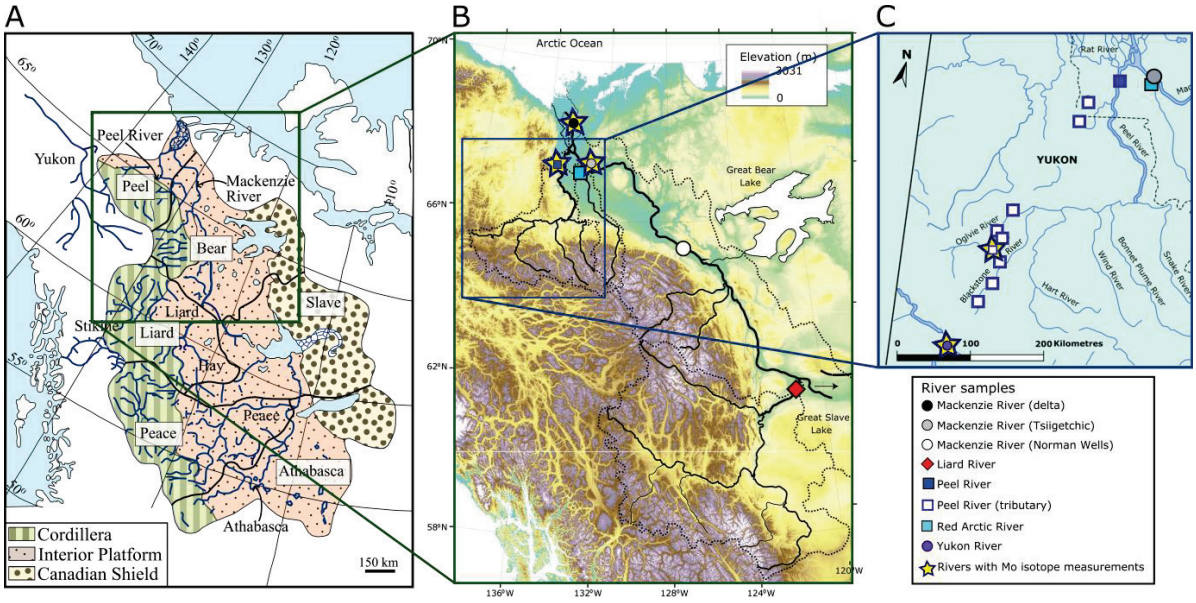

Figure 5.2 Sampling of the Mackenzie River Basin, northern Canada. A. Main lithological sub-divisions (Cordillera, Interior Platform and Canadian Shield) and the major sub-basins (Peel, Bear, Liard, Slave, Peace and Athabasca) of the Mackenzie River Basin (modified from Millot et al., 2003). **B.** Location of major rivers sampled within the Mackenzie River Basin (modified from Hilton et al., 2015). **C.** Location of sampling sites along Peel tributaries. Samples included in the Mo isotope analysis are marked with stars.

In Iceland, sampling focussed on the Skaftá River catchment, which drains the Skaftárjökull area of the Vatnajökull glacier in the south of the island (Figure 5.3). Although this region is predominantly basaltic, the Skaftá River is sourced directly from the Vatnajökull glacier, which covers sulfide rich rocks from the tholeiitic rock suite (Jónsdóttir, 2008; Torssander, 1989). Bedrock ages here range from Quaternary to Recent. Average physical erosion rates are ~2084 t km^{-2} yr^{-1}, whilst the average chemical weathering rates are 150 t km^{-2} yr^{-1} (Gislason et al., 1996; Pogge von Strandmann et al., 2006).

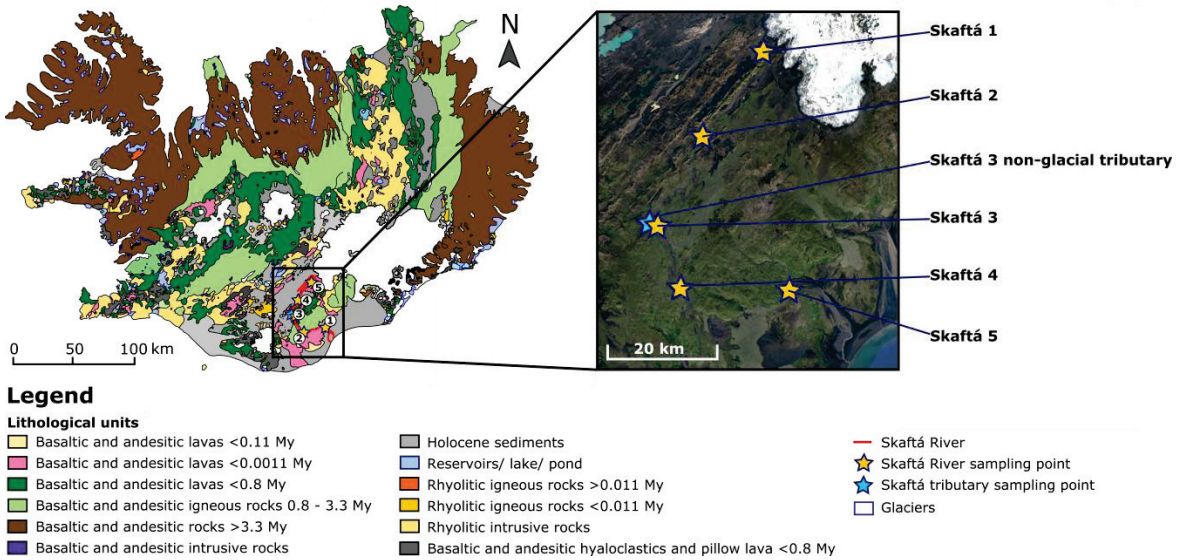

Figure 5.3 Geological map and sampling localities in Iceland. Geological map is adapted from Oskarsdottir et al. (2011). Inset shows sampling localities along the Skaftá River.

5.2.2 Sample collection

To assess the primary controls and processes affecting $\delta^{98/95}$Mo values in rivers, we sampled the dissolved load and the solid products of weathering and erosion, including weathered colluvium from hillslopes, suspended river sediments and relatively un-weathered river bed materials of sand and finer grade. A summary of the number of samples from each study region used for $\delta^{98/95}$Mo analyses and additional water samples included in Mo abundance analyses is provided in Table 5.1.

5.2.2.1 Dissolved load

In the Southern Alps, river waters (n = 51) were collected from the centre of river channels at their surface. Catchments were sampled 2–6 times over a 1 month period (14/09/14 – 03/10/14) under different discharge regimes. Each water sample (7–8 litres) was transferred into a clean bucket and decanted to sterile plastic bags. The sample bags were weighed to determine the sample volume, prior to water filtration through 142 mm diameter, 0.2 µm polyethersulfone (PES) filters in pre-cleaned filter units within a day of collection. Samples were stored in acid-cleaned low-density polyethylene (LDPE) bottles in the dark at 4°C. All water samples intended for cation and trace

metal analysis were acidified in the field to pH ~2 following published methods (Dalai et al., 2002; Hilton et al., 2014) with an un-acidified aliquot kept for anion analyses. Out of the total 51 samples collected, 13 samples from the major rivers draining the western Southern Alps and 3 from the eastern Southern Alps were also selected for Mo isotope analysis (Figure 5.1).

Thirteen samples from across the Mackenzie River Basin, Canada, were collected by similar methods over 2009–2013, including the Liard and Arctic Red tributaries to the Mackenzie River and several tributaries to the Peel River. These river waters were used to assess patterns in Mo abundance and its source across the basin (Figure 5.2). Four samples from the Mackenzie River Basin and the one sample from the Yukon River catchment, Canada, were utilized for the Mo isotope analyses. Similar methods were used to collect water samples from the Skaftá River catchment in southern Iceland (n = 10) in 2013 and 2014, and five of the samples collected in 2014 were included in a Mo isotope analysis. In addition, in the western Southern Alps, two 250 mL rainwater samples were collected from the Franz Josef area over separate 10 h periods to evaluate the potential atmospheric contribution of Mo to the river waters.

5.2.2.2 Solid materials

In the western Southern Alps, soils are generally thin and weathering profiles are often poorly developed (Larsen et al., 2014). However, in an attempt to characterize Mo behaviour in the weathering zone, and to assess the potential for isotope fractionation of Mo occurring within soils (King et al., 2016; Siebert et al., 2015), we measured the Mo isotope composition of surface soils through to more weathered colluvium on the forested hillslopes of Alex Knob, which drains to the Doherty Creek catchment. Four ~500 cm^3 sized samples of weathered colluvium from 10 to 70 cm depth below the soil surface were collected at three sites. Four surface soil samples comprising a mixture of litter and mineral soil were collected using a metal trowel, and transferred to sterile plastic bags.

To help constrain the chemical composition of the least weathered portion of the river load, river bed material samples from the Southern Alps (n = 13) and Canada (n = 5) were analysed to help constrain the composition of the catchment averaged river bed materials (Dellinger et al., 2014; Galy et al., 2008). Samples were collected from channel edges or from bank deposits that represent the fine fraction deposited during high flow regimes, and transferred to sterile plastic bags. In addition, the composition of suspended sediment was measured to evaluate any materials in the rivers that may retain a signature of rocks, mixed with modern weathering processes (Dellinger et al., 2014). Suspended sediment was immediately rinsed from the filters using filtered river water and transferred to clean amber-glass vials. All suspended sediments were freeze-dried upon return to laboratories within two weeks and weighed.

5.2.3 Molybdenum concentration determination

Molybdenum concentrations in the dissolved river loads were determined by direct calibration against a pure Mo standard that was diluted to varying extents in 0.5M HNO_3 to form solutions with a concentration range comparable to that observed in the samples. The samples were analysed using a quadrupole inductively coupled mass spectrometer (Q-ICP-MS, X-Series) at Durham University. The Mo concentrations of water samples processed for $\delta^{98/95}$Mo were also quantified as an output of the double spike method (Rudge et al., 2009). These were ~12% higher than the direct calibration data (***Chapter 2***, Figure 2.13). Although the direct measurements are precise, the accuracy may be lower because only synthetic standards were used. All reported data in the main text are from the direct calibration method to enable consistency in the comparison across all samples. However, where the most accurate numbers were important for interpretation purposes (Figure 5.12) we used the $[Mo]_{diss}$ data quanitified by ID MC-ICP-MS on the same sample aliquot also processed for $\delta^{98/95}$Mo analysis. The IAPSO standard measured by ID MC-ICP-MS yielded a concentration of 10.9 ± 0.51 ng g^{-1} (n = 5, ±2 SE), in agreement with published values of 10 and 11 ng g^{-1} (Greber et al., 2012). Duplicate sample data are provided in the data tables (section 5.7).

Before digesting solid samples for Mo concentration analysis, sediments were first powdered using a zirconium disc mill. Homogenizing bedload samples by crushing permitted an assessment of the average bulk Mo composition of the rocks at the catchment-scale. The powdered solid samples (surface soil, weathered colluvium, river bed materials) and suspended particulates (non-powdered) were then digested in a 2:1 mix of concentrated HF-HNO_3 (6 mL total) for 72 hours at 120ºC and then evaporated. The dried sample was further digested in a 2:1 mix of concentrated HNO_3-HCl (4.5 mL) for 48 h at 120ºC, and then evaporated, and then 3 mL of 16M HNO_3 followed by 5 mL of 6M HCl was added. After the solution was evaporated, the residue was re-dissolved in 10 mL of 1M HCl and a small aliquot (0.5 mL) was extracted for concentration analysis. These initial Mo concentration measurements were acquired on the Q-ICP-MS at Durham University and were used to calculate the ideal spike volume required for $\delta^{98/95}$Mo analysis (based on a 1:1 spike-sample ratio). The Mo concentrations in solid samples were quantified to higher accuracy and precision using isotope dilution methods on the same samples subsequently processed for $\delta^{98/95}$Mo determination by multiple collector inductively coupled plasma mass spectrometry (MC-ICP-MS, Thermo-Fischer Neptune: ***Chapter 2***, section 2.5). Replicate and duplicate concentration analyses on the standards IAPSO and BHVO-1 by isotope dilution methods produced data in agreement to within 8 and 4%, respectively (***Chapter 2***, Figure 2.14).

5.2.4 Molybdenum isotope analysis

For Mo isotope analysis in all sample types, Mo was separated and purified using anion exchange chromatography. In summary, for river waters, between 30 and 500 mL of the water was doped

with a known amount of a ^{97}Mo-^{100}Mo double spike solution to achieve a combined Mo mass of ~100 ng and a spike-sample mix ratio of 1:1. The chemistry was modified from that described by Pearce et al. (2009). The spiked water sample was evaporated to dryness before being re-dissolved in 5 mL 0.5M HCl for loading on to 2 mL of anion exchange resin (Bio-Rad AG1-X8) in a column. The resin was pre-cleaned with 20 mL 8M HNO_3, 10 mL 6M HCl, 10 mL 1M HCL, 5 mL 1M HF and 10 mL 3M HNO_3, and preconditioned with 5 mL 0.5M HCl. The sample was loaded on to the anion exchange resin in 5 mL 0.5M HCl, and the bulk matrix was washed through with 5 mL 0.5M HCl, 10 mL 0.5M HCl + 1M HF, 8 mL 4M HCl and 12 mL 1M HF. The Mo was finally eluted in 12 mL 3M HNO_3.

For the solid samples, the chemistry was based on the method of Willbold et al. (2016). The columns were pre-cleaned with 10 mL 0.5M HCl, 10 mL 2M NH_4NO_3 + 2M NH_4OH, 10 mL 8M HNO_3, 5 mL 1M HF and 10 mL 0.5M HCl. The columns were then preconditioned in 3 mL 3M HCl. After concentration checks via Q-ICP-MS, the remaining 1M HCl solution from the digestion process was spiked, before being evaporated and brought up in 4.75 mL of 3M HCl for loading. Immediately prior to loading, 0.25 mL of ascorbic acid was also added to the samples to oxidise Fe from Fe^{2+} to Fe^{3+} and enhance removal of Fe adsorbed to the resin matrix. The volume of anion exchange resin used was 1 mL. A bulk wash with 3 mL 3M HCL followed. A 13 mL mixture consisting of 0.5M + 0.5% H_2O_2 was then added to the columns in 1 mL aliquots for the first 3 mL, and 5 mL aliquots for the final 10 mL, to elute residual Fe. Zinc was eluted in 10 mL 1M HF. The Mo aliquot was collected in 12 mL of 1M HCl in acid cleaned Teflon beakers. The total procedural blanks for processing Mo in this study ranged from 0.1–1.7 ng g^{-1} with a mean blank [Mo] = 0.75 ± 0.51 ng g^{-1} (n = 16, ±1 SD).

Isotope measurements were made using a MC-ICP-MS (Thermo-Fischer Neptune) in the Arthur Holmes Geochemistry Laboratories, Durham University. Samples were introduced to the instrument using an Aridus II desolvator and a Savillex PFA20 nebuliser at 150–200 ng g^{-1} concentration in 0.5M HNO_3. The data were deconvolved using IsoSpike, which is an add-in to IGOR Pro (Paton et al., 2011). Mass bias was corrected for using the double spike method (Pearce et al., 2009). Data are presented in delta notation ($\delta^{98/95}Mo$), reported relative to the NIST SRM 3134 standard reference material (SRM) (Equation 5.1), where $\delta^{98/95}Mo_{NIST\text{-}3134}$ = 0‰. We note, however, that different isotope ratios (e.g. $^{97}Mo/^{95}Mo$) and alternative normalisations have been used, relative to different purified Mo standard solutions, such as 'mean ocean water molybdenum' (Siebert et al., 2001) or more recently to a non-zero value of NIST SRM 3134 (e.g. Greber et al., 2012). Consequently, in this study we have ensured that, where necessary, reported literature Mo isotope data have been re-calculated to $\delta^{98/95}Mo$ = 0‰ for NIST SRM 3134.

Equation 5.1 $$\delta^{98}Mo_{sample} = \left[\left(\frac{^{98/95}Mo_{sample}}{^{98/95}Mo_{NIST3134}}\right) - 1\right] \times 1000\ [‰]$$

The long-term $\delta^{98/95}$Mo machine reproducibility was determined by measurement of an in-house Romil standard run under the same instrumental conditions, which gave $\delta^{98/95}$Mo = 0.046 ± 0.029‰ (n = 99, ±2 SD). The long term reproducibility of the IAPSO seawater reference material is $\delta^{98/95}$Mo = 2.07 ± 0.06‰ (n = 5, ±2 SD) (***Chapter 2***: Figure 2.17), which is indistinguishable from the mean published value of 2.08 ± 0.10‰ (Goldberg et al., 2013). Full procedural duplicate analyses on two water samples provided data in agreement to within 0.02‰ and these data were averaged and reported with ±2 SD error on the mean value. Duplicate analyses on 12 sediment samples produced data in agreement to within 0.1‰, with a mean difference of 0.025‰. The long-term reproducibility on the BHVO-1 basalt reference material processed in each analysis is $\delta^{98/95}$Mo = 0.19 ± 0.04‰ (n = 21, ±2 SD) (***Chapter 2***: Figure 2.17). Sample reproducibility for solid samples is shown in Figure 2.18 in ***Chapter 2***: all samples fall within the ±2 SD error of the 0.05‰ fits of a 1:1 line.

5.2.5 Molybdenum sequential extraction: leaching experiment

Two suspended sediment samples from the western Southern Alps were subjected to two sequential extractions following established methods (Chan and Hein, 2007). The first extraction consisted of leaching with 10% acetic acid (HAc, Ultrapure). Approximately 1g of suspended load particulates from a glacial catchment (Fox: sample NZ14-86) and a catchment with glaciers confined to headwaters (Cook: sample NZ14-69) were each mixed with 40 mL of ultrapure HAc in capped Teflon beakers. The mixtures were then agitated in an ultrasonic water bath for 45 min, after which the particles were allowed to settle over 24 h. The supernatants were pipetted off with acid-cleaned pipette tips. The remaining residues were subsequently dissolved in distilled 2M HCl and the solutions agitated in an ultrasonic water bath for 45 min, after which they were placed on a hotplate at 70°C for 2 h. The final residues were left to settle over 24 h and then the HCl leach supernatant was pipetted off. Here after, we refer to the two extractable fractions as the HAc-leachable fraction and the HCl-leachable fraction. The supernatants corresponding to both the HAc-leachable fractions and the HCl-leachable fractions were evaporated to dryness and redissolved in 0.5M HNO_3 for Mo abundance and isotope analysis.

Metal cations, such as Mo, can complex with inorganic soil constituents such as carbonates, sulfates, hydroxides and sulphides to form either precipitates or positively charged complexes. These complexation and precipitation reactions are both pH dependent (Alghanmi et al. 2015). In the sequential extraction process described herein, the HAc was intended to remove loosely bound exchangeable Mo (Chan and Hein, 2007; Wimpenny et al., 2010) and to target any Mo present in carbonate phases (Henkel et al., 2016). The HCl leach was intended to remove Mo tightly bound to

Fe and Mn (oxyhydr)oxide-oxide residues from the particulates (Chan and Hein, 2007; Wimpenny et al., 2010). Previous studies have noted the effectiveness of HCl for attacking water soluble, acid-soluble and exchangeable Mo (Siebert et al., 2015). Consequently, we anticipate that Mo present within easily reducible and poorly crystalline Fe (and Mn) hydroxides and oxyhydroxides will most likely be extracted by HCl leaching (Henkel et al., 2016; Siebert et al., 2015; Wiederhold et al., 2007). Organic matter is not thought to be extracted in either the HAc or HCl leaches. Prior studies suggest the need for an additional leaching agent, such as H_2O_2, to extract Mo associated with the oxidizable fraction (e.g. Siebert et al., 2015).

5.2.6 Additional data

Major ion concentrations in water samples were analysed by Ion Chromatography (Thermo Scientific Dionex) at the Department of Geography, Durham University. Cation and anion standards and a certified reference standard (Lethbridge-03) were run to validate the analytical results. Data on the rhenium (Re) composition of the dissolved load and solid products were determined by isotope dilution coupled to analysis by Q-ICP-MS (Thermo Scientific X-Series) (***Chapters 3***, Horan et al., 2017; ***Chapter 4***) and are included for comparison to the behaviour of Mo. In river bed materials and soils, the total organic carbon concentration ([OC], %) was measured following a 0.2M HCl leach protocol (Galy et al., 2007). Aliquots of samples were combusted and the concentration and stable isotope composition of OC ($\delta^{13}C$, ‰) was determined using a Costech elemental analyser coupled to a Thermo Scientific Delta V Advantage isotope ratio mass spectrometer (EA-IRMS) at Durham University.

5.3. Results

5.3.1. Southern Alps, New Zealand

5.3.1.1 River bed materials

The river bed materials from the western Southern Alps have Mo concentrations, $[Mo]_{BM}$, of 0.14–0.65 µg g^{-1} (Figure 5.4), with a mean value of 0.29 ± 0.08 µg g^{-1} (n = 12, ±2 SE) (Table 5.2). However, there are differences between the river bed materials from the Fox and Waiho catchments relative to the catchments that do not have large valley glaciers: the former have mean $[Mo]_{BM}$ = 0.46 ± 0.21 µg g^{-1} (n = 3, ±2 SE), while the latter have mean $[Mo]_{BM}$ = 0.23 ± 0.04 µg g^{-1} (n = 9, ±2 SE). The isotope composition of the river bed materials, $\delta^{98/95}Mo_{BM}$, in the western Southern Alps ranges from -0.43 to -0.12‰ (Figure 5.4), with a mean value of $\delta^{98/95}Mo_{BM}$ = -0.31 ± 0.05 ‰ (n = 12, ±2 SE), although we observe some variability in the isotope composition of the bed materials between the two types of catchment. The Fox and Waiho catchments have a mean $\delta^{98/95}Mo_{BM}$ = -0.24 ± 0.07‰ (n = 3, ±2 SE), which is slightly higher than the river bed materials collected from the less glaciated sites, where mean $\delta^{98/95}Mo_{BM}$ = -0.33 ± 0.05‰ (n = 9, ±2 SE);

although the values are indistinguishable at the ±2 SE level. In the eastern Southern Alps, coarse angular debris collected from close to the pro-glacial lake of the Hooker glacier has a Mo concentration of 0.16 μg g^{-1} and an isotope composition of -0.34 ± 0.05‰ (±2 SD), while coarse debris collected from the banks of the Tasman River, which also flows from a glacial lake has a higher concentration of 0.31 μg g^{-1} and a much heavier $\delta^{98/95}$Mo composition (0.35 ± 0.01‰, ±2 SD). However, as only two measurements are available from the eastern Southern Alps and the properties of the sample materials are very different, these data are not considered alongside data from the other river catchments.

5.3.1.2 River suspended load

The river suspended particulates in the western Southern Alps have Mo concentrations, $[Mo]_{SPM}$, that range from 0.33–0.82 μg g^{-1} (Figure 5.4). The average concentration is approximately 70% higher than that of the river bed materials: mean $[Mo]_{SPM}$ = 0.49 ± 0.10 μg g^{-1} (n = 9, ±2 SE) (Table 5.3). In common with the river bed material samples, the Mo concentrations in the suspended sediments from the two glacial catchments trend towards slightly higher values than those in the less glaciated catchments. In the Fox and Waiho catchments, the mean $[Mo]_{SPM}$ = 0.54 ± 0.29 μg g^{-1} (n = 3, ±2 SE), while the catchments with <45% glacial cover have mean $[Mo]_{SPM}$ = 0.47 ± 0.07 μg g^{-1} (n = 6, ±2 SE); however, based on the available data, these are the same within error. The Mo isotope composition of the suspended materials in all catchments ranges from -0.16 to -0.38‰. The mean isotope composition of the suspended materials is -0.27 ± 0.08‰ (n = 9, ±2 SE). In the Fox and Waiho rivers, the mean isotope composition is $\delta^{98/95}Mo_{SPM}$ = -0.25 ± 0.09‰ (n = 3, ±2 SE), compared to $\delta^{98/95}Mo_{SPM}$ = -0.33 ± 0.04‰ (n = 6, ±2 SE) in the less glaciated catchments. Therefore, the isotope compositions of the suspended sediments from both the catchments dominated by valley glaciers (glacial coverage >45%) and those without are indistinguishable. The suspended load mean $\delta^{98/95}Mo_{SPM}$ value appears to be slightly higher than the mean $\delta^{98/95}Mo_{BM}$ value, but they are also the same within ±2 SE (Figure 5.4). This suggests that the suspended load together with the bed materials closely reflect the catchment bedrock and provide a starting composition against which to reference the effects of weathering (Supplementary Figure 5.1). Figure 5.4 illustrates the clustering of river bed materials and suspended load sediments in Mo isotope–concentration space.

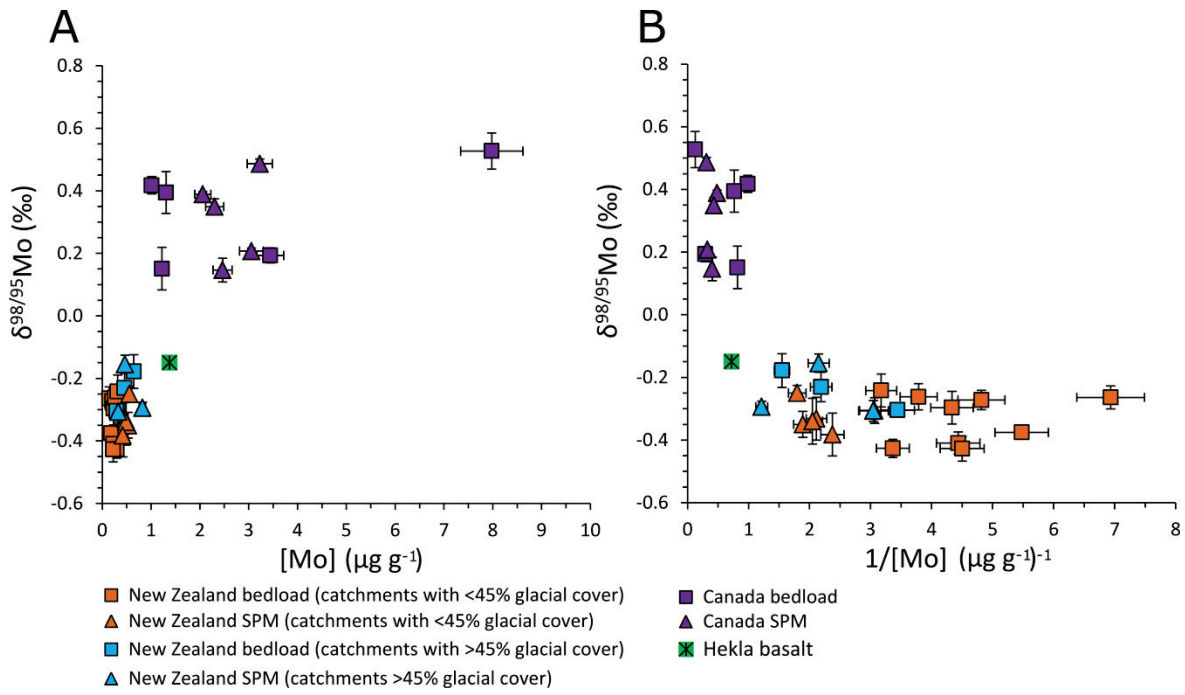

Figure 5.4 Mo concentration and Mo isotope composition of the river sediments from catchments in the western Southern Alps, New Zealand and Canada. A. Relationship between the $\delta^{98/95}$Mo composition and concentration. **B.** Relationship between the $\delta^{98/95}$Mo composition and reciprocal of concentration. The separation of the data from the different study locations reflects the different composition of the source rocks. Note the overlap in the data from river suspended particulate matter (SPM) and river bed materials. The composition of Hekla basalts is taken from Yang et al. (2015). Analytical errors (±2 SD) for $\delta^{98/95}$Mo values and the long-term % errors for the concentration data are indicated.

5.3.1.3 Soils

To understand the relationship between chemical weathering and Mo release to the rivers we evaluate the concentration and isotope composition of Mo in a selection of weathering products from the Alex Knob hillslopes of the Docherty River catchment in the western Southern Alps. Soils are a major component of the Mo cycle and Mo fractionation has previously been observed in these environments (King et al., 2016; Siebert et al., 2015). In addition, we assess Mo abundance and Mo isotope composition as a function of soil organic matter concentration in an attempt to better understand the controls on Mo retention and fractionation (Figure 5.5).

The abundance of Mo is relatively invariant in the soil materials (Table 5.4). Mean [Mo] in the surface soil litter is 0.30 ± 0.07 µg g^{-1} (n = 5, ±2 SE), where mean OC = 8.34 ± 3.15% (n = 5, ±2 SE). In the colluvium samples, mean [Mo] = 0.28 ± 0.05 µg g^{-1} (n = 4, ±2 SE) and mean [OC] = 1.17 ± 0.29%. The Mo abundance of the local river bed material (NZ14-90) is $[Mo]_{BM}$ = 0.26 µg g^{-1}. The OC in this sample is rock-derived and has a much lower concentration, relative to the soil materials, of 0.21 wt. % (Figure 5.5A). The surface soil litters are dominated by modern primary productivity, and have enriched OC values of 4.4 to 13.2 wt. % and, consequently, the lowest [Mo]/[OC] ratios (Figure 5.1B). In contrast, the low OC concentration of the river bedload results

in this sample having a much higher [Mo]/[OC] ratio. The colluvium samples have [Mo]/[OC] ratios that fall between the bedload and the soil litter values, perhaps representing the mixing between deeper weathered mineral horizons dominated by rock fragments with high [Mo]/[OC] and surface layers rich in recently photosynthesised organic matter with high [Mo]/[OC].

We find that surface soil litters have a mean $\delta^{98/95}$Mo = -0.23 ± 0.11‰ (n = 5, ±2 SE), which is the same within error as the local river bed material ($\delta^{98/95}$Mo = -0.26 ± 0.04‰, ±2 SD) (Table 5.4). Two litter samples are indistinguishable from the bed material, while two litter samples are isotopically heavier than the bed materials (by ~0.15‰) and one is lighter (by ~0.1‰) (Figure 5.5). Previous observations on organic rich soils document a net enrichment in heavier isotopes compared to the original bedrock (Siebert et al., 2015) but this is not clear from our New Zealand data. In contrast, the weathered colluvium sediments contain isotopically lighter Mo (mean $\delta^{98/95}$Mo = -0.52 ± 0.28‰; n = 4, ±2 SE ‰), with $\delta^{98/95}$Mo values extending to -0.90 ± 0.07‰ (±2 SD) in the deepest soil horizon. Therefore, the degree of fractionation between the colluvium and the bedrock (characterised by the bed materials) in the western Southern Alps greatly exceeds the fractionation observed between the plant litter samples and the bed materials. The strong fractionation within the deep colluvium samples suggests that isotopically light Mo is preferentially retained deep within the weathering zone.

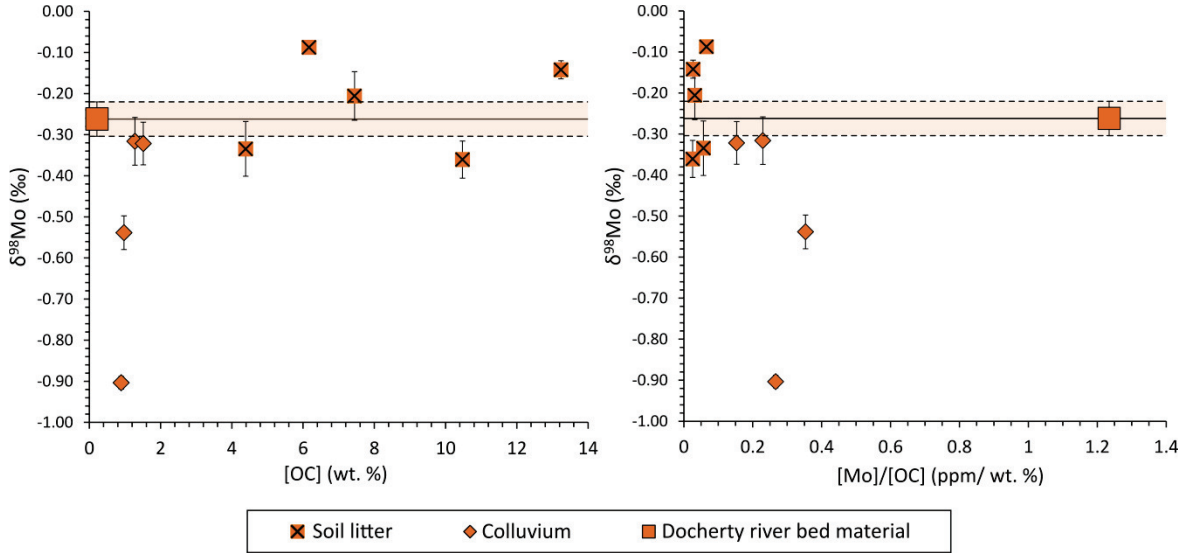

Figure 5.5 Patterns in Mo distribution and composition in soils from the Docherty River catchment, western Southern Alps. A. Relationship between the Mo isotope composition and organic carbon concentration in soil materials. Surface soil litters are enriched in OC and have isotope compositions that are similar to the river bed material, while deeper soil horizons have lower OC and lower $\delta^{98/95}$Mo values. **B.** Relationship between the Mo isotope composition of soil materials and the relative abundance of Mo to organic carbon. Local river bed materials are dominated by Mo while soils are richer in organic matter, particularly in the case of the soil litters. In both figures, the solid horizontal line indicates the $\delta^{98/95}$Mo isotope value of the Docherty River bedload ($\delta^{98/95}$Mo = –0.26 ± 0.04‰, ±2 SD) and the shaded area within the dashed lines represents the ±2 SD error on this value.

5.3.1.4 River waters

In the western Southern Alps, the dissolved Mo concentration, $[Mo]_{diss}$, ranges from 1.1–16.9 nmol L^{-1} with a mean value of 7.1 ± 1.2 nmol L^{-1} (n = 51, ±2 SE) (Table 5.5). This is similar to the global average dissolved concentration of 8.0 nmol L^{-1} (Miller et al., 2011). The $[Mo]_{diss}$ values in the two catchments that host valley glaciers, the Fox and the Waiho, are higher: mean $[Mo]_{diss}$ = 13.0 ± 1.3 nmol L^{-1} (n = 9, ±2 SE). The two rainwater samples collected from the Waiho catchment have very low $[Mo]_{diss}$ of 0.07 and 0.12 nmol L^{-1}, indicating that atmospheric inputs of Mo are negligible in this setting. These rainwater samples have slightly higher concentrations than rain measured in Haiwaii: 0.06 nmol L^{-1} and 0.08 nmol L^{-1} (King et al. 2016). A hydrothermal sample collected in the upstream area of the Karangarua catchment also contained small amounts of Mo compared to the river waters: $[Mo]_{diss}$ = 0.24 nmol L^{-1}. Rivers on the eastern flank of the Southern Alps have mean $[Mo]_{diss}$ = 7.5 ± 2.3 nmol L^{-1} (n = 5, ±2 SE), so are similar in this regard to the western flank.

The $\delta^{98/95}Mo_{diss}$ values of the river waters in the western Southern Alps catchments range from 0.00‰ to 0.32‰ (Figure 5.6), with a mean $\delta^{98/95}Mo_{diss}$ = 0.12 ± 0.05‰ (n = 13, ±2 SE). There appears to be a small difference between catchments dominated by fluvial incision, which have a mean $\delta^{98}Mo$ = 0.06 ± 0.03‰ (n = 8, ±2 SE), and the Fox and Waiho rivers that host valley glaciers, which have a mean $\delta^{98/95}Mo$ = 0.19 ± 0.08‰ (n = 4, ±2 SE). A sample collected close to the Haast estuary has a heavier $\delta^{98}Mo$ composition of 0.28 ± 0.03 ‰ (±2 SD). In the rivers in the eastern Southern Alps, Mo is isotopically lighter: $\delta^{98/95}Mo$ values are -0.16‰ and 0.03‰ in the Hooker River and -0.19‰ in the Tasman River. Figure 5.7 illustrates that there is no linear correlation between $\delta^{98/95}Mo_{diss}$ and $[Mo]_{diss}$ and could suggest that several mixing and/or fractionation processes must be operating in the catchments to set the Mo isotope composition (see section 5.4).

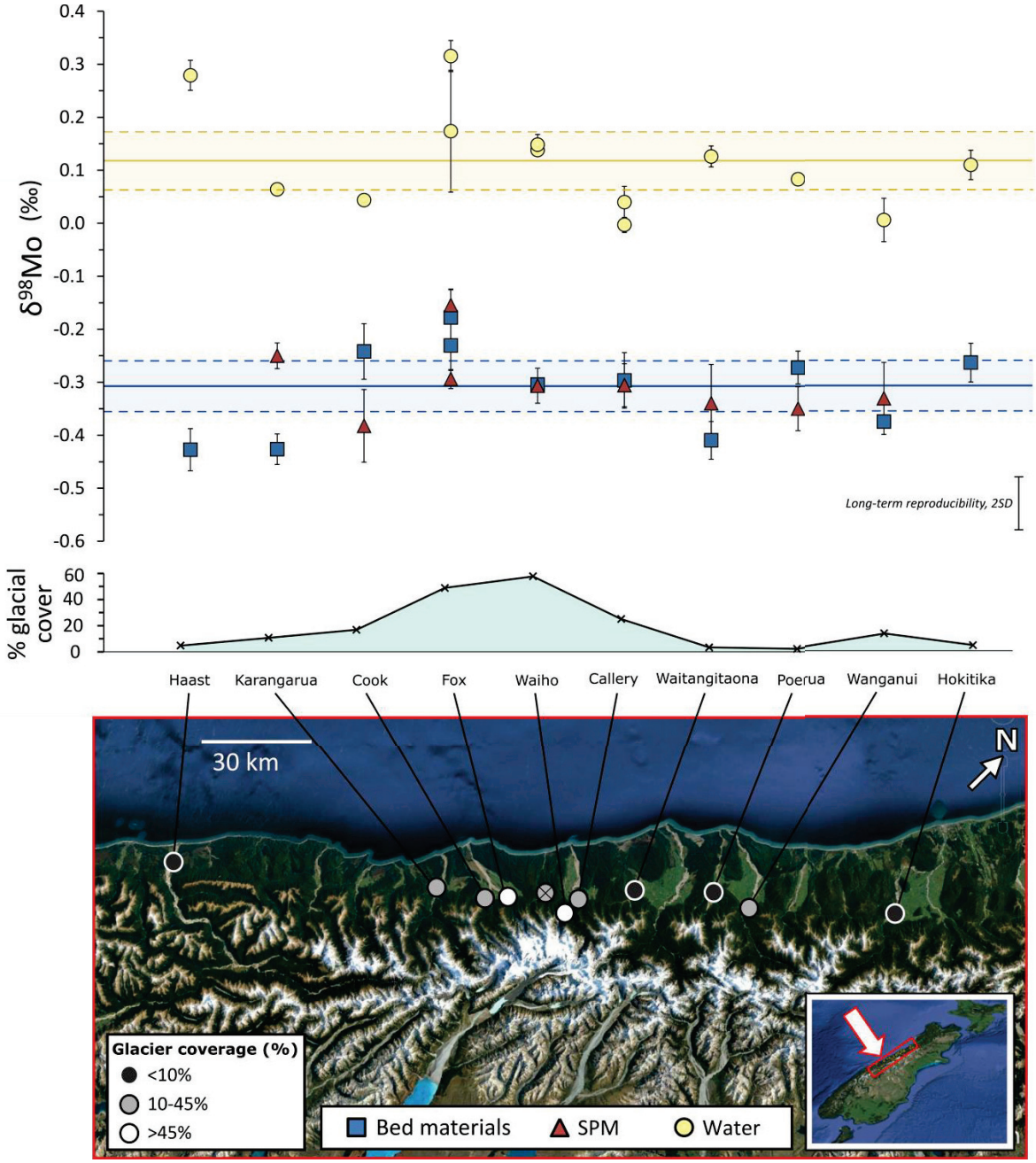

Figure 5.6 Spatial patterns in $\delta^{98/95}$Mo values across the western Southern Alps in river waters, river suspended particulate matter (SPM) and river bed materials. The names of the studied catchments are provided above the map. Glacial coverage is indicated by circles marking sampling localities (Horan et al., 2017). The dissolved load in all catchments indicates that Mo is isotopically heavy in the river waters relative to the river sediments. The suspended load and river bed materials show similar isotope values. Analytical errors are marked as ±2 SD. The solid blue line is the mean composition of the river bed materials ($\delta^{98/95}Mo_{BM}$ = -0.31 ± 0.05 ‰; n = 12, ±2 SE) and the shaded blue band shows the ±2 SE error on this mean. The solid yellow line is the mean composition of the river water samples ($\delta^{98/95}Mo_{diss}$ = 0.12 ± 0.05‰ (n = 13, ±2 SE) and the shaded yellow band shows the ±2 SE error on this mean. The Docherty catchment where soil samples were collected is marked with an X through a grey circle.

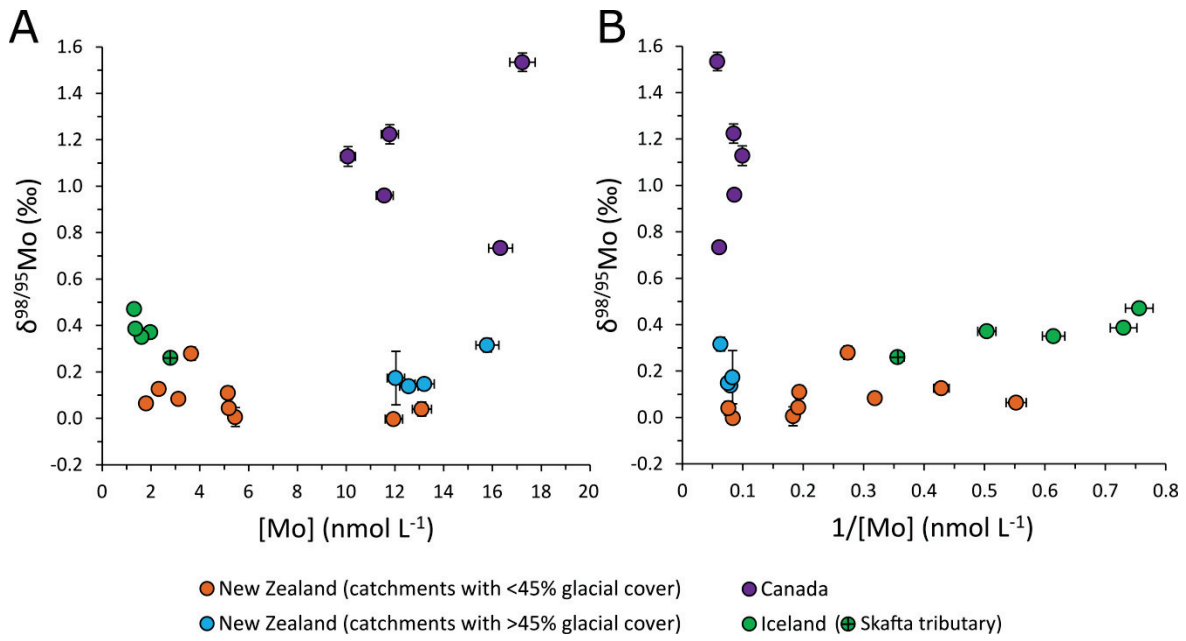

Figure 5.7 Mo concentration and Mo isotope composition of river waters from catchments in the western Southern Alps, New Zealand, Iceland and Canada. A. Relationship between the $\delta^{98/95}$Mo composition and concentration. **B.** Relationship between the $\delta^{98/95}$Mo composition and the reciprocal of concentration. Note the lack of correlation between the Mo isotope composition and the Mo concentration. Analytical errors (±2 SD) for $\delta^{98/95}$Mo values and the long-term % errors for the concentration data are indicated.

5.3.2 Mackenzie River Basin

5.3.2.1 River bed materials

In the Mackenzie River bed materials, the $[Mo]_{BM}$ = 1.01 µg g^{-1} at Tsiigetchic and 1.31 µg g^{-1} at the delta, with $\delta^{98/95}Mo_{BM}$ values of 0.42 ± 0.03‰ (±2 SD) and $\delta^{98/95}Mo_{BM}$ = 0.39 ± 0.07‰ for Tsiigetchic and the delta, respectively. The river bed sediments from the Peel and the Ogilvie catchments have the highest concentrations of Mo: these are 3.44 µg g^{-1} and 7.97 µg g^{-1}, respectively. In the Peel, $\delta^{98/95}Mo_{BM}$ = 0.19 ± 0.02‰ (±2 SD), and in the Ogilvie $\delta^{98/95}Mo_{BM}$ = 0.52 ± 0.06‰ (±2 SD). In the Yukon catchment, the Mo concentration in the river bed material is found to be similar to the Mackenzie (1.22 µg g^{-1}) but the $\delta^{98/95}Mo_{BM}$ value is lower at 0.15 ± 0.07‰ (±2 SD) (Figure 5.4).

5.3.2.2 River suspended sediments

In the Mackenzie river, the suspended load $[Mo]_{SPM}$ at Tsiigetchic and the delta are similar, with values of 2.06 µg g^{-1} and 2.30 µg g^{-1}, respectively. The $\delta^{98/95}Mo_{SPM}$ composition is also very similar across these sites, with a value of 0.39 ± 0.01‰ (±2 SD) at the Tsiigetchic sampling locality and 0.35 ± 0.03‰ (±2 SD) at the delta. In the Peel catchment, the suspended load has a Mo concentration, $[Mo]_{SPM}$, of 3.06 µg g^{-1} and a $\delta^{98/95}Mo_{SPM}$ value of 0.21 ± 0.01‰ (±2 SD). In the Ogilvie catchment, $[Mo]_{SPM}$ is the highest of the five sites studied with a value of 3.23 µg g^{-1} and the $\delta^{98/95}$Mo composition is the heaviest, at 0.49 ± 0.02‰ (±2 SD). In the Yukon River, the Mo

concentration of the suspended load is similar to the Mackenzie (2.47 μg g^{-1}) but the water has an isotopically light composition of $\delta^{98/95}$Mo = 0.15 ± 0.04‰ (±2 SD) (Figure 5.4).

5.3.2.3 River water

In the Mackenzie River Basin, $[Mo]_{diss}$ values range from 0.2–119 nmol L^{-1} (n = 16, Table 5.5). For the Mackenzie River, sampled at Tsiigetchic and the delta, $[Mo]_{diss}$ values are 10.1 and 11.6 nmol L^{-1}, respectively. These values are similar to those measured on samples collected in 2004 from the same locality (2.8–13.2 nmol L^{-1}; Miller et al., 2011). The Peel River has an average $[Mo]_{diss}$ of 12.9 nmol L^{-1}, while its tributary, the Ogilvie River, has a mean concentration of 16.4 nmol L^{-1}. The Yukon River, sampled at Dawson, has a concentration of 16.3 nmol L^{-1}. The greatest spread in $[Mo]_{diss}$ is observed in the tributaries feeding the Peel River. For example, the upper section of Engineer Creek has $[Mo]_{diss}$ = 118.9 nmol L^{-1}, which is the highest concentration measured across the Mackenzie River Basin, while a Peel tributary to the north of the basin (sampled at 67.13862ºN, 136.00302ºW) has the lowest measured $[Mo]_{diss}$ at just 0.21 nmol L^{-1}; barely elevated above the rainwater values in the western Southern Alps (section 5.3.1.4).

In terms of their Mo isotope compositions, the Canadian samples are isotopically very heavy (Figure 5.7). The Mackenzie River sampled at Tsiigetchic has a $\delta^{98/95}Mo_{diss}$ = 1.13 ± 0.04‰ (±2 SD), while downstream at the delta $\delta^{98/95}Mo_{diss}$ = 0.96 ± 0.01‰ (±2 SD). The Peel and the Ogilvie drain the same sub-basin and have $\delta^{98/95}Mo_{diss}$ =1.22 ± 0.04‰ (±2 SD) and $\delta^{98/95}Mo_{diss}$ = 1.53 ± 0.04‰ (±2 SD), respectively. The Yukon River at Dawson has a $\delta^{98/95}Mo_{diss}$ = 0.73 ± 0.02‰ (±2 SD).

5.3.3 Iceland

5.3.3.1 Bedrock

The Skaftá River and its tributary to the west (63.91005ºN, 18.59857ºW) (Figure 5.3) drain predominantly basaltic lithology. The composition of this basalt rock is likely to be similar to the basaltic lavas at the Hekla volcano sampled by Yang et al. (2015), which are in close geographical proximity to the Skaftá River catchment. These lavas have a mean [Mo] = 1.38 μg g^{-1} and $\delta^{98/95}$Mo = -0.15‰ (Yang et al., 2015).

5.3.2.2 River water

In the Skaftá River, $[Mo]_{diss}$ concentrations are fairly consistent across the sample years 2013–2014 at Skaftá sites 1–4. Here, $[Mo]_{diss}$ ranges from 1.2 to 1.9 nmol L^{-1} (n = 7). Lower $[Mo]_{diss}$ values are found close to the Vatnajökull glacier (0.67 nmol L^{-1}) at Skaftá site 5, which was sampled in 2014. A tributary to the Skaftá River that is not sourced from the glacier had a mean $[Mo]_{diss}$ of 2.45 nmol L^{-1}.

At Skaftá sites 1 and 2, we find $\delta^{98/95}Mo_{diss}$ = 0.38 ± 0.05‰ (±2 SD) and 0.36 ± 0.05‰ (±2 SD), respectively, so they are indistinguishable within error. Upstream at Skaftá site 3 we quantify $\delta^{98/95}Mo_{diss}$ = 0.39 ± 0.05‰ (±2 SD) and at Skaftá site 4 we find $\delta^{98/95}Mo_{diss}$ = 0.47 ± 0.05‰ (±2 SD). The $\delta^{98/95}Mo_{diss}$ data therefore show a tendency to increase with proximity to the Vatnajökull glacier. At the non-glacially sourced Skaftá tributary, the $\delta^{98/95}Mo_{diss}$ values are slightly lower at 0.26 ± 0.05‰ (±2 SD). Previously, the Skaftá River has been documented to have a Mo concentration of 1.56 nmol L^{-1} and a $\delta^{98/95}$Mo composition of 0.24‰ (± 0.40‰, ±2 SD) (Pearce et al., 2010a) close to our Skaftá site 2 sampling locality. Previously published Mo isotope data for rivers from Iceland also indicate that glacial rivers tend to be enriched in heavy Mo isotopes compared to non-glacial systems (Pearce et al., 2010a).

5.3.4 Leachates from suspended particulates

The sequential extraction procedure separated two major fractions of Mo in the suspended particulate matter collected from the Fox (NZ14-86) and Cook (NZ14-69) river catchments (Table 5.6). The Mo concentration of the HAc fractions was very low for both NZ14-69 (0.14 μg g^{-1}) and NZ14-86 (0.07 μg g^{-1}). In contrast, the HCl leach removed a greater proportion of Mo. This had a concentration of 0.93 μg g^{-1} for NZ14-69 and 0.34 μg g^{-1} for NZ14-86. The remaining residue had 0.31 μg g^{-1} of Mo in NZ14-69 and 0.30 μg g^{-1} in NZ14-86. This inner core of the sediment grains is likely to be a direct reflection of the unweathered bedrock composition, explaining why it does not vary greatly between the catchments.

In analogy to Li leaching experiments (Chan and Hein, 2007), we infer that the HAc-leachable fractions contain adsorbed and carbonate-bound Mo, while the HCl-soluble fraction consists of structurally bound Mo in Mn and Fe (oxyhydr)oxide mineral structures and potentially also some organic matter. Total leachable Mo contents are calculated as the sum of Mo in the HAc and HCl leachate fractions. In sample NZ14-69, 1% of the total sample Mo was leached by HAc and 24% by HCl, giving a total leachable content of 25%. In sample NZ14-86, 1% of the total sample Mo was leached by HAc and 20% by HCl, giving a similar total leachable content of 21%. The selective extractions of Mo suggest that the association of Mo with the inner organic matter and silicate or oxide residue of the grains dominates retention, with adsorption on Fe and Mn (oxyhydr)oxides playing a smaller role. The low mass of Mo removed by acetic acid suggests Mo present in carbonate phases is negligible.

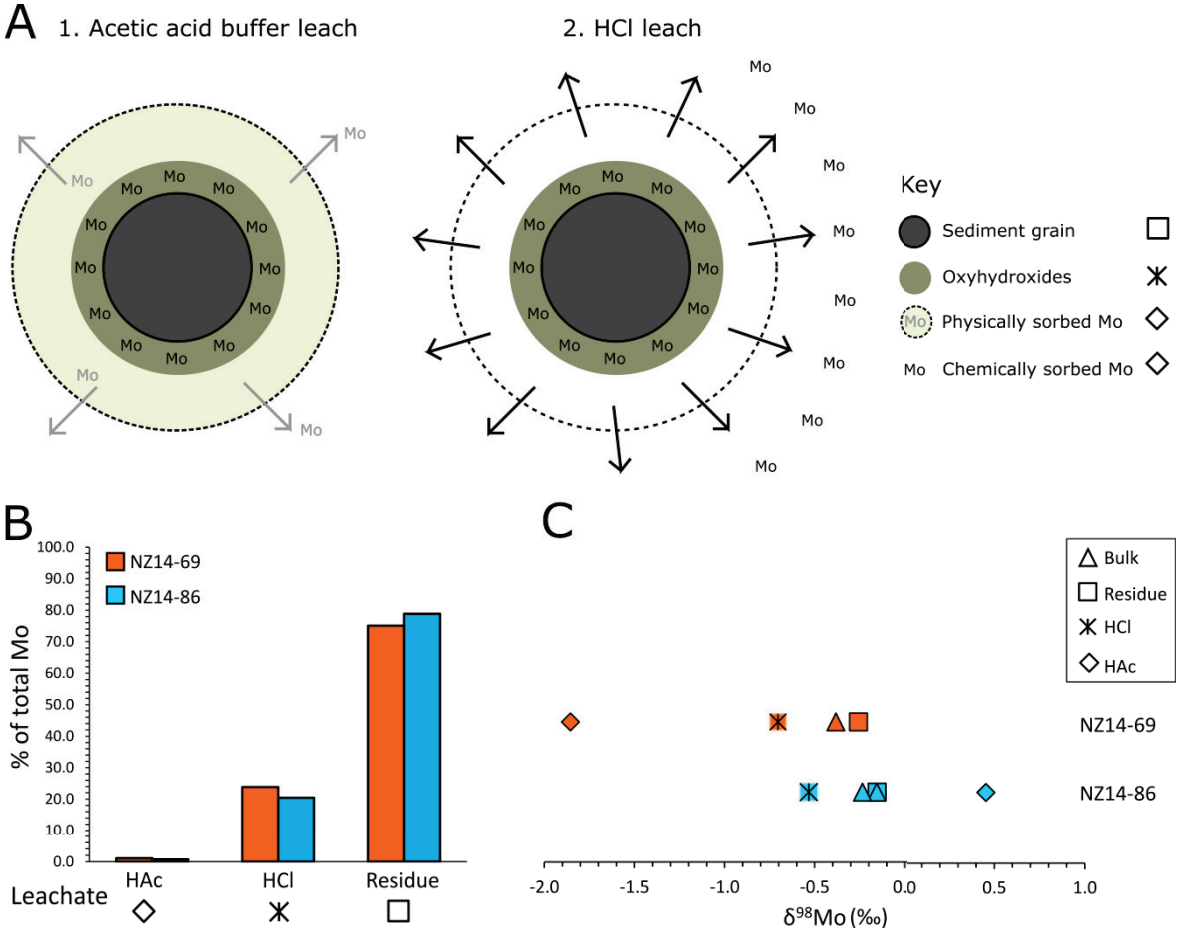

Figure 5.8 Distribution of Mo and $\delta^{98/95}$Mo composition of leachates from river suspended sediments. **A.** Schematic diagram illustrating the two step leach method used to extract Mo from the suspended sediments. The suspended sediments are from the Cook and Fox Rivers draining the western Southern Alps: the Fox catchment is dominated by a valley glacier (glacial coverage = 49%) while the Cook catchment has only 17% glacial cover. **B.** Proportion of total Mo in each fraction of the leaching experiment. **C.** Molybdenum isotope composition of each fraction of the leaching experiment.

The bulk $\delta^{98/95}$Mo composition of NZ14-69 is -0.38 ± 0.07‰ (±2 SD). This is lower than the bulk composition of NZ14-86 ($\delta^{98/95}$Mo = -0.15 ± 0.03‰, ±2 SD). The HCl leach of NZ14-86 contains isotopically lighter Mo ($\delta^{98/95}Mo_{HCl}$ = -0.53 ± 0.01‰) than the bulk and residue fraction ($\delta^{98/95}Mo_{residue}$ = -0.15 ± 0.01 ±2 SD). A slightly higher fractionation is observed in NZ14-69, with a $\delta^{98/95}$Mo of -0.70 ± 0.07‰ (±2 SD) measured in the HCl leach compared to -0.26 ± 0.03‰ (±2 SD) in the residue and -0.38‰ (±2 SD) in the bulk (Figure 5.8). The leachate data suggest that lightly bound Mo (from the HAc leach) is a minor component and it does not appear to have a systematic offset in its isotope composition. However, the HCl leach contains ~21–25% of the Mo and it is isotopically lighter than the bulk rock and residues. Furthermore, the leachate data indicate no significant difference in the fractionation factor of the leachable fraction and the bulk composition of suspended sediments in the Fox and Cook catchments; these are 0.37 and 0.32‰, respectively. The suspended sediments likely reflect a mixture of unweathered rocks and weathered hillslope colluvium, which contains a layer of oxides dominated by light Mo. Similarity in the

isotope composition of the oxide coating leached from both suspended sediments could indicate that secondary mineral phases may be responsible for locking up isotopically light Mo (e.g. Barling and Anbar, 2004; Goldberg et al., 2009), which is also found in the New Zealand mineral soils (Figure 5.4).

5.3.5 Summary of results

The five Canadian catchments have river bed materials with a mean $\delta^{98/95}Mo_{BM}$ that is higher (by ~0.7‰) than those derived from the metasedimentary rocks in New Zealand and the basaltic silicate rocks in Iceland (Yang et al., 2015). The $\delta^{98/95}$Mo values of the suspended load sediments are similar to the river bed materials in both the New Zealand and Canadian catchments (Supplementary Figure 5.1), which reflects the fact that suspended load materials can contain large quantities of unweathered material when erosion rates are moderate to high. These data are summarised in Figure 5.9.

In New Zealand, Canada and Iceland, river waters have a range in dissolved river Mo concentrations that span three orders of magnitude (Supplementary Figure 5.2). Overall, all $[Mo]_{diss}$ data from New Zealand and Iceland fall towards the lower end of published concentration data from global rivers (global $[Mo]_{diss}$ = 0.45–59 nmol L^{-1}: Miller et al., 2011). The river catchments in the Mackenzie River Basin demonstrate a wider range in Mo concentration (0.2–119 nmol L^{-1}). The $\delta^{98/95}Mo_{diss}$ values for the New Zealand rivers also fall at the low range of published global river measurements ($\delta^{98/95}Mo_{diss}$ = 0.15‰ to 2.40‰; Archer and Vance, 2008; Neubert et al., 2011; Pearce et al., 2010a; Voegelin et al., 2012; Wang et al., 2015). In contrast, the $\delta^{98/95}Mo_{diss}$ values of the Peel, Ogilvie, Mackenzie and Yukon Rivers are all higher than the global river average. The water samples from the Skaftá River, Iceland, have Mo isotope compositions that are heavy when compared to those from New Zealand, but they are isotopically light relative to the Canadian rivers.

Together, the dissolved Mo isotope composition of all river water samples are systematically heavier than the local river bed materials and suspended sediments (Figure 5.9), with a mean fractionation factor of 0.42‰ in the less glaciated western Southern Alps, 0.45‰ in the Fox and Waiho catchments and ~0.78‰ for the Canadian catchments. The mean fractionation between the Mo isotope composition of the Skaftá River samples and the Hekla basalts (Yang et al., 2015) is 0.67‰. These observations are broadly consistent with published data (Archer and Vance, 2008; Pearce 2010a), which indicate that the modern average riverine $\delta^{98/95}Mo_{diss}$ (~0.45‰) is higher than the average upper continental crust, where $\delta^{98/95}$Mo = 0.05 to 0.15‰ (Voegelin et al., 2014).

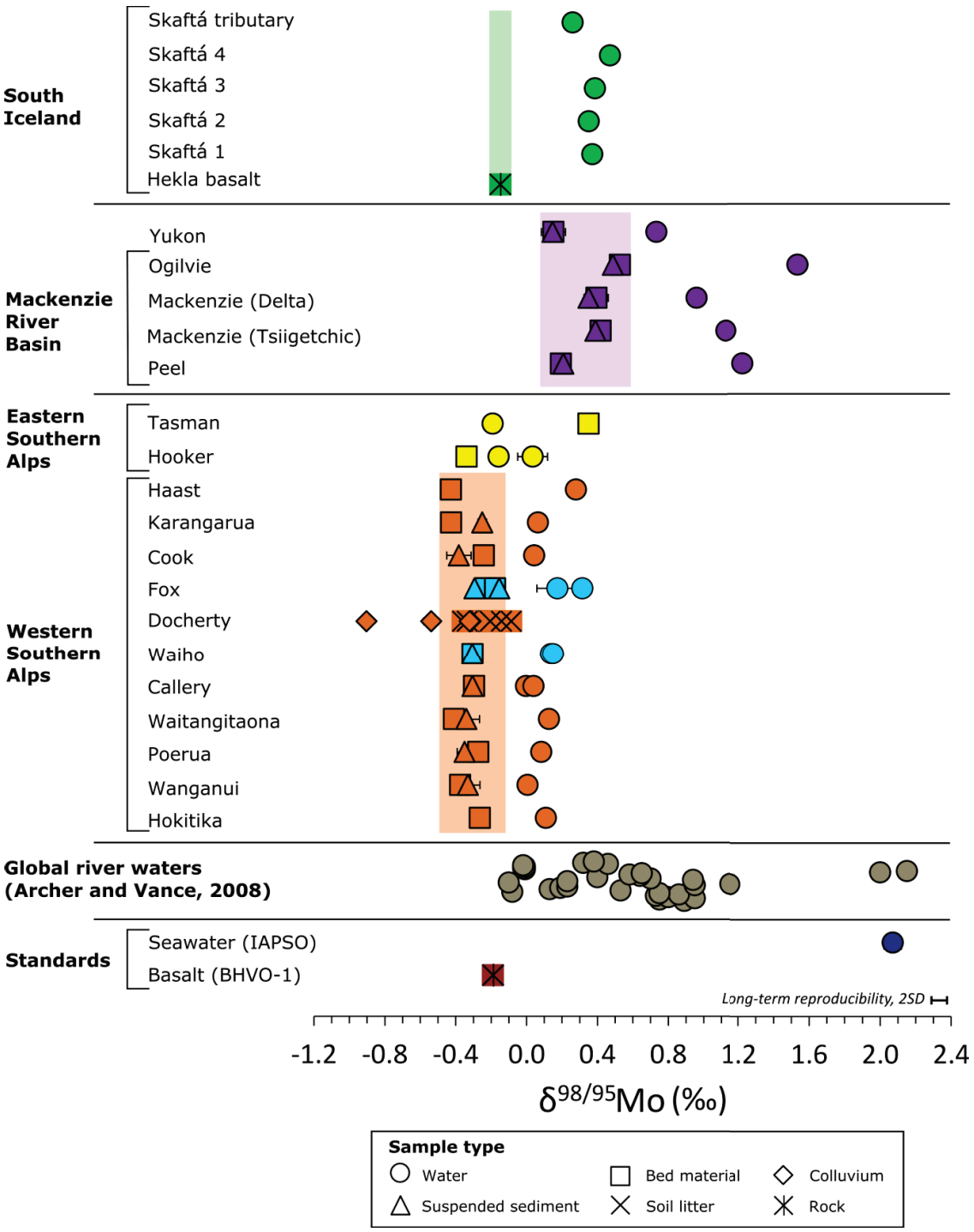

Figure 5.9 Distribution of $\delta^{98/95}$Mo in soils, river sediments, and the dissolved load of river catchments. Data from New Zealand, Canada and Iceland (this study) are shown alongside data for global rivers (Archer and Vance, 2008) and the BHVO-1 and IAPSO standards. Orange and purple shaded areas show the spread in the composition of the river bed materials for New Zealand and Canada, respectively. Green shaded area represents the isotope composition of Icelandic basalts sampled at Hekla, based on data reported in Yang et al. (2015). Most analytical errors (±2 SD) are smaller than the symbol size. The long-term reproducibility of the BHVO-1 and IAPSO standards (0.05‰) is indicated.

5.4. Discussion

The new Mo isotope data from river catchments in New Zealand, Iceland and northern Canada offer insight on the major controls on river $\delta^{98/95}Mo_{diss}$ values. We start by considering the sources of Mo from parent lithology and atmospheric deposition, before examining the processes that may fractionate Mo isotopes. The latter may include the adsorption of Mo to Fe-Mn (oxyhydr)oxide and/or organic matter, and the uptake/cycling of Mo by the biosphere. These processes are responsible for governing the ultimate $\delta^{98/95}Mo_{diss}$ composition of continental runoff.

5.4.1 A source control on the Mo isotope composition of rivers

5.4.1.1 Insights on the sources of dissolved Mo from ion ratios

To interpret the potential drivers of Mo fractionation in rivers, it is important to evaluate the relative contribution of different mineral and organic phases that deliver Mo to the river dissolved load during the weathering of rocks. The main phases involved are thought to be silicates, sulfides and organic carbon (Miller et al., 2011; Neubert et al., 2011). To evaluate their inputs, we use the dissolved ion ratios [Mo]/[Na*] and [Mo]/[SO_4^{2-}] contained in river waters. [Na*] is the Na concentration corrected for atmospheric input ([Na*] = [Na] - ([Cl]*0.85)). Dissolved riverine Na* concentrations, $[Na^*]_{diss}$, retain a signal of the relative patterns of silicate weathering, while dissolved riverine SO_4^{2-} concentrations, $[SO_4^{2-}]_{diss}$, broadly reflect the oxidative weathering of sulfides, if evaporite inputs are minimal. The approach of using ion ratios to interpret Mo source is analogous to the approach used to interpret the source of other major (Gaillardet et al., 1999) and trace elements, such as Re, to the dissolved load (Dalai et al., 2002; ***Chapter 4***).

To define the [Mo]/[Na*] and [Mo]/[SO_4^{2-}] composition of the endmembers, we combine Mo, Na and S concentration data for specific lithologies and individual minerals from this study with published data. For the sulfide-rich endmember, we focus on the data available from sulfides extracted from sedimentary rocks (Norman et al., 2003; Sundby et al., 2004), which have an average [Mo]/[S] ratio of 0.00016 μmol mol^{-1} and an average [Mo]/[Na] ratio of 0.0152 μmol mol^{-1}. For the silicate endmember, we use dissolved load data from the tributary to the Skaftá River in southern Iceland that drains purely basaltic terrain: the [Mo]/[Na*] is 0.0070 mmol mol^{-1} and the [Mo]/[SO_4^{2-}] ratio is 0.095 mmol mol^{-1}. In this tributary, the main supply of Mo to surface waters will be from the dissolution plagioclase and pyroxene from the basaltic lava, as well as volcanic glass (Arnorsson and Oskarsson, 2007). For comparison, the composition of the Icelandic basalt BIR-1, a United States Geological Survey (USGS) standard reference material, has also been plotted (Figure 5.10) (Jochum et al., 2005). This standard comes from the Reykjavik dolerites, which are a group of lava flows most likely from shield volcanos dating from the youngest interglacial periods (USGS, 2017). For the rock-derived organic carbon endmember composition,

we use published data on coals, which have >75% wt. % OC (Dai et al., 2015). The average of these data have [Mo]/[Na] = 607.9 mmol mol^{-1} and [Mo]/[SO_4^{2-}] = 1.80 mmol mol^{-1}. Although the endmember compositions chosen here may not fully represent those in each catchment, the dissolved Mo in the rivers of this study can be well described by the ternary mixture between rock-derived organic carbon, silicates and sulfides (Figure 5.10).

Within the mixing space we find that data from the Skaftá River, Iceland, fall between the sulfide and silicate endmembers, which is consistent with a rhyoltic-basaltic basement being drained in this catchment (Figure 5.3), and highlights the role of sulfide oxidation. However, the contribution of sulfide minerals to the $[Mo]_{diss}$ appears to be ~1%. In contrast, this mixing model would suggest that the samples from the Mackenzie River Basin all fall closer to the mixing line between the petrogenic organic carbon (OC_{petro}) and sulfide endmembers, with the dissolution of sulfides playing a greater role in the Peel catchment and its tributaries (e.g. the Ogilvie, Rock, Engineer and Blackstone rivers). Dissolved load data from a tributary in the Peel catchment that drains rocks with high sulfide content (Beaulieu et al., 2011) has a [Mo]/[SO_4^{2-}] ratio that is similar to that of the literature data (0.000094 mmol mol^{-1}), but it has a higher [Mo]/[Na*] ratio of 0.00039 mmol mol^{-1} and therefore falls outside of the mixing space. The contribution of silicate minerals to the $[Mo]_{diss}$ budget appears to play a smaller role in the Canadian catchments than in Iceland. Data from the Southern Alps suggest that all three mineral phases deliver Mo to the dissolved load but the input from OC_{petro} dominates (>90%). This is consistent with the lower sulfide content of the rocks here, compared to the Canadian rivers (Koons and Craw, 1991; Beaulieu et al., 2011).

Overall, with the endmembers defined as shown here (Figure 5.10), the Mo in the dissolved load of the New Zealand rivers and the main river channels in the Mackenzie River Basin appears to be predominantly (>90%) derived from OC_{petro}. In reality, this end member may have lower [Mo]/[SO_4^{2-}] and [Mo]/[Na*] ratios than the coal samples used in the mixing model, which are likely to capture freshwater/lacustrine settings with lower [SO_4] and [Na] and higher [Mo] in the water during deposition (Dai et al., 2015). Marine organic matter in sedimentary rocks may have lower [Mo] (Dai et al., 2015; Neubert , 2008), and much higher [Na] and [SO_4^{2-}], with resultant lower [Mo]/[SO_4^{2-}] and [Mo]/[Na*] ratios. The mixing model therefore probably quantifies an upper bound on the OC_{petro} Mo contribution and a lower bound on the sulfide Mo contribution to the dissolved load. Future work should seek to constrain the compositions of these endmembers in more detail.

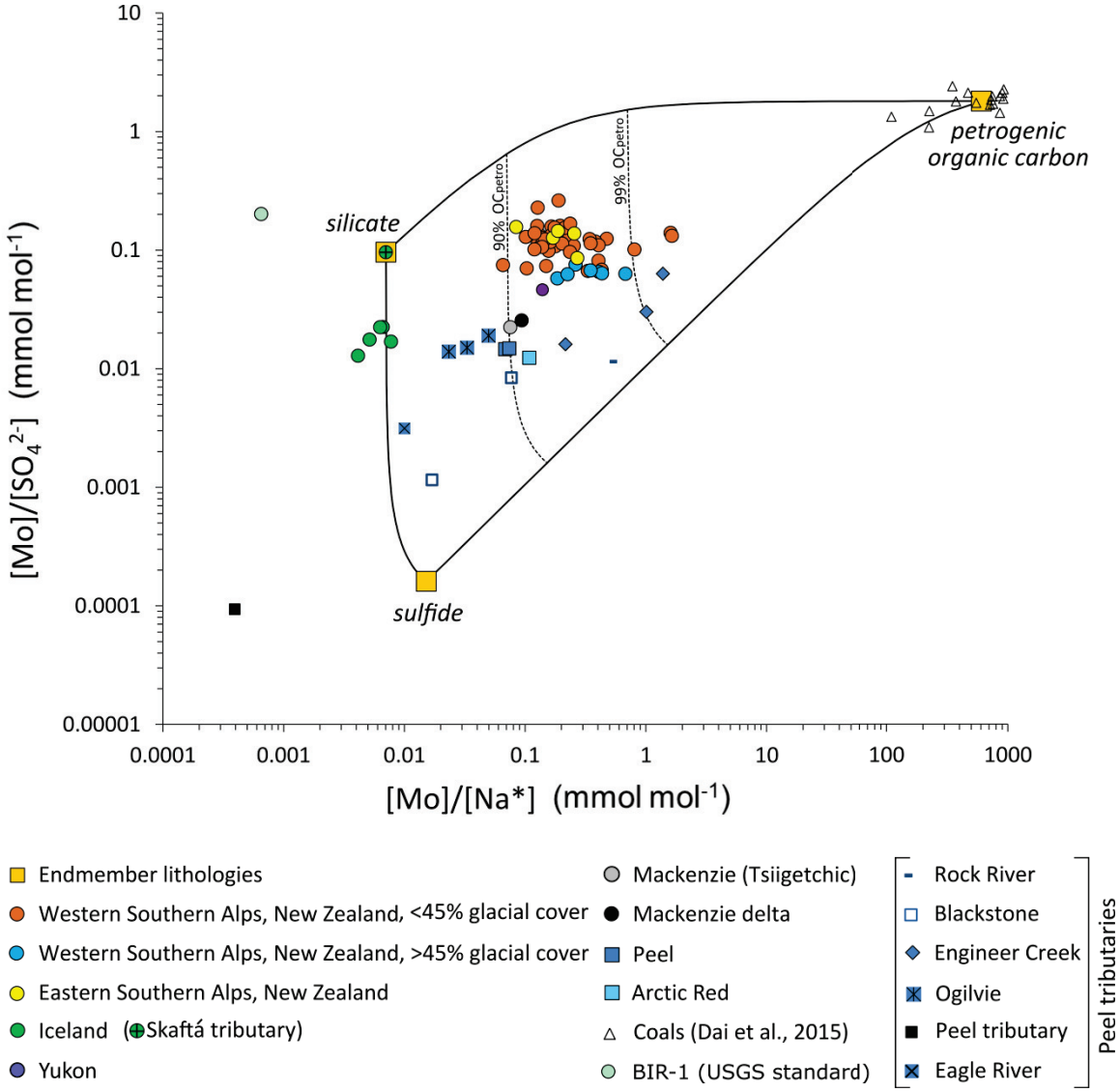

Figure 5.10 Relationship between dissolved [Mo]/[SO_4^{2-}] and [Mo]/[Na*] across a range of river catchments in New Zealand, Canada and Iceland. The chemical composition of the river water reflects a weathering contribution from several mineral phases. The relative location of silicates, sulfides and petrogenic organic carbon are inferred from ion ratio studies on these phases. Data for the petrogenic organic carbon endmember are from a suite of coal samples measured by Dai et al. (2015). A compilation of data from sedimentary rocks (Sundby et al., 2004) are used for the sulfide endmember, assuming a mean [Na] of sulphides = 88 µmol g^{-1} (Norman et al., 2002) and a mean [S] = 16670 µmol/g. This mixing model implies that Mo is sourced mainly from silicates in Iceland and petrogenic organic carbon in the Southern Alps and Canada. The percentage contribution of OC_{petro} is indicated with black dotted lines: 99% and 90%. The $[Na]_{diss}$ concentrations were corrected for atmospheric contribution using [Cl^-], giving $[Na^*]_{diss}$ (e.g. Gaillardet et al., 1999, Millot et al., 2003) for Canada and Iceland samples. New Zealand data reflect Na rather than Na* because the cyclic correction causes some of the Na concentrations to become negative, indicating this correction would overestimate any seawater input.

5.4.1.2 The effect of lithology and primary mineral dissolution on $\delta^{98/95}Mo_{diss}$

The broad-scale patterns in the Mo isotope composition of the rivers studied here can be attributed to differences in the composition of the bedrocks undergoing weathering and erosion. In the Southern Alps of New Zealand, the river bed materials have the lowest $\delta^{98/95}Mo_{BM}$ values (mean $\delta^{98/95}Mo_{BM}$ = -0.31 ± 0.05‰). The river bed materials collected from the Mackenzie River Basin

and Yukon River have the highest $\delta^{98/95}Mo_{BM}$ values, ranging from 0.15‰ to 0.53‰. These differences are consistent with the relatively OC-poor greywacke sandstone of the Southern Alps (Roser and Cooper, 1990), which may represent oxic depositional conditions favouring the sequestration of Mo that is depleted in heavier isotopes (i.e. ^{98}Mo). In contrast, some of the black shales of the Mackenzie River Basin reflect deposition under euxinic conditions (Johnston et al., 2012), when mineral phases retain a Mo isotope composition more similar to seawater (Kendall et al., 2017). In Iceland, as first order indication of the composition of the bedrock lithology in the Skaftá River catchments, we consider basalts sampled within close geographical proximity, which have a mean $\delta^{98/95}Mo$ = -0.15‰ (Yang et al., 2015). These have a composition that falls within the range expected for the upper continental crust (e.g. Liang et al., 2017; Willbold and Elliott, 2017). The differences between localities in terms of the $\delta^{98/95}Mo$ values of the source materials are reflected in the dissolved Mo isotope composition in the rivers. The river waters with the lightest Mo isotope values are found in New Zealand (0.00‰ to 0.32‰), followed by Iceland (0.26‰ to 0.47‰) and the Mackenzie and Yukon rivers (0.73 to 1.53‰) (Figure 5.9).

However, despite a broad lithological control on $\delta^{98/95}Mo_{diss}$ being evident, every setting shows fractionation between the river waters and the source material: rivers are always enriched in heavy Mo isotopes (Figure 5.9). The shift to more positive values in the river waters could reflect the incongruent dissolution of a mineral phase in the rocks that has heavier $\delta^{98/95}Mo$ values. This is likely to be a reduced phase, such as sulfide and/or organic matter, which undergoes less fractionation at the time of formation (Kendell et al., 2017) and thus records a $\delta^{98/95}Mo$ value that is closer to seawater (e.g. IAPSO seawater standard $\delta^{98/95}Mo = 2.07 \pm 0.06$‰). Sulfide minerals and rock organic matter weather faster than silicate phases, and previous work has shown that this is especially true in glacial settings (Torres et al., 2017; Tranter et al., 2002). However, this mechanism does not seem a plausible explanation for the patterns in the data due to three reasons. Firstly, we observe Mo isotope fractionation between the river dissolved loads and the river bed materials that is similar across all catchments (range is 0.4–0.8%), despite the large variability in the minerals sourcing Mo to the dissolved load (Figure 5.10). For the New Zealand and Canadian rivers, the majority of the dissolved Mo is derived from OC_{petro} whereas in the Skaftá River catchment, Iceland, OC_{petro} does not contribute to the dissolved Mo concentrations. Therefore in the Skaftá catchment, the dissolution of sulfide minerals in the basaltic bedrock would need to drive all of the fractionation observed; this seems unlikely given the low proportion of sulfide derived Mo in the rivers (Figure 5.10). Secondly, when we consider the concentrations of Mo in the dissolved load and river bed materials relative to rhenium (Re) concentrations in these materials, we observe evidence for Mo being lost from the dissolved load, with the greatest loss occurring in the rivers with the highest $\delta^{98}Mo$. As discussed further in section 5.4.2.1, Re is thought to be sourced from

similar mineral phases to Mo (Miller et al., 2011); therefore we expect both Mo and Re to follow similar trends in the dissolved load during weathering. However, the variable relationship between Mo and Re across the catchments suggests that a further mechanism is required to explain the data. Thirdly, we find evidence in deep soils (Figure 5.5) and on the coatings of suspended load particles (Figure 5.8) for a Mo component that has a much lower $\delta^{98/95}$Mo values than the river bed materials or dissolved load (Figure 5.9). Therefore, we surmise that in the studied catchments where there is evidence for loss of Mo in the dissolved load, incongruent dissolution of minerals cannot be a dominant control on the fractionation of the Mo isotopes between river waters and river sediments.

5.4.1.3 A role for atmospheric Mo inputs

As soils develop over time, atmospheric inputs can have an increasing influence on soil chemical budgets (Kennedy et al., 1998; Porder et al., 2007). Previous work on soil profiles developed on basaltic bedrock in Hawaii has suggested that atmospheric inputs of Mo from volcanic aerosols and/or ash and precipitation (and potentially anthropogenic sources) can play a role in setting the Mo mass budget and isotope signature of soil, especially in older and wetter soils (King et al., 2016; Siebert et al. 2015). However, aside from volcanic inputs, it is not clear how atmospheric inputs of Mo may influence the Mo isotope mass balance of river catchments. In the western Southern Alps, the mean annual precipitation is high, at ~4–6 m yr^{-1} along the range front (Henderson and Thompson, 1999), but the measured $[Mo]_{diss}$ was only 68.8 pmol L^{-1} and 117.8 pmol L^{-1}; this equates to a precipitation input of ~3–6 × 10^{-5} g yr^{-1} of Mo. In contrast, physical and chemical denudation in this setting supply ~10 mm yr^{-1} of rock mass to the surface (Hicks et al., 2011; Jacobson et al., 2003) with a [Mo] = 0.29 μg g^{-1}, which equates to ~700 × 10^{-5} g yr^{-1} of Mo. From this simplified mass balance, it appears as though Mo inputs from the atmosphere are minimal in this setting, and therefore their role for setting the $\delta^{98/85}$Mo values of soils and river waters is also negligible. In Iceland, an input of volcanic ash may affect the Mo content of the soils (e.g. King et al., 2016). However, ash may not necessarily alter $\delta^{98/95}$Mo values relative to underlying parent material if it has a similar chemical composition (Moune et al., 2012; Siebert et al., 2015).

5.4.2 A process control on the Mo isotope composition of rivers

5.4.2.1 Quantifying bulk Mo cycling and Mo isotope fractionation

To better evaluate the role of weathering processes for setting the isotope composition of Mo in the weathering zone, we first consider Mo abundance in relation to the behaviour of Re, another mobile trace element sourced primarily from organic mineral phases. Rhenium is established as one of the most mobile and soluble elements during chemical weathering (Colodner et al., 1993; Hilton et al., 2014). However, in contrast to Mo, it is not thought to be incorporated into secondary weathering products (Colodner et al., 1993; Miller et al., 2011). Colluvium samples from the

western Southern Alps support this inference. The $[Mo]_{COL}$ = 0.26 ± 0.05 μg g^{-1} (n = 4, ±2 SE), which is similar to the average of river bed materials, $[Mo]_{BM}$ = 0.29 ± 0.08 μg g^{-1} (n = 12, ±2 SE), suggesting some Mo is retained during weathering. In contrast, the mean $[Re]_{COL}$ = 29 ± 6 pg g^{-1} (n = 4, ±2 SE), which is much lower than that measured in the bed materials ($[Re]_{BM}$ = 118 ± 21 pg g^{-1}, n = 31, ±2 SE: ***Chapter 3***, Horan et al., 2017), suggesting more efficient loss of Re, relative to Mo, from the weathering zone.

Molybdenum concentrations in the river waters do not show a linear relationship with dissolved Re concentrations across all of the catchments (Figure 5.11). This indicates that congruent weathering together with simple dilution-evaporation cannot explain the patterns in the data as these processes would result in co-variation of element concentrations (White and Blum, 1995). It appears that the main separation from a linear trend occurs in samples from the Fox and Waiho catchments, where there are higher concentrations of Re and Mo. The Mo concentrations therefore appear to be influenced by a process that extracts Mo from the dissolved load and this is effect most apparent in more heavily glaciated areas.

We can consider this offset in the context of the fraction of Mo left in solution. The fraction of Mo left in solution after secondary mineral formation ($f\mathrm{Mo}_{diss}$) can be estimated by Equation 5.2, in analogy to the approach used to examine the uptake of lithium during secondary mineral formation (Dellinger et al., 2015; Millot et al., 2010).

Equation 5.2
$$f\mathrm{Mo}_{\mathrm{diss}} = \frac{([\mathrm{Mo}]/[\mathrm{X}])_{\mathrm{diss}}}{([\mathrm{Mo}]/[\mathrm{X}])_{\mathrm{rock}}}$$

In Equation 5.2, [X] is the concentration of a mobile soluble element that is retained in solution. $([Mo]/[X])_{diss}$ is the ratio of those elements in the dissolved products of weathering (i.e. carried in the river dissolved load), and $([Mo]/[X])_{rock}$ is the ratio of the elements in unweathered bedrocks. Here, we take [X] to be Re, given the high solubility of the Re anion upon oxidation and its documented mobility in river systems (Colodner et al., 1993; Hilton et al., 2014), together with the similarity in the mineral phases thought to source both Re and Mo to the dissolved load (e.g. Miller et al., 2011). Although it is possible that Re may be assimilated by algae in river environments, as has been documented in marine settings (Racionero-Gómez et al., 2016), the extent of this process in the terrestrial environment is unknown. Furthermore, the uptake and sequestration of Mo by similar (macro) algae has been documented (e.g. Kowalski et al., 2013) and we might expect the magnitude of this process, if it also occurs in river waters, to be greater for Mo relative to Re, given the ~100 fold higher concentrations of Mo in rivers (Miller et al., 2011) and the low reduction potential of Mo oxidation states, which make this element well-suited to be a co-factor in enzymes

that catalyse redox reactions (Kendall et al., 2017). Consequently, any potential removal of Re from the river waters through this process is likely to be negligible relative to Mo.

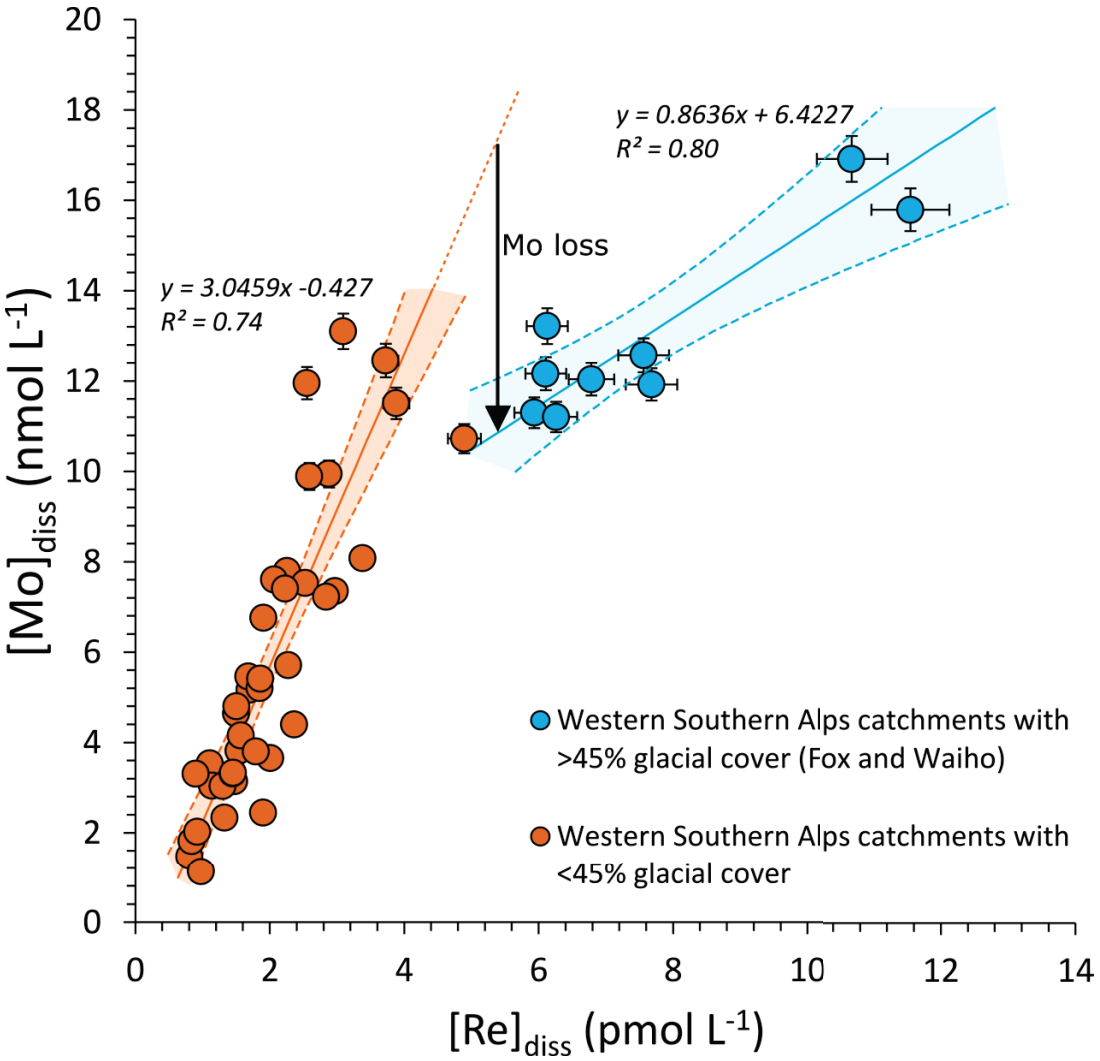

Figure 5.11 Relationship between Mo and Re abundance in the river waters of the western Southern Alps. There is a decoupling of the relationship between $[Mo]_{diss}$ and $[Re]_{diss}$ that is particularly apparent in the two catchments hosting valley glaciers (the Fox and Waiho) indicated by the blue circles; the rate of increase in Mo concentration is lower than that observed for Re, implying that Mo may be removed from the dissolved load in some catchments. Errors are 3% deviations for [Mo] concentrations and 5% deviations for [Re], based on typical reproducibility of duplicate sample analyses. Error ellipses were calculated using Isoplot with a Model 2 fit (Ludwig, 2008).

To constrain $([Mo]/[Re])_{rock}$ in the western Southern Alps, we use the average composition of river bed materials ($[Mo]_{BM}/[Re]_{BM}$ = 2.4 ± 0.47 (μg g^{-1}) (ng g^{-1})$^{-1}$; ±2 SE, n = 12) because lithological variability is relatively small along strike of the Alpine Fault (Hilton et al., 2008; Mortimer 2004) and these bed materials should integrate the composition of sediments eroded from large areas of the catchments. In the larger rivers of the Mackenzie River Basin, we use the individual catchment river bed materials because lithology is more variable across the different catchments here (Beaulieu et al., 2011). A $f\mathrm{Mo}_{diss}$ value of 1 suggests that Mo is not re-incorporated in secondary minerals after its initial dissolution (congruent dissolution). A $f\mathrm{Mo}_{diss}$ value of 0 indicates that all of

the Mo initially dissolved has been re-incorporated into secondary weathering products. At steady state, a $f\text{Mo}_{diss}$ value greater than 1 should not be possible. If $f\text{Mo}_{diss}$ is >1, it suggests that either Re and Mo may not be released congruently, Re may not be completely mobile, and/or the system is not at steady state over the time period of sampling. The latter is a possibility for Mo, as it is used by plants in nitrogenase enzymes and it may be cycled through biomass and soil to varying extents over seasonal time periods.

To investigate the behaviour of Mo in the river waters in more detail, we examine $f\text{Mo}_{diss}$ alongside the $\delta^{98/95}\text{Mo}_{diss}$ (dissolved load) relative to $\delta^{98/95}\text{Mo}_{BM}$ (bed materials) to quantify the bulk isotope fractionation. The dissolved load of all rivers is fractionated toward high $\delta^{98/95}$Mo values compared to the source rock ($\delta^{98/95}\text{Mo}_{BM}$) (Figure 5.9). Despite the diversity in our studied catchments, when examined together the results are quite striking: the bulk fractionation of Mo, $\Delta^{98/95}\text{Mo}_{diss\text{-}BM}$ (i.e. the difference between $\delta^{98/95}\text{Mo}_{diss}$ and $\delta^{98/95}\text{Mo}_{BM}$), in the catchments from New Zealand, Canada and Iceland, all show a dependency on the fraction of Mo left in solution, $f\text{Mo}_{diss}$ (Figure 5.12). As the fraction of Mo left in solution decreases, there is an increase in $\Delta^{98/95}\text{Mo}_{diss\text{-}BM}$, which implies a relative loss of light Mo isotopes is driving the river waters to isotopically heavier values. When the data from the western Southern Alps are considered, we also find that the data from the glacial catchments trend toward higher $\Delta^{98/95}\text{Mo}_{diss\text{-}BM}$ and lower $f\text{Mo}_{diss}$ values relative to data from catchments with lower glacial cover. In the Fox glacial catchment in the western Southern Alps, we also observe changes in the Mo concentration and Mo isotope composition of the river water as it flows from the head of the glacier to a sampling point located approximately 2 km downstream. The $[\text{Mo}]_{diss}$ decreases from 15.8 to 12.0 nmol L^{-1}, while $\delta^{98/95}$Mo increases from 0.17 ± 0.11‰ (±2 SD) to 0.32 ± 0.03‰ (±2 SD). This could suggest that light Mo is extracted from the dissolved load during riverine transit, or in waters flowing through moraines and hillslopes that contribute to the flow downstream. In contrast, in the glacial Skaftá River catchment, Iceland, the highest Mo concentrations and heaviest Mo isotope compositions are found closest to the Vatnajökull glacier (section 5.3.2.2). This difference may reflect the longer flow path of the Skaftá River: close to the glacier greater Mo fractionation may be apparent due to the high fine particulate load on to which Mo may adsorb (section 5.4.2.3), whereas at the far downstream Skaftá sampling sites (Figure 5.3) the sediment load is reduced and the extent of fractionation appears to be more limited.

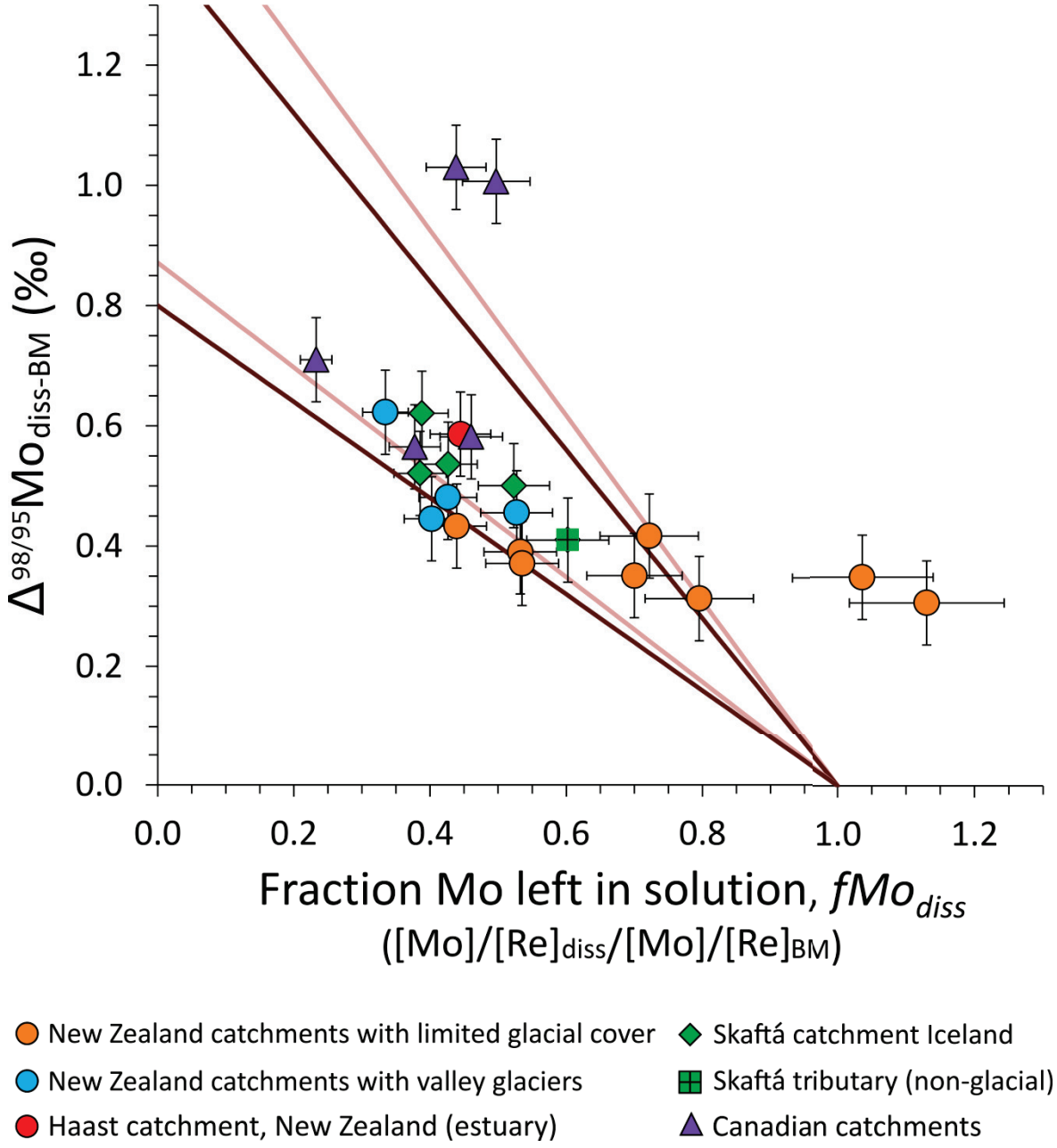

Figure 5.12 The behaviour of Mo in solution. The degree of isotope fractionation of Mo in the dissolved load relative to the river bedload ($\Delta^{98/95}Mo_{diss\text{-}BM} = \delta^{98/95}Mo_{diss} - \delta^{98/95}Mo_{BM}$) as a function of the fraction of Mo remaining in solution ($fMo_{diss} = ([Mo]/[Re]_{diss}/[Mo]/[Re]_{BM})$). Vertical error bars are ±0.07‰, which is the propagated long-term reproducibility of the IAPSO and BHVO-1 standards on the dissolved and bedload data. Horizontal bars are ±10%, which is the propagated uncertainty on the concentration measurements of Re and Mo for the dissolved load and bed materials. The $[Mo]_{diss}$ data are those quantified by ID MC-ICP-MS. The $[Mo]/[Re]_{BM}$ and $\delta^{98/95}Mo_{BM}$ data for the western Southern Alps are averaged data from all river bed materials. The lines indicate experimental model results for the fractionation associated with uptake of light Mo on to Fe-Mn (oxyhyr)oxides: pale pink lines are based on the model of Barling and Anbar (2004), where $\Delta^{98/95}Mo_{sec\text{-}diss}$ ranges from -0.87 to -1.54‰; brown lines are based on the model of Goldberg et al. (2009), where $\Delta^{98/95}Mo_{sec\text{-}diss}$ ranges from -0.8‰ to -1.4‰ for adsorption on to magnetite through to goethite.

5.4.2.2 The role of Mo cycling in the biosphere

Molybdenum plays an important role in the functioning of ecosystems and the combined effect of redox reactions operating in soils and the action of biological processes has the potential to drive

changes in the oxidation state and/or speciation of Mo, inducing isotope fractionation (Barling and Anbar, 2004; King et al., 2016; Siebert et al., 2015). Molybdenum can bind to soil organic matter through ligand exchange and specific adsorption (Wichard et al., 2009). This means organic matter can regulate long-term Mo retention and loss from soils via dissolution and leaching pathways (Marks et al., 2015). The retention of Mo by the modern biosphere could drive the fractionation patterns observed here (Dahl et al., 2013; McManus et al., 2006; Siebert et al., 2015; Wichard et al., 2009). In addition, Mo is important in the biogeochemical cycle of nitrogen in plants and it is actively taken up by the biosphere for incorporation into the enzymes nitrogenase and nitrate reductase (Bellenger et al., 2008; Boyd et al., 2011; Glass et al., 2009). Mo isotope fractionation can occur during the reactions associated with these enzymes; for example, assimilation of Mo by the nitrogen-fixing soil bacterium, *A. Vinelandii*. The kinetic fractionation involved results in organic matter having a low $\delta^{98/95}$Mo value and the residue becoming enriched in the heavy isotopes (Barron et al., 2009; Jean et al., 2013; Liermann et al., 2005; Silvester, 1989; Wasylenki et al., 2007; Wurzburger et al., 2012; Zerkle et al., 2011).

The soil materials from the Docherty catchment in the western Southern Alps indicate that Mo concentrations are similar or enhanced relative to the local river bed materials across a range of organic carbon (OC) concentrations. This implies that Mo is being retained across soil horizons, not just in the upper organic-rich soil litter (Figure 5.5). The deeper soils materials are low in OC but have similar [Mo], which results in there being no correlation between soil OC concentration and Mo abundance (Supplementary Figure 5.3). In the surface soil litters, we do not observe a clear trend toward heavy isotope compositions predicted by experimental fractionation factors (Liermann et al., 2005; Wasylenki et al., 2007); only two of the soil litters have resolvably heavier $\delta^{98/95}$Mo values relative to the river bed materials (Figure 5.4). Nevertheless, the soil sample set is small and the cycling of Mo in organic matter cannot be ruled out as a control on the $\delta^{98/95}Mo_{diss}$ of the New Zealand rivers (and other catchments). However, to fully explain the dataset, we must turn to other processes that fractionate Mo isotopes.

5.4.2.3 The role of secondary mineral formation: Fe and Mn (oxyhydr)oxides

Adsorption of Mo to Fe and Mn (oxyhydr)oxides is associated with the preferential uptake of lighter Mo isotopes from solution (Bibak and Borggard, 1994; Goldberg et al., 1996; Lang and Kaupenjohann, 2003; Xu et al., 2013). In fact, the largest modern sink for Mo (45–70%) is thought to occur via adsorption of molybdate to ferromanganese (oxyhydr)oxides under oxic conditions in marine sediments (Barling et al., 2001; Barling and Anbar, 2004; McManus et al., 2006; Siebert et al., 2003). Detailed experimental work on Mo adsorption to Mn and Fe (oxyhydr)oxides points to the preferential scavenging of light isotopes by these mineral phases (Barling and Anbar, 2004; Goldberg et al., 2012; Malinovsky et al., 2007; Siebert et al., 2003; Wasylenki et al., 2008).

The degree of Mo adsorption onto Mn and Fe (oxyhydr)oxides is thought to be strongly pH-dependent (Kim and Zeitlin, 1968), and is limited at pH values >6.5. Between pH values 3–5, Mo may be strongly adsorbed to Fe, Mn, and aluminium (Al) oxides (Goldberg et al., 2002; Goldberg and Forster, 1998; Karimian and Cox, 1979; Xu et al., 2006), but at higher pH values, Mo solubility increases and there is decreased adsorption. The latter is associated with increased Mo loss as the soluble molybdate (MoO_4^{2-}). The river waters in New Zealand, Canada and Iceland had pH values mostly between 7 and 8.5 at the time of sampling (Table 5.5), indicating that Mo adsorption to (oxyhydr)oxides should be limited in the waters. However, water within soils is expected to have a greater concentration of CO_2 species from soil respiration and therefore lower pH values than water exposed to the atmosphere. Thus, the greatest adsorption of Mo should take place in these lower pH waters. Fractionations between the solid and dissolved phase also vary with mineralogy, increasing in the order magnetite ($\Delta^{98/95}Mo_{diss\text{-}adsorbed}$ = 0.83 ± 0.60‰) < ferrihydrite ($\Delta^{98/95}Mo_{diss\text{-}adsorbed}$ = 1.11 ± 0.15‰) < goethite ($\Delta^{98/95}Mo_{diss\text{-}adsorbed}$ = 1.40 ± 0.48‰) < hematite ($\Delta^{98/95}Mo_{diss\text{-}adsorbed}$ = 2.19 ± 0.54‰) (Goldberg et al., 2009). The adsorption of light Mo to Mn and Fe (oxyhydr)oxides in the soils of the river catchments would result in the soil porewaters becoming enriched in the heavier isotopes of Mo (i.e. ^{98}Mo), which will subsequently be transferred to the river waters.

The soil samples from New Zealand support an important role for Fe and Mn (oxyhydr)oxides. The deep, OC-poor soils have low $\delta^{98/95}Mo$ values (Figure 5.5), which are consistent with the fractionation observed in experimental studies (Barling and Anbar, 2004; Goldberg et al., 2009). The deeper soil horizons have the greatest potential to scavenge Mo due to their longer residence time and greater build-up of weathering residues and we find they have the greatest fractionation relative to the local bedrock. The sequential extractions of Mo from river suspended loads also support an important role for Fe and Mn (oxyhydr)oxides. The leachate data indicate similar proportions of Mo are contained within oxides and (oxyhydr)oxides on the suspended sediment collected in the Fox (20%) and Cook (24%) rivers. The isotopically lighter composition of this oxide-bearing HCl leachate (Figure 5.8) is also consistent with the lower $\delta^{98/95}Mo$ values of weathered colluvium being explained by the presence of Fe and Mn (oxyhydr)oxide coatings (Barling and Anbar 2004).

5.4.2.4 Insight from a mass balance model

To examine whether the experimentally derived fractionation factors for Mo uptake by Fe and Mn (oxyhydr)oxides (Barling and Anbar, 2004; Goldberg et al., 2009) are consistent with the river data we explore a mass balance model (Bouchez et al., 2013; Dellinger et al., 2015; Georg et al., 2007; Johnson et al., 2004). Here, the weathering zone is considered to be an open flow-through system over which Mo is released in dissolved form during the dissolution of primary minerals and

removed from solution by incorporation into secondary minerals; as quantified by $f\text{Mo}_{diss}$ (Equation 5.2). At steady state, all of the dissolution and precipitation input and output fluxes are balanced, $f\text{Mo}_{diss}$ <1 and the Mo isotope composition of the dissolved phase may be modelled following the method of Bouchez et al. (2013):

Equation 5.3 $$\delta^{98/95}\text{Mo}_{diss} = \delta^{98/95}\text{Mo}_{rock} - \Delta^{98/95}\text{Mo}_{sec\text{-}diss} \times (1 - f\text{Mo}_{diss})$$

where $\delta^{98/95}\text{Mo}_{rock}$ is the Mo isotope composition of the rock undergoing weathering and $\Delta^{98/95}\text{Mo}_{sec\text{-}diss}$ is the isotope fractionation factor between secondary products and the dissolved load:

Equation 5.4 $$\Delta^{98/95}\text{Mo}_{sec\text{-}diss} = \delta^{98}\text{Mo}_{sec} - \delta^{98}\text{Mo}_{diss} = 1000 \ln (\alpha_{sec\text{–}diss}) = 1000 \ln (0.9982 \pm 0.005)$$

where $\delta^{98/95}\text{Mo}_{sec}$ corresponds to the Mo isotope composition of the solid weathering products and $\alpha_{sec\text{-}diss}$ is the fractionation factor (Barling and Anbar, 2004). Equation 5.3 can be re-written in terms of the difference in the isotope composition between the rocks and the dissolved phase:

Equation 5.5 $$\delta^{98/95}\text{Mo}_{diss} - \delta^{98/95}\text{Mo}_{rock} = -\Delta^{98/95}\text{Mo}_{sec\text{-}diss} \times (1 - f\text{Mo}_{diss})$$

which in this case is assumed to be closely equivalent to $(\delta^{98/95}\text{Mo}_{diss} - \delta^{98/95}\text{Mo}_{BM})$.

To explore the range of predicted values as a function of $f\text{Mo}_{diss}$, values of $\Delta^{98/95}\text{Mo}_{sec\text{-}diss}$ are taken from the experimental data of Goldberg et al. (2009) and Barling and Anbar (2004). These range from –0.8‰ to –1.4‰ for adsorption on to magnetite through to goethite (Goldberg et al. 2009). The modelled batch fractionation factors can explain the majority of the variability in the $f\text{Mo}_{diss}$ and $\Delta^{98/95}\text{Mo}_{diss\text{-}BM}$ values of the rivers in our study locations, where the slope of the correlation from the river catchments with fMo_{diss} <1 is –0.63 (n = 19, r^2 = 0.7); this regression excludes the two Canadian samples that sit away from the bulk of the data (Figure 5.12).

Variability in the $\delta^{98/95}\text{Mo}_{diss}$ across all catchments would therefore appear to be arising from a process with similar $\alpha_{sec\text{-}diss}$ and similar associated mass exchange between reservoirs, with the different catchments merely being characterised by different extents of this reaction. The more heavily glaciated river catchments in the western Southern Alps have higher $\Delta^{98/95}\text{Mo}_{diss\text{-}BM}$ values. This is also true of samples collected closer to the source of the Skaftá glacial river, Iceland. Increased adsorption of Mo to Fe and Mn (oxyhydr)oxides) in environments where fine sediment particles are more abundant has been invoked in other locations as a potential 'glacial' control on $\delta^{98/95}\text{Mo}_{diss}$ values (Pearce et al., 2010a). A larger difference between $\delta^{98}\text{Mo}_{diss}$ and $\delta^{98}\text{Mo}_{BM}$

($\Delta^{98/95}Mo_{diss\text{-}BM}$ = 0.59‰) is also found in the Haast catchment from the western Southern Alps, relative to similar catchments from this setting that have glaciers limited to headwaters (mean $\Delta^{98/95}Mo$ = 0.37 ± 0.03‰, n = 8, ±2 SE). Data from this catchment also sit towards lower values of $f Mo_{diss}$. The offset may be explained by the proximity of this Haast River sampling site to the Haast estuary, where the interaction of Mo with flocculating fine sediments could drive the $\delta^{98}Mo_{diss}$ to heavier values. Desorption of isotopically light Mo from particulates may occur in some estuaries (Pearce et al., 2010a) whereas in others, as appears the case here, isotopically light Mo may be retained in estuarine sediments, causing the release of isotopically heavy Mo to the oceans (Rahaman et al., 2014). Interestingly, in the Mackenzie River Basin, the weathering intensity of silicate minerals is minor (Dellinger et al., 2014), yet here we see evidence for a process-driven Mo isotope fractionation of >0.7‰. The current weathering regime in this basin appears to promote Fe-Mn (oxyhydr)oxide formation.

There are outliers in $\Delta^{98/95}Mo_{diss\text{-}BM}$ versus $f Mo_{diss}$ space that cannot be explained by the simple model. First, the Peel and Ogilvie rivers have larger $\Delta^{98/95}Mo_{diss\text{-}BM}$ values than predicted by the mass balance model (Figure 5.7). This could be a consequence of uncertainty regarding the composition of un-weathered materials and/or the behaviour of Mo and Re during weathering, or it may reflect the action of microbes. Enhanced sulfide weathering in these catchments (Figure 5.10) may be associated with microbial activity preferentially extracting light Mo isotopes for metabolic processes; a mechanism that could induce additional fractionation. Second, two river water samples from the Callery catchment, in the western Southern Alps, have values of $f Mo_{diss}$ that exceed 1. This apparent gain of Mo relative to Re could reflect non-steady state release of Mo from the biosphere, although the impact on the isotope ratio is less clear based on the soil litter $\delta^{98/95}Mo$ values (Figure 5.4). Alternatively, it is possible that the average $[Mo]/[Re]_{BM}$ ratio used in the calculation of $f Mo_{diss}$ for the Callery River does not well represent the rocks being weathered in this catchment. If the catchment specific bedloads are used, we find that $f Mo_{diss}$ becomes 0.73 and 0.79 for the two samples from the Callery River catchment. However, using individual bedloads for all of the catchments in the western Southern Alps would also cause two data points to have $f Mo_{diss}$ values >1, suggesting that in other cases the catchment geology composition would not be fully captured by a single river bed material sample.

5.4.3 Global implications

The measurements from New Zealand, Iceland, and the Mackenzie and Yukon rivers provide new insight into the controls on the Mo isotope composition of continental runoff. This has implications for our understanding of the global controls on river $\delta^{98/95}Mo$ more generally and the resulting composition of seawater. Our data indicate an initial source control on the Mo isotope composition. Weathering reactions can supply dissolved Mo to rivers varying by ~1.5‰ due to different $\delta^{98/95}Mo$

values of rocks (and minerals) undergoing weathering (Figure 5.9). However, we show that the subsequent partitioning of Mo between the dissolved load and solid weathering products ($f\text{Mo}_{diss}$, Equation 5.2) plays a major role in governing the final Mo isotope composition of the dissolved load (Figure 5.12). In analogy to the behaviour of Li in river waters (Dellinger et al., 2015; Pogge von Strandmann et al., 2012; Tipper et al., 2012; Wimpenny et al., 2010), light isotopes of Mo appear to be preferentially removed from solution into secondary weathering products, leaving river waters with heavier $\delta^{98/95}$Mo values. In the preceding sections, our discussion highlighted the importance of Mo fractionation via the incorporation of light isotopes of Mo into Fe-Mn hydroxides in the weathering zone. This mechanism is able to explain the fractionation patterns across a variety of catchments worldwide that contrast with each other in terms of lithology, biological cover and erosion processes; thereby highlighting the potential importance of this removal pathway for the global Mo cycle.

Variability in the type and intensity of chemical weathering through geological time may influence the bulk average value of $\delta^{98/95}$Mo in river runoff. Large variations in weathering intensity are thought to have occurred at various times in Earth history; for example, in association with changes in climate or terrestrial vegetation (Algeo and Scheckler, 1998; Kump et al., 2000; Ravizza et al., 2001; Raymo and Ruddiman, 1992; Walker et al., 1981). Glacial-interglacial cycles may shift the relative dominance of chemical and physical weathering, and associated changes in precipitation and biological productivity may affect the degree of soil weathering and soil organic matter content (Siebert et al., 2015). Glaciation can enhance oxidative weathering reactions (***Chapter 3***, Horan et al., 2017; Torres et al., 2017) and in periods of increased glaciation, the increased rate of Mo mobilisation from hillslopes, together with higher sediment yields, may increase the opportunity for fractionation.

Ultimately, changes in the flux of Mo to the oceans, and/or in the isotope composition of riverine Mo as a result of changing weathering sources and shifts in Mo retention in soils, could influence the long-term ocean Mo isotope budget on timescales greater than the residence time of Mo in seawater (~440 ka: Miller et al., 2011). An analogy for the behaviour of Mo can be made with Li isotopes. Seawater Li isotopes recorded in carbonate minerals show an increase in δ^{7}Li over the Cenozoic (Misra and Froelich, 2012). The reasons for this shift are debated (e.g. Dellinger et al., 2015; Li and West, 2014), but the role of riverine Li inputs and the isotope composition of continental runoff is often invoked as a major player (Misra and Froelich, 2012). Rivers dominate the Mo input to the oceans (***Chapter 1***: Figure 1.11), suggesting that the Mo isotope budget may be sensitive to similar processes. For example, if changes in physical denudation rate and/or mechanism, such as glacial processes, result in opportunities to enhance Fe-Mn (oxyhydr)oxide formation during weathering, this will shift $\delta^{98/95}$Mo values further away from lithologically driven

starting values. On a regional scale, these changes may significantly alter the river input to the ocean, and will be particularly influential in restricted basins (Siebert et al., 2015). Shifts of as little as ~0.3‰ in continental runoff could have a profound impact on how $\delta^{98/95}$Mo values of sedimentary rocks are used to reconstruct palaeoredox conditions. For example, the same proportion of Mo removed in euxinic settings may not produce sediments with the same values of $\delta^{98/95}$Mo at different periods in Earth's history if the $\delta^{98/95}$Mo composition of the continental input changes. Therefore, revised estimations of the percentage of the ocean that is euxinic (e.g. Owens et al., 2013; Reinhard et al., 2013) may be required.

5.5 Conclusion

The Mo isotope composition of continental runoff ($\delta^{98/95}Mo_{diss}$) places a major control on the $\delta^{98/95}$Mo composition of seawater, and therefore it is relevant for the use of Mo isotopes to examine palaeoredox conditions. The $\delta^{98/95}Mo_{diss}$ values may also record information on the style and intensity of weathering, the formation of secondary minerals, and the biogeochemical cycle of nitrogen. To improve our understanding of the $\delta^{98/95}Mo_{diss}$ values of rivers, we measured Mo isotopes in river catchments of the Southern Alps of New Zealand, the Mackenzie and Yukon in Canada, and the Skaftá River catchment in Iceland, to reveal a source (e.g. bedrock lithology and mineral phase) versus a process (secondary mineral formation) control on $\delta^{98/95}Mo_{diss}$. Molybdenum may be sourced from silicate, sulfide and organic carbon mineral phases and we estimated the relative contribution of each using the ion ratios $[Mo]/[SO_4^{2-}]$ and [Mo]/[Na*]. In the Southern Alps and Canada, dissolved Mo appears to be predominantly sourced from OC_{petro}, with a slightly higher role for sulfide oxidation in several of the smaller Canadian catchments. In contrast, in Iceland Mo appears to be mainly derived from silicate minerals. The Mo isotope composition of river waters varies between New Zealand (0.00 to 0.32‰), Iceland (0.26 to 0.47‰) and the Mackenzie and Yukon rivers (0.73 to 1.53‰). These shifts are broadly consistent with the variability in the composition of the source rocks being weathered.

We reveal significant further variability in $\delta^{98/95}Mo_{diss}$ of ~0.4‰ to 0.8‰, relative to river bed materials, that is associated with different extents of Mo removal from the dissolved phase. In all catchments, $\delta^{98/95}Mo_{diss}$ values are higher than the corresponding river bed materials. The degree of bulk fractionation between the dissolved phase and river bed materials varies as a function of the fraction of Mo left in solution, which can be quantified using the ratio of Mo to Re in the dissolved load versus the river bed materials. The patterns in the data from New Zealand, Canada and Iceland are consistent with experimentally derived fractionation factors for Mo uptake to Fe-Mn (oxyhydr)oxide minerals. However, we are unable to completely rule out the potential role of organic matter in fractionating Mo isotopes. In the western Southern Alps, New Zealand, the $\delta^{98/95}$Mo river data are complemented by $\delta^{98/95}$Mo measurements for soil horizons, where deep

weathered colluvium, with low OC content, appears to be the corresponding Mo reservoir that is enriched in light isotopes. Extractions of isotopically light Mo from coatings on suspended load particles also support these observations. Together, the data demonstrate the importance of secondary weathering processes in removing Mo from solution in river catchments and playing a major role in setting the $\delta^{98/95}Mo_{diss}$ composition. Changes in weathering regimes and weathering intensities in river catchments could therefore give rise to secular changes in $\delta^{98/95}Mo_{diss}$ values that may influence the Mo isotope composition of lakes, coastal regions and potentially the Mo isotope composition of seawater.

5.6 Supplementary Figures

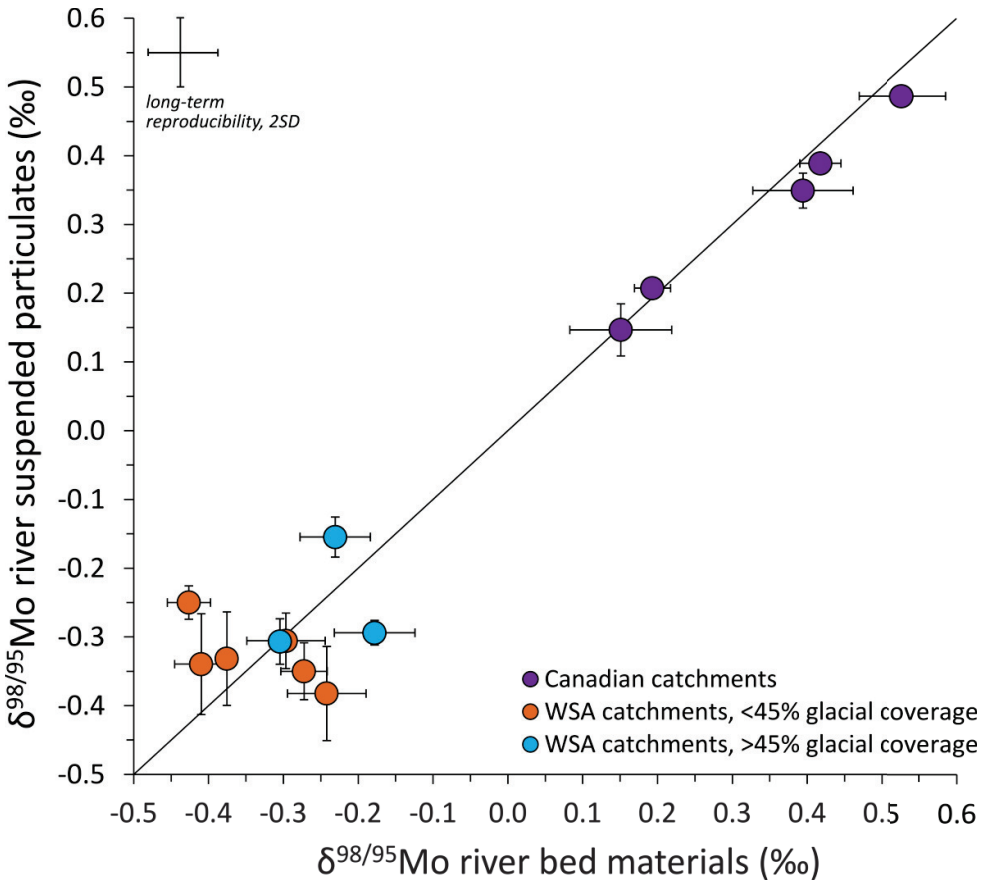

Supplementary Figure 5.1 Relationship between the Mo isotope composition of river bed materials and the isotope composition of the suspended river particulates for the western Southern Alps (WSA) and Canadian catchments. The line indicated is a 1:1 relationship between the two sediment types: the data have a close agreement to this line. The error bars are ±2 SD on the mean value of replicates from an analytical session.

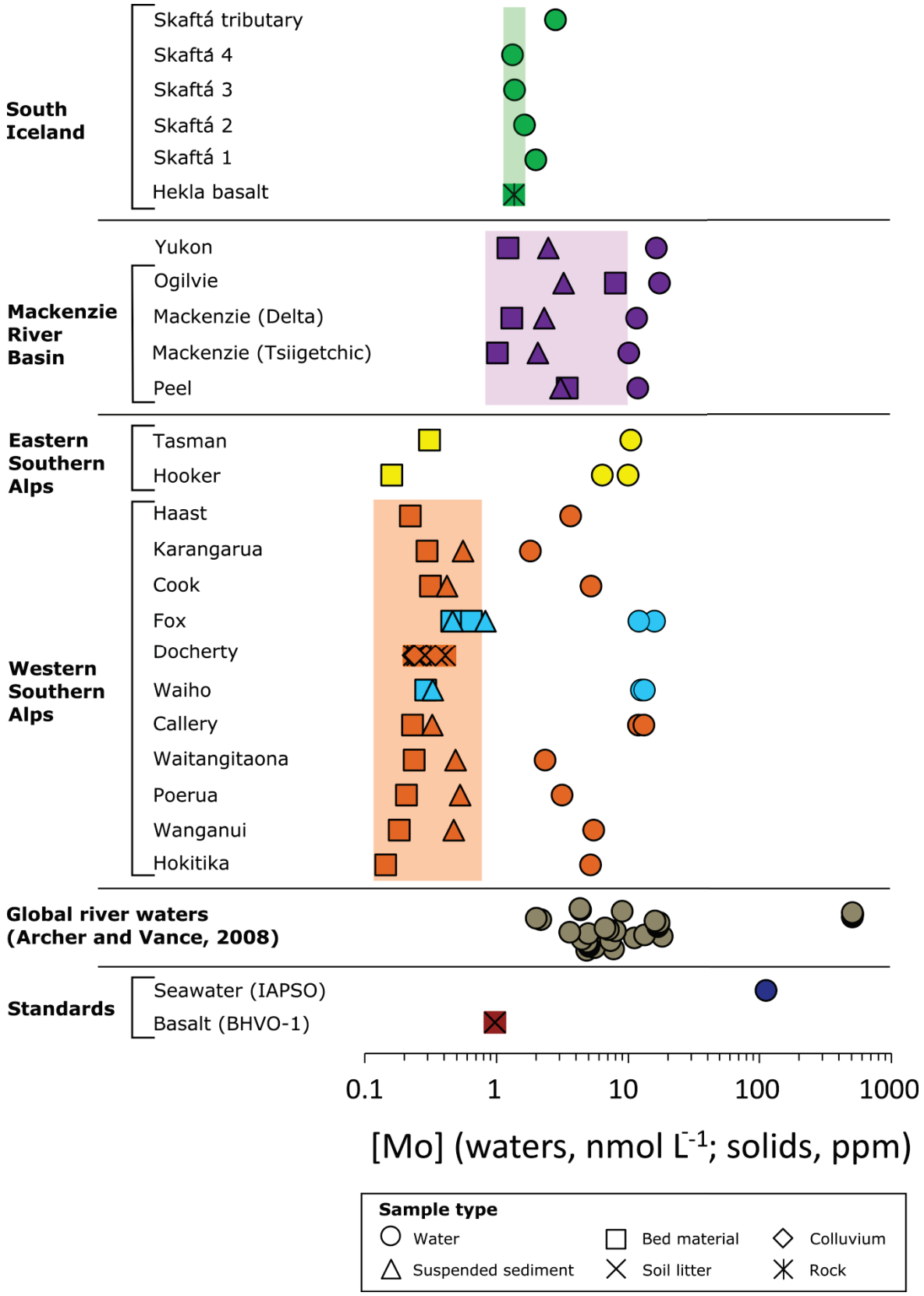

Supplementary Figure 5.2 Concentrations of Mo in the river dissolved loads, suspended loads, soils and bed materials from river catchments sampled in New Zealand, Canada and Iceland. The dissolved Mo concentration in global rivers (Archer and Vance, 2008) and in the seawater (IAPSO) and basalt (BHVO-1) standards are indicated for comparison. Errors are smaller than the symbol size.

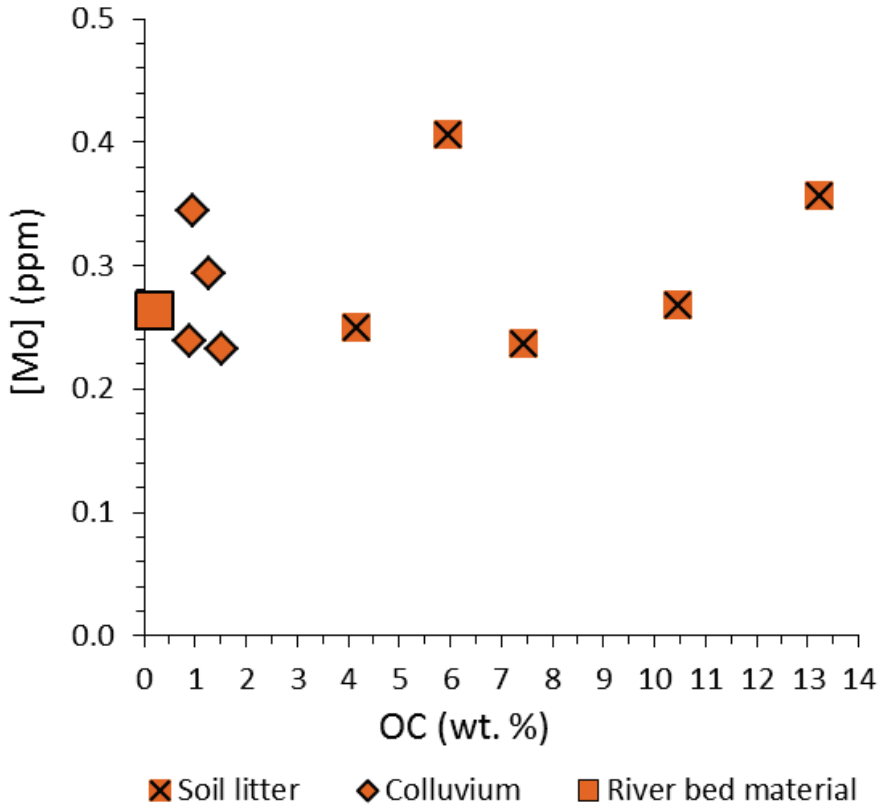

Supplementary Figure 5.3 Relationship between Mo and organic carbon (OC) concentrations in soil material from the western Southern Alps. Surface soil litters are enriched in OC but all materials have similar Mo concentrations. The composition of the local river bed material at Docherty Creek is indicated. Long-term percentage error on duplicate analyses is smaller than symbol size.

5.7 Data Tables

Table 5.1 | Summary of samples included in $\delta^{98/95}$Mo and Mo abundance analyses.

Location	**Samples used in Mo isotope analyses**			**Additional water samples used in Mo abundance analyses**	
Western Southern Alps, New Zealand	River water Suspended particulates River bed materials Soils	13 9 12 9	*Catchments: Hokitika, Wanganui, Poerua, Waitangitaona, Callery, Waiho, Fox, Cook, Karangarua, Haast, Docherty*	38	*Catchments: Whataroa, Makawhio, Copland, in addition to the same sample localities and tributaries of rivers used in isotope analyses*
Eastern Southern Alps, New Zealand	River water River bed materials	3 2	*Catchments: Hooker, Tasman*	-	
Mackenzie River Basin and Yukon	River water Suspended particulates River bed materials	5 5 5	*Catchments: Peel, Mackenzie (Tsiigetchic), Mackenzie (delta), Ogilvie, Yukon*	8	*Catchments: Arctic Red, Liard, tributaries of the Peel, in addition to the same sample localities as those used in isotope analyses*
Iceland	River water	5	*2014 samples: Skaftá sites 1–4 and non-glacial Skaftá tributary*	5	*2013 Skaftá sites 1–3, non-glacial Skaftá tributary; 2014 Skaftá 5*

Table 5.2 | River bed materials.

Location	Sample ID	Catchment	Collection date	Latitude (deg)	Longitude (deg)	$[Re]_{BM}$ (pg g^{-1})	$[OC]_{BM}$ %	$\delta^{98/95}Mo$ (‰)	2SD (‰)	Replicates	Mo (µg g^{-1})
Western Southern Alps, New Zealand	NZ14-19	Hokitika	14/09/2014	42.95557 S	171.01666 E	87.20	0.11	-0.264	0.037	2	0.14
	NZ14-23	Wanganui	15/09/2014	43.16322 S	170.62808 E	77.80	0.08	-0.376	0.001	2	0.18
	NZ14-38	Poerua	16/09/2014	43.15672 S	170.50438 E	81.10	0.17	-0.272	0.031	3	0.21
	NZ14-35	Waitangitaona	16/09/2014	43.28241 S	170.30812 E	251.50	0.18	-0.410	0.036	3	0.24
	NZ14-49	Callery	16/09/2014	43.39675 S	170.18344 E	66.20	0.08	-0.297	0.052	2	0.23
	NZ14-92	Waiho	27/09/2014	43.41808 S	170.18065 E	103.70	0.11	-0.305	0.011	4	0.29
	NZ14-90	Docherty Creek	27/09/2014	43.38486 S	170.13333 E	111.90	0.21	-0.262	0.042	3	0.26
	NZ14-90 duplicate							-0.258	0.055	3	0.25
	NZ14-64	Fox	18/09/2014	43.49958 S	170.05521 E	241.20	0.13	-0.231	0.047	3	0.46
	NZ14-67	Fox	19/09/2014	43.48704 S	170.02962 E	235.70	0.19	-0.178	0.054	4	0.65
	NZ14-67 duplicate							-0.118	0.066	3	0.53
	NZ14-70	Cook	19/09/2014	43.49912 S	169.9653 E	113.90	0.18	-0.242	0.052	3	0.32
	NZ14-72	Karangarua	19/09/2014	43.57515 S	169.8051 E	76.10	0.17	-0.426	0.029	3	0.30
	NZ14-76	Haast	19/09/2014	43.85398 S	169.05496 E	116.70	0.13	-0.427	0.040	3	0.22
Eastern Southern Alps, New Zealand	NZ14-115	Hooker Glacier	04/10/2014	44.03936 S	169.37926 E	72.50	0.06	-0.339	0.004	2	0.16
	NZ14-119	Tasman River	04/10/2014	43.70715 S	170.17097 E	82.10	0.06	0.349	0.014	3	0.31
Mackenzie River Basin, Canada	CAN09-41	Peel, Fort McPherson	21/7/2009	67.33189 N	134.86912 W	4356		0.193	0.024	5	3.44
	CAN09-48	Mackenzie, Tsiigehtchic	22/7/2009	67.44935 N	133.74064 W	739.6		0.418	0.027	4	1.01
	CAN10-27	Mackenzie Delta, Middle Channel, Inuvik	8/9/2010	68.44568 N	134.21349 W	1498		0.394	0.067	3	1.31
	CAN13-10	Ogilvie, Dempster	20/07/2013	65.56789 N	138.17824 W	11354	0.90	0.527	0.058	3	7.98
Yukon, Canada	CAN13-23	Yukon, Dawson City	21/07/2013	64.04846 N	139.45628 W	1044	0.50	0.151	0.068	3	1.22

Table 5.3 | River suspended load.

Location	Sample	Catchment	Collection date	Latitude (deg)	Longitude (deg)	$[Re]_{SPM}$ (pg g^{-1})	$\delta^{98/95}$Mo (‰)	2SD (‰)	Replicates	Mo (µg g^{-1})
Western Southern Alps, New Zealand	NZ14-40	Wanganui	16/09/2014	43.15522 S	170.62608 E		-0.332	0.068	3	0.47
	NZ14-37	Poerua	16/09/2014	43.15672 S	170.50438 E		-0.350	0.041	3	0.53
	NZ14-37 duplicate					137.07	-0.348	0.057	3	0.63
	NZ14-34	Waitangitaona	16/09/2014	43.28241 S	170.30812 E		-0.340	0.073	5	0.49
	NZ14-47	Waiho	16/09/2014	43.41813 S	170.18060 E	116.11	-0.307	0.033	3	0.33
	NZ14-47 duplicate						-0.247	0.079	3	0.32
	NZ14-48	Callery	16/09/2014	43.39675 S	170.18344 E	103.30	-0.306	0.040	3	0.33
	NZ14-48 duplicate					93.79	-0.386	0.066	3	0.31
	NZ14-66	Fox	18/09/2014	43.48704 S	170.02962 E	332.16	-0.294	0.018	3	0.82
	NZ14-66 duplicate					322.72	-0.283	0.031	3	0.79
	NZ14-86	Fox	27/09/2014			112.43	-0.155	0.029	3	0.47
	NZ14-86 duplicate						-0.235	0.071	3	0.34
	NZ14-69	Cook	19/09/2014	43.49912 S	169.96530 E		-0.382	0.069	3	0.42
	NZ14-71	Karangarua	19/09/2014	43.57515 S	169.80510 E		-0.250	0.024	3	0.56
	NZ14-71 duplicate						-0.280	0.024	3	0.53
Mackenzie River Basin, Canada	CAN13-68	Peel, Fort Macpherson	26/07/2013	67.33448 N	134.87762 W		0.207	0.009	3	3.06
	CAN13-74	Mackenzie, Tsiigehtchic	26/07/2013	67.45818 N	133.72734 W		0.389	0.008	3	2.06
	CAN13-58	Mackenzie Delta, Middle Channel	24/07/2013	68.41313 N	134.08893 W		0.349	0.025	3	2.30
	CAN13-34	Ogilvie, Dempster Bridge	22/07/2013	65.36216 N	138.30226 W		0.487	0.016	3	3.23
Yukon, Canada	CAN13-17	Yukon, Dawson City	21/07/2013	64.04846 N	139.45628 W		0.147	0.038	3	2.46

Table 5.4 | Soil materials from the western Southern Alps.

Location	ID	Lat. (°S)	Long. (°E)	Sample type	[OC_{total}] %	Re (pg g^{-1})	$\delta^{98/95}$Mo	2SD	Replicates	[Mo] (µg g^{-1})
Alex Knob, Docherty Creek, western Southern Alps, New Zealand	NZ14-54	43.40796	170.16727	Weathered colluvium	1.26	36.1	-0.316	0.058	3	0.29
	NZ14-55	43.40602	170.16171	Weathered colluvium	1.54	31.4	-0.322	0.052	3	0.23
	NZ14-56	43.40602	170.16171	Weathered colluvium	0.88	23.7	-0.904	0.016	2	0.24
	NZ14-56 duplicate						-0.813	0.045	3	0.25
	NZ14-59	43.40596	170.16115	Weathered colluvium	0.96	24.2	-0.539	0.041	2	0.34
	NZ14-59 duplicate						-0.423	0.100	3	0.34
	NZ14-57	43.40596	170.16115	Surface soil	4.16	24.7	-0.335	0.066	2	0.25
	NZ14-58	43.40596	170.16115	Surface soil	5.97	21.3	-0.087	0.010	3	0.41
	NZ14-58 duplicate						-0.150	0.028	3	0.42
	NZ14-60	43.40596	170.16115		13.24	52	-0.142	0.022	3	0.36
	NZ14-61	43.40909	170.16335	Surface soil	10.48	27	-0.361	0.045	3	0.27
	NZ14-61 duplicate						-0.239	0.070	3	0.28
	NZ14-62	43.41448	170.15887	Surface soil	7.44	21.7	-0.206	0.059	3	0.24
	NZ14-90	43.38486	170.13333	Local river bed material	0.21	111	-0.262	0.042	3	0.26
	NZ14-90 duplicate						-0.258	0.055	3	0.25

Table 5.5 | River waters.

Location	Catchment	Collection date	Sample	Latitude (degrees)	Longitude (degrees)	pH	T (ºC)	Na^+ (µmol L^{-1})	K^+ (µmol L^{-1})	Mg^{2+} (µmol L^{-1})	Ca^{2+} (µmol L^{-1})	F^- (µmol L^{-1})	Cl^- (µmol L^{-1})	SO_4^{2-} (µmol L^{-1})	Total Alkalinity (µmol L^{-1})	HCO_3^- (µmol L^{-1})	$[Re]_{diss}$ (pmol L^{-1})	$[Mo]_{diss}$ (nmol L^{-1}) Q-ICP-MS	$[Mo]_{diss}$ (nmol L^{-1}) MC-ICP-MS	$\delta^{98/95}$ Mo (‰)	2SD (‰)	n	fMo_{diss}	$\Delta^{98/95}Mo_{diss-BM}$
Western Southern Alps, New Zealand	Hokitika	14/09/2014	NZ14-14	42.89427 S	171.13238 E	8.52	8.8	66.09	15.13	11.93	162.25	1.05	35.83	25.88	449	441	1.91	6.76						
		14/09/2014	NZ14-16	42.88324 S	171.15501 E	8.52	11.2	101.30	29.49	17.70	216.75	2.11	47.11	34.30	614	603	2.26	7.80						
		14/09/2014	NZ14-18	42.95557 S	171.01666 E	8.36	8.4	57.83	25.38	13.99	186.50	1.58	31.31	32.74	506	500	1.70	5.16	5.84	0.110	0.028	5	0.72	0.42
		14/09/2014	NZ14-20	42.74549 S	171.00066 E	8.2	11.3	83.48	32.05	22.22	178.25	1.58	53.88	29.62	435	432	1.54	3.82						
		26/09/2014	NZ14-77	44.23183 S	169.23164 E	8.31	8.3	47.39	20.00	9.47	119.25	0.53	34.70	21.83	350	346	1.10	3.50						
		26/09/2014	NZ14-79	42.74551 S	171.00058 E	8.06	9.6	67.83	25.38	14.40	135.75	1.05	46.83	22.14	394	392	1.11	3.53						
	Wanganui	15/09/2014	NZ14-22	43.16322 S	170.62808 E	8.14	8.9	259.57	37.18	11.52	251.50	4.21	217.21	74.84	954	947	2.88	9.95						
		15/09/2014	NZ14-24	43.03586 S	170.44994 E	8.34	9.9	116.52	51.28	23.05	352.50	2.11	67.14	67.66	930	920	2.53	7.53						
		16/09/2014	NZ14-40	43.15522 S	170.62608 E	8.14	6.4	53.91	19.49	7.00	130.25	1.05	59.52	41.47	423	420	1.69	5.46	6.36	0.006	0.041	2	0.80	0.31
		26/09/2014	NZ14-81	43.15533 S	170.62608 E	7.98	8.3	56.09	23.85	7.82	159.50	0.53	40.34	30.25	410	408	1.50	4.64						
	Poerua	15/09/2014	NZ14-26	43.20627 S	170.52100 E	8.43	7.5	31.74	42.82	9.47	257.75	1.05	28.21	89.18	818	807	3.73	12.46						
		15/09/2014	NZ14-28	43.13449 S	170.48598 E	8.21	9.9	46.96	50.51	12.76	263.00	1.05	43.44	80.14	883	875	3.38	8.08						
		16/09/2014	NZ14-37	43.15672 S	170.50438 E	7.74	8	71.74	31.79	13.58	139.50	0.53	85.19	31.49	306	305	1.47	3.14	3.73	0.083	0.008	2	0.53	0.39
		26/09/2014	NZ14-82	43.15686 S	170.50215 E	7.92	8.8	46.09	32.56	9.05	132.00	0.53	44.85	25.88	347	346	1.14	3.04						
	Whataroa	15/09/2014	NZ14-30	43.29351 S	170.41246 E	8.02	8.4	80.43	20.51	13.99	304.50	1.58	34.70	63.61	725	721	2.07	7.60						
		15/09/2014	NZ14-32	43.16091 S	10.37680 E	7.73	10.7	118.26	49.49	33.74	513.25	2.11	60.37	58.93	1280	1276	2.37	4.40						
		16/09/2014	NZ14-41	43.28552 S	170.40111 E	8.21	6.4	60.00	15.13	9.88	204.00	1.05	36.39	35.86	479	475	1.51	4.80						
		26/09/2014	NZ14-83	43.28552 S	170.40121 E	8.04	7.5	43.04	13.59	7.00	150.00	0.53	29.34	24.63	353	350	0.90	3.31						
		02/10/2014	NZ14-110	43.28548 S	170.40146 E	8.25	8.4	80.87	21.03	14.81	298.00	1.58	35.54	60.18	741	734	2.23	7.41						
	Waitangitaona	16/09/2014	NZ14-34	43.28241 S	170.30812 E	8.2	7	58.26	30.00	14.81	129.75	1.05	50.21	31.81	327	324	1.33	2.33	2.77	0.126	0.020	2	0.44	0.43
		26/09/2014	NZ14-84	43.2822 S	170.30545 E	7.86	8	41.30	23.08	8.64	80.00	0.53	37.52	14.97	163	162	0.81	1.47						
	Waiho	16/09/2014	NZ14-44	43.44185 S	170.17308 E	8.43	2	37.83	63.59	33.33	323.75	1.05	23.41	193.02	907	896	6.11	12.16						
		16/09/2014	NZ14-47	43.41813 S	170.18060 E	8.48	3.8	53.48	88.97	52.26	493.50	1.05	26.80	192.08	1111	1095	7.56	12.57	14.45	0.138	0.003	2	0.40	0.45
		27/09/2014	NZ14-91	43.41808 S	170.18065 E	8.26	4.4	45.65	90.51	48.97	446.00	0.53	22.85	165.89	1017	1008	5.94	11.30						
		02/10/2014	NZ14-107	43.61212 S	169.85655 E	8.34	4.1	57.83	88.72	55.56	491.50	1.05	21.16	198.63	1109	1097	6.13	13.22	15.34	0.148	0.019	3	0.53	0.46
	Callery	16/09/2014	NZ14-48	43.39675 S	170.18344 E	8.43	5.4	74.78	35.90	22.22	398.00	1.05	26.23	94.79	894	882	2.55	11.96	13.70	-0.003	0.014	2	1.13	0.30

Location	Catchment	Collection date	Sample	Latitude (degrees)	Longitude (degrees)	pH	T (°C)	Na^+ (µmol L^{-1})	K^+ (µmol L^{-1})	Mg^{2+} (µmol L^{-1})	Ca^{2+} (µmol L^{-1})	F^- (µmol L^{-1})	Cl^- (µmol L^{-1})	SO_4^{2-} (µmol L^{-1})	Total Alkalinity (µmol L^{-1})	HCO_3^- (µmol L^{-1})	$[Re]_{diss}$ (pmol L^{-1})	$[Mo]_{diss}$ (nmol L^{-1}) Q-ICP-MS	$[Mo]_{diss}$ (nmol L^{-1}) MC-ICP-MS	$\delta^{98/95}$ Mo (‰)	2SD (‰)	n	fMo_{diss}	$\Delta^{98/95}Mo_{diss-BM}$
Western Southern Alps, New Zealand	Callery	27/09/2014	NZ14-93	43.39678 S	170.18346 E	8.35	6.9	45.65	24.87	13.99	264.75	1.05	25.11	90.12	851	842	2.59	9.89						
		02/10/2014	NZ14-108	43.39725 S	170.18408 E	8.42	6.8	58.70	29.74	17.28	317.75	1.05	24.82	115.06	1032	1019	3.09	13.10	15.22	0.040	0.030	3	1.04	0.35
	Waiho/ Callery confluence	02/10/2014	NZ14-109	43.3933 S	170.18042 E	8.43	6.5	77.39	52.56	32.51	447.75	1.05	26.23	134.39	1085	1071	4.55	12.97						
	Hare Mare	27/09/2014	NZ14-87	43.44046 S	170.07457 E	8.29	9.4	71.30	68.97	29.63	368.75	2.11	52.75	131.90	1011	1001	4.89	10.73						
	Docherty	27/09/2014	NZ14-89	43.38486 S	170.13333 E	8.05	9.5	63.04	28.21	20.99	128.25	1.05	51.90	21.52	419	416	1.46	3.33						
	Fox	18/09/2014	NZ14-63	43.49958 S	170.05521 E	8.62	1.1	56.52	105.13	58.85	441.00	1.05	20.59	266.29	1345	1318	10.67	16.92						
		18/09/2014	NZ14-66	43.48704 S	170.02962 E	8.52	3.3	112.61	144.10	92.18	722.75	1.58	32.16	274.09	1620	1595	11.55	15.79	18.33	0.315	0.029	5	0.33	0.62
		19/09/2014	NZ14-68	43.48704 S	170.02956 E	8.94	4.2	80.87	121.28	58.02	482.00	1.05	44.85	148.74	1178	1131	6.26	11.20						
		27/09/2014	NZ14-85	43.48598 S	170.02983 E	8.31	3.6	76.52	115.64	63.79	549.25	1.05	27.64	190.83	1290	1277	7.68	11.92						
		27/09/2014	NZ14-86			8.67	1.1	50.87	111.79	57.20	463.00	0.53	19.18	178.98	1058	1035	6.78	12.04	13.73	0.174	0.115	2	0.43	0.48
	Cook	19/09/2014	NZ14-69	43.49912 S	169.9653 E	8.48	6.4	51.74	28.46	16.87	174.25	0.53	47.95	41.78	438	431	1.85	5.20	6.16	0.044	0.007	2	0.70	0.35
		29/09/2014	NZ14-98	43.49902 S	169.96536 E	8.31	7.8	57.83	51.03	32.92	369.25	1.05	28.49	92.92	882	873	3.88	11.51						
	Karangarua	19/09/2014	NZ14-71	43.57515 S	169.8051 E	8.18	7.3	45.65	19.49	10.29	91.00	0.00	41.75	16.84	224	223	0.84	1.81	2.13	0.064	0.000	2	0.54	0.37
		29/09/2014	NZ14-97	43.57513 S	169.8051 E	8.05	9.2	49.13	28.21	17.28	171.25	1.05	31.31	52.70	628	624	2.28	5.71						
		30/09/2014	NZ14-100	43.63503 S	169.95711 E	8.02	9.1	53.91	25.13	32.92	319.75	1.05	20.87	64.86	885	881	2.97	7.35						
		01/10/2014	NZ14-103	43.62964 S	169.94629 E	7.88	6.6	45.65	38.97	17.28	121.25	0.53	26.80	32.43	412	410	1.86	5.41						
		01/10/2014	NZ14-105	43.61212 S	169.89484 E	8.05	8.1	77.39	36.41	28.40	257.00	1.05	30.18	57.37	744	739	2.84	7.23						
		03/10/2014	NZ14-111	43.57394 S	169.80774 E	7.99	7	47.83	24.36	15.23	139.25	0.53	30.47	28.69	375	373	1.30	3.04						
	Paringa	19/09/2014	NZ14-73	43.71198 S	169.49315 E	7.95	8.0	43.91	21.54	8.23	91.25	0.53	41.18	16.53	224	223	0.93	2.02						
		29/09/2014	NZ14-94	43.71133 S	169.49055 E	8.14	9.2	56.09	35.90	16.05	183.75	1.05	35.83	35.55	334	331	1.57	4.15						
	Makawhio (Jacob's river)	29/09/2014	NZ14-95	43.57327 S	169.67892 E	7.71	9.5	56.52	34.36	17.70	155.50	1.05	38.65	34.92	402	401	1.91	2.44						
		03/10/2014	NZ14-112	43.57354 S	169.67828 E	7.5	7.2	38.70	17.18	8.23	65.50				182	181	0.98	1.13						
	Haast	19/09/2014	NZ14-75	43.85398 S	169.05496 E	8.09	8.6	59.57	21.54	20.99	220.50	1.05	37.80	34.30	606	602	2.01	3.65	4.25	0.279	0.028	2	0.44	0.59
		03/10/2014	NZ14-113	43.85398 S	169.05486 E	8.00	8.4	57.39	19.74	19.75	205.75	1.05	34.98	32.74	571	568	1.45	3.31						
	Haast	03/10/2014	NZ14-114	44.03936 S	169.37927 E	8.02	7.3	46.52	7.44	18.93	169.50	1.05	17.49	27.44	402	400	1.80	3.80						
	Hydrothermal	30/09/2014	NZ14-102	43.62964 S	169.94629 E	7.02	55.5	17508.70	712.82	184.36	742.25	48.42	4761.64	0.94	22415	22398	0.11	0.24						

Location	Catchment	Collection date	Sample	Latitude (degrees)	Longitude (degrees)	pH	T (°C)	Na^+ (µmol L^{-1})	K^+ (µmol L^{-1})	Mg^{2+} (µmol L^{-1})	Ca^{2+} (µmol L^{-1})	F^- (µmol L^{-1})	Cl^- (µmol L^{-1})	SO_4^{2-} (µmol L^{-1})	Total Alkalinity (µmol L^{-1})	HCO_3^- (µmol L^{-1})	$[Re]_{diss}$ (pmol L^{-1})	$[Mo]_{diss}$ (nmol L^{-1}) Q-ICP-MS	$[Mo]_{diss}$ (nmol L^{-1}) MC-ICP-MS	$\delta^{98/95}$ Mo (‰)	2SD (‰)	n	fMo_{diss}	$\Delta^{98/95}Mo_{diss}$ -BM
Western Southern Alps, New Zealand	Rainwater	15/09/2014	NZ14-RW1	43.389672 S	170.183759 E			55.65	3.08	4.94	5.50						0.16	0.12						
	Rainwater	02/10/2014	NZ14-RW2	43.389672 S	170.183759 E			60.00	3.08	4.53	2.75						0.15	0.07						
Eastern Southern Alps, New Zealand	Hooker	04/10/2014	NZ14-116	43.69284 S	170.09869 E	8.39	2.1	30.87	11.28	16.46	169.25	0.53	8.74	74.21	525	518	0.91	6.34	7.33	-0.158	0.049	3		
	Hooker	04/10/2014	NZ14-117	43.69269 S	170.09903 E	8.29	4.1	48.26	15.64	28.81	279.75	0.53	11.00	72.03	655	649	1.24	9.94		0.034	0.084	3		
	Tasman	04/10/2014	NZ14-118	43.70715 S	170.17097 E	8.43	3.2	67.39	17.44	15.23	240.75	0.53	7.33	82.32	547	540	1.05	10.43	12.10	-0.192	0.036	3		
	Jollie	05/10/2014	NZ14-120	43.86295 S	170.17560 E	8.24	8.4	58.70	7.44	14.40	129.75	1.05	9.31	27.44	357	354	0.86	4.29						
	Hooker, Jollie and Tasman confluence	05/10/2014	NZ14-122	43.99801 S	170.19449 E	8.31	7.7	42.61	9.49	10.29	129.50	1.05	8.74	45.53	482.13	477.07	1.05	6.59						
Mackenzie River Basin, Canada	Liard, Fort Simpson	15/7/2009	CAN09-04	61.83573 N	121.28505 W			74.18	14.35	378.63	881.28	4.31	8.83	337.68		1688	19.12							
	Liard, Fort Simpson	13/9/2010	CAN10-46	61.82340 N	121.2976 W			100.11	17.78	408.00	945.87	4.60	22.38	469.69			23.07							
	Liard, Fort Simpson	13/9/2010	CAN10-48	61.8230 N	121.29759 W			98.02	17.30	402.98	922.43	4.50	21.85	471.69			23.38							
	Peel, Fort McPherson	21/7/2009	CAN09-39	67.33231 N	134.86882 W			138.50	14.48	622.60	1122.87	4.52	44.93	667.13		2163	15.37							
	Peel, Fort McPherson	19/07/2013	CAN13-01	67.33448 N	134.87762 W	7.92	19.5	205.72	17.33	797.60	1451.19		42.22	966.90		2588	25.75	14.09						
	Peel, Fort McPherson	26/07/2013	CAN13-81	67.33448 N	134.87762 W			159.04	12.68	690.40	1162.18		36.51	797.14		2350	19.31	11.79	12.98	1.224	0.041	2	0.44	1.03
	Peel, Fort McPherson	11/6/2011	CAN11-79					141.76	16.90	625.71	1080.20	3.75	48.15	705.17			15.94							
	Mackenzie, Fort Simpson	16.07.2009	CAN09-07	61.85104 N	121.27722 W			149.25	22.96	258.67	673.76	3.02	197.33	226.77		1439	11.54							
	Mackenzie, Tsiigehtchic	22/7/2009	CAN09-47	67.45836 N	133.72329 W			122.13	19.08	364.92	822.16	5.89	145.66	365.40		1564	15.30							
	Mackenzie, Tsiigehtchic	7/9/2010	CAN10-14	67.45796 N	133.72699 W			146.39	22.19	462.04	1020.98	5.38	196.66	461.04			16.21							
	Mackenzie, Tsiigehtchic	11/6/2011	CAN11-68					110.14	23.03	312.09	778.16	3.86	131.34	304.83			15.68							
	Mackenzie, Tsiigehtchic	26/07/2013	CAN13-82	67.45818 N	133.72734 W			133.59	19.23	398.33	868.36		188.97	451.03		1918	17.87	10.08	11.07	1.128	0.042	2	0.23	0.71
	Mackenzie Delta, Inuvik	24/07/2013	CAN13-65	68.41313 N	134.08893	8.04	16.9	123.64	18.29	384.71	842.04		163.42	454.22		1973	19.57	11.58	12.50	0.960	0.007	2	0.38	0.57
	Mackenzie Delta, Inuvik	8/9/2010	CAN10-26	68.4343 N	134.2222			158.76	21.74	460.50	991.26	4.21	167.38	444.51			17.90							
	Mackenzie Delta, Inuvik	14/6/2011	CAN11-100					197.25	21.51	291.08	713.16						15.01							
	Arctic Red, Tsiigehtchic	22/7/2009	CAN09-50	67.42609 N	133.77866 W			143.35	21.68	570.39	1152.73	5.72	16.15	854.42		1552	22.46							
	Arctic Red, Tsiigehtchic	7/9/2010	CAN10-18	67.43958 N	133.7553 W			133.08	18.58	840.25	1382.91	4.52	23.55	1141.46			13.96							
	Arctic Red, Tsiigehtchic	26/07/2013	CAN13-83					120.48	15.54	759.36	1217.25		15.08	1057.73		2162	18.16	13.04						
	Ogilvie River, Dempster	20/07/2013	CAN13-09	65.71532 N	137.99249 W	8.1	12.1	400.80	12.16	776.69	1561.40		91.79	1051.88		2674	34.80	19.96						

Location	Catchment	Collection date	Sample	Latitude (degrees)	Longitude (degrees)	pH	T (°C)	Na^+ (µmol L^{-1})	K^+ (µmol L^{-1})	Mg^{2+} (µmol L^{-1})	Ca^{2+} (µmol L^{-1})	F^- (µmol L^{-1})	Cl^- (µmol L^{-1})	SO_4^{2-} (µmol L^{-1})	Total Alkalinity (µmol L^{-1})	HCO_3^- (µmol L^{-1})	$[Re]_{diss}$ (pmol L^{-1})	$[Mo]_{diss}$ (nmol L^{-1}) Q-ICP-MS	$[Mo]_{diss}$ (nmol L^{-1}) MC-ICP-MS	$\delta^{98/95}$ Mo (‰)	2SD (‰)	n	fMo_{diss}	$\Delta^{98/95}Mo_{diss-BM}$
Mackenzie River Basin, Canada	Ogilvie River, Dempster bridge	20/07/2013	CAN13-12	65.36131 N	138.17824 W	8.26	12.9	521.85	11.32	691.58	1249.46		73.13	1147.58		2703	27.92	17.23	18.94	1.534	0.040	2	0.50	1.01
	Ogilvie River Dempster Bridge	22/07/2013	CAN13-33i	65.36216 N	138.30226 W	7.81	13.8	513.38	9.68	525.63	940.27		22.22	861.89		1819	21.88	12.00						
	Eagle River Nr Eagle Plains	19/07/2013	CAN13-05	66.44326 N	136.71062 W	7.44	13.9	619.13	19.37	809.37	1401.04		19.33	1978.73		1256	39.83	6.20						
	Engineer Creek, Dempster bridge	20/07/2013	CAN13-13	65.35699 N	123.29301 W	8.08	12.2	229.06	21.91	1210.06	2534.39		329.31	3070.56		2834	76.50	49.35						
	Upper Engineer Creek, Dempster	22/07/2013	CAN13-29	65.10129 N	138.35582 W	6.98	9.2	85.87	15.23	893.66	3019.72		37.71	1881.58		3412	99.89	118.93						
	Upper Engineer Creek (upstream Red Creek), Dempster	22/07/2013	CAN13-30	65.17129 N	138.36353 W	6.99	10.3	65.61	12.89	902.38	2025.11		33.85	2202.97		2296	80.56	66.25						
	Blackstone, Dempster bridge	20/07/2013	CAN13-14	64.60593 N	138.34065 W	7.77	10.6	155.83	12.75	1174.57	1353.20		5.31	2280.78		1394	14.40	2.63						
	West Blackstone, Dempster bridge	22/07/2013	CAN13-25	64.83523 N	138.36215 W	7.75	11	77.50	12.24	529.57	886.71		12.17	710.71		1628	14.69	5.96						
	Rock River, Dempster	23/07/2013	CAN13-45	66.91653 N	136.34325 W	7.89	9	25.50	8.60	690.98	1884.46		9.55	1124.15		2890	14.49	12.91						
	Peel tributary, Dempster	23/07/2013	CAN13-47	67.13862 N	136.00302 W	6.97	9.3	546.51	21.17	1132.31	866.52		4.85	2288.50		96	1.46	0.21						
Yukon, Canada	Yukon, Dawson City	21/07/2013	CAN13-22	64.04846 N	139.45628 W	8.22	15.5	117.45	45.39	350.49	748.38		15.71	353.91		1713	16.90	16.33	17.68	0.733	0.020	2	0.46	0.58
Iceland	Skaftá	19/08/2014	Skaftá-1	63.79233 N	18.03727 W	8.02		299.51	14.36	115.23	223.75	5.26	137.66	88.56	630		4.22	1.98	1.70	0.371		1	0.39	0.52
		08/2013	Skaftá-1	63.79233 N	18.03727 W													1.94						
	Skaftá	19/08/2014	Skaftá-2	63.79277 N	18.49555 W	8.47		258.17	12.31	87.24	176.75	4.74	77.86	72.97	676		3.26	1.63	1.78	0.351		1	0.52	0.50
		08/2013	Skaftá-2	63.79277 N	18.49555 W													1.80						
	Skaftá	19/08/2014	Skaftá-3G	63.91005 N	18.59857 W	7.31		265.37	9.49	108.23	228.00	3.68	47.39	77.95			3.49	1.37	1.55	0.386		1	0.43	0.54
	Skaftá	19/08/2014	Skaftá-4	64.07949 N	18.40699 W	7.67		320.26	12.82	141.56	312.50	4.74	48.80	103.21			3.80	1.32	1.54	0.471		1	0.39	0.62
		08/2013	Skaftá-4	64.07949 N	18.40699 W													1.23						
	Skaftá	20/08/2014	Skaftá-5	64.2398 N	18.14071 W	8.96		86.08	5.64	23.87	96.25	1.05	13.82	39.60	424		1.67	0.67						
	Skaftá tributary	19/08/2014	Skaftá-3NG	63.91005 N	18.59857 W	5.91		398.41	10.26	23.46	59.25	4.21	77.57	29.31			4.99	2.81	3.13	0.260		1	0.60	0.41
		08/2013	Skaftá-3NG	63.91005 N	18.59857 W													2.10						

Table 5.6 | Leaching experiment.

Location	Sample	Catchment	Leach phase	$\delta^{98/95}$Mo (‰)	2SD (‰)	Replicates	Mo (µg g^{-1})	% of total Mo
Western Southern Alps. New Zealand	NZ14-69	Cook	Bulk	-0.382	0.069	3	0.42	100
			HAc	-1.855		1	0.14	1.1
			HCl	-0.704	0.068	2	0.93	23.9
			Residue	-0.257	0.026	3	0.31	75.1
	NZ14-86	Fox	Bulk	-0.155	0.029	3	0.47	100
			HAc	0.455		1	0.07	0.6
			HCl	-0.533	0.006	2	0.34	20.5
			Residue	-0.154	0.008	3	0.30	78.9

5.8 References

Alghanmi, S.I., Al Sulamia, A.F., El-Zayat, T.A., Alhogbi, B.G., Abdel Salam, M., 2015. Acid leaching of heavy metals from contaminated soil collected from Jeddah, Saudi Arabia: kinetic and thermodynamics studies. International Soil and Water Conservation Research, 196–208.

Algeo, T.J., Lyons, T.W., 2006. Mo–total organic carbon covariation in modern anoxic marine environments: Implications for analysis of paleoredox and paleohydrographic conditions. Paleoceanography 21.

Algeo, T.J., Scheckler, S.E., 1998. Terrestrial-marine teleconnections in the Devonian: links between the evolution of land plants, weathering processes, and marine anoxic events. Philos. Trans. R. Soc. London B Biol. Sci. 353, 113–130.

Archer, C., Vance, D., 2008. The isotopic signature of the global riverine molybdenum flux and anoxia in the ancient oceans. Nat. Geosci. 1, 597–600.

Arnold, G.L., Anbar, A.D., Barling, J., Lyons, T.W., 2004. Molybdenum isotope evidence for widespread anoxia in mid-proterozoic oceans. Science 304, 87–90.

Arnorsson, S., Oskarsson, N., 2007. Molybdenum and tungsten in volcanic rocks and in surface and < 100 degrees C ground waters in Iceland. Geochim. Cosmochim. Acta 71, 284–304.

Barling, J., Anbar, A.D., 2004. Molybdenum isotope fractionation during adsorption by manganese oxides. Earth Planet. Sci. Lett. 217, 315–329.

Barling, J., Arnold, G.L., Anbar, A.D., 2001. Natural mass-dependent variations in the isotopic composition of molybdenum. Earth Planet. Sci. Lett. 193, 447–457.

Barron, A.R., Wurzburger, N., Bellenger, J.P., Wright, S.J., Kraepiel, A.M.L., Hedin, L.O., 2009. Molybdenum limitation of asymbiotic nitrogen fixation in tropical forest soils. Nat. Geosci. 2, 42–45.

Beaulieu, E., Goddéris, Y., Labat, D., Roelandt, C., Calmels, D., Gaillardet, J., 2011. Modeling of water-rock interaction in the Mackenzie basin: Competition between sulfuric and carbonic acids. Chem. Geol. 289, 114–123.

Bellenger, J.P., Wichard, T., Kutska, A.B., Kraepiel, A.M.L., 2008. Uptake of molybdenum and vanadium by a nitrogen-fixing soil bacterium using siderophores. Nat. Geosci. 1, 243–246.

Bertine, K.K., Turekian, K.K., 1973. Molybdenum in marine deposits. Geochim. Cosmochim. Acta 37, 1415–1434.

Bibak, A., Borggard, O.K., 1994. Molybdenum adsorption by aluminium and iron-oxides and humic-acid. Soil Sci. 158, 323–328.

Bostick, B.C., Fendorf, S., Helz, G.R., 2003. Differential adsorption of molybdate and tetrathiomolybdate on pyrite (FeS_2). Environ. Sci. Technol. 37, 285–291.

Bouchez, J., Von Blanckenburg, F., Schuessler, J.A., 2013. Modeling novel stable isotope ratios in the weathering zone. Am. J. Sci. 313, 267–308.

Boyd, E.S., Anbar, A.D., Miller, S., Hamilton, T.L., Lavin, M., Peters, J.W., 2011. A late methanogen origin for molybdenum-dependent nitrogenase. Geobiology 9, 221–232.

Brabets, T.P., Wang, B., Meade, R.H., U.S. Dept. of the Interior, U.S.G.S., Branch of Information, S., 2000. Environmental and hydrologic overview of the Yukon River basin, Alaska and Canada, Water-Resources Investigations Report.

Calmels, D., Gaillardet, J., Brenot, A., France-Lanord, C., 2007. Sustained sulfide oxidation by physical erosion processes in the Mackenzie River basin: Climatic perspectives. Geology 35, 1003–1006.

Carson J.N.; Conly, F.M.., M.A.. J., 1998. Magnitude and Sources of Sediment Input to the Mackenzie Delta, Northwest Territories, 1974-94. Arctic 51, 116–124.

Chan, L.H., Hein, J.R., 2007. Lithium contents and isotopic compositions of ferromanganese

deposits from the global ocean. Deep. Res. Part Ii-Topical Stud. Oceanogr. 54, 1147–1162.

Colodner, D., Sachs, J., Ravizza, G., Turekian, K., Edmond, J., Boyle, E., 1993. The geochemical cycle of rhenium: a reconnaissance. Earth Planet. Sci. Lett. 117, 205–221.

Dahl, T.W., Chappaz, A., Fitts, J.P., Lyons, T.W., 2013. Molybdenum reduction in a sulfidic lake: Evidence from X-ray absorption fine-structure spectroscopy and implications for the Mo paleoproxy. Geochim. Cosmochim. Acta 103, 213–231.

Dai, S.F., Seredin, V. V, Ward, C.R., Hower, J.C., Xing, Y.W., Zhang, W.G., Song, W.J., Wang, P.P., 2015. Enrichment of U-Se-Mo-Re-V in coals preserved within marine carbonate successions: geochemical and mineralogical data from the Late Permian Guiding Coalfield, Guizhou, China. Miner. Depos. 50, 159–186.

Dalai, T.K., Singh, S.K., Trivedi, J.R., Krishnaswami, S., 2002. Dissolved rhenium in the Yamuna River System and the Ganga in the Himalaya: Role of black shale weathering on the budgets of Re, Os, and U in rivers and CO_2 in the atmosphere. Geochim. Cosmochim. Acta 66, 29–43.

Dean, W.E., Piper, D.Z., Peterson, L.C., 1999. Molybdenum accumulation in Cariaco basin sediment over the past 24 ky: a record of water-column anoxia and climate. Geology 27, 507–510.

Dellinger, M., Gaillardet, J., Bouchez, J., Calmels, D., Galy, V., Hilton, R.G., Louvat, P., France-Lanord, C., 2014. Lithium isotopes in large rivers reveal the cannibalistic nature of modern continental weathering and erosion. Earth Planet. Sci. Lett. 401, 359–372.

Dellinger, M., Gaillardet, J., Bouchez, J., Calmels, D., Louvat, P., Dosseto, A., Gorge, C., Alanoca, L., Maurice, L., 2015. Riverine Li isotope fractionation in the Amazon River basin controlled by the weathering regimes. Geochim. Cosmochim. Acta 164, 71–93.

Dickson, A.J., 2017. A molybdenum-isotope perspective on Phanerozoic deoxygenation events. Nat. Geosci.

Gaillardet, J., Dupre, B., Louvat, P., Allegre, C.J., 1999. Global silicate weathering and CO_2 consumption rates deduced from the chemistry of large rivers. Chem. Geol. 159, 3–30.

Galy, V., Beyssac, O., France-Lanord, C., Eglinton, T., 2008. Recycling of Graphite During Himalayan Erosion: A Geological Stabilization of Carbon in the Crust. Science 322, 943–945.

Galy, V., Bouchez, J., France-Lanord, C., 2007. Determination of total organic carbon content and delta C-13 in carbonate-rich detrital sediments. Geostand. Geoanalytical Res. 31, 199–207.

Georg, R.B., Reynolds, B.C., West, A.J., Burton, K.W., Halliday, A.N., 2007. Silicon isotope variations accompanying basalt weathering in Iceland. Earth Planet. Sci. Lett. 261, 476–490.

Gislason, S.R., Arnorsson, S., Armannsson, H., 1996. Chemical weathering of basalt in southwest Iceland: Effects of runoff, age of rocks and vegetative/glacial cover. Am. J. Sci. 296, 837–907.

Glass, J.B., Wolfe-Simon, F., Anbar, A.D., 2009. Coevolution of metal availability and nitrogen assimilation in cyanobacteria and algae. Geobiology 7, 100–123.

Goldberg, S., Forster, H.S., 1998. Factors affecting molybdenum adsorption by soils and minerals. SOIL Sci. 163, 109–114.

Goldberg, S., Forster, H.S., Godfrey, C.L., 1996. Molybdenum Adsorption on Oxides, Clay Minerals, and Soils. Soil Sci. Soc. Am. J. 60, 425–432.

Goldberg, S., Lesch, S.M., Suarez, D.L., 2002. Predicting molybdenum adsorption by soils using soil chemical. parameters in the constant capacitance model. Soil Sci. Soc. Am. J. 66, 1836–1842.

Goldberg, T., Archer, C., Vance, D., Poulton, S.W., 2009. Mo isotope fractionation during adsorption to Fe (oxyhydr)oxides. Geochim. Cosmochim. Acta 73, 6502–6516.

Goldberg, T., Archer, C., Vance, D., Thamdrup, B., McAnena, A., Poulton, S.W., 2012. Controls

on Mo isotope fractionations in a Mn-rich anoxic marine sediment, Gullmar Fjord, Sweden. Chem. Geol. 296, 73–82.

Goldberg, T., Gordon, G., Izon, G., Archer, C., Pearce, C.R., McManus, J., Anbar, A.D., Rehkämper, M., 2013. Resolution of inter-laboratory discrepancies in Mo isotope data: an intercalibration. J. Anal. At. Spectrom. 28, 724.

Greber, N.D., Pettke, T., Nägler, T.F., 2014. Magmatic–hydrothermal molybdenum isotope fractionation and its relevance to the igneous crustal signature. Lithos 190, 104–110.

Greber, N.D., Siebert, C., Nägler, T.F., Pettke, T., 2012. $\delta^{98/95}$Mo values and Molybdenum Concentration Data for NIST SRM 610, 612 and 3134: Towards a Common Protocol for Reporting Mo Data. Geostand. Geoanalytical Res. 36, 291–300.

Gupta, U.C., Pasricha, N.S., Nayyar, V.K., Singh, R., 1997. Molybdenum in Agriculture. Nature Publishing Group.

Hall, D.K., Riggs, G.A., 2011. Normalized-Difference Snow Index (NDSI). In: Singh, V.P., Singh, P., Haritashya, U.K. (Eds.), Encyclopedia of Snow, Ice and Glaciers. Springer Netherlands, Dordrecht, pp. 779–780.

Helz, G.R., Miller, C. V, Charnock, J.M., Mosselmans, J.F.W., Pattrick, R.A.D., Garner, C.D., Vaughan, D.J., 1996. Mechanism of molybdenum removal from the sea and its concentration in black shales: EXAFS evidence. Geochim. Cosmochim. Acta 60, 3631–3642.

Henderson, R.D., Thompson, S.M., 1999. Extreme rainfalls in the Southern Alps of New Zealand. J. Hydrol.

Henkel, S., Kasten, S., Poulton, S.W., Staubwasser, M., 2016. Determination of the stable iron isotopic composition of sequentially leached iron phases in marine sediments. Chem. Geol. 421, 93–102.

Hicks, D.M., Shankar, U., McKerchar, A.I., Basher, L., Lynn, I., Page, M., Jessen, M., 2011. Suspended sediment yields from New Zealand rivers. J. Hydrol. (wellingt. North) 50, 81–142.

Hilton, R.G., Gaillardet, J., Calmels, D., Birck, J.-L., 2014. Geological respiration of a mountain belt revealed by the trace element rhenium. Earth Planet. Sci. Lett. 403, 27–36.

Hilton, R.G., Galy, A., Hovius, N., 2008. Riverine particulate organic carbon from an active mountain belt: Importance of landslides. Global Biogeochem. Cycles 22.

Hilton, R.G., Galy, V., Gaillardet, J., Dellinger, M., Bryant, C., O'Regan, M., Grocke, D.R., Coxall, H., Bouchez, J., Calmels, D., 2015. Erosion of organic carbon in the Arctic as a geological carbon dioxide sink. Nature 524, 84-U162.

Horan, K., Hilton, R.G., Selby, D., Ottley, C.J., Gröcke, D.R., Hicks, M., Burton, K.W., 2017. Mountain glaciation drives rapid oxidation of rock-bound organic carbon. Sci. Adv. 3.

Hovius, N., Stark, C.P., Allen, P.A., 1997. Sediment flux from a mountain belt derived by landslide mapping. Geology 25, 231–234.

Jacobson, A.D., Blum, J.D., 2003. Relationship between mechanical erosion and atmospheric CO2 consumption in the New Zealand Southern Alps. Geology 31, 865–868.

Jacobson, A.D., Blum, J.D., Chamberlain, C.P., Craw, D., Koons, P.O., 2003. Climatic and tectonic controls on chemical weathering in the New Zealand Southern Alps. Geochim. Cosmochim. Acta 67, 29–46.

Jean, M.E., Phalyvong, K., Forest-Drolet, J., Bellenger, J.P., 2013. Molybdenum and phosphorus limitation of asymbiotic nitrogen fixation in forests of Eastern Canada: Influence of vegetative cover and seasonal variability. Soil Biol. Biochem. 67, 140–146.

Jochum, K.P., Nohl, U., Herwig, K., Lammel, E., Stoll, B., Hofmann, A.W., 2005. GeoReM: A New Geochemical Database for Reference Materials and Isotopic Standards. Geostandards and Geoanalytical Research 29, 333–338.

Johnson, C.M., Beard, B.L., Albarede, F., 2004. Overview and general concepts, in: Johnson,

C.M., Beard, B.L., Albarede, F. (Eds.), Geochemistry of Non-Traditional Stable Isotopes. pp. 1–24.

Johnston, D.T., Macdonald, F.A., Gill, B.C., Hoffman, P.F., Schrag, D.P., 2012. Uncovering the Neoproterozoic carbon cycle. Nature 483, 320.

Jónsdóttir, Jón.F., 2008. A runoff map based on numerically simulated precipitation and a projection of future runoff in Iceland / Une carte d'écoulement basée sur la précipitation numériquement simulée et un scénario du futur écoulement en Islande. Hydrol. Sci. J. 53, 100–111.

Kariman, N., Cox, F.R., 1979. Molybdenum availability as predicted from selected chemical properties. Agron. J. 71, 63–65.

Kendall, B., Dahl, T.W., Anbar, A.D., 2017. the Stable Isotope Geochemistry of Molybdenum. Rev. Mineral. Geochemistry 82, 683–732.

Kennedy, M.J., Chadwick, O.A., Vitousek, P.M., Derry, L.A., Hendricks, D.M., 1998. Changing sources of base cations during ecosystem development, Hawaiian Islands. Geology 26, 1015–1018.

Kim, Y.S., Zeitlin, H., 1968. Determination of molybdenum in seawater. Limnol. Oceanogr. 13, 534-.

King, E.K., Thompson, A., Chadwick, O.A., Pett-Ridge, J.C., 2016. Molybdenum sources and isotopic composition during early stages of pedogenesis along a basaltic climate transect. Chem. Geol. 445, 54–67.

Koons, P.O., Craw, D., 1991. Gold mineralization as a consequence of continental collision: an example from the Southern Alps, New Zealand. Earth Planet. Sci. Lett. 103, 1–9.

Kowalski, N., Dellwig, O., Beck, M., Gräwe, U., Neubert, N., Nägler, T.F., Badewien, T.H., Brumsack, H.J., van Beusekom, J.E.E., Böttcher, M.E., 2013. Pelagic molybdenum concentration anomalies and the impact of sediment resuspension on the molybdenum budget in two tidal systems of the North Sea. Geochim. Cosmochim. Acta 119, 198–211.

Kump, L.R., Brantley, S.L., Arthur, M.A., 2000. Chemical Weathering, Atmospheric CO_2, and Climate. Annu. Rev. Earth Planet. Sci. 28, 611–667.

Lang, F., Kaupenjohann, M., 2003. Immobilisation of molybdate by iron oxides: effects of organic coatings. Geoderma 113, 31–46.

Larsen, I.J., Almond, P.C., Eger, A., Stone, J.O., Montgomery, D.R., Malcolm, B., 2014. Rapid Soil Production and Weathering in the Southern Alps, New Zealand. Science 343, 637–640.

Li, G., West, A.J., 2014. Evolution of Cenozoic seawater lithium isotopes: Coupling of global denudation regime and shifting seawater sinks. Earth Planet. Sci. Lett. 401, 284–293.

Liang, Y.H., Halliday, A.N., Siebert, C., Fitton, J.G., Burton, K.W., Wang, K.L., Harvey, J., 2017. Molybdenum isotope fractionation in the mantle. Geochim. Cosmochim. Acta 199, 91–111.

Liermann, L.J., Guynn, R.L., Anbar, A., Brantley, S.L., 2005. Production of a molybdophore during metal-targeted dissolution of silicates by soil bacteria. Chem. Geol. 220, 285–302.

Ludwig, K. R. (2008). Isoplot 3.71, Berkeley Geochronology Center, Berkeley, California.

Malinovsky, D., Hammarlund, D., Ilyashuk, B., Martinsson, O., Gelting, J., 2007. Variations in the isotopic composition of molybdenum in freshwater lake systems. Chem. Geol. 236, 181–198.

Marks, J.A., Perakis, S.S., King, E.K., Pett-Ridge, J., 2015. Soil organic matter regulates molybdenum storage and mobility in forests. Biogeochemistry 125, 167–183.

Marsh, E.E., Goldfarb, R.J., Hart, C.J., Johnson, C.A., 2003. Geology and geochemistry of the Clear Creek intrusion-related gold occurrences, Tintina Gold Province, Yukon, Canada. Can. J. Earth Sci. 40, 681–699.

Mathez, E. A., Duba, A. G. Peach, C. L. Léger, A. Shankland, T. J. and Plafker G., 1995. Electrical conductivity and carbon in metamorphic rocks of the Yukon-Tanana Terrane, Alaska. J.

Geophys. Res., 100, 10187–10196.

McManus, J., Berelson, W.M., Severmann, S., Poulson, R.L., Hammond, D.E., Klinkhammer, G.P., Holm, C., 2006. Molybdenum and uranium geochemistry in continental margin sediments: Paleoproxy potential. Geochim. Cosmochim. Acta 70, 4643–4662.

McManus, J., Nagler, T.F., Siebert, C., Wheat, C.G., Hammond, D.E., 2002. Oceanic molybdenum isotope fractionation: Diagenesis and hydrothermal ridge-flank alteration. Geochemistry Geophys. Geosystems 3.

Miller, C.A., Peucker-Ehrenbrink, B., Walker, B.D., Marcantonio, F., 2011. Re-assessing the surface cycling of molybdenum and rhenium. Geochim. Cosmochim. Acta 75, 7146–7179.

Millot, R., Gaillardet, J., Dupre, B., Allegre, C.J., 2003. Northern latitude chemical weathering rates: Clues from the Mackenzie River Basin, Canada. Geochim. Cosmochim. Acta 67, 1305–1329.

Millot, R., Vigier, N., Gaillardet, J., 2010. Behaviour of lithium and its isotopes during weathering in the Mackenzie Basin, Canada. Geochim. Cosmochim. Acta 74, 3897–3912.

Misra, S., Froelich, P.N., 2012. Lithium Isotope History of Cenozoic Seawater: Changes in Silicate Weathering and Reverse Weathering. Science 335, 818–823.

Morford, J.L., Emerson, S., 1999. The geochemistry of redox sensitive trace metals in sediments. Geochim. Cosmochim. Acta 63, 1735–1750.

Mortimer, N., 2004. New Zealand's geological foundations. Gondwana Res. 7, 261–272.

Moune, S., Sigmarsson, O., Schiano, P., Thordarson, T., Keiding, J.K., 2012. Melt inclusion constraints on the magma source of Eyjafjallajökull 2010 flank eruption. J. Geophys. Res. Solid Earth 117, 1–13.

Neubert, N., Heri, A.R., Voegelin, A.R., Nägler, T.F., Schlunegger, F., Villa, I.M., 2011. The molybdenum isotopic composition in river water: Constraints from small catchments. Earth Planet. Sci. Lett. 304, 180–190.

Neubert, N., Nägler, T.F., Böttcher, M.E., 2008. Sulfidity controls molybdenum isotope fractionation into euxinic sediments: Evidence from the modern Black Sea. Geology 36, 775–778.

Nibourel, L., Herman, F., Cox, S.C., Beyssac, O., Lavé, J., 2015. Provenance analysis usiä Raman spectroscopy of carbonaceous material: A case study in the Southern Alps of New Zealand. J. Geophys. Res. Earth Surf. 120, 2056–2079.

Noordmann, J., Weyer, S., Montoya-Pino, C., Dellwig, O., Neubert, N., Eckert, S., Paetzel, M., Boettcher, M.E., 2015. Uranium and molybdenum isotope systematics in modern euxinic basins: Case studies from the central Baltic Sea and the Kyllaren fjord (Norway). Chem. Geol. 396, 182–195.

Norman, M., Robinson, P., Clark, D., 2003. Major- and trace-element analysis of sulfide ores by laser-ablation ICP-MS, solution ICP-MS, and XRF: New data on international reference materials. Can. Mineral. 41, 293–305.

Oskarsdottir, S.M., Gislason, S.R., Snorrason, A., Halldorsdottir, S.G., Gisladottir, G., 2011. Spatial distribution of dissolved constituents in Icelandic river waters. J. Hydrol. 397, 175–190.

Owens, J.D., Gill, B.C., Jenkyns, H.C., Bates, S.M., Severmann, S., Kuypers, M.M.M., Woodfine, R.G., Lyons, T.W., 2013. Sulfur isotopes track the global extent and dynamics of euxinia during Cretaceous Oceanic Anoxic Event 2. Proc. Natl. Acad. Sci. 110, 18407–18412.

Paton, C., Hellstrom, J., Paul, B., Woodhead, J., Hergt, J., 2011. Iolite: Freeware for the visualisation and processing of mass spectrometric data. J. Anal. At. Spectrom. 26, 2508.

Pearce, C.R., Burton, K.W., Pogge von Strandmann, P.A.E., James, R.H., Gislason, S.R., 2010a. Molybdenum isotope behaviour accompanying weathering and riverine transport in a basaltic

terrain. Earth Planet. Sci. Lett. 295, 104–114.

Pearce, C.R., Coe, A.L., Cohen, A.S., 2010b. Seawater redox variations during the deposition of the Kimmeridge Clay Formation, United Kingdom (Upper Jurassic): Evidence from molybdenum isotopes and trace metal ratios. Paleoceanography 25.

Pearce, C.R., Cohen, A.S., Parkinson, I.J., 2009. Quantitative Separation of Molybdenum and Rhenium from Geological Materials for Isotopic Determination by MC-ICP-MS. Geostand. Geoanalytical Res. 33, 219–229.

Peucker-Ehrenbrink, B., Hannigan, R.E., 2000. Effects of black shale weathering on the mobility of rhenium and platinum group elements. Geology 28, 475–478.

Pogge von Strandmann, P.A.E., Opfergelt, S., Lai, Y.J., Sigfússon, B., Gislason, S.R., Burton, K.W., 2012. Lithium, magnesium and silicon isotope behaviour accompanying weathering in a basaltic soil and pore water profile in Iceland. Earth Planet. Sci. Lett. 339–340, 11–23.

Pogge von Strandmann, P.A.E., Burton, K.W., James, R.H., van Calsteren, P., Gislason, S.R., Mokadem, F., 2006. Riverine behaviour of uranium and lithium isotopes in an actively glaciated basaltic terrain. Earth Planet. Sci. Lett. 251, 134–147.

Porder, S., Hilley, G.E., Chadwick, O.A., 2007. Chemical weathering, mass loss, and dust inputs across a climate by time matrix in the Hawaiian Islands. Earth Planet. Sci. Lett. 258, 414–427.

Racionero-Gómez, B., Sproson, A.D., Selby, D., Gröcke, D.R., Redden, H., Greenwell, H.C., 2016. Rhenium uptake and distribution in phaeophyceae macroalgae, Fucus vesiculosus. R. Soc. Open Sci. 3, 160161.

Rahaman, W., Goswami, V., Singh, S.K., Rai, V.K., 2014. Molybdenum isotopes in two Indian estuaries: Mixing characteristics and input to oceans. Geochim. Cosmochim. Acta 141, 407–422.

Raiswell, R., Plant, J., 1980. The incorporation of trace-elements into pyrite during diagenesis of black shales, Yorkshite, England. Econ. Geol. 75, 684–699.

Ravizza, G., Norris, R.N., Blusztajn, J., Aubry, M.-P., 2001. An osmium isotope excursion associated with the Late Paleocene thermal maximum: Evidence of intensified chemical weathering. Paleoceanography 16, 155–163.

Raymo, M.E., Ruddiman, W.F., 1992. Tectonic focing of Late Cenozoic climate. Nature 359, 117–122.

Reeder, S.W., Hitchon, B., Levinson, A.A., 1972. Hydrogeochemistry of the surface waters of the Mackenzie River drainage basin, Canada—I. Factors controlling inorganic composition. Geochim. Cosmochim. Acta 36, 825–865.

Reinhard, C.T., Planavsky, N.J., Robbins, L.J., Partin, C.A., Gill, B.C., Lalonde, S. V., Bekker, A., Konhauser, K.O., Lyons, T.W., 2013. Proterozoic ocean redox and biogeochemical stasis. Proc. Natl. Acad. Sci. 110, 5357–5362.

Roser, B.P., Cooper, A.F., 1990. Geochemistry and terrane affiliation of Haast Schist from the western Southern Alps, New Zealand. New Zeal. J. Geol. Geophys. 33, 1–10.

Rudge, J.F., Reynolds, B.C., Bourdon, B., 2009. The double spike toolbox. Chem. Geol. 265, 420–431.

Scheiderich, K., Helz, G.R., Walker, R.J., 2010. Century-long record of Mo isotopic composition in sediments of a seasonally anoxic estuary (Chesapeake Bay). Earth Planet. Sci. Lett. 289, 189–197.

Scott, C., Lyons, T.W., Bekker, A., Shen, Y., Poulton, S.W., Chu, X., Anbar, A.D., 2008. Tracing the stepwise oxygenation of the Proterozoic ocean. Nature 452, 456–459.

Siebert, C., Nagler, T.F., von Blanckenburg, F., Kramers, J.D., 2003. Molybdenum isotope records as a potential new proxy for paleoceanography. Earth Planet. Sci. Lett. 211, 159–171.

Siebert, C., Pett-Ridge, J.C., Opfergelt, S., Guicharnaud, R.A., Halliday, A.N., Burton, K.W., 2015. Molybdenum isotope fractionation in soils: Influence of redox conditions, organic matter, and atmospheric inputs. Geochim. Cosmochim. Acta 162, 1–24.

Silvester, W.B., 1989. Molybdenum limitation of asymbiotic nitrogen fixation in forests of Pacific Northwest America. Soil Biol. Biochem. 21, 283–289.

Sundby, B., Martinez, P., Gobeil, C., 2004. Comparative geochemistry of cadmium, rhenium, uranium, and molybdenum in continental margin sediments. Geochim. Cosmochim. Acta 68, 2485–2493.

Tipper, E.T., Calmels, D., Gaillardet, J., Louvat, P., Capmas, F., Dubacq, B., 2012. Positive correlation between Li and Mg isotope ratios in the river waters of the Mackenzie Basin challenges the interpretation of apparent isotopic fractionation during weathering. Earth Planet. Sci. Lett. 333, 35–45.

Tippett, J.M., Kamp, P.J.J., 1993. Fission-track analysis of the Late Cenozoic vertical kinematics of continental Pacific crust, South Island, New Zealand. J. Geophys. Res. Earth 98, 16119–16148.

Torres, M.A., Moosdorf, N., Hartmann, J., Adkins, J.F., West, A.J., 2017. Glacial weathering, sulfide oxidation, and global carbon cycle feedbacks. Proc. Natl. Acad. Sci.

Torssander, P., 1989. Sulfur isotope ratios of icelandic rocks. Contrib. to Mineral. Petrol. 102, 18–23.

U.S.G.S., 2017. U.S. Geological Survey Certificate of Analysis Icelandic Basalt, BIR-1. Available at: https://crustal.usgs.gov/geochemical_reference_standards/icelandic.html. (Accessed: October 2017).

Verplanck, P.L., Mueller, S.H., Goldfarb, R.J., Nordstrom, D.K., Youcha, E.K., 2008. Geochemical controls of elevated arsenic concentrations in groundwater, Ester Dome, Fairbanks district, Alaska. Chem. Geol. 255, 160–172.

Voegelin, A.R., Naegler, T.F., Pettke, T., Neubert, N., Steinmann, M., Pourret, O., Villa, I.M., 2012. The impact of igneous bedrock weathering on the Mo isotopic composition of stream waters: Natural samples and laboratory experiments. Geochim. Cosmochim. Acta 86, 150–165.

Voegelin, A.R., Pettke, T., Greber, N.D., von Niederhäusern, B., Nägler, T.F., 2014. Magma differentiation fractionates Mo isotope ratios: Evidence from the Kos Plateau Tuff (Aegean Arc). Lithos 190, 440–448.

Walker, J.C.G., Hays, P.B., Kasting, J.F., 1981. A negative feedback mechanism for the long-term stabilization of Earth's surface temperature. J. Geophys. Res. Ocean. 86, 9776–9782.

Wang, Z.B., Ma, J.L., Li, J., Wei, G.J., Chen, X.F., Deng, W.F., Xie, L.H., Lu, W.J., Zou, L., 2015. Chemical weathering controls on variations in the molybdenum isotopic composition of river water: Evidence from large rivers in China. Chem. Geol. 410, 201–212.

Wasylenki, L.E., Anbar, A.D., Liermann, L.J., Mathur, R., Gordon, G.W., Brantley, S.L., 2007. Isotope fractionation during microbial metal uptake measured by MC-ICP-MS. J. Anal. At. Spectrom. 22, 905–910.

Wasylenki, L.E., Rolfe, B.A., Weeks, C.L., Spiro, T.G., Anbar, A.D., 2008. Experimental investigation of the effects of temperature and ionic strength on Mo isotope fractionation during adsorption to manganese oxides. Geochim. Cosmochim. Acta 72, 5997–6005.

Wasylenki, L.E., Weeks, C.L., Bargar, J.R., Spiro, T.G., Hein, J.R., Anbar, A.D., 2011. The molecular mechanism of Mo isotope fractionation during adsorption to birnessite. Geochim. Cosmochim. Acta 75, 5019–5031.

Wheat, C.G., Mottl, M.J., Rudnicki, M., 2002. Trace element and REE composition of a low-temperature ridge-flank hydrothermal spring. Geochim. Cosmochim. Acta 66, 3693–3705.

Wheeler, J O; Hoffman, P F; Card, K D; Davidson, A; Sanford, B V; Okulitch, A V; Roest, W.R., 1996. Geological map of Canada. Nat. Resour. Canada.

White, A.F., Blum, A.E., 1995. Effects of climate on chemical-weathering in watersheds. Geochim. Cosmochim. Acta 59, 1729–1747.

Wichard, T., Mishra, B., Myneni, S.C.B., Bellenger, J.-P., Kraepiel, A.M.L., 2009. Storage and bioavailability of molybdenum in soils increased by organic matter complexation. Nat. Geosci. 2, 625–629.

Wiederhold, J.G., Teutsch, N., Kraemer, S.M., Halliday, A.N., Kretzschmar, R., 2007. Iron isotope fractionation in oxic soils by mineral weathering and podsolization. Geochim. Cosmochim. Acta 71, 5821–5833.

Willbold, M., Hibbert, K., Lai, Y.J., Freymuth, H., Hin, R.C., Coath, C., Vils, F., Elliott, T., 2016. High-Precision Mass-Dependent Molybdenum Isotope Variations in Magmatic Rocks Determined by Double-Spike MC-ICP-MS. Geostand. Geoanalytical Res. 40, 389–403.

Wimpenny, J., James, R.H., Burton, K.W., Gannoun, A., Mokadem, F., Gíslason, S.R., 2010. Glacial effects on weathering processes: New insights from the elemental and lithium isotopic composition of West Greenland rivers. Earth Planet. Sci. Lett. 290, 427–437.

Wurzburger, N., Bellenger, J.P., Kraepiel, A.M.L., Hedin, L.O., 2012. Molybdenum and phosphorus interact to constrain asymbiotic nitrogen fixation in tropical forests. PLoS One 7.

Xu, N., Braida, W., Christodoulatos, C., Chen, J.P., 2013. A Review of Molybdenum Adsorption in Soils/Bed Sediments: Speciation, Mechanism, and Model Applications. Soil Sediment Contam. 22, 912–929.

Xu, N., Christodoulatos, C., Braida, W., 2006. Adsorption of molybdate and tetrathiomolybdate onto pyrite and goethite: Effect of pH and competitive anions. Chemosphere 62, 1726–1735.

Yang, J., Siebert, C., Barling, J., Savage, P., Liang, Y.H., Halliday, A.N., 2015. Absence of molybdenum isotope fractionation during magmatic differentiation at Hekla volcano, Iceland. Geochim. Cosmochim. Acta 162, 126–136.

Zerkle, A.L., Scheiderich, K., Maresca, J.A., Liermann, L.J., Brantley, S.L., 2011. Molybdenum isotope fractionation by cyanobacterial assimilation during nitrate utilization and N_2 fixation. Geobiology 9, 94–106.

Chapter 6

Conclusion

Hooker glacier and river in the eastern Southern Alps, New Zealand; September 2014

Summary: This chapter provides the reader with a summary of the work presented in earlier chapters and outlines the major implications of the study and areas for future work.

6.1 Overview

The weathering and redox processes operating at Earth's surface play an important role in setting the chemical composition of rivers, oceans and the atmosphere through geological time. The concentration and isotope composition of elements affected by redox reactions can help to constrain the magnitude and controls on weathering reactions, including those relevant to Earth's geological carbon cycle and global climate change.

In this study, the concentrations of the redox sensitive elements rhenium (Re) and molybdenum (Mo) and the isotope composition of Mo were investigated in detail amongst a range of geological materials in contrasting environments. River waters, river suspended and bedload sediments, and soil materials were collected in the mountainous catchments of the Southern Alps, New Zealand; the Mackenzie River Basin, northern Canada; and the Skaftá River in southern Iceland. The selected sites host contrasting bedrock lithology, experience different erosion rates and have variable extents of glacial and forest cover. Consequently, samples from these locations can provide new insight on what controls the mobility and isotope fractionation of elements in the Critical Zone.

A major focus of this study was to investigate the rates and controls on the oxidative weathering of petrogenic organic carbon (OC_{petro}), which is a major source of carbon dioxide to the atmosphere over geological time. The samples collected offer a unique opportunity to achieve this aim, with the net carbon budget for river catchments in New Zealand and the Mackenzie River Basin being calculated as a result of this work. The samples also provide the first data to identify subtle fractionations in Mo isotopes during weathering and erosion in river catchments and linked these changes to the amount of Mo remaining in solution. Consequently, the cycling of Mo in terrestrial environments and the associated controls on the isotope composition of Mo in rivers and seawater through time may now be better understood.

6.2 The principle conclusions

The research of this thesis highlights and delivers four major conclusions with respect to our current understanding of oxidative weathering and the cycling of redox sensitive elements in Earth's surface environments.

6.2.1 The Re proxy for quantifying OC_{petro} oxidation

We evaluated the potential for dissolved Re concentrations in river waters to be used as a proxy for tracing the oxidative weathering of OC_{petro} at the catchment scale. Previously, the Re proxy for tracking OC_{petro} oxidation has only been explored to a limited extent; for example in the river

catchments of Taiwan (Hilton et al., 2014), the Yamuna River system in the Himalaya (Dalai et al., 2002), and in weathering studies of soils (Jaffe et al., 2002). Here, in the river catchments of the Mackenzie River Basin, Canada, and the Southern Alps, New Zealand, we combined estimates of dissolved Re flux with measurements of the [Re]/[OC] composition of the local bedrock to estimate CO_2 emissions by OC_{petro} oxidation. The low level concentrations of dissolved Re in the river waters were reproducible down to the sub-pmol L^{-1} concentration range using an isotope dilution technique coupled with column chemistry to separate and concentrate dissolved Re. Our method for quantifying OC_{petro} oxidation accounted for the potential difference in the mobility of Re and CO_2, the fraction of Re derived from non-OC_{petro} sources, and the presence of OC_{petro} in forms less susceptible to oxidation (i.e. graphite). Mixing models using dissolved [Re]/[Na] and [Re]/[SO_4] ratios alongside compiled measurements from silicate, sulfide and OC_{petro} phases allowed the proportion of $[Re]_{diss}$ derived from OC_{petro} to be estimated. This was most relevant in the Mackenzie River Basin, where sulfide-rich rocks in the catchments have been highlighted to be significant in the weathering cycle (e.g. Calmels et al., 2007; Torres et al., 2014). Our data indicated that all of the major river channels studied had >85% of Re derived from OC_{petro}, validating the use of the Re proxy for interpreting OC_{petro} weathering fluxes.

6.2.2 The net geological carbon budget of mountain river catchments

The net geological carbon budget of several catchments in the Mackenzie River Basin and the western Southern Alps were calculated using our new constraints on OC_{petro} oxidation rates, together with published data on silicate and carbonate weathering and organic carbon burial rates. In the Southern Alps, the CO_2 emissions from OC_{petro} oxidation were quantified as $14\ ^{+9}/_{-5}$ tC km^{-2} yr^{-1} for the catchments with limited glacial cover (Whataroa) and $30\ ^{+20}/_{-11}$ tC km^{-2} yr^{-1} for a glacial catchment (Waiho). Consequently, the river catchments without valley glaciers have net carbon fluxes that are negative (net carbon sink of 25 tC km^{-2} yr^{-1} for the Whataroa catchment), whereas the two catchments with valley glaciers, the Fox and Waiho catchments, appear to operate as sources for atmospheric CO_2 (net carbon source of 23 tC km^{-2} yr^{-1} for the Waiho catchment). In contrast, OC_{petro} oxidation rates in the Mackenzie River Basin for the Mackenzie, Peel, Arctic Red and Liard River catchments are an order of magnitude lower, at $0.38\ ^{+0.10}/_{-0.09}$ tC km^{-2} yr^{-1}, $0.79\ ^{+0.23}/_{-0.19}$ tC km^{-2} yr^{-1}, $0.66\ ^{+0.19}/_{-0.16}$ tC km^{-2} yr^{-1} and $0.84\ ^{+0.23}/_{-0.20}$ tC km^{-2} yr^{-1}, respectively. Under the present climate conditions, the Mackenzie River catchment is a net sink for atmospheric CO_2 of $1.2\ ^{+0.33}/_{-0.30}$ tC km^{-2} yr^{-1}.

6.2.3 The role of erosion and glaciation in setting the OC_{petro} oxidation rate

Previous work has alluded to the potential link between OC_{petro} oxidative weathering fluxes and erosion rate (Hilton et al., 2014). Here, we find that the low CO_2 emissions in the Mackenzie River Basin, relative to those in the western Southern Alps, are in line with the ten-fold lower rates of

erosion in this setting (Figure 4.7, ***Chapter 4***). By combining our new Re data from the Southern Alps and the Mackenzie River Basin with data compiled from catchments around the World, we find that a global link exists between dissolved Re fluxes (after accounting for bedrock composition) and physical erosion rate, emphasising the importance of mineral supply for oxidative weathering fluxes (Figure 3.2, ***Chapter 3***).

Within the western Southern Alps, the role of glaciation is highlighted as a further key control on oxidative weathering fluxes. In this setting, lithology, precipitation and erosion rates are similar across the river catchments, but glacial coverage varies considerably, from 2–58%. We find that the catchments hosting valley glaciers (the Fox and Waiho), and even moderate amounts of headwater glaciation, have higher dissolved Re yields and implied higher rates of oxidative weathering for a given physical erosion rate, relative to non-glaciated catchments.

To explain this observation, we propose that the following three mechanisms are important: i) the physical breakdown of rocks by abrasion and grinding processes driven by glacier movement, together with frost cracking and freeze/thaw cycles, generates an abundance of fine sediment with a high reactive surface area that is exposed for oxidation (Anderson, 2005; Hales and Roering, 2009); ii) the reduced development of vegetation and soil in glaciated terrains lessens the demand for oxygen by heterotrophic respiration (Bardgett et al., 2007), so oxygen may penetrate deeper into exposed rock surfaces; and iii) the activity of microbes sub-glacially and in moraines may facilitate OC_{petro} oxidation (e.g. Tranter et al., 2002; Wadham et al., 2004). In mountain catchments around the world, dissolved Re yields are elevated in sites where glaciation is present (Figure 3.2, ***Chapter 3***), implying a global link between mountain glaciation and enhanced emissions of atmospheric CO_2 during weathering of OC_{petro} bearing rocks.

6.2.4. Molybdenum isotopes as tracers of primary and secondary weathering

Molybdenum isotopes are powerful tracers of the processes operating within Earth's Critical Zone. Here, we demonstrate that river δ^{98}Mo values are likely to reflect both the source material and the processing of Mo following its release during oxidative weathering. A heavy Mo isotope composition dissolved in rivers relative to river sediments is observed across all catchments in New Zealand, Canada and Iceland, which supports previous observations in global river settings (e.g. Archer and Vance, 2008). By providing paired dissolved and particulate Mo isotope measurements from multiple catchments, we are able to attribute this global trend to the fraction of Mo that remains in solution post-release during oxidative weathering. We find that weathering processes in soils can fractionate Mo isotopes, with the deepest soil horizons being enriched in isotopically light Mo relative to soil litters. Our soil data are consistent with an important role for (oxyhydr)oxides in sequestering light Mo and driving the fractionation (e.g. Barling and Anbar, 2004; Goldberg et al.,

2009): the fractionation induced by the adsorption of Mo onto Mn and Fe (oxyhydr)oxide particles in experimental work is similar to the fractionation required to explain our field data; we also find that the (oxyhydr)oxides leached from river suspended sediments are isotopically light. Although we are unable to rule out a potential role of organic matter in the cycling and fractionation of Mo isotopes, we find little correspondence between the concentration of Mo and organic matter in different soil horizons, suggesting the two are not tightly coupled.

The results of this work emphasise how a better understanding of the processes controlling the Mo isotope composition of river waters is central to our understanding of the variability in the Mo isotope composition of the oceans through geological time. For example, changes in weathering patterns will impact on the river $\delta^{98/95}$Mo composition and subsequently the $\delta^{98/95}$Mo value of seawater. Hence, our interpretations of the extent of ocean anoxia and euxinia are reliant on better constraints on the Mo composition of inputs to seawater and the factors that might cause them to change.

6.3 Wider Implications of research

This study illustrates how patterns in redox sensitive element chemistry may be tied to different rates of erosion, weathering and biological processing. The elements studied here, Re and Mo, offer insight into the mechanisms through which atmospheric gas concentrations, climatic conditions and the chemical composition of the ocean may be adjusted. It is hoped that this research will improve understanding of the carbon transfers taking place in geological history that are often neglected from carbon cycle models, while lending some insight into how climatic transitions into periods of glaciation on Earth may be buffered by weathering and understood through cycling of elements in Earth's Critical Zone.

The results from the western Southern Alps (***Chapter 3***) suggest that transitions to global glaciation may be stalled by weathering of organic carbon bearing rocks, because as glaciers begin to establish, the increased atmospheric CO_2 generated through enhanced OC_{petro} oxidation could limit further ice growth. The decline in O_2 concentrations over the Cenozoic (Stolper et al., 2017) (Figure 6.1A) may be linked to increases in the rate of OC_{petro} oxidation under an icehouse climate. Over the past 8 Ma, under this cooling climate, there is evidence for worldwide acceleration of mountain erosion (Figure 6.1B) (Herman et al., 2013). These findings tie in with our observations that increased oxidative weathering at high physical erosion rates will drive enhanced O_2 consumption and CO_2 release as carbon is transferred between the atmosphere and lithospheric storage over geological timescales (10^4–10^6 years). Based on a modelling analysis, the atmospheric oxygen reservoir of the Cenozoic is sufficiently large to accommodate changes in sulfide oxidation (Torres et al., 2014), without changing atmospheric O_2 concentrations outside of known bounds.

However, this model does not fully capture the actual expected changes in atmospheric O_2; this O_2 budget also depends on fluxes in the organic carbon cycle and the average oxidation state of this carbon, which are variable (LaRowe and Van Cappellen, 2011) and poorly constrained (Torres et al., 2017). Coal weathering experiments imply that the O_2 consumption rate during OC_{petro} oxidation is two to three orders of magnitude lower than for pyrite oxidation in water (Chang and Berner, 1999). Therefore, we might expect the flux of oxygen consumed by weathering OC_{petro} over the Cenozoic to be set by the organic matter content at depth and the erosion rate rather than the atmospheric oxygen concentration (Bolton et al., 2006). However, a better understanding of the patterns in atmospheric oxygen concentrations and an appreciation of the mass of carbon that is being weathered at the global scale are required.

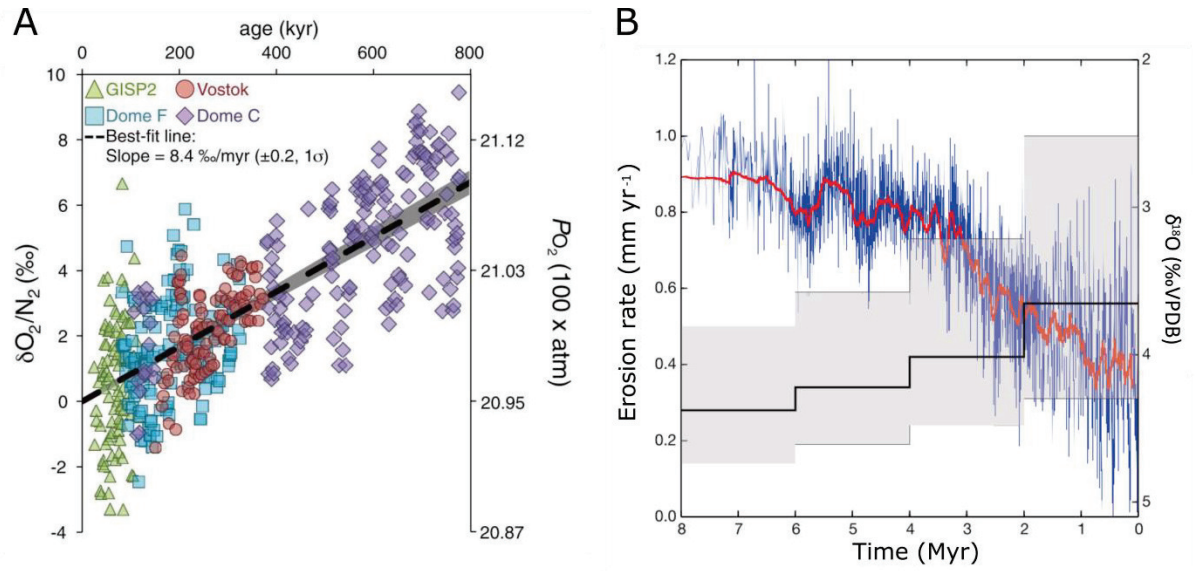

Figure 6.1 Patterns in atmospheric gas concentrations and erosion over the past 8 Ma. A. Decline in atmospheric oxygen as recorded by gases trapped in ice core records (Stolper et al., 2016). Different ice core records are marked by different colours. **B.** Rise in erosion rates over the same time period (Herman et al., 2013). The median (black line) and standard deviation (grey area) were estimated from the distributions of erosion rates over each 2 Myr time interval: 18,000 bedrock thermochronometric ages from around the world together with a formal inversion procedure were used to estimate temporal and spatial variations (Herman et al., 2013). The blue line depicts a raw $\delta^{18}O$ data compilation over the same time interval, which serves as a proxy for global climate fluctuations (Zachos et al., 2001) and the red line corresponds to the moving average for this data. VPDB is the Vienna Pee-Dee belemnite standard.

The relationship between OC_{petro} oxidation and glaciation has the potential to be explored using numerical models to understand the behaviour of other weathering reactions under different climate regimes. In fact, a recent study by Torres et al. (2017) suggests glaciation may also be an important mechanism for enhancing sulfide oxidation rates and carbonate weathering by sulfuric acid. This additional CO_2 release from the oxidative weathering of sedimentary rocks (Calmels et al., 2007) would seem to act in tandem with OC_{petro} oxidation (Horan et al., 2017). Over the last 800 ka, data on CO_2 minima and δD, which is a proxy for Antarctic atmospheric temperature, are similar (Galbraith and Eggleston, 2017). Consequently, it has been suggested that the coldest, lowest CO_2

states are fixed because of one or more stabilizing feedbacks that resisted further cooling, on a timescale of <10 kyr. Our observations suggest that the oxidative weathering of OC_{petro} may be a plausible mechanism by which glaciation might be self-limiting, particularly if it acts alongside sulfide oxidation to drive a negative feedback. Figure 6.2 illustrates that the response of the OC_{petro} weathering reaction to changing climate conditions may offer a previously unrecognised buffering mechanism that will operate over the required timescales and explain the behaviour of the climate system.

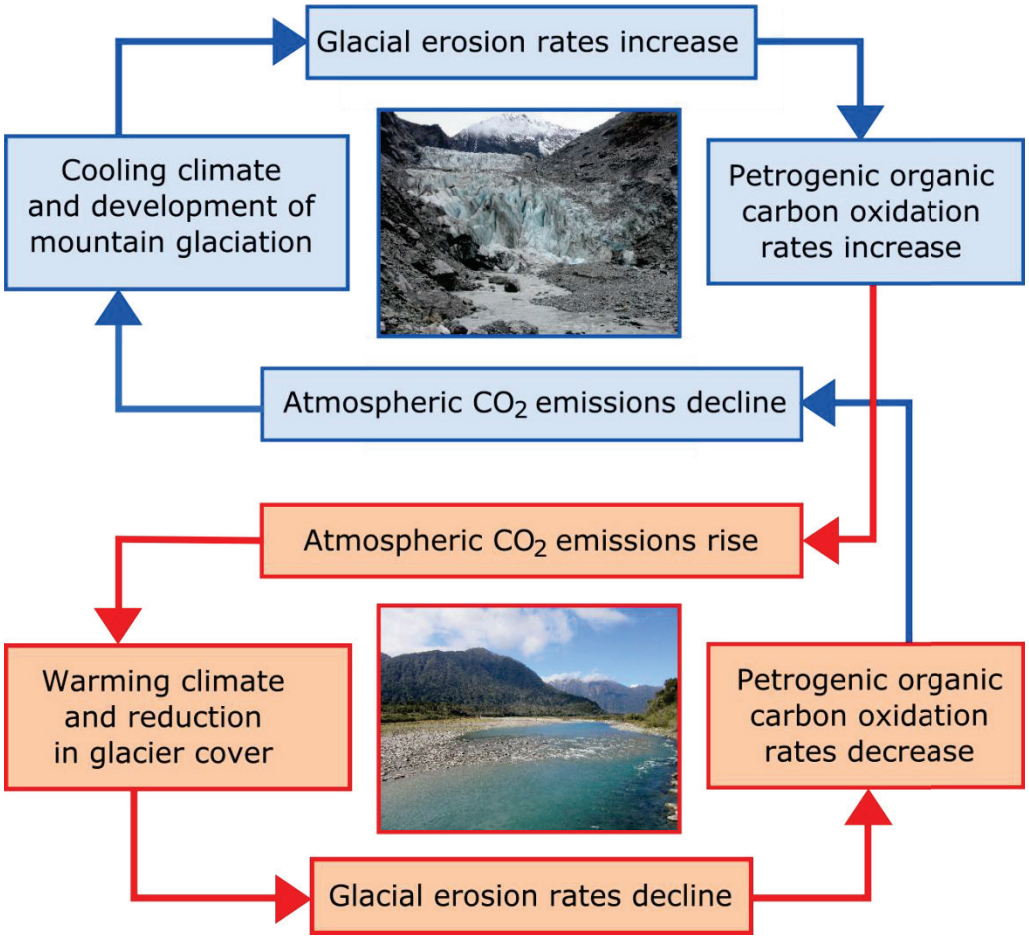

Figure 6.2 Glacially mediated chemical weathering rates drive carbon cycling and climate change on glacial–interglacial to geological timescales. In times of cooling, increased glaciation shifts the balance of the global carbon cycle by increasing CO_2 emissions to the atmosphere–ocean system, potentially limiting the progress of glaciation through greenhouse gas warming. As the planet warms, the extent of glaciation diminishes and CO_2 emissions fall.

The observation of persistent cooling over the Cenozoic would appear to conflict with the buffering mechanism proposed (Figure 6.2). However, atmospheric carbon dioxide concentrations have remained considerably above 190 µg g^{-1} for most of the Cenozoic (e.g. Anagnostou et al., 2016; Zachos et al., 2008). The effectiveness of this feedback loop may therefore be most apparent once CO_2 levels of ~190 µg g^{-1} are approached, and provide an explanation for the apparent cap of CO_2

minima at this value (Galbraith and Eggelston, 2017). Under cooling climate conditions, the development of glaciers in sub-tropical mountainous regions should enhance both erosion (Herman et al., 2013) and the OC_{petro} oxidation rate. Thus, from the mid-Oligocene onwards and particularly towards Plio-Pleistocene time when atmospheric CO_2 levels of ~190 μg g^{-1} were reached (e.g. Zachos et al., 2008), the importance of this weathering process should have increased.

In addition to OC_{petro} oxidation, there have been four other temperature dependent negative feedback mechanisms, outlined in Galbraith and Eggleston (2017), that have been proposed to explain the apparent limit to global cooling and CO_2 minima. The first relates to the freezing point of seawater, which would prevent waters feeding the deep ocean from being cooled below -2ºC (Adkins, 2002). Second, the CO_2 impact on temperature may be reduced in the cold state. Third, there could be a physical mechanism that prevents further lowering of CO_2 as the Earth becomes cold, such as a limit to the extent of sea ice in the Southern Ocean, which could influence ocean circulation (Ferrari et al., 2014) and regulate outgassing (Brovkin et al., 2012; Gildor et al., 2002; Stephens and Keeling, 2000). Fourth, there may be a mechanism acting to increase the ocean-atmosphere C inventory or shift C from the ocean to the atmosphere, in response to falling CO_2. Silicate weathering rates are thought to decrease as terrestrial temperatures and precipitation decrease, which would lead to an increase in the carbon inventory, stabilizing atmospheric CO_2 over $>10^5$ yr timescales. Alternatively, the dependence of photosynthetic organisms on CO_2 may be important because photosynthesis rates decrease under cooling climates, slowing the accumulation of carbon in vegetation, soils, and the ocean, and potentially providing a stabilizing feedback via an increase in the ocean atmosphere carbon pool.

These mechanisms may have acted alongside OC_{petro} oxidation to varying extents to buffer against extreme CO_2 minima. However, their effectiveness as isolated feedback processes appears problematic for the following reasons. With regards to the first mechanism, it has been noted that the temperature of the deep ocean has little effect on the global atmosphere and no such cooling limit has been highlighted by climate models (Galbraith and Eggleston, 2017). Consequently, any effect of an oceanic temperature limit on atmospheric temperature may take considerable time to play out in via the atmospheric C cycle. The second mechanism also seems unlikely given that current climate models show an increasing sensitivity to radiative forcing as climate cools (e.g. Manabe and Bryan, 1985). With regards to mechanism three, if this temperature-sensitive feedback only acts on the air-sea partitioning of CO_2, it would not have been sensitive to changes in the combined air–sea–carbon inventory (Galbraith and Eggleston, 2017). Explaining the CO_2 minima may require changes in C budgets to be considered, which may be facilitated by changes in sea ice coverage but unlikely to be driven by it. Also, this mechanism might be expected to have prevented the ‘snowball’ Earth episodes in the Neoproterozoic (Galbraith and Eggleston, 2017), but this did

not happen. In contrast, OC_{petro} oxidation would not be expected to have been as highly prevalent in the Neoproterozoic, despite widespread glaciation, due to the lower levels of atmospheric oxygen (Lyons et al., 2014) and the lower burial of organic carbon in the early Earth (Bjerrum and Canfield, 2004). In the Neoproterozoic, some intervals of high $\delta^{13}C$ punctuated by abrupt swings to low $d^{13}C$ are thought to reflect intense oxidative weathering of organic matter in rocks as the result of the initial establishment of an oxygen-rich atmosphere (Kump et al., 2011). Nevertheless, the global extent of OC_{petro} oxidation would perhaps have been incapable of circumventing snowball Earth episodes at this time and this does not undermine the likely importance of OC_{petro} oxidation in buffering against CO_2 minima later on in Earth's history, such as during the late Cenozoic. Lastly, in regard to the fourth mechanism, the reaction time of silicate weathering may be too slow to provide a strong control on the $<10^4$ yr timescale of glacial CO_2 minima (Torres et al., 2017) and the reduced activity of photosynthetic organisms would not provide a mechanism to circumvent the low CO_2 state. In this study, however, we highlight the important role that the weathering of rocks plays in not only the sequestration of C but also in its release to the atmosphere–carbon inventory.

Although the drawdown of CO_2 by silicate weathering would act to oppose this negative feedback, silicate weathering alone is unlikely to compete with the rates of CO_2 production. In contrast to silicate weathering, it is possible that the more rapid reaction kinetics of OC_{petro} oxidation will lead to more immediate effects on the atmospheric CO_2 reservoir. The weathering of carbon-bearing rocks and sulfide minerals occurs at a faster rate than the weathering of silicate minerals (Chang and Berner, 1999) and the microbial facilitation of these reactions in sub-glacial environments (e.g. Telling et al., 2015; Tranter et al., 2002) causes them to be elevated, even at the low temperatures that may inhibit silicate weathering (Anderson, 2005). These reactions are also sensitive to climate (***Chapter 3–4***, Horan et al., 2017; Torres et al., 2017) and oxidative weathering reactions are capable of linking the observations in atmospheric gas concentrations to the temperature and climate state experienced at Earth's surface. As temperatures drop and mountain glaciation increases, rates of oxidative weathering should also increase globally; providing the required resistance, via increased CO_2 emissions, to any further cooling (Figure 6.2). Given the observed imbalance in the study catchments C budgets of up to ~ 10s of Mt C yr^{-1} (***Chapters 3 & 4***) it is likely that these effects will play out over millions of years. To better appreciate the timescales involved a C cycle modelling approach would probably be required.

Additional weathering of glacially derived silicate material during fluvial transport could shift the overall weathering balance toward CO_2 consumption (Torres et al., 2017). However, in reality, significant amounts of glacial debris are deposited without such reworking, so additional weathering of glacial detritus would not necessarily negate enhanced weathering of OC_{petro} (or sulfide oxidation: Torres et al., 2017). Consequently, previous speculation that glaciation may be

promoted through silicate weathering seems unlikely (Foster and Vance, 2006; Sharp et al., 1995). Earlier in Earth's history, when atmospheric O_2 concentrations were low, for example in the Archaean and Palaeoproterozoic (Lyons et al., 2014), glacially driven CO_2 release by oxidative weathering may have been less active. In this instance, the effectiveness of an oxidative weathering feedback may have been reduced and the carbon fluxes associated with silicate weathering may have been relatively more important and glaciations more globally pervasive (Torres et al., 2017).

Dynamic fluctuations in surface oxygenation are also likely to influence the extent of oxidative weathering of Mo from rocks and the subsequent isotope fractionation of Mo in river catchments. A greater magnitude of Mo isotope fractionation has been tied to the adsorption of Mo to Mn oxides during transient episodes of O_2 production (Algeo and Scheckler, 1998; Planavsky et al., 2014). Such behaviour would drive the $\delta^{98/95}$Mo composition of continental rivers to heavier values and would affect our interpretations of the evolution of seawater composition and the degree of anoxia or euxinia in the local depositional environment. For example, using mass balance calculations, Duan et al. (2010) showed that in a largely anoxic world, the $\delta^{98/95}$Mo of a small seawater Mo reservoir is susceptible to significant modification by isotope fractionation, thus enabling high seawater $\delta^{98/95}$Mo to occur without extensive oxygenation. Further work to elucidate the role of climate and atmospheric gas concentrations on Mo isotope behaviour would be beneficial.

6.4 Potential research opportunities

The main opportunities for future research may lie within the following areas:

1. An assessment of the amount of Re that is oxidised during transit in rivers. In the steep mountain catchments of New Zealand, the opportunity for oxidation of Re in solid materials is thought to be limited to hillslopes and most Re contained within river sediments should be exported offshore, escaping oxidation. In addition, we found no evidence for weathering in the suspended particulates of the Mackenzie River, despite the longer routing system. However, it would be important to evaluate the proportion of Re transported in the dissolved load versus the solid products of erosion as a function of the starting composition of the rock in larger river systems, such as the Ganges or the Amazon, where losses of OC_{petro} from the solid phase have been observed (Bouchez et al., 2010; Galy et al., 2008). It may also be beneficial to study the sediments deposited on river banks and floodplains to examine potential loci for oxidative weathering over different timescales.

2. We lack a conclusive explanation for the relative roles of physical and biogeochemical mechanisms underpinning enhanced oxidative weathering in glaciated mountain catchments (***Chapter 3***). Further work, examining the nature of the sediment in glacial catchments, for example grain surface area and shape, the nature of microbial activity and measurements on oxygen

availability with depth in weathering profiles across different catchments may help to support the idea that physical abrasion together with a lower heterotrophic demand for oxygen and microbial activity are facilitating faster rates of OC_{petro} oxidation in glaciated sites. More generally, the role of microbial communities in the breakdown of organic matter in rocks is also not clear, but it is possible that in glacial environments, in particular, such biological activity is driving enhanced rates of oxidation (Bottrell and Tranter, 2002; Tranter et al., 2002). At present, experiments have focussed on constraining abiotic reactions. However, assimilation into a live microbial biomass may initiate the weathering of rock organic carbon prior to CO_2 release (e.g. Telling et al., 2015). These biological processes may be mediated by external pH and temperature, but the extent to which this may be the case is not clear.

3. It would be interesting to explore patterns of oxidative weathering in glaciated terrains that are not confined to mountain belts to see whether glaciation can enhance weathering at sites where erosion rates are lower and temperatures less favourable to weathering kinetics. It would also be informative to compare rates of oxidative weathering in these systems over time, perhaps assessing the weathering rates in exposed moraines and sediments deposited close to or underneath an actively retreating glacier. High present-day sediment fluxes from glaciated catchments (Herman et al., 2013; Koppes and Montgomery, 2009) and the oscillations in the osmium isotope composition of seawater over Quaternary glacial–interglacial cycles (Georg et al., 2013) support a causative rather than coincidental relationship between glaciers, erosion, and oxidative weathering fluxes (Torres et al., 2017). However, it remains unclear whether this is a transient effect of deglaciation or a long-term sustained increase in erosion and oxidation. It would also be interesting to explore the relative proportion of water added to the rivers that has percolated through debris on the valley sides, sub-glacially and from moraine seeps. This would allow for a better appreciation of where weathering is localised within the glaciated river catchments and whether the exposure of material in moraines during glacial retreat is likely to be significant for further accelerating the OC_{petro} oxidation rate.

4. Whether ReO_4^- and CO_2 are released stoichiometrically during weathering of OC_{petro} is a key outstanding question, which would much improve our understanding of the Re proxy. The degree of decoupling between Re and C, perhaps due to differences in mobility upon oxidation, and the potential controls on this decoupling, such as erosion rate, are unclear. It may helpful to better resolve this term in the OC_{petro} weathering flux calculations in order to accurately translate Re budgets into CO_2 emissions. One method to achieve this may be to conduct experiments to directly trap CO_2 gas generated during oxidation (Keller and Bacon, 1998), in the field or in the laboratory. Carbon isotopes (^{14}C, ^{13}C, ^{12}C) in trapped CO_2 and biomarkers may also help to track organic matter evolution in the solid residue. The CO_2 fluxes quantified by these approaches could then be

compared with Re-derived estimates of OC_{petro} oxidation based on dissolved load fluxes in a given river catchment.

5. Further data are required to constrain the composition of mineral phases that deliver Re and Mo to the dissolved load. In particular, we are currently limited to a small selection of data on coal units to estimate the composition of the OC_{petro} endmember. Although dissolved Re appears to be almost entirely derived from OC_{petro} oxidation, even with ~10% deviations in the endmember positions, more detailed studies on the element composition of the endmembers could increase confidence in our estimates of dissolved river Re derived from OC_{petro}. In addition, Re isotopes could offer more insight on Re source (Miller et al., 2015).

6. Alongside Re, other redox sensitive platinum group elements could be explored as complementary tools to understand oxidative weathering reactions and to add strength to the value of the Re proxy. Re isotopes may also lend insight into the weathering reactions involved. Applying a variety of high-resolution multi-proxy techniques to assess patterns of geochemical cycling and environmental change in under-sampled areas would be particularly beneficial, for example in polar glaciated terrains.

7. Better understanding the isotope fractionation that exists between rivers (mean $\delta^{98}Mo$ = ~0.45‰; Archer and Vance, 2008) and the eroding upper crust (~0.0 to 0.15‰; e.g. Liang et al., 2017) remains a key research priority. The potential for greater Mo fractionation in glaciated catchments, relative to catchments with little or no glaciation, is not entirely clear from the available data in the western Southern Alps. Patterns in Mo sequestration in glacial catchments could be investigated further by sequentially extracting Mo from the weathering products. It would also be interesting to investigate whether Mo isotope fractionation occurs on or under the glaciers. The potential influence of oxygen availability and biological cover on Mo release or retention could also be studied further.

8. The behaviour of Mo in large river systems, where erosion rates are low and the degree of weathering at deeper soil horizons potentially large, relative to mountain belts, is unknown. It may be possible that the amount of Mo remaining dissolved in river waters could help to quantify the rate of secondary weathering. However, more data are required, particularly in sites where secondary weathering products are well developed as coatings on particles. This could be informative for understanding the longer-term controls on river $\delta^{98/95}Mo$. The Mo isotope composition of river water plays a central role in setting the isotope composition of the oceans; therefore this would also be relevant for improving the characterisation of the Mo inputs to models of ocean $\delta^{98/95}Mo$ through time. Future developments in Re isotopes, alongside Mo isotopes, may

lend further insight into the rates of secondary weathering in soils, on river sediments, or during biological processing within catchments, particularly over different climate states.

6.5 References

Adkins, J.F., 2002. The Salinity, Temperature, and delta ^{18}O of the Glacial Deep Ocean. Science 298, 1769–1773.

Algeo, T.J., Scheckler, S.E., 1998. Terrestrial-marine teleconnections in the Devonian: links between the evolution of land plants, weathering processes, and marine anoxic events. Philos. Trans. R. Soc. London B Biol. Sci. 353, 113–130.

Anagnostou, E., John, E.H., Edgar, K.M., Foster, G.L., Ridgwell, A., Inglis, G.N., Pancost, R.D., Lunt, D.J., Pearson, P.N., 2016. Changing atmospheric CO_2 concentration was the primary driver of early Cenozoic climate. Nature 533, 380–398.

Anderson, S.P., 2005. Glaciers show direct linkage between erosion rate and chemical weathering fluxes. Geomorphology 67, 147–157.

Archer, C., Vance, D., 2008. The isotopic signature of the global riverine molybdenum flux and anoxia in the ancient oceans. Nat. Geosci. 1, 597–600.

Bardgett, R.D., Richter, A., Bol, R., Garnett, M.H., Bäumler, R., Xu, X., Lopez-Capel, E., Manning, D.A.C., Hobbs, P.J., Hartley, I.R., 2007. Heterotrophic microbial communities use ancient carbon following glacial retreat. Biol. Lett. 3, 487–490.

Barling, J., Anbar, A.D., 2004. Molybdenum isotope fractionation during adsorption by manganese oxides. Earth Planet. Sci. Lett. 217, 315–329.

Bjerrum, C.J. and Canfield, D.E., 2004. New insights into the burial history of organic carbon on the early Earth. Geochemistry, Geophysics, Geosystems 5(8), 1–9.

Bolton, E.W., Berner, R.A., Petsch, S.T., 2006. The weathering of sedimentary organic matter as a control on atmospheric O_2: II. Theoretical modeling. Am. J. Sci. 306, 575–615.

Bottrell, S.H., Tranter, M., 2002. Sulphide oxidation under partially anoxic conditions at the bed of the Haut Glacier d'Arolla, Switzerland. Hydrol. Process. 16, 2363–2368.

Bouchez, J., Beyssac, O., Galy, V., Gaillardet, J., France-Lanord, C., Maurice, L., Moreira-Turcq, P., 2010. Oxidation of petrogenic organic carbon in the Amazon floodplain as a source of atmospheric CO_2. Geology 38, 255–258.

Brovkin, V., Ganopolski, A., Archer, D., Munhoven, G., 2012. Glacial CO_2 cycle as a succession of key physical and biogeochemical processes. Clim. Past 8, 251–264.

Calmels, D., Gaillardet, J., Brenot, A., France-Lanord, C., 2007. Sustained sulfide oxidation by physical erosion processes in the Mackenzie River basin: Climatic perspectives. Geology 35, 1003–1006.

Chang, S.B., Berner, R.A., 1999. Coal weathering and the geochemical carbon cycle. Geochim. Cosmochim. Acta 63, 3301–3310.

Dalai, T.K., Singh, S.K., Trivedi, J.R., Krishnaswami, S., 2002. Dissolved rhenium in the Yamuna River System and the Ganga in the Himalaya: Role of black shale weathering on the budgets of Re, Os, and U in rivers and CO_2 in the atmosphere. Geochim. Cosmochim. Acta 66, 29–43.

Duan, Y., Anbar, A.D., Arnold, G.L., Lyons, T.W., Gordon, G.W., Kendall, B., 2010. Molybdenum isotope evidence for mild environmental oxygenation before the Great Oxidation Event. Geochim. Cosmochim. Acta 74, 6655–6668.

Ferrari, R., Jansen, M.F., Adkins, J.F., Burke, A., Stewart, A.L., Thompson, A.F., 2014. Antarctic sea ice control on ocean circulation in present and glacial climates. Proc. Natl. Acad. Sci. 111, 8753–8758.

Foster, G.L., Vance, D., 2006. Negligible glacial-interglacial variation in continental chemical weathering rates. Nature 444, 918–921.

Galbraith, E.D., Eggleston, S., 2017. A lower limit to atmospheric CO_2 concentrations over the past 800,000 years. Nat. Geosci. 10, 295.

Galy, V., Beyssac, O., France-Lanord, C., Eglinton, T., 2008. Recycling of Graphite During Himalayan Erosion: A Geological Stabilization of Carbon in the Crust. Science 322, 943–945.

Georg, R.B., West, A.J., Vance, D., Newman, K., Halliday, A.N., 2013. Is the marine osmium isotope record a probe for CO_2 release from sedimentary rocks? Earth Planet. Sci. Lett. 367, 28–38.

Gildor, H., Tziperman, E., Toggweiler, J.R., 2002. Sea ice switch mechanism and glacial-interglacial CO_2 variations. Glob. Biogeochem. Cycles 16, 1032.

Goldberg, T., Archer, C., Vance, D., Poulton, S.W., 2009. Mo isotope fractionation during adsorption to Fe (oxyhydr)oxides. Geochim. Cosmochim. Acta 73, 6502–6516.

Hales, T.C., Roering, J.J., 2009. A frost "buzzsaw" mechanism for erosion of the eastern Southern Alps, New Zealand. Geomorphology 107, 241–253.

Herman, F., Seward, D., Valla, P.G., Carter, A., Kohn, B., Willett, S.D., Ehlers, T.A., 2013. Worldwide acceleration of mountain erosion under a cooling climate. Nature 504, 423.

Hilton, R.G., Gaillardet, J., Calmels, D., Birck, J.-L., 2014. Geological respiration of a mountain belt revealed by the trace element rhenium. Earth Planet. Sci. Lett. 403, 27–36.

Horan, K., Hilton, R.G., Selby, D., Ottley, C.J., Gröcke, D.R., Hicks, M., Burton, K.W., 2017. Mountain glaciation drives rapid oxidation of rock-bound organic carbon. Sci. Adv. 3.

Jaffe, L.A., Peucker-Ehrenbrink, B., Petsch, S.T., 2002. Mobility of rhenium, platinum group elements and organic carbon during black shale weathering. Earth Planet. Sci. Lett. 198, 339–353.

Keller, C.K., Bacon, D.H., 1998. Soil respiration and georespiration distinguished by transport analyses of vadose CO_2, (CO_2)-C-13, and (CO_2)-C-14. Global Biogeochem. Cycles 12, 361–372.

Koppes, M.N., Montgomery, D.R., 2009. The relative efficacy of fluvial and glacial erosion over modern to orogenic timescales. Nat. Geosci. 2, 644–647.

Kump, L.R., Junium, C., Arthur, M.A., Brasier, A., Fallick, A., Melezhik, V., Lepland, A., CČrne, A.E., Luo, G., 2011. Isotopic evidence for massive oxidation of organic matter following the Great Oxidation Event. Science 334, 1694–1696.

LaRowe, D.E., Van Cappellen, P., 2011. Degradation of natural organic matter: A thermodynamic analysis. Geochim. Cosmochim. Acta 75, 2030–2042.

Liang, Y.H., Halliday, A.N., Siebert, C., Fitton, J.G., Burton, K.W., Wang, K.L., Harvey, J., 2017. Molybdenum isotope fractionation in the mantle. Geochim. Cosmochim. Acta 199, 91–111.

Lyons, T.W., Reinhard, C.T., Planavsky, N.J., 2014. The rise of oxygen in Earth's early ocean and atmosphere. Nature 506, 307–315.

Manabe, S., Bryan, K., 1985. CO_2-induced change in a coupled ocean-atmosphere model and its paleoclimatic implications. J. Geophys. Res. 90, 11,611-689,707.

Miller, C.A., Peucker-Ehrenbrink, B., Schauble, E.A., 2015. Theoretical modeling of rhenium isotope fractionation, natural variations across a black shale weathering profile, and potential as a paleoredox proxy. Earth Planet. Sci. Lett. 430, 339–348.

Planavsky, N.J., Asael, D., Hofmann, A., Reinhard, C.T., Lalonde, S. V., Knudsen, A., Wang, X., Ossa Ossa, F., Pecoits, E., Smith, A.J.B., Beukes, N.J., Bekker, A., Johnson, T.M., Konhauser, K.O., Lyons, T.W., Rouxel, O.J., 2014. Evidence for oxygenic photosynthesis half a billion years before the Great Oxidation Event. Nat. Geosci. 7, 283–286.

Sharp, M., Tranter, M., Brown, G.H., Skidmore, M., 1995. Rates of chemical denudation and CO_2 in a glacier-covered alpine catchment. Geology 23, 61–64.

Stephens, B.B., Keeling, R.F., 2000. The influence of Antarctic sea ice on glacial-interglacial CO_2 variations. Nature 404, 171–174.

Stolper, D.A., Bender, M.L., Dreyfus, G.B., Yan, Y., Higgins, J.A., 2016. A Pleistocene ice core record of atmospheric O_2 concentrations. Science 353, 1427–1430.

Telling, J., Boyd, E.S., Bone, N., Jones, E.L., Tranter, M., MacFarlane, J.W., Martin, P.G., Wadham, J.L., Lamarche-Gagnon, G., Skidmore, M.L., Hamilton, T.L., Hill, E., Jackson, M., Hodgson, D.A., 2015. Rock comminution as a source of hydrogen for subglacial ecosystems. Nat. Geosci. 8, 851.

Torres, M.A., Moosdorf, N., Hartmann, J., Adkins, J.F., West, A.J., 2017. Glacial weathering, sulfide oxidation, and global carbon cycle feedbacks. Proc. Natl. Acad. Sci.

Torres, M.A., West, A.J., Li, G., 2014. Sulphide oxidation and carbonate dissolution as a source of CO_2 over geological timescales. Nature 507, 346–349.

Tranter, M., Sharp, M.J., Lamb, H.R., Brown, G.H., Hubbard, B.P., Willis, I.C., 2002. Geochemical weathering at the bed of Haut Glacier d'Arolla, Switzerland - a new model. Hydrol. Process. 16, 959–993.

Wadham, J.L., Bottrell, S., Tranter, M., Raiswell, R., 2004. Stable isotope evidence for microbial sulphate reduction at the bed of a polythermal high Arctic glacier. Earth Planet. Sci. Lett. 219, 341–355.

Zachos, J.C., Dickens, G.R, Zeebe, R.E., 2008. An early Cenozoic perspective on greenhouse warming and carbon-cycle dynamics. Nature 451, 279–283.

Zachos, J., Pagani, M., Sloan, L., Thomas, E., Billups, K., 2001. Trends, rhythms, and aberrations in global climate 65 Ma to present. Science 292, 686–693.

Appendix

Publication

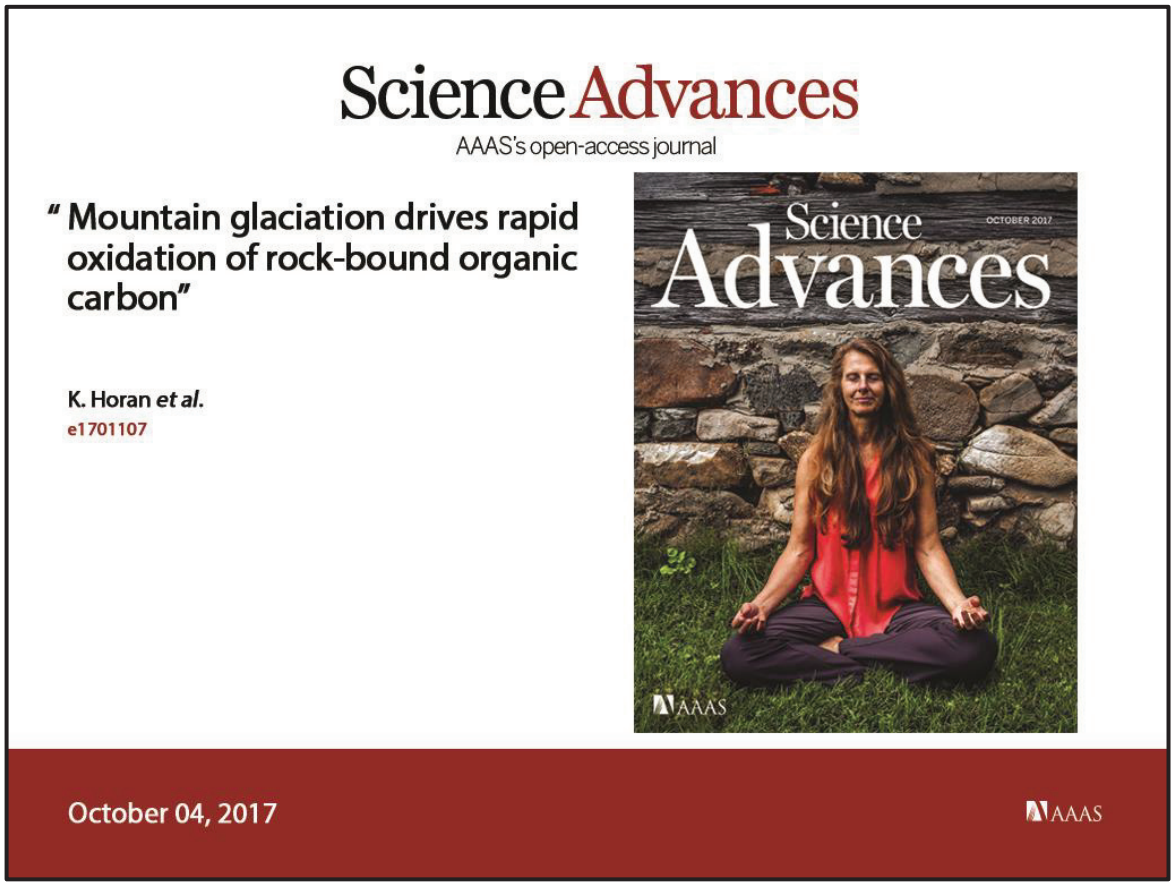

Citation: Horan, K., Hilton, R.G., Selby, D., Ottley, C.J., Gröcke, D.R., Hicks, M., Burton, K.W., 2017. Mountain glaciation drives rapid oxidation of rock-bound organic carbon. Sci. Adv. 3. doi:10.1126/sciadv.1701107

SCIENCE ADVANCES | RESEARCH ARTICLE

CLIMATOLOGY

Mountain glaciation drives rapid oxidation of rock-bound organic carbon

Kate Horan,[1]* Robert G. Hilton,[2] David Selby,[1] Chris J. Ottley,[1] Darren R. Gröcke,[1] Murray Hicks,[3] Kevin W. Burton[1]

Copyright © 2017 The Authors, some rights reserved; exclusive licensee American Association for the Advancement of Science. No claim to original U.S. Government Works. Distributed under a Creative Commons Attribution License 4.0 (CC BY).

Over millions of years, the oxidation of organic carbon contained within sedimentary rocks is one of the main sources of carbon dioxide to the atmosphere, yet the controls on this emission remain poorly constrained. We use rhenium to track the oxidation of rock-bound organic carbon in the mountain watersheds of New Zealand, where high rates of physical erosion expose rocks to chemical weathering. Oxidative weathering fluxes are two to three times higher in watersheds dominated by valley glaciers and exposed to frost shattering processes, compared to those with less glacial cover; a feature that we also observe in mountain watersheds globally. Consequently, we show that mountain glaciation can result in an atmospheric carbon dioxide source during weathering and erosion, as fresh minerals are exposed for weathering in an environment with high oxygen availability. This provides a counter mechanism against global cooling over geological time scales.

INTRODUCTION

The exposure of organic matter in rocks to oxidative weathering at Earth's surface releases carbon dioxide (CO_2) to the atmosphere from long-term (>10^6 years) storage in the lithosphere and consumes atmospheric oxygen (O_2) (*1*–*3*). The global CO_2 emissions from the oxidation of rock-derived organic carbon [petrogenic OC (OC_{petro})] are estimated to be 40 to 100 × 10^6 metric tons of carbon (tC) per year (*1*). Over million-year (geological) time scales, this emission represents the main source of atmospheric CO_2 alongside volcanism and metamorphism (*1*–*4*) and plays a role in setting atmospheric O_2 concentrations (*2*, *5*). Geological CO_2 emissions are removed from the atmosphere by chemical weathering of silicate minerals by carbonic acid coupled to carbonate precipitation (*4*, *6*) and the burial of recently photosynthesized OC (*3*, *7*). These atmospheric CO_2 drawdown mechanisms are regulated by erosion, temperature, and runoff and are thought to stabilize CO_2 concentrations and global climate (*6*). However, we have little understanding of the factors controlling OC_{petro} oxidation rate (*1*, *8*, *9*) and hence how millennial-scale changes in climate (*10*) might modify this major CO_2 emission.

Chemical weathering of OC_{petro} proceeds as surficial gases and fluids permeate through sedimentary rocks, oxidizing organic matter and releasing CO_2 (*1*). The kinetics of OC_{petro} weathering appear to be ~10 times faster than the kinetics of silicate mineral weathering (*11*). Faster reaction kinetics imply that shorter fluid residence times are required to reach chemical equilibrium and maximize weathering fluxes during OC_{petro} oxidation (*6*), compared to acid hydrolysis silicate weathering (*6*, *12*). When considered together with the high concentrations of O_2 in the present-day atmosphere, weathering models suggest that the OC_{petro} oxidation rate is set by the mineral supply rate in most locations globally (*13*). Microorganisms may also be important facilitators of OC_{petro} oxidation (*14*). On the basis of these observations, we propose that mountain glaciation could significantly enhance OC_{petro} oxidation rates due to a combination of physical and biogeochemical factors: (i) frost cracking and abrasive glacial grinding processes, which produce fine sediment with more surface area in an environment with high water availability (*15*, *16*); (ii) lower vegetation and soil cover that can increase the availability of O_2 to exposed bedrock and in deeper soil horizons; and (iii) the activity of microorganisms catalyzing weathering, both subglacially and during primary ecological succession on moraines (*14*, *17*–*19*). Previous work has suggested that sulfide oxidation is enhanced subglacially (*18*, *20*). If OC_{petro} oxidation rates also increase, CO_2 release may be highest during periods of repeated mountain glaciation over millennia (*21*) and may provide a mechanism for countering cooling trends in Earth's climate over time scales of 100 thousand years to millions of years.

Here, we examine the potential for mountain glaciation to increase OC_{petro} oxidation rates. We focus on the mountain watersheds of the western Southern Alps, New Zealand (Fig. 1A), where lithological contrasts are relatively small along strike of the Alpine Fault (*22*), but glacial coverage is variable (*23*). Previous work has suggested that high silicate weathering rates (*20*, *24*) are facilitated by rapid soil production (*25*) and mineral supply by bedrock landslides (*26*). Here, we assess the rates of oxidative weathering and the role of mountain glaciers using river water and sediment samples from 13 watersheds (see Materials and Methods). We also collected samples from two watersheds in the eastern Southern Alps that host glaciers but have lower physical erosion rates and from the Waipaoa River in North Island, which has a high erosion rate but no glaciers (*24*). In addition, we compile measurements from mountain watersheds draining OC_{petro}-bearing sedimentary rocks in North America (Yukon and Mackenzie) and Asia (Taiwan rivers, Ganges, and Brahmaputra) (*9*, *27*).

To assess and quantify OC_{petro} oxidation rates, we measured the concentration of the redox-sensitive trace element rhenium (Re) in river waters ($[Re]_{diss}$), river bed materials ($[Re]_{BM}$), weathered colluvium and surface soils on hillslopes ($[Re]_{COL}$) using isotope dilution and inductively coupled plasma mass spectrometry (ICP-MS) (see Materials and Methods). The close association of Re and OC_{petro} in sedimentary rocks (*28*) and the solubility of Re upon oxidation during weathering (*29*) (present as the soluble perrhenate oxyanion, ReO_4^-, in soils and rivers with pH values between 5.5 and 9.5) have led previous studies to suggest that Re can trace OC_{petro} oxidation (*1*, *9*, *30*, *31*). For river watersheds with similar runoff and bedrock composition, the dissolved Re concentration, $[Re]_{diss}$, has been shown to reflect the relative rate of oxidative weathering (*9*). The dissolved Re discharge (mol $year^{-1}$) or dissolved Re yield (mol km^{-2} $year^{-1}$) provides a more direct means to quantify the oxidative weathering yield (*1*, *9*, *30*, *31*). The dissolved Re yield has been

[1]Department of Earth Sciences, Durham University, Durham DH1 3LE, UK. [2]Department of Geography, Durham University, Durham DH1 3LE, UK. [3]National Institute of Water and Atmospheric Research, Christchurch, New Zealand.
*Corresponding author. Email: kate.horan@durham.ac.uk

used to estimate the associated CO_2 emissions by OC_{petro} oxidation when the Re to OC_{petro} ratio of the rocks undergoing weathering has been characterized (*9*). The main uncertainties in the use of the Re proxy derive from the following: (i) As a soluble element, Re may be mobilized more effectively during weathering than the CO_2 derived from OC_{petro} oxidation (*30*); (ii) Re may be hosted in silicate and sulfide minerals (*27*); and (iii) graphitic OC_{petro} is less susceptible to oxidation (*32*).

RESULTS

River bed materials and weathered colluvium

The mean organic carbon (OC) weight percentage in river bed materials, $[OC]_{BM}$, from the western Southern Alps is 0.13 ± 0.01 weight % (wt %) (n = 31, ±2 SE), and the mean stable carbon isotope composition is $\delta^{13}C$ = −22.5 ± 0.6‰ (n = 31, ±2 SE). For comparison, the $[OC]_{BM}$ values are lower than those in Taiwan (*9*) but more than double those measured in the Himalaya (*32*). The mean values of river bed materials are similar to previous measurements from this location (*22*, *33*) and to the mean of bedrock values in the western Southern Alps, [OC] = 0.15 ± 0.05 wt % and $\delta^{13}C$ = −21.1 ± 1.1‰ (n = 11, ±2 SE) (*22*), suggesting that they are dominated by OC_{petro}, with minor inputs from biospheric OC generated by recent photosynthesis by C_3 plants ($\delta^{13}C$ ~ −28‰). The river bed materials have less variability in their average composition when compared to bedrock, which likely reflects the integration of OC_{petro}-bearing sediment from landslides and mass wasting processes, which can erode OC_{petro} from large areas of the watershed (*34*, *35*). The river sediments downstream are a mixture of these inputs (*22*). Although the river bed materials have a slightly lower OC concentration than bedrock in the mountain belt, they are indistinguishable within the variability in the means and can therefore provide a robust method to assess the watershed-averaged bedrock composition (*22*, *32*, *36*). This is consistent with findings in other erosive settings where bedrock landslides excavate deep into the landscape, tap into unweathered rock, and supply it to rivers in the sand-silt-clay fraction of river sediments (*37*).

The mean Re concentration in river bed materials, $[Re]_{BM}$, is 118 ± 21 parts per trillion (ppt) (n = 31, ±2 SE) (table S1). Although this Re concentration is low for sedimentary rocks (*38*), it is in line with the low $[OC]_{BM}$ in the western Southern Alps and consistent with organic matter being a dominant host of Re in sediments (*28*). The mean $[Re]_{BM}/[OC]_{BM}$ ratio is 0.9 ± 0.2 × 10^{-7} g g^{-1} (n = 31, ±2 SE), and there is no systematic variability along strike of the Alpine Fault (that is, no variability with latitude and longitude).

We examine samples of weathered colluvium collected from hillslopes in the western Southern Alps for loss of OC_{petro} and Re (table S2). In the Docherty Creek watershed, which neighbors the Waiho River, weathered colluvium has a mean $[Re]_{COL}$ = 29 ± 6 ppt (n = 4, ±2 SE), compared to local river bed materials downstream at Docherty Creek (NZ14-90; $[Re]_{BM}$ = 112 ppt). Soil litter samples are also depleted in Re (table S2). This is expected if Re loss occurs during oxidative weathering. The mean OC content of the colluvium, $[OC]_{COL}$ = 1.2 ± 0.3 wt % (n = 4, ±2 SE), is higher than that of the local river bed materials (NZ14-90; $[OC]_{BM}$ = 0.21 wt %). However, organic matter in the colluvium has a stable isotopic composition (mean $\delta^{13}C$ = −25.9 ± 0.4‰) and radiocarbon activity (reported as fraction modern, F_{mod} = 0.80 ± 0.09) that are very different from the expected rock inputs (NZ14-90; $\delta^{13}C$ = −21.2‰ and expected F_{mod} ~ 0). The values suggest an important contribution from biospheric OC in these samples (*22*).

To assess the OC_{petro} content of the colluvium and to account for biospheric OC, we use $\delta^{13}C$ and F_{mod} values in a mixing analysis (see Materials and Methods). The high $[OC]_{COL}$ of these samples and the relatively low OC_{petro} content of rocks in this mountain range (*22*), together with the observation that century-aged biospheric OC is important in these New Zealand soils (fig. S1), result in uncertainty on the absolute OC_{petro} contents. The mean $[OC_{petro}]$ of the weathered colluvium is calculated as 0.15 ± 0.06% (n = 4, ±2 SE), which is lower than that of the river bed material. The data are consistent with OC_{petro} loss during weathering on hillslopes. The coupled loss of Re and OC_{petro} during chemical weathering supports previous measurements on soil from the Ohio Shale (table S2) (*30*), the Himalaya (*39*), and Taiwan (*9*). The weathered colluvium from New Zealand and published soil data show that Re is generally more mobile during OC_{petro} weathering, and so we account for this when estimating the OC_{petro} weathering rate using the dissolved Re flux (see Materials and Methods).

River waters

The major dissolved ions in rivers draining the western Southern Alps (Ca^{2+}, Mg^{2+}, Na^+, and K^+) characterize the overall weathering processes

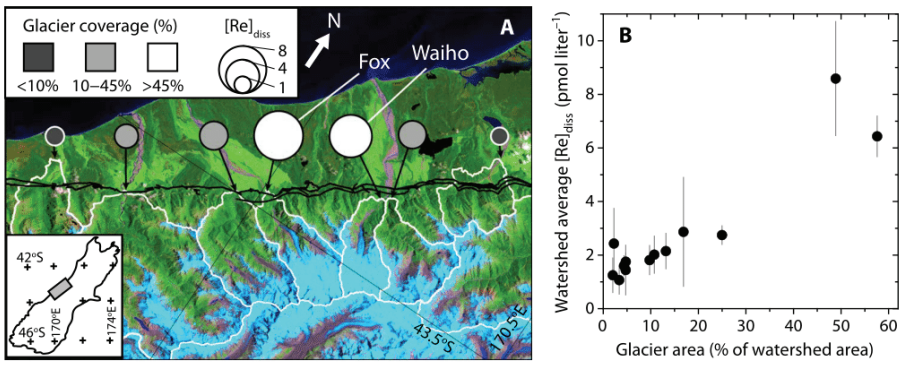

Fig. 1. The western Southern Alps, New Zealand. (**A**) Watersheds for the central part of the study area where glacier area varies most, with watershed boundaries marked in white. The black line is the Alpine Fault trace. Image is from Landsat ETM (Enhanced Thematic Mapper) (31 December 2002), shown to illustrate glacial coverage. The watershed-averaged dissolved Re concentration, $[Re]_{diss}$ (pmol $liter^{-1}$), is shown as the circle size, and the shading reflects the percentage watershed area with glaciers (*23*). Inset shows the location of the study area on South Island, New Zealand. (**B**) Positive relationship between watershed-averaged $[Re]_{diss}$ and the percentage of the watershed area covered by glaciers (n = 13, r = 0.93, r^2 = 0.87, P < 0.001). Gray whiskers are ±2 SE on the mean $[Re]_{diss}$ values.

and reflect a source rock comprising metasedimentary silicate rocks hosting trace carbonate minerals (fig. S2A). The water measurements from this study in 2014 are consistent with sampling campaigns in 1998, 1999, and 2000 (*20*, *24*). Notably, all sampling campaigns find higher relative HCO_3^- and Ca^{2+} concentrations in the heavily glaciated Fox and Waiho rivers (fig. S2A), which probably reflects the higher susceptibility of carbonate minerals to acid hydrolysis reactions in these watersheds. The overlap of the data sets collected from different years, seasons, and flow regimes (fig. S2, A and B) suggests that spatial patterns in dissolved ion composition are retained despite the potential for seasonal and flood-event scale variability (*40*).

The $[Re]_{diss}$ values in western Southern Alps rivers range from 0.81 to 11.55 pmol liter^{-1}, with a mean = 3.05 ± 0.69 pmol liter^{-1} (n = 51, ±2 SE) (table S3). There is a distinct variability between different watersheds (Fig. 1A), with the Waiho and Fox watersheds having the highest mean $[Re]_{diss}$ values throughout the sampling period. Mean $[Re]_{diss}$ is not correlated with $[Re]_{BM}$ in the western Southern Alps, suggesting that the bedrock geology does not set the spatial pattern in $[Re]_{diss}$. When all the data are considered together, the watershed-averaged $[Re]_{diss}$ is correlated with the proportion of area covered by glaciers upstream (Fig. 1B; r^2 = 0.87, P < 0.001, n = 13).

The $[Re]_{diss}$ values are generally low compared to those measured in river waters globally (*27*) and in rivers draining metasedimentary rocks in Taiwan, which have values ranging from ~5 to 25 pmol liter^{-1} (*9*). However, when $[Re]_{diss}$ values are normalized to the concentration of Re in river bed materials, $[Re]_{BM}$ (*9*, *32*, *36*), the values are more similar to those in Taiwan. In the western Southern Alps, watersheds dominated by river erosion and bedrock landslides (that is, not by glacial erosion processes) have a mean $[Re]_{diss}$ = 1.92 ± 0.76 pmol liter^{-1} and mean $[Re]_{BM}$ = 105 ± 20 ppt, giving a $[Re]_{diss}/[Re]_{BM} = 3.4 \pm 1.4 \times 10^{-3}$ (pg g^{-1}/pg g^{-1}), which is slightly higher than that measured in Taiwan, where the average $[Re]_{diss}/[Re]_{BM}$ is $3.3 \pm 0.5 \times 10^{-3}$. The two mountain belts have comparable physical erosion rates (*9*, *24*), suggesting that Re mobility is similar between sites despite the contrasts in bedrock geology. The $[Re]_{diss}/[Re]_{BM}$ values are more than double in the Waiho and Fox watersheds that host valley glaciers and have extensive glacial coverage.

To estimate oxidative weathering yields, we quantify the dissolved Re yield (mol km^{-2} year^{-1}) in watersheds where we have annual water discharge estimates (*41*). These are in the Hokitika, Whataroa, Haast, and Waiho rivers (tables S4 and S5). Our river water samples from 2014 cover a relatively narrow dynamic range in water flow especially in the glacial watershed (~0.5 to 1.5 times mean flow values) but do not show significant dilution at a higher flow (fig. S2C and table S5). This suggests that the annual water discharge (Q_{annual}, m^3 year^{-1}) (*41*) and our mean $[Re]_{diss}$ for each large watershed can together provide a reliable estimate of dissolved Re flux. However, the average ion concentrations collected at lower Q_w may overestimate the dissolved ion flux, if ions are diluted at a high flow (*40*). We find that using an average concentration does not systematically overestimate or underestimate the dissolved Re yield (see Materials and Methods). To assess the role of seasonal and/or interannual variability, we plot our major ion data (for example, Ca^{2+}) alongside daily water discharge (Q_w, m^3 s^{-1}) for the Whataroa and Hokitika watersheds (fig. S1B) and compare this to published data from 1998 to 1999 (*24*) and 2000 to 2001 (fig. S2B) (*20*). The broad consistency in ion concentrations and ion ratios suggest that annual and seasonal variability may be of second-order importance when compared to contrasts between different watersheds. Rainwater and hydrothermal water samples (table S3) have very low $[Re]_{diss}$ (<0.2 pmol liter^{-1}), so no correction is made to the Re flux from these inputs.

Global compilation

Published data are compiled from watersheds around the world that allow for a comparison to our findings in New Zealand (table S6). The required data are as follows: (i) dissolved Re concentration ($[Re]_{diss}$); (ii) watershed-averaged bedrock Re composition, an indication of which is provided by $[Re]_{BM}$; (iii) annual water discharge to estimate dissolved Re yield; and (iv) suspended sediment yield as a proxy of physical erosion rate (*9*, *20*, *22*, *27*, *41*–*45*). We also add new measurements of river water and bed material samples from the Jollie and Hooker watersheds draining the eastern Southern Alps, the Waipaoa River in North Island, New Zealand, and the Yukon River and Mackenzie River in Canada, which we collected using similar methods. We estimate the dissolved Re yield for each of these sites and account for variability in the bedrock geology by normalizing the Re yield to the measured $[Re]_{BM}$. We quantify the upstream area covered by glaciers from published work or by using the World Glacier Inventory as we do for the western Southern Alps (see Materials and Methods). We find dissolved Re yield (normalized by $[Re]_{BM}$) increases with increasing annual suspended sediment yields across the data set (Fig. 2), supporting previous work from Taiwan (*9*). However, watersheds with mountain glaciation upstream of the sampling locations (where glaciers cover >1% of the area) have a higher dissolved Re yield for a given suspended sediment yield (Fig. 2).

DISCUSSION

The erosion rates in the western Southern Alps are high (4000 to 10,000 t km^{-2} year^{-1}) and comparable to those in Taiwan (*9*, *24*). The similarity in Re mobility between these settings agrees with the notion that high erosion rates can enhance oxidative weathering of OC_{petro} and the release of Re to the dissolved load of rivers (*9*). This probably reflects the rapid soil formation in the western Southern Alps (*25*) and is consistent with an important role of bedrock landslides for exposing bedrock clasts in landslide deposits and focusing hydrological pathways in landslide scars (*26*). In the global data compilation, we find that suspended sediment yield (a proxy for physical erosion rate) is correlated with dissolved Re yield (Fig. 2). This suggests that OC_{petro} oxidation is supply-limited in many locations, as predicted by the relatively fast kinetics of OC_{petro} oxidation and the high atmospheric O_2 concentrations at present (*11*, *13*). This contrasts with acid hydrolysis weathering of silicate minerals, which is thought to be kinetically limited at the high erosion rates experienced in mountain belts (*6*, *12*). The implication is that for watersheds underlain by sedimentary rocks, increased erosion may result in a less effective CO_2 drawdown by silicate weathering, whereas CO_2 release by oxidative weathering of OC_{petro} continues to increase (Fig. 2).

In the western Southern Alps, we find that glacial cover is a major control on the average $[Re]_{diss}$ measured in watersheds (Fig. 1B). This is not only the case for the watersheds with large valley glaciers (the Waiho and Fox; Fig. 1A): Glacial processes appear to enhance oxidative weathering to some degree in all watersheds. Although this may seem to conflict with the idea that OC_{petro} oxidation in mountains is already supply-limited (*9*), there are characteristics of glacial watersheds, such as (i) physical mechanisms that increase effective surface area (*15*, *16*) and (ii) biogeochemical mechanisms that increase O_2 availability and the competitiveness of microbial communities (*17*), which mean that for the same physical erosion rate, oxidation rate may be further enhanced. Physical mechanisms include glacial abrasion (*16*), which can supply large quantities of fine material for weathering within the glacial system and in the deposited moraines. At higher elevations on steep rock walls,

freeze/thaw cycles and frost cracking driven by sustained subzero temperatures and water availability in the porous bedrock can also increase the supply of fresh, fine material to O_2 in the air and water (*15*). Biogeochemical factors work in parallel, with limited vegetation and soil development in glacial watersheds resulting in less demand for O_2 by heterotrophic respiration (*17*). Oxygen could therefore penetrate deeper into exposed rock surfaces (*11*, *13*). Microbial communities also facilitate OC_{petro} oxidation (*1*, *14*) and are active both subglacially (*18*, *19*) and in moraines colonized by organisms during primary succession (*17*).

The mechanisms described here are not unique to watersheds of the western Southern Alps but should operate wherever mountain glaciation occurs on OC_{petro}-bearing rocks. In the glaciated eastern Southern Alps watersheds, erosion rates are lower than those in the western Southern Alps (*15*, *20*, *24*), and so lower OC_{petro} oxidation rates may be expected (*9*). However, when compared to watersheds with similar erosion rates in unglaciated Taiwan, the glaciated watersheds have higher dissolved Re yields (Fig. 2). The glacier-free Waipaoa River data are consistent with the data from Taiwan. When we examine larger rivers draining OC_{petro}-bearing sedimentary rocks (table S6), we find that a global pattern starts to emerge (Fig. 2). Erosion rate is a first-order control on oxidative weathering rate (dissolved Re yield), but watersheds hosting glaciers (>1% of the watershed area; for example, Yukon, Brahmaputra, Ganges, and Southern Alps) have dissolved Re yields that are up to three times greater for a given erosion rate than watersheds with very low glacial coverage, regardless of the basin area.

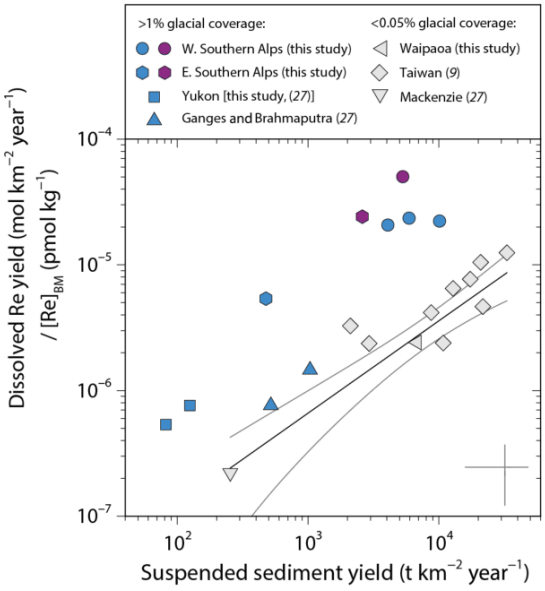

Fig. 2. Dissolved Re yield in mountain watersheds around the world draining sedimentary rocks as a function of suspended sediment yield. Dissolved Re yields (mol km^{-2} $year^{-1}$) have been normalized to river bed material Re concentration ($[Re]_{BM}$, pmol kg^{-1}) to account for lithological variability between watersheds (table S6). Gray whiskers show ±50% of the values. Gray symbols represent watersheds with <0.05% of their area covered by glaciers, with the power law best fit to data shown by the black line and the 95% confidence intervals shown in gray [$y = (4.1 \pm 3.4 \times 10^{-9})x^{(0.7 \pm 0.1)}$, $r^2 = 0.82$, $P < 0.001$, $n = 12$]. Blue symbols represent watersheds with glaciers covering >1% of the watershed area, and purple symbols represent watersheds with the highest coverage of glaciers (>40%).

The dissolved Re yield can be used to estimate the CO_2 oxidation yield, J_{CO2} (gC km^{-2} $year^{-1}$), by OC_{petro} oxidation (*1*, *9*, *30*, *31*). First, there must be good constraint on the Re-to-OC ratio of the sedimentary rocks and the behavior of Re and OC_{petro} during weathering. In the western Southern Alps, the river bed materials provide an estimate of watershed-averaged [Re] and [OC_{petro}], and their compositions are similar to measured bedrocks. The weathered colluvium confirms coupled Re and OC_{petro} loss (fig. S2 and table S2) (*1*, *9*, *31*). To quantify the CO_2 release, the dissolved Re yield in grams (J_{Re}, g km^{-2} $year^{-1}$) is combined with the $[OC]_{BM}/[Re]_{BM}$ (g g^{-1}) (Eq. 1).

$$J_{CO2} = J_{Re} \times \left([OC]_{BM}/[Re]_{BM}\right) \times f_C \times (1 - f_{graphite}) \quad (1)$$

We correct the estimated CO_2 release to account for the relative mobility of Re and OC_{petro} during weathering in soils, with f_C being the ratio between percentage loss of OC_{petro} in soil versus percentage loss of Re in soil. This factor also accounts for the role of sulfide and silicate minerals as trace sources of dissolved Re (*9*, *27*). On the basis of the published data from soils (*9*, *30*, *39*) and our measurements from the western Southern Alps (table S3), f_C is expected to be <1 but >0.5. To account for the presence of graphite, which may not be oxidized, we vary the fraction of OC_{petro} as graphite ($f_{graphite}$) from 0.5 to 0, informed by measurements from the study location (*33*). The CO_2 oxidation flux, J_{CO2} (gC km^{-2} $year^{-1}$), is calculated using a Monte Carlo simulation to account for these uncertainties (see Materials and Methods).

In the western Southern Alps, watersheds with limited glacial coverage are estimated to release $14\ ^{+9}/_{-5}$ tC km^{-2} $year^{-1}$ (Whataroa) by OC_{petro} oxidation using the Re proxy (table S4). These are similar to OC_{petro} oxidation yields estimated in Taiwan where erosion rates are similar (*9*). This suggests that the Re proxy is producing consistent results at the watershed scale. The Re-derived estimate of CO_2 flux from OC_{petro} oxidation for the glaciated Waiho watershed is approximately double, at $30\ ^{+20}/_{-11}$ tC km^{-2} $year^{-1}$. These values are similar to seasonal measurements of soil respiration in a primary succession on sedimentary rocks exposed by recent glacial retreat in Svalbard (~10 to 24 tC km^{-2} $year^{-1}$, based on monthly averaged data) (*46*) but lower than typical rates of soil respiration in mineral soils that contain non–rock-derived organic matter (*47*). Although the uncertainties on the CO_2 fluxes are relatively large on the basis of our current understanding of Re and OC_{petro} mobility, the difference between the glaciated watersheds and the other watersheds is larger than these uncertainties (table S4).

In watersheds where mountain glaciers are confined to headwaters, the Re-derived estimates of CO_2 release do not negate CO_2 drawdown by silicate weathering [~2 to 10 tC km^{-2} $year^{-1}$ (*24*)] and by erosion and sedimentary burial of biospheric OC [Fig. 3; ~40 tC km^{-2} $year^{-1}$ (*22*)]. In stark contrast, the doubling of the OC_{petro} oxidation rate in the Waiho watershed converts it into a net CO_2 source during erosion and weathering (Fig. 3). At present, the Waiho and Fox rivers drain less than 5% of the sampled area (Fig. 1A), so the enhanced glacial contribution to CO_2 fluxes from OC_{petro} oxidation has a modest influence across the mountain belt. However, under more heavily glaciated conditions, the Southern Alps would be primed to act as a CO_2 source. Accelerated OC_{petro} oxidation driven by the physical and biogeochemical mechanisms that we have identified may have increased CO_2 emissions (Fig. 2). The heavily glaciated western Southern Alps watersheds indicate that biospheric OC erosion and burial will also decrease as glacial cover increases. In addition, at high erosion rates and high rates of mineral supply, silicate weathering rates are very sensitive to temperature and

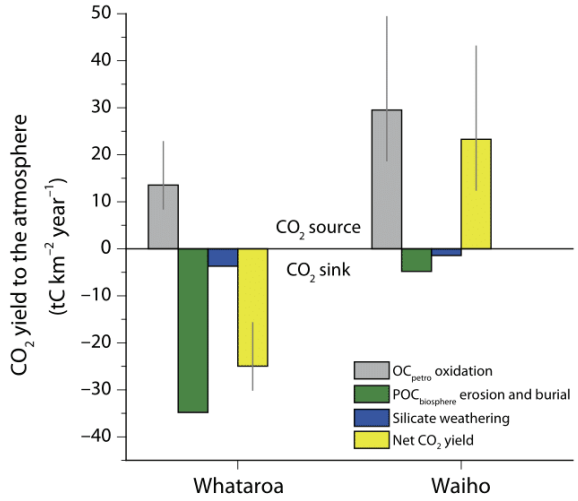

Fig. 3. Net carbon balance due to erosion and weathering in the western Southern Alps. Two watersheds with contrasting glacial coverage area are shown: the Whataroa (9.7% glacier coverage) and the Waiho (57.6% glacier coverage). The CO_2 release to the atmosphere by OC_{petro} weathering (this study; from dissolved Re measurements) is shown alongside the CO_2 drawdown by erosion and burial of biospheric particulate OC ($POC_{biosphere}$) (*22*) and silicate weathering (*20*, *24*).

runoff (*6*, *12*), and cooler temperatures may decrease rates of CO_2 drawdown (Fig. 3).

The global CO_2 emissions by OC_{petro} oxidation remain to be better quantified. Nevertheless, they are probably as large as those from volcanic degassing (*1*). To evaluate the strength of this feedback in glaciated mountain belts for counteracting global cooling and for potentially having the capacity to end a glaciation, both the OC_{petro} presence and abundance in glaciated mountain ranges must be taken into account. By way of example, the Himalaya has the potential to be a key site for CO_2 fluxes by OC_{petro} oxidation because it hosts OC_{petro}-bearing Tethyan Sedimentary Series shales at high altitudes. Furthermore, around the world, rocks containing OC_{petro} have been subject to repeated mountain glaciation throughout the Late Cenozoic. Enhanced OC_{petro} oxidation in locations such as the Rockies, the Andes, and the European Alps (*21*) could have driven these sites to operate as important CO_2 sources and O_2 sinks during sustained periods of global cooling and glaciation over 10^4 to $>10^6$ years (*5*). OC_{petro} oxidation could act in tandem with transient CO_2 emissions from enhanced sulfide oxidation and weathering of carbonate minerals by sulfuric acid, during glaciation (*48*). Although the global fluxes are difficult to quantify from the available data (Fig. 2), enhanced OC_{petro} oxidation associated with more extensive glacial erosion processes is consistent with the ~2% decline in atmospheric O_2 recorded in ice cores over the past 800,000 years (*5*). If the decline in atmospheric O_2 results from changes in OC burial versus OC_{petro} oxidation alone, it implies a net CO_2 release of ~3×10^{11} mol $year^{-1}$ or ~3 to 4×10^6 tC $year^{-1}$ (*5*). This corresponds to only a modest (~6%) increase in global OC_{petro} oxidation rates (*1*) over this period in which the duration and intensity of glaciation increased (*21*). We propose that the link between OC_{petro} weathering and mountain glaciation offers a previously unrecognized feedback between climate and the carbon cycle, where increased CO_2 emissions act to counter further global cooling during the Late Cenozoic.

MATERIALS AND METHODS

Sample collection

Samples were collected from 13 watersheds in the western Southern Alps, which drain to the west of the main divide, two draining the eastern Southern Alps to the east of the main divide and the Waipaoa River in North Island, New Zealand (tables S1 to S3). Together, these watersheds allowed us to examine the dual roles of physical erosion rate (*9*) and glacial coverage on OC_{petro} weathering. The Southern Alps is a steep mountain belt built by transpression along the Alpine Fault. The western flank has a temperate climate, with a high erosion rate driven by orographic precipitation (exceeding 8 m $year^{-1}$), steep slopes, and bedrock landslides, which expose OC_{petro} in metasedimentary rocks (*34*). Previous work has documented high rates of silicate and carbonate weathering in the western Southern Alps (*20*, *24*). Erosion dominates the denudation, with the largest percentage of chemical denudation occurring in the Haast watershed (5%) (*24*). Along the western Southern Alps, the metamorphic grade varies perpendicular to the Alpine Fault strike, but the sedimentary protolith is similar in all watersheds, and the OC_{petro} content ranges from ~0.1 to ~0.2% (*22*, *33*). In contrast, there are significant differences in glacial coverage (Fig. 1A), including two watersheds with large valley glaciers (Waiho and Fox) and some frontal watersheds with very minimal glacial coverage (for example, Waitangitaona). The eastern Southern Alps is also dominated by glacial processes but experiences lower precipitation (<2 m $year^{-1}$), lower rates of bedrock landsliding (*15*), and slower long-term exhumation rates (*49*). As a result, the chemical denudation rates are also lower (*50*). The Waipaoa River in North Island, New Zealand drains lower metamorphic grade OC_{petro}-bearing sedimentary rocks at high erosion rates but lacks glacial influence (*51*, *52*).

To assess OC_{petro} oxidation in the western Southern Alps, we sampled the dissolved products of chemical weathering, weathered colluvium on hillslopes, and relatively unweathered river bed materials of sand and finer grade. River waters (n = 51) were collected from the center of river channels at their surface. Watersheds were sampled two to six times over 1 month (14 September 2014 to 03 October 2014) at variable flow to examine the hydrological variability of the dissolved ions released from chemical weathering (*40*). Water samples were decanted to sterile plastic containers before filtration through 0.2-μm polyethersulfone filters with a diameter of 142 mm within a day of collection and stored in acid-cleaned low-density polyethylene bottles. Alkalinity measurements were made by Gran titration on an aliquot of filtered water. All water samples intended for cation and Re analysis were acidified in the field to pH ~2 (*9*, *31*), with an unacidified aliquot for anion analyses. Two 250-ml rainwater samples were collected over 10-hour periods (table S1).

In the western Southern Alps, soils are thin and weathering profiles are often poorly developed (*25*). Landslide-derived colluvium is an important locus of weathering (*26*). Therefore, to characterize Re and OC_{petro} behavior in the weathering zone, we collected ~500-cm^3-sized bulk samples of weathered colluvium at discrete depths between 10 and 70 cm below the soil surface at three sites on the forested hillslopes of Alex Knob, which drains to the Docherty Creek watershed. We also collected surface soil samples from the upper 3 cm that comprised a mixture of litter and mineral soil (n = 5) using a metal trowel and transferred samples to sterile plastic bags (table S3).

River bed material samples (n = 31) were also collected to help constrain the composition of unweathered materials (tables S2 and S3) (*9*). Samples were taken from channel edges or bank deposits that were taken to represent the sand-to-silt fraction deposited on the river bed during recent flow regimes and transferred to sterile plastic

bags. River water samples and bed materials were also collected from the eastern Southern Alps and Waipaoa River using these methods (table S2).

Geochemical analyses

Dissolved Re concentrations in river water samples ($[Re]_{diss}$, pmol liter^{-1}) were measured by isotope dilution quadrupole ICP-MS (Q-ICP-MS) in conjunction with anion exchange column chemistry to preconcentrate and purify Re. Between 30 and 500 ml of water samples was doped with a known amount of tracer solution consisting of enriched ^{185}Re and evaporated to dryness, with the dried sample dissolved in HNO_3 before anion exchange column chemistry.

Solid samples (surface soil, weathered colluvium, and river bed materials) were ground to a fine powder before acid digestion to generate an integrated bulk sample. Homogenizing bedload samples permitted assessment of the average Re composition of the rocks at the watershed scale for each river because fluvial transit times are short. A known weight of powder (~0.5 g) was doped with a known amount of ^{185}Re spike and digested in a 6:3 HF-HNO_3 mix (9 ml) for 24 hours at 120°C and then evaporated. The dried sample was further digested in a 2:1 mix of HNO_3-HCl (3 ml) for 24 hours at 120°C and then evaporated. Re was isolated and purified using a NaOH-acetone solvent extraction methodology (*53*).

The Re isotope composition of the purified Re aliquots were determined in a 0.8 N HNO_3 medium using a Thermo Fisher Scientific X-Series Q-ICP-MS at Durham University. The procedural blank was ~1% of the lowest concentration samples. Uncertainties in the Re abundance were determined by error propagation of uncertainties in Re mass spectrometry measurements, blank abundance and isotopic compositions, spike calibrations, and reproducibility of standard Re isotopic values. Repeat analyses of $[Re]_{diss}$ in a river water standard, SLRS-5, gave a concentration of 59.8 ± 1.7 ppt (n = 12, ±2 SE), in agreement with the previously reported value of 66 ± 12 ppt (*54*).

Major ion concentrations in water samples were analyzed by ion chromatography. Cation and anion standards and a certified reference standard (LETHBRIDGE-03) were run to validate the analytical results. The HCO_3^- concentration was estimated using total alkalinity, temperature, and pH (measured in the field) data inputted to CO2SYS (*55*). The charge balance of dissolved cations ($TZ^+ = Na^+ + K^+, 2Mg^{2+} + 2Ca^{2+}$) and dissolved anions ($TZ^- = Cl^- + HCO_3^- + 2SO_4^{2-}$) was determined ($[TZ^+ - TZ^-]/[TZ^+ + TZ^-]$) as a measure of data quality (*20*). This was 11% across all samples, within the combined uncertainty and similar to previous work in this location (*20*).

In river bed materials, surface soils, and weathered colluvium, the OC concentration ([OC], %) was measured following a 0.2 N HCl leach protocol (*56*), which was tested on samples from this location to ensure full removal of detrital carbonates. Aliquots of samples were combusted, and the concentration and stable isotope composition of OC ($\delta^{13}C$, ‰) were determined using a Costech elemental analyzer coupled to a Thermo Fisher Scientific Delta V Advantage isotope ratio mass spectrometer at Durham University. Corrections for procedural and instrument blanks were applied, and the result normalized to the composition of international standards (reported relative to Vienna Pee Dee Belemnite with a precision of 0.2‰). The radiocarbon activity (reported as the fraction modern, F_{mod}) was measured on four colluvium samples and two soil litters by accelerator mass spectrometry at the University of California, Irvine Keck Carbon Cycle facility, following graphitization. Sample preparation background was subtracted based on measurements of ^{14}C-free coal processed through the full protocol (table S3).

OC_{petro} content of weathered colluvium

To assess the OC_{petro} content of the weathered colluvium samples and to account for OC derived from recent productivity (biospheric OC), we adopted a mixing analysis based on observations of $\delta^{13}C$ and F_{mod} values. The ^{14}C activity of sedimentary rocks is generally considered to be below the analytical background, that is, F_{mod} = 0, and thus distinct from modern biospheric OC (F_{mod} ~ 1) and degraded soil of ~1000 years old (F_{mod} ~ 0.9). The $\delta^{13}C$ of OC_{petro} in the Southern Alps was ^{13}C-enriched ($\delta^{13}C$ ~ −21 to −22‰) compared to the terrestrial biosphere (dominated by C_3 plants) (*22*).

The stable isotope composition of an element shown against the reciprocal of its concentration can reveal mixing trends or processes that alter the concentration and fractionate isotopes. Surface soil litters are OC-rich and ^{13}C-depleted, and they describe a linear trend between $\delta^{13}C_{org}$ and 1/[OC], albeit one that only describes ~40% of the variability in the data. This is consistent with the degradation of plant-derived OC in surface soils, loss of OC, and enrichment in ^{13}C (fig. S2A). In contrast, the weathered colluvium samples define a different linear trend, which we interpret as a mixture of degraded biospheric organic matter (originally derived from the surface soil) with ^{13}C-enriched, OC-poor material from the sedimentary rocks (fig. S2B). The intercept of these two trends implies that the degraded soil OC has a value of −26.8 ± 0.8‰ (propagating the 95% uncertainty bounds on the linear trends).

The weathered colluvium samples are also ^{14}C-depleted (fig. S2B), which is consistent with OC_{petro} addition. The samples can be described by a linear trend between F_{mod} and $\delta^{13}C_{org}$ that intercepts biospheric and petrogenic OC (fig. 2B). Using the "degraded soil" $\delta^{13}C_{org}$ value (fig. S2A) and the trend defined by the samples, we estimated the F_{mod} of the biospheric OC in these samples as F_{mod} = 0.93 ± 0.36. These values and their uncertainties were used in a two-component end member mixing model (*51*) to quantify the fraction of OC_{petro} (f_{petro}) and the corresponding $[OC]_{petro}$ ($f_{petro} \times [OC]$) (table S3). This approach does not consider additional aging of biospheric OC, which would act to reduce the F_{mod} of the biospheric OC. We therefore calculated an upper bound on the $[OC_{petro}]$ and a lower bound on the loss of OC_{petro} during weathering. The weathered colluvium samples had an average $[OC_{petro}]$ = 0.15 ± 0.06% (n = 4, ±2 SE), which is lower than the local river bed materials in this watershed ($[OC]_{BM}$ = 0.21%) (table S3). Coupled loss of Re and OC_{petro} during chemical weathering supports measurements on soils from the Ohio Shale (table S1) (*30*), the Himalaya (*39*), and Taiwan (*9*). These data sets generally show that Re is more mobile during weathering, and so the dissolved Re flux must be corrected when estimating an OC_{petro} weathering rate (*9*).

Dissolved Re flux

To assess whether the average of the ion concentrations collected at low Q_w may overestimate the dissolved ion flux, we compared the flux calculated using an average concentration method to that calculated by a rating curve method (taking into account dilution) using published data sets from the study location (*24*). For these data, the average measured $[Ca^{2+}]$ multiplied by the mean annual runoff returns a Ca^{2+} flux of 4.21 × 10^8 mol year^{-1} for the Hokitika River. If we model the $[Ca^{2+}]$-Q_w relationship (fig. S1B) as a power law rating curve (*57*) and apply it to the daily Q_w data from 1971 to 2015, the annual Ca^{2+} flux = 4.39 × 10^8 mol year^{-1}. The methods agree within 4%, with the average concentration method slightly underestimating flux. In comparison, for the SO_4^{2-} flux, which also shows dilution with Q_w in published data (*24*), the difference in estimated fluxes is 3%. Assuming similar dilution trends for $[Re]_{diss}$ as for $[Ca^{2+}]$ and $[SO_4^{2-}]$, which is suggested on the basis of

the available data (fig. S2C), results in a <5% underestimation of flux. Although a longer time series sampling would be informative for tracking the dissolved ion source and linking it to hydrological pathways (*40*, *57*), an average concentration with an accuracy of within ~5% is adequate for calculating the flux.

Quantification of OC_{petro} oxidation rate and its uncertainty

To convert the dissolved Re flux to an estimate of CO_2 release, there are known uncertainties related to the behavior of Re and OC_{petro} during weathering (*1*, *9*). The main uncertainties in this setting are as follows: (i) Because Re is a soluble element, oxidative weathering may mobilize Re more effectively during early soil formation, meaning that some Re measured in river waters does not correspond to release of CO_2 at the weathering site (*30*); (ii), partly related to (i), some dissolved Re may come from sulfide and silicate minerals (*9*, *27*); and (iii) graphitic OC_{petro} may not be susceptible to oxidation and remain in the soil (*32*, *58*). Regarding point (i) and (ii), soils from Taiwan suggest congruent dissolution of Re, and loss of OC_{petro} can occur during weathering of young, thin soils (*9*). On a soil profile developed on OC_{petro}-rich shale from Ohio (*30*), Re depletion reaches 100% in the most highly weathered soil, whereas OC_{petro} loss is ~70% (table S1). The data from weathered colluvium in the western Southern Alps are more consistent with the Ohio Shale than Taiwan. For point (iii), graphite is present in rocks within a kilometer of the Alpine Fault, making up almost 50% of the OC (*33*), and its measured abundance decreases to small amounts ~10 to 20 km from the Alpine Fault (*59*).

To account for and quantify the uncertainties on the CO_2 flux estimate we used a Monte Carlo simulation. This includes uncertainty on the dissolved Re flux, the measured variability in $[OC]_{BM}/[Re]_{BM}$, and the assumptions (i), (ii), and (ii) above. For each watershed (area = A km^2), we used ±2 SE on the mean for the $[Re]_{diss}$ and the $[OC]_{BM}/[Re]_{BM}$ ratio. To account for the relative mobility of Re and OC_{petro} during weathering (*30*), we defined f_C as the ratio between the percentage loss of OC_{petro} in soil compared to bedrock and the percentage loss of Re in soil compared to bedrock. On the basis of published work, we varied f_C from 0.5 to 1 (*9*, *30*). To account for the presence of graphite, which may not be oxidized, we varied the fraction of OC_{petro} as graphite ($f_{graphite}$) from 0.5 to 0, informed by measurements from the study location (*33*). The CO_2 oxidation flux, J_{CO2} (gC km^{-2} $year^{-1}$), was then calculated using Eq. 1.

The Monte Carlo simulation was run 100,000 times for each watershed, with a "full probability" distribution for each variable. We reported the median value ± 1 SD range. This reflects the present state of knowledge of the Re proxy for OC_{petro} oxidation. Future work should seek to refine this approach and reduce the uncertainties, for a better understanding of f_C and $f_{graphite}$. By doing so, it may be possible to quantify watershed-scale fluxes using Re measurements more widely (*1*).

Quantification of glacier cover using the World Glacier Inventory

The relative importance of glacial processes in the watersheds of the western Southern Alps was quantified using glacier locations and areas from the World Glacier Inventory (*23*). The total sum of glacier area (km^2) was quantified for each watershed using ArcGIS, with flow routing algorithms to isolate drainage areas (table S4). In the global data set, published estimates were used (table S6).

Biospheric OC erosion and burial

Previous work has estimated the erosion rate of biospheric OC in watersheds of the western Southern Alps (*22*). To estimate how this contributes to CO_2 drawdown, we required an estimate of the burial efficiency of OC. On the basis of a recent global compilation (*44*), the sediment yield to an offshore basin plays an important role in setting the burial efficiency of OC. This is because sediment accumulation rate is a first-order control on OC burial efficiency in many marine environments (*60*). Using the sediment yield of ~6000 to 10,000 t km^{-2} $year^{-1}$ for the western Southern Alps (*22*), the burial efficiency would be predicted to be from ~40% to 100% based on the global data set (*44*). A high burial efficiency would be consistent with the very high preservation potential of terrestrial palynomorphs offshore from the western Southern Alps (*61*). To provide a conservative estimate of biospheric OC burial, we used the lowest value in this range (40%) and multiplied the erosional export flux (*22*) by the OC burial efficiency to estimate CO_2 drawdown by biospheric OC erosion as shown in Fig. 3.

SUPPLEMENTARY MATERIALS

Supplementary material for this article is available at http://advances.sciencemag.org/cgi/content/full/3/10/e1701107/DC1

fig. S1. Weathered colluvium from the western Southern Alps.
fig. S2. Dissolved major ion concentrations in the western Southern Alps.
table S1. River bed materials.
table S2. Re and OC_{petro} in weathered colluvium.
table S3. Major ion and Re concentration data for water samples from the Southern Alps, New Zealand.
table S4. Western Southern Alps watershed average data and dissolved Re yield estimates.
table S5. Hydrological data for watersheds with river gauging stations.
table S6. Global watershed averaged Re measurements from mountain rivers draining sedimentary rocks.
Reference (*62*–*66*)

REFERENCES AND NOTES

1. S. T. Petsch, Weathering of organic carbon, in *Treatise on Geochemistry* (Elsevier, ed. 2, 2014), vol. 12, pp. 217–238.
2. R. A. Berner, D. E. Canfield, A new model for atmospheric oxygen over phanerozoic time. *Am. J. Sci.* **289**, 333–361 (1989).
3. C. France-Lanord, L. A. Derry, Organic carbon burial forcing of the carbon cycle from Himalayan erosion. *Nature* **390**, 65–67 (1997).
4. R. A. Berner, K. Caldeira, The need for mass balance and feedback in the geochemical carbon cycle. *Geology* **25**, 955–956 (1997).
5. D. A. Stolper, M. L. Bender, G. B. Dreyfus, Y. Yan, J. A. Higgins, A Pleistocene ice core record of atmospheric O_2 concentrations. *Science* **353**, 1427–1430 (2016).
6. K. Maher, C. P. Chamberlain, Hydrologic regulation of chemical weathering and the geologic carbon cycle. *Science* **343**, 1502–1504 (2014).
7. J. M. Hayes, H. Strauss, A. J. Kaufman, The abundance of ^{13}C in marine organic matter and isotopic fractionation in the global biogeochemical cycle of carbon during the past 800 Ma. *Chem. Geol.* **161**, 103–125 (1999).
8. S. T. Petsch, R. A. Berner, T. I. Eglinton, A field study of the chemical weathering of ancient sedimentary organic matter. *Org. Geochem.* **31**, 475–487 (2000).
9. R. G. Hilton, J. Gaillardet, D. Calmels, J.-L. Birck, Geological respiration of a mountain belt revealed by the trace element rhenium. *Earth Planet. Sci. Lett.* **403**, 27–36 (2014).
10. J. Zachos, M. Pagani, L. Sloan, E. Thomas, K. Billups, Trends, rhythms, and aberrations in global climate 65 Ma to present. *Science* **292**, 686–693 (2001).
11. S. Chang, R. A. Berner, Coal weathering and the geochemical carbon cycle. *Geochim. Cosmochim. Acta* **63**, 3301–3310 (1999).
12. A. J. West, Thickness of the chemical weathering zone and implications for erosional and climatic drivers of weathering and for carbon-cycle feedbacks. *Geology* **40**, 811–814 (2012).
13. E. W. Bolton, R. A. Berner, S. T. Petsch, The weathering of sedimentary organic matter as a control on atmospheric O_2: II. Theoretical modeling. *Am. J. Sci.* **306**, 575–615 (2006).
14. S. T. Petsch, T. I. Eglinton, K. J. Edwards, ^{14}C-dead living biomass: Evidence for microbial assimilation of ancient organic carbon during shale weathering. *Science* **292**, 1127–1131 (2001).
15. T. C. Hales, J. J. Roering, A frost "buzzsaw" mechanism for erosion of the eastern Southern Alps, New Zealand. *Geomorphology* **107**, 241–253 (2009).
16. S. P. Anderson, Glaciers show direct linkage between erosion rate and chemical weathering fluxes. *Geomorphology* **67**, 147–157 (2005).
17. R. D. Bardgett, A. Richter, R. Bol, M. H. Garnett, R. Bäumler, X. Xu, E. Lopez-Capel, D. A. C. Manning, P. J. Hobbs, I. R. Hartley, W. Wanek, Heterotrophic microbial communities use ancient carbon following glacial retreat. *Biol. Lett.* **3**, 487–490 (2007).

18. M. Tranter, M. J. Sharp, H. R. Lamb, G. H. Brown, B. P. Hubbard, I. C. Willis, Geochemical weathering at the bed of Haut Glacier d'Arolla, Switzerland—A new model. *Hydrol. Process.* **16**, 959–993 (2002).
19. J. L. Wadham, S. Bottrell, M. Tranter, R. Raiswell, Stable isotope evidence for microbial sulphate reduction at the bed of a polythermal high Arctic glacier. *Earth Planet. Sci. Lett.* **219**, 341–355 (2004).
20. A. D. Jacobson, J. D. Blum, C. P. Chamberlain, D. Craw, P. O. Koons, Climatic and tectonic controls on chemical weathering in the New Zealand Southern Alps. *Geochim. Cosmochim. Acta* **67**, 29–46 (2003).
21. F. Herman, D. Seward, P. G. Valla, A. Carter, B. Kohn, S. D. Willett, T. A. Ehlers, Worldwide acceleration of mountain erosion under a cooling climate. *Nature* **504**, 423–426 (2013).
22. R. G. Hilton, A. Galy, N. Hovius, Riverine particulate organic carbon from an active mountain belt: Importance of landslides. *Global Biogeochem. Cycles* **22**, GB1017 (2008).
23. National Snow and Ice Data Center, "World Glacier Inventory" (2016); http://nsidc.org/.
24. W. B. Lyons, A. E. Carey, D. M. Hicks, C. A. Nezat, Chemical weathering in high-sediment-yielding watersheds, New Zealand. *J. Geophys. Res. Earth Surf.* **110**, F01008 (2005).
25. I. J. Larsen, P. C. Almond, A. Eger, J. O. Stone, D. R. Montgomery, B. Malcolm, Rapid soil production and weathering in the Southern Alps, New Zealand. *Science* **343**, 637–640 (2014).
26. R. Emberson, N. Hovius, A. Galy, O. Marc, Chemical weathering in active mountain belts controlled by stochastic bedrock landsliding. *Nat. Geosci.* **9**, 42–45 (2016).
27. C. A. Miller, B. Peucker-Ehrenbrink, B. D. Walker, F. Marcantonio, Re-assessing the surface cycling of molybdenum and rhenium. *Geochim. Cosmochim. Acta* **75**, 7146–7179 (2011).
28. D. Selby, R. A. Creaser, Re–Os geochronology of organic rich sediments: An evaluation of organic matter analysis methods. *Chem. Geol.* **200**, 225–240 (2003).
29. D. Colodner, J. Sachs, G. Ravizza, K. Turekian, J. Edmond, E. Boyle, The geochemical cycle of rhenium: A reconnaissance. *Earth Planet. Sci. Lett.* **117**, 205–221 (1993).
30. L. A. Jaffe, B. Peucker-Ehrenbrink, S. T. Petsch, Mobility of rhenium, platinum group elements and organic carbon during black shale weathering. *Earth Planet. Sci. Lett.* **198**, 339–353 (2002).
31. T. K. Dalai, S. K. Singh, J. R. Trivedi, S. Krishnaswami, Dissolved rhenium in the Yamuna river system and the Ganga in the Himalaya: Role of black shale weathering on the budgets of Re, Os, and U in rivers and CO_2 in the atmosphere. *Geochim. Cosmochim. Acta* **66**, 29–43 (2002).
32. V. Galy, O. Beyssac, C. France-Lanord, T. Eglinton, Recycling of graphite during Himalayan erosion: A geological stabilization of carbon in the crust. *Science* **322**, 943–945 (2008).
33. L. Nibourel, F. Herman, S. C. Cox, O. Beyssac, J. Lavé, Provenance analysis using Raman spectroscopy of carbonaceous material: A case study in the Southern Alps of New Zealand. *J. Geophys. Res. Earth Surf.* **120**, 2056–2079 (2015).
34. N. Hovius, C. P. Stark, P. A. Allen, Sediment flux from a mountain belt derived by landslide mapping. *Geology* **25**, 231–234 (1997).
35. L. J. Reusser, P. R. Bierman, Using meteoric 10Be to track fluvial sand through the Waipaoa River basin, New Zealand. *Geology* **38**, 47–50 (2010).
36. M. Dellinger, J. Gaillardet, J. Bouchez, D. Calmels, V. Galy, R. G. Hilton, P. Louvat, C. France-Lanord, Lithium isotopes in large rivers reveal the cannibalistic nature of modern continental weathering and erosion. *Earth Planet. Sci. Lett.* **401**, 359–372 (2014).
37. R. G. Hilton, A. Galy, N. Hovius, M.-J. Horng, H. Chen, Efficient transport of fossil organic carbon to the ocean by steep mountain rivers: An orogenic carbon sequestration mechanism. *Geology* **39**, 71–74 (2011).
38. A. Dubin, B. Peucker-Ehrenbrink, The importance of organic-rich shales to the geochemical cycles of rhenium and osmium. *Chem. Geol.* **403**, 111–120 (2015).
39. A.-C. Pierson-Wickmann, L. Reisberg, C. France-Lanord, Behavior of Re and Os during low-temperature alteration: Results from Himalayan soils and altered black shales. *Geochim. Cosmochim. Acta* **66**, 1539–1548 (2002).
40. K. Maher, The role of fluid residence time and topographic scales in determining chemical fluxes from landscapes. *Earth Planet. Sci. Lett.* **312**, 48–58 (2011).
41. D. M. Hicks, U. Shankar, A. I. McKerchar, L. Basher, I. Lynn, M. Page, M. Jessen, Suspended sediment yields from New Zealand rivers. *J. Hydrol.* **50**, 81–142 (2011).
42. O. Korup, Landslide-induced river channel avulsions in mountain catchments of southwest New Zealand. *Geomorphology* **63**, 57–80 (2004).
43. S. J. Dadson, N. Hovius, H. Chen, W. B. Dade, M.-L. Hsieh, S. D. Willett, J.-C. Hu, M.-J. Horng, M.-C. Chen, C. P. Stark, D. Lague, J.-C. Lin, Links between erosion, runoff variability and seismicity in the Taiwan orogen. *Nature* **426**, 648–651 (2003).
44. V. Galy, B. Peucker-Ehrenbrink, T. Eglinton, Global carbon export from the terrestrial biosphere controlled by erosion. *Nature* **521**, 204–207 (2015).
45. M. M. Dornblaser, R. G. Striegl, Suspended sediment and carbonate transport in the Yukon River Basin, Alaska: Fluxes and potential future responses to climate change. *Water Resour. Res.* **45**, W06411 (2009).
46. Y. S. Bekku, A. Kume, T. Masuzawa, H. Kanda, T. Nakatsubo, H. Koizumi, Soil respiration in a high arctic glacier foreland in Ny-Alesund, Svalbard. *Polar Biosci.* **17**, 36–46 (2004).
47. C. E. Hicks Pries, C. Castanha, R. C. Porras, M. S. Torn, The whole-soil carbon flux in response to warming. *Science* **355**, 1420–1423 (2017).
48. M. A. Torres, N. Moosdorf, J. Hartmann, J. F. Adkins, A. J. West, Glacial weathering, sulfide oxidation, and global carbon cycle feedbacks. *Proc. Natl. Acad. Sci. U.S.A.* **114**, 8716–8721 (2017).
49. J. M. Tippett, P. J. J. Kamp, Fission track analysis of the Late Cenozoic vertical kinematics of continental pacific crust, South Island, New Zealand. *J. Geophys. Res. Solid Earth* **98**, 16119–16148 (1993).
50. A. D. Jacobson, J. D. Blum, Relationship between mechanical erosion and atmospheric CO_2 consumption in the New Zealand Southern Alps. *Geology* **31**, 865–868 (2003).
51. E. L. Leithold, N. E. Blair, D. W. Perkey, Geomorphologic controls on the age of particulate organic carbon from small mountainous and upland rivers. *Global Biogeochem. Cycles* **20**, GB3022 (2006).
52. B. Gomez, N. A. Trustrum, D. M. Hicks, K. M. Rogers, M. J. Page, K. R. Tate, Production, storage, and output of particulate organic carbon: Waipaoa River basin, New Zealand. *Water Resour. Res.* **39**, 1161 (2003).
53. V. M. Cumming, S. W. Poulton, A. D. Rooney, D. Selby, Anoxia in the terrestrial environment during the late Mesoproterozoic. *Geology* **41**, 583–586 (2013).
54. D. Yeghicheyan, C. Bossy, M. Bouhnik Le Coz, C. Douchet, G. Granier, A. Heimburger, F. Lacan, A. Lanzanova, T. C. C. Rousseau, J.-L. Seidel, M. Tharaud, F. Candaudap, J. Chmeleff, C. Cloquet, S. Delpoux, M. Labatut, R. Losno, C. Pradoux, Y. Sivry, J. E. Sonke, A compilation of silicon, rare earth element and twenty-one other trace element concentrations in the natural river water reference material SLRS-5 (NRC-CNRC). *Geostand. Geoanal. Res.* **37**, 449–467 (2013).
55. E. R. Lewis and D. W. R. Wallace, Program Developed for CO_2 System Calculations (ORNL/CDIAC-105, 1998).
56. V. Galy, J. Bouchez, C. France-Lanord, Determination of total organic carbon content and $\delta^{13}C$ in carbonate-rich detrital sediments. *Geostand. Geoanal. Res.* **31**, 199–207 (2007).
57. E. T. Tipper, M. J. Bickle, A. Galy, A. J. West, C. Pomiès, H. J. Chapman, The short term climatic sensitivity of carbonate and silicate weathering fluxes: Insight from seasonal variations in river chemistry. *Geochim. Cosmochim. Acta* **70**, 2737–2754 (2006).
58. J. Bouchez, O. Beyssac, V. Galy, J. Gaillardet, C. France-Lanord, L. Maurice, P. Moreira-Turcq, Oxidation of petrogenic organic carbon in the Amazon floodplain as a source of atmospheric CO_2. *Geology* **38**, 255–258 (2010).
59. O. Beyssac, S. C. Cox, J. Vry, F. Herman, Peak metamorphic temperature and thermal history of the Southern Alps (New Zealand). *Tectonophysics* **676**, 229–249 (2016).
60. N. E. Blair, R. C. Aller, in *Annual Review of Marine Science*, C. A. Carlson, S. J. Giovannoni, Eds. (Annual Reviews, 2012), vol. 4, pp. 401–423.
61. M. T. Ryan, R. M. Newnham, G. B. Dunbar, M. J. Vandergoes, A. B. H. Rees, H. Neil, S. L. Callard, B. V. Alloway, H. Bostock, Q. Hua, B. M. Anderson, Exploring the source-to-sink residence time of terrestrial pollen deposited offshore Westland, New Zealand. *Rev. Palaeobot. Palyno.* **230**, 37–46 (2016).
62. S. E. Tank, P. A. Raymond, R. G. Striegl, J. W. McClelland, R. M. Holmes, G. J. Fiske, B. J. Peterson, A land-to-ocean perspective on the magnitude, source and implication of DIC flux from major Arctic rivers to the Arctic Ocean. *Global Biogeochem. Cycles* **26**, GB4018 (2012).
63. W. W. Immerzeel, M. F. P. Bierkens, Seasonal prediction of monsoon rainfall in three Asian river basins: The importance of snow cover on the Tibetan plateau. *Int. J. Climatol.* **30**, 1835–1842 (2010).
64. A.-C. Pierson-Wickmann, L. Reisberg, C. France-Lanord, The Os isotopic composition of Himalayan river bedloads and bedrocks: Importance of black shales. *Earth Planet. Sci. Lett.* **176**, 203–218 (2000).
65. Y. Huh, J.-L. Birck, C. J. Allègre, Osmium isotope geochemistry in the Mackenzie River basin. *Earth Planet. Sci. Lett.* **222**, 115–129 (2004).
66. T. P. Brabets, B. Wang, R. H. Meade, "Environmental and hydrologic overview of the Yukon River basin, Alaska and Canada," *Water-Resources Investigations Report* (2000).

Acknowledgments: We thank S. Hawley for field assistance; X. Xu for performing ^{14}C analyses; and E. Unsworth, J. Hesselink, and A. Hayton for laboratory support. **Funding:** K.H. was funded by the Natural Environment Research Council (NERC) PhD award (NE/L501724/1). D.G. acknowledges funding from NERC (NE/H020756/1). Fieldwork was funded by a Durham University Grant (Building Research Links in New Zealand) to R.G.H. R.G.H. was also supported by the European Research Council (ERC starting grant 678779, ROC-CO2). D.S. acknowledges the TOTAL Endowment Fund. **Author contributions:** R.G.H. conceived the research and designed the study with K.W.B. and K.H. K.H. and R.G.H. collected the samples. K.H. undertook the geochemical analyses under the supervision of D.S., C.J.O., R.G.H., D.R.G., and K.B. K.H. interpreted the data with R.G.H., K.B., and D.S. M.H. provided the hydrological data. K.H. and R.G.H. wrote the manuscript with input from D.S. and K.B. **Competing interests:** The authors declare that they have no competing interests. **Data and materials availability:** All data needed to evaluate the conclusions in the paper are present in the paper and/or the Supplementary Materials. Additional data related to this paper may be requested from the authors.

Submitted 7 April 2017
Accepted 12 September 2017
Published 4 October 2017
10.1126/sciadv.1701107

Citation: K. Horan, R. G. Hilton, D. Selby, C. J. Ottley, D. R. Gröcke, M. Hicks, K. W. Burton, Mountain glaciation drives rapid oxidation of rock-bound organic carbon. *Sci. Adv.* **3**, e1701107 (2017).

ScienceAdvances

Mountain glaciation drives rapid oxidation of rock-bound organic carbon

Kate Horan, Robert G. Hilton, David Selby, Chris J. Ottley, Darren R. Gröcke, Murray Hicks and Kevin W. Burton

Sci Adv **3** (10), e1701107.
DOI: 10.1126/sciadv.1701107

ARTICLE TOOLS http://advances.sciencemag.org/content/3/10/e1701107

SUPPLEMENTARY MATERIALS http://advances.sciencemag.org/content/suppl/2017/10/02/3.10.e1701107.DC1

REFERENCES This article cites 61 articles, 19 of which you can access for free
http://advances.sciencemag.org/content/3/10/e1701107#BIBL

PERMISSIONS http://www.sciencemag.org/help/reprints-and-permissions

Use of this article is subject to the Terms of Service

Science Advances (ISSN 2375-2548) is published by the American Association for the Advancement of Science, 1200 New York Avenue NW, Washington, DC 20005. 2017 © The Authors, some rights reserved; exclusive licensee American Association for the Advancement of Science. No claim to original U.S. Government Works. The title *Science Advances* is a registered trademark of AAAS.